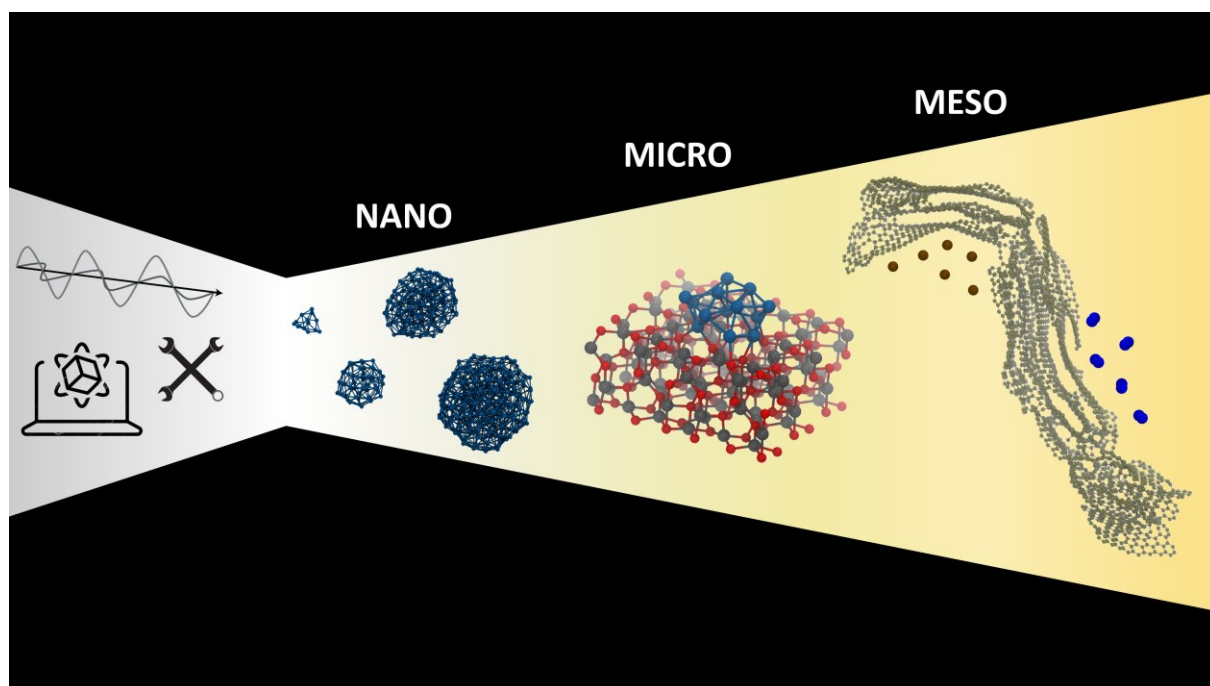**Università degli Studi di Torino**

Doctoral School of the University of Torino

PhD Programme in Chemical and Materials Sciences XXXVI cycle

Surface phenomena at metal nanoparticles and their supports: an experimental and theoretical approach

Alberto Ricchebuono

Supervisor:

Prof. Elena Groppo

Università degli Studi di Torino

Doctoral School of the University of Torino

PhD Programme in Chemical and Materials Sciences XXXVI cycle

Surface phenomena at metal nanoparticles and their supports: an experimental and theoretical approach

Candidate:	**Alberto Ricchebuono**
Supervisor:	**Prof. Elena Groppo**
Jury Members:	**Dr. Frederic C. Meunier** IRCELYON CNRS – Université Claude Bernard de Lyon
	Prof. Alessandro Trovarelli Dipartimento Politecnico di Ingegneria e Architettura University of Udine
	Prof. Piero Ugliengo Dipartimento di Chimica University of Torino

Head of the Doctoral School: Prof. Eleonora Bonifacio

PhD Programme Coordinator: Prof. Bartolomeo Civalleri

Torino, 2024

Table of Contents

Chapter 3 - Unravelling the CO-induced dynamic behaviour of Al_2O_3-supported Pd nanoparticles at room temperature........................ 67

Chapter 1

Introduction

1.1 Supported Pd and Pt nanoparticles as heterogeneous catalysts

A catalyst is a substance able to accelerate chemical reactions without being altered during it, and it does so by "activating" the substrates, allowing them to react and be converted to the products.[1] If the catalytic process happens at an interface, then it is called heterogeneous catalysis, where the reactants and catalyst exist in different phases. Heterogeneous catalysts are most frequently employed in the form of solid powders and the reactants in the form of gases or liquids.[1–4]

Supported metal nanoparticles (NPs) are one of the most relevant categories of heterogeneous catalysts and, among them, precious metals such as Pd and Pt find employment in a variety of applications as heterogeneous catalysts. For example, besides being applied in fuel cells, Pt NPs constitute the active phase in catalysts for the oxidation of organic compounds and pollutants, hydrogenation of biomass and reforming, while Pd-based heterogeneous catalysts are routinely utilized in the purification of the terephthalic acid and pollutant removal, as well as in the synthesis of fine and bulk chemicals.[3] The reason why Pd and Pt NPs have become fundamental in a manifold of processes primarily resides in their electronic structure that makes them able to split and activate several molecules of extreme importance, such as H_2, NO, CO, CO_2, O_2 and hydrocarbons in general.[5–9]

However, the nature of these NPs alone is not sufficient to justify such an intensive application, thus forcing to consider the active contribution of support materials as well. Besides aiding the stabilization of NPs increasing their exposed surface (and thus their activity),[10] metal-support interactions (MSI) are known to play an active role in heterogenous catalysis. Typical phenomena which involve MSI are charge transfers and spillover (i.e. transfer of adsorbed atomic species) between the support and the metallic phase, creation of interfacial sites, migration of metallic atoms on the support and vice versa, as well as support-induced alterations of the NP's morphology.[11,12]

Metal oxides (like Al_2O_3, ZrO_2 and CeO_2) and activated carbons (ACs) are the most employed supports for these metals in heterogenous catalysis.[13–15] If metal oxides can be preferred when their surface chemistry can be exploited (especially in the case of ZrO_2 and CeO_2),[15,16] ACs have found a wide employment due to their high specific surface area (SSA, easily exceeding 1000 m^2/g), high availability of their precursors, low cost of production, stability under reaction conditions and easy recovery of the metallic phase from the exhaust catalyst by combustion.[17] Metal oxides and ACs can be prepared according to different synthetic routes, in which the nature of the precursors and the different activation procedure can strongly influence the surface and textural properties of the material.[15–19] Thus, the fine choice of the right support for dispersing Pd and Pt NPs is fundamental to optimize the performances of the final catalyst.

1.2 Heterogeneous catalysts are complex systems

Heterogeneous catalysts and, particularly, those based on supported metal nanoparticles are generally complex systems characterized by a structural and chemical heterogeneity (Figure 1). The first aspect that stands behind their complex nature is that heterogenous catalysts are

composite materials, that can feature not only many different active phases and supports, but also dopants, alloys and/or mixed phases.[20] Besides having the possibility to expose many different crystal facets, both metal NPs and the supports can show different particle sizes and morphologies within the same catalyst.[21] Moreover, these materials are often characterised by a great number of defects of diverse nature and by a low crystallinity (depending both on the catalyst's nature and on the synthetic approach) which further complicates their comprehension.[22] Moreover, the structure and properties of both the metallic phase and the support can be drastically affected by their interactions with the surrounding environment. Indeed, heterogeneous catalysts can easily undergo reconstructions and modifications after interactions with adsorbates (e.g. reagents, products, solvents, ecc.), thus modifying their properties under reaction conditions.[23]
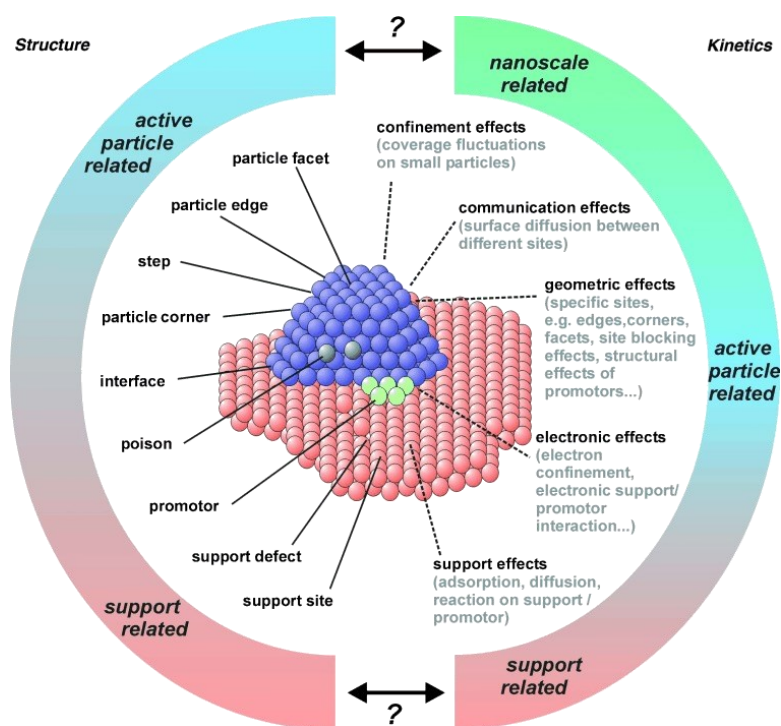
Figure 1. The various elements contributing to the complexity of heterogeneous catalysts are here exemplified for a model metal NP supported on a metal oxide. Adapted from ref. 24.

As a result of the intrinsic complexity of heterogenous catalysts, their exhaustive characterization has faded into the background in the past, making their development mainly based on an empirical trial and error approach.[23,24] Indeed, the most efficient industrial heterogeneous catalysts, such as those used in refining plants,[4] were discovered empirically thanks to sharp chemical intuition. Therefore, many aspects of their structure-activity relationship and their behaviour under reaction conditions are yet to be clarified. A large portion of the nowadays' scientific research on heterogeneous catalysts is thus focused on filling this gap, aiming at exploiting an atomic-level knowledge of these systems to achieve a rational design of new catalysts with enhanced activity and selectivity,[27,28] as well as employable in more environment-friendly and less energetically demanding processes.[29]

1.3 Experiments and simulations as a tool to unravel complex features of heterogeneous catalysts

An accurate control of the catalytic performances of heterogeneous catalysts requires advanced knowledge of the structure of their numerous active sites and of the origin of their catalytic properties, at the atomic scale. Unfortunately, in the light of the extreme complexity of these materials discussed in the previous section, this is not an easy task. The greatest obstacle that is faced when approaching the experimental study of these systems is that the respective contributions of each type of catalytic site, reagent, support contribution, etc. are generally convoluted and/or overlapped in the experimental or catalytic response. In the past, there was a preferred interest into approaching this issue through the synthesis of simple model systems (featuring high crystallinity and a few chemical components) to isolate the single contributions.[30–34] Even though this approach has been able to lead to outstanding advances in the field, the most effective trend in modern research is to exploit the coupling of

several characterization techniques to catch different aspects of the same phenomenon, that must be finally reunited into a closer understanding of the catalyst's behaviour. This working scheme, applied to the design of sophisticated *in situ* and *operando* methodologies has allowed to unravel the complex experimental response of heterogeneous catalysts in many cases.[35–39]

In this scenario, computational chemistry is a powerful tool, which can provide with complementary atomic-scale insight to corroborate and guide experimental observations. Similarly to what outlined for the experimental side, the preferred approach adopted since the 1980s has been to simulate strongly simplified systems (within the paradigm of the ideal surface at low coverage) in static conditions, in order to catch the most general trends of the system at issue.[40–44] The birth of Density Functional Theory (DFT) in 1998[45] and the development of modern high-performance computing (HPC) facilities has opened the path to more sophisticated calculations. This has led to the possibility of running chemically accurate calculations on more complex systems featuring up to a few hundreds of atoms, taking explicitly into account the interaction of the metallic phase with the support, and eventually accessing insight on the catalysts behaviour at the atomic scale by means of DFT molecular dynamics.[22]

Still, given the extreme complexity and structural heterogeneity of heterogeneous catalysts, in some cases, building realistic models forces to take into consideration a great number of different structures and/or bigger models (featuring more than a few hundred of atoms), which often falls beyond the current possibilities of DFT.[46] Aimed to overcome this issue, the last decade has witnessed the birth of a manifold of low-cost computational methods based on semi-empirical approximations, molecular mechanics, neural networks and

machine learning potentials.[47–50] These methods, relying on stronger approximations than DFT, have been developed with the scope of trading some accuracy and transferability for computational speed and are thus applicable to larger and more complex systems (Figure 2). If opportunely validated, these methods can serve as a powerful tool to be employed at the early stages of the simulation to explore the potential energy landscape (PES) of heterogeneous catalysts.[51–53] Providing in this way researchers with a great number of more or less complex candidate structures to undergo a refinement at DFT level, this "multilevel" approach can lead to an accurate computation of molecular properties with an unprecedented insight.
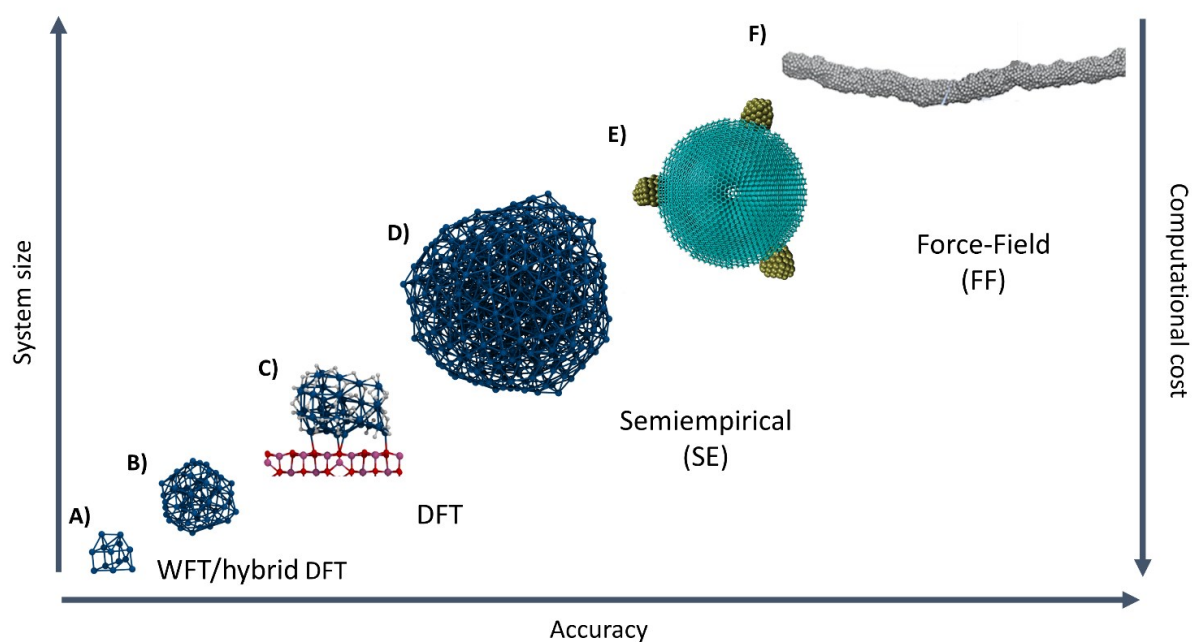
Figure 2. The size-cost-accuracy relationship in modern computational chemistry is outlined for systems ranging from a Pt_{13} NP, which can be simulated at the highest levels of theory (i.e. Wavefunction theory (WFT) and hybrid DFT) up to a Pt nanowire, whose simulation, featuring thousands of atoms, is only affordable at the lowest levels of theory. Images (C), (E) and (F) are adapted, respectively, from ref. 54, 55 and 56.

1.4 Purpose and structure of the PhD thesis

This PhD project was inserted within a long-lasting collaboration between the Department of Chemistry of the University of Torino and the Catalyst Division of Chimet S.p.A. (https://www.chimet.com), an Italian company leader in the recovery and refining of precious metals. In the light of the previous discussion, the aim of the work was to couple experimental and computational methods to correlate structure and reactivity of industrial catalysts consisting of Pd and Pt nanoparticles supported on activated carbons or Al_2O_3. In particular, most of the efforts were directed to three main research questions, each one constituting a chapter of the thesis, as discussed in the following.

1.4.1 The applicability of low-cost computational methods in the simulation of Pt NPs

An evaluation of the performances of some known low-cost methods for the reproduction of structural features of Pt NPs of different size was performed. The PBE-dDsC functional (within the plane-wave formalism) was employed to benchmark the semiempirical DFTB and GFNn-xTB (n = 0,1,2) and the reactive force-field ReaxFF. Performances were evaluated by comparing several size-dependent features (such as relative stabilities, structural descriptors and amorphization energies) computed with the different methods. Four datasets were investigated: (1) 14 Pt_{13} ordered and amorphous NPs; (2) 54 Pt_{13} amorphous NPs; (3) 93 Pt_{55} amorphous NPs; (4) cuboctahedral and amorphous NPs of stoichiometry Pt_{13}, Pt_{55}, Pt_{147}, Pt_{309}, Pt_{561}. The amorphization of Pt_{147}, Pt_{309}, Pt_{561} was achieved through ReaxFF molecular dynamics (MD). While DFTB performs quite well over all the selected structures, GFN2-xTB and the cheaper GFN0-xTB show a general predilection for amorphous geometries. The performances of DFTB and, particularly, of GFN2-xTB are found to worsen with the increasing size of the system, while GFN0-xTB and ReaxFF undergo the opposite trend. An additional annealing of the big-sized Pt_{147}, Pt_{309}, Pt_{561} NPs at GFN0-xTB level was found to improve the similarity of

the geometries to the PBE-dDsC standard, suggesting that GFN0-xTB could be useful to fasten the screening procedure through amorphous big-sized Pt NPs.

1.4.2 The adsorbate-induced ductility of metal NPs

The interaction of small molecular probes with metal NPs has been widely investigated in the past, but very few evidence of adsorbate-induced surface reconstructions were reported, mainly due to experimental and computational limitations. With the improvements in the performances of characterization methods (e.g. in situ TEM or high-resolution spectroscopies), as well as in the potential of computational simulation, more and more studies are currently addressing this topic successfully. Nowadays, there is ample experimental and computational evidence that catalysts based on metal NPs can modify their structure in the presence of adsorbates and/or under reaction conditions with consequences on their activity, selectivity and stability. However, very few literature has faced the problem of adsorbate-induced surface reconstruction for Pd-based systems so far.

A great part of this work was devoted to collect experimental and computational evidence of a CO-induced surface reconstruction occurring on an industrial 5 wt.% Pd/Al_2O_3 catalyst, already widely characterized in the past in this same research group. We targeted the issue of a possible CO-induced surface reconstruction through a multi-technique approach, featuring Adsorption Microcalorimetry, IR spectroscopy, CO sorption measurements and DFT simulation. A series of experiments were carried out by sending little incremental doses of CO at room temperature on the catalyst activated at 120 °C under dynamic vacuum and H_2-reduced at the same temperature. While CO sorption provided us with accurate and detailed adsorption isotherms, microcalorimetry allowed us to measure the averaged heat of adsorption of CO as a function of coverage. Concurrently, IR spectroscopy made us able to

distinguish the different adsorption sites. The CO adsorption isotherm presents a marked step region when the adsorbed amount of CO is close to the monolayer (i.e., just before reaching the plateau). This step couples with an unexpected re-increasing in the heat of adsorption detected by microcalorimetry. In the same conditions, the IR band associated to 3-fold hollow CO at (111)-like environments mildly shifts towards higher frequency, while the band ascribed to bridged CO at (100)-like environments decreases in intensity and those ascribed to top CO massively increase. Results from a multicomponent spectral fitting procedure point out that the massive growth of the top carbonyl band is due to a sudden increment in the defective carbonyl families.

DFT calculations were carried out by adopting the infinite slab approach. The surface energy (Γ_{hkl}) of diverse Pd facets (100, 110, 111, 210, 211, 310) was calculated both for the pristine facets and the same facets at CO saturation coverage. The optimization of the (100) facet at saturation coverage reports a slight corrugation of the Pd surface, suggesting that the aforementioned experimental observations can be explained by a surface reconstruction.

Finally, additional adsorbate-induced phenomena involving other metals (Pt and Ru) and probes (H_2), have been also explored during this PhD work, as part of the enlarged collaborations involving Chimet S.p.A. In this frame, I had the occasion to actively participate to multiple beamtimes (being the main proponent of one of those), both at synchrotron (ESRF and SLS) and at neutrons (ILL) facilities.

1.4.3 The characterization of the micro- and meso-structure of activated carbons

Activated carbons are extremely popular microporous materials that currently find a great variety of applications: from catalysts supports to catalysts themselves, components of electrochemical cells, storage materials, etc. However, the debate on their micro- and meso-

structure and its impact on the activity of these materials remains open. The reason behind this resides both in the highly disordered nature of these materials and in the limitations affecting routine techniques (for example, gas-volumetry and conventional x-ray Diffraction (XRD)) employed for their characterization. In the last decade, the widely accepted model of activated carbons as an ensemble of nanoscopic flat graphitic platelets, disorderly stacked to create voids (i.e. micropores), has been widely challenged. The contribution of curved domains could be necessary to increase the comprehension of experimental data from several techniques. Above all, the broadening of the XRD peaks in ACs, conventionally merely attributed to their nano-crystallinity, can be indeed explained also with the existence of curved layers. Arising from the presence of non-hexagonal rings formed during the activation process, their contribution could give the micro- and meso-structure of ACs a quite different look compared with the conventional model.

The third chapter of this thesis was devoted to the structural characterization of activated carbons employed as supports for metal NPs at the micro- and meso-scale. The experiments were focused on five samples of different origin (wood, peat) and activation (steam, H_3PO_4). Two of them were further oxidized with HNO_3. The porosity of the activated carbons was first characterized with N_2, Ar, and CO_2 sorption respectively at 77, 87 and 273 K, coupled with Non Local Density Functional Theory (NL-DFT). Though the Brunauer-Emmet-Teller (BET) areas calculated from N_2 and Ar isotherms are similar, Pore Size Distributions (PSDs) inferred from the same isotherms by means of NLDFT appear significantly different. We attributed this discrepancy to the higher accuracy of the isotherms obtained with Ar, the latter being spheric and a smaller, less-interacting probe than N_2. By inferring PSDs from CO_2 isotherms (this last featuring a smaller kinetic diameter than Ar) we pointed out the existence of diverse family of ultra-micropores.

Given the limitations of conventional techniques, a promising alternative to characterize the structural features of ACs from the micro to the meso-scale is represented by Small Angle Neutron Scattering (SANS). Small Angle Scattering is generally known as suitable for accessing structural and morphological information both for crystalline and amorphous samples. Moreover, SANS can provide insight about pore accessibility by filling the pores with a contrast matching agent, such as D_2O. Thus, relying on our Ar-PSDs, we carried out a SANS experiment with the aim of enhancing our knowledge not only on the PSD, but also on (1) the spatial organization of the pores in the carbon matrix, (2) the existence and abundance of curved carbon domains and (3) the accessibility of the micropores thanks to contrast matching with D_2O. A preliminary analysis of the collected scattering intensities points out a strong agreement between SANS and Ar sorption data.

References

(1)   Chorkendorff, I.; Niemantsverdriet, J. W. *Concepts of Modern Catalysis and Kinetics*; Wiley, 2017.

(2)   Boudart, M.; Davis, B. H.; Heinemann, H. Introduction. In *Handbook of Heterogeneous Catalysis*; John Wiley & Sons, Ltd, 1997; pp 1–48. https://doi.org/https://doi.org/10.1002/9783527619474.ch1.

(3)   Ndolomingo, M. J.; Bingwa, N.; Meijboom, R. Review of Supported Metal Nanoparticles: Synthesis Methodologies, Advantages and Application as Catalysts. *J. Mater. Sci.* **2020**, *55* (15), 6195–6241. https://doi.org/10.1007/s10853-020-04415-x.

(4)   Lloyd, L. *Handbook of Industrial Catalysts*; Fundamental and Applied Catalysis; Springer US, 2011.

(5)   Saillard, J. Y.; Hoffmann, R. C-H and H-H Activation in Transition Metal Complexes and on Surfaces. *J. Am. Chem. Soc.* **1984**, *106* (7), 2006–2026. https://doi.org/10.1021/ja00319a020.

(6)   Horiuti, I.; Polanyi, M. Exchange Reactions of Hydrogen on Metallic Catalysts. *Trans. Faraday Soc.* **1934**, *30*, 1164–1172. https://doi.org/10.1039/tf9343001164.

(7)   Zaera, F. Key Unanswered Questions about the Mechanism of Olefin Hydrogenation Catalysis by Transition-Metal Surfaces: A Surface-Science Perspective. *Phys. Chem. Chem. Phys.* **2013**, *15* (29), 11988–12003. https://doi.org/10.1039/C3CP50402F.

(8)   Hamada, H.; Haneda, M. A Review of Selective Catalytic Reduction of Nitrogen Oxides with Hydrogen and Carbon Monoxide. *Appl. Catal. A Gen.* **2012**, *421–422*, 1–13. https://doi.org/10.1016/j.apcata.2012.02.005.

(9)   Mazumder, V.; Lee, Y.; Sun, S. Recent Development of Active Nanoparticle Catalysts

        for Fuel Cell Reactions. *Adv. Funct. Mater.* **2010**, *20* (8), 1224–1231.

        https://doi.org/10.1002/adfm.200902293.

(10)   Zhong, C. J.; Maye, M. M. Core–Shell Assembled Nanoparticles as Catalysts. *Adv.*

        Mater. **2001**, *13* (19), 1507–1511. https://doi.org/https://doi.org/10.1002/1521-

        4095(200110)13:19<1507::AID-ADMA1507>3.0.CO;2-#.

(11)   van Deelen, T. W.; Hernández Mejía, C.; de Jong, K. P. Control of Metal-Support

        Interactions in Heterogeneous Catalysts to Enhance Activity and Selectivity. *Nat.*

        Catal. **2019**, *2* (11), 955–970. https://doi.org/10.1038/s41929-019-0364-x.

(12)   Liu, J. (Jimmy). Advanced Electron Microscopy of Metal–Support Interactions in

        Supported Metal Catalysts. *ChemCatChem* **2011**, *3* (6), 934–948.

        https://doi.org/https://doi.org/10.1002/cctc.201100090.

(13)   Rodríguez-Reinoso, F.; Sepúlveda-Escribano, A. Carbon as Catalyst Support. In *Carbon*

        Materials for Catalysis; 2008; pp 131–155.

        https://doi.org/https://doi.org/10.1002/9780470403709.ch4.

(14)   Auer, E.; Freund, A.; Pietsch, J.; Tacke, T. Carbons as Supports for Industrial Precious

        Metal Catalysts. *Appl. Catal. A Gen.* **1998**, *173* (2), 259–271.

        https://doi.org/https://doi.org/10.1016/S0926-860X(98)00184-7.

(15)   Misono, M. Chapter 2 - Chemistry and Catalysis of Mixed Oxides. In *Heterogeneous*

        Catalysis of Mixed Oxides; Misono, M. B. T.-S. in S. S. and C., Ed.; Elsevier, 2013; Vol.

        176, pp 25–65. https://doi.org/https://doi.org/10.1016/B978-0-444-53833-8.00002-8.

(16)   Hu, J.; Chen, L.; Richards, R. Properties, Synthesis and Applications of Highly Dispersed

Metal Oxide Catalysts. In *Metal Oxide Catalysis*; 2008; pp 613–663.
https://doi.org/https://doi.org/10.1002/9783527626113.ch16.

(17) Rodríguez-Reinoso, F. Production and Applications of Activated Carbons. In *Handbook of Porous Solids*; 2002; pp 1766–1827.
https://doi.org/https://doi.org/10.1002/9783527618286.ch24a.

(18) González-García, P. Activated Carbon from Lignocellulosics Precursors: A Review of the Synthesis Methods, Characterization Techniques and Applications. *Renew. Sustain. Energy Rev.* **2018**, *82*, 1393–1414.
https://doi.org/https://doi.org/10.1016/j.rser.2017.04.117.

(19) Pines, H.; Haag, W. O. Alumina: Catalyst and Support. I. Alumina, Its Intrinsic Acidity and Catalytic Activity1. *J. Am. Chem. Soc.* **1960**, *82* (10), 2471–2483.
https://doi.org/10.1021/ja01495a021.

(20) Loza, K.; Heggen, M.; Epple, M. Synthesis, Structure, Properties, and Applications of Bimetallic Nanoparticles of Noble Metals. *Adv. Funct. Mater.* **2020**, *30* (21), 1909260.
https://doi.org/https://doi.org/10.1002/adfm.201909260.

(21) Liu, P.; Qin, R.; Fu, G.; Zheng, N. Surface Coordination Chemistry of Metal Nanomaterials. *J. Am. Chem. Soc.* **2017**, *139* (6), 2122–2131.
https://doi.org/10.1021/jacs.6b10978.

(22) Chizallet, C.; Raybaud, P. Density Functional Theory Simulations of Complex Catalytic Materials in Reactive Environments: Beyond the Ideal Surface at Low Coverage. *Catal. Sci. Technol.* **2014**, *4* (9), 2797–2813. https://doi.org/10.1039/c3cy00965c.

(23) Newton, M. A. Dynamic Adsorbate/Reaction Induced Structural Change of Supported

Metal Nanoparticles: Heterogeneous Catalysis and Beyond. *Chem. Soc. Rev.* **2008**, *37* (12), 2644–2657. https://doi.org/10.1039/b707746g.

(24) Libuda, J. Molecular Beams and Model Catalysis: Activity and Selectivity of Specific Reaction Centers on Supported Nanoparticles. *ChemPhysChem* **2004**, *5* (5), 625–631. https://doi.org/https://doi.org/10.1002/cphc.200400049.

(25) WEISSER, O.; LANDA, S. 1 - HISTORICAL REVIEW OF THE DEVELOPMENT AND APPLICATION OF SULPHIDE CATALYSTS; WEISSER, O., LANDA their Properties and Applications, S. B. T.-S. C., Eds.; Pergamon, 1973; pp 11–14. https://doi.org/https://doi.org/10.1016/B978-0-08-017556-0.50005-8.

(26) Schueth, F.; Busch, O.; Hoffmann, C.; Johann, T.; Kiener, C.; Demuth, D.; Klein, J.; Schunk, S.; Strehlau, W.; Zech, T. High-Throughput Experimentation in Oxidation Catalysis. *ChemInform* **2003**, *34* (20), 55–66. https://doi.org/10.1002/chin.200320278.

(27) Jin, R.; Li, G.; Sharma, S.; Li, Y.; Du, X. Toward Active-Site Tailoring in Heterogeneous Catalysis by Atomically Precise Metal Nanoclusters with Crystallographic Structures. *Chem. Rev.* **2021**, *121* (2), 567–648. https://doi.org/10.1021/acs.chemrev.0c00495.

(28) Ahmadi, M.; Mistry, H.; Roldan Cuenya, B. Tailoring the Catalytic Properties of Metal Nanoparticles via Support Interactions. *J. Phys. Chem. Lett.* **2016**, *7* (17), 3519–3533. https://doi.org/10.1021/acs.jpclett.6b01198.

(29) Kalidindi, S. B.; Jagirdar, B. R. Nanocatalysis and Prospects of Green Chemistry. *ChemSusChem* **2012**, *5* (1), 65–75. https://doi.org/https://doi.org/10.1002/cssc.201100377.

(30) Ertl, G.; Freund, H. Catalysis and Surface Science. *Phys. Today* **1999**, *52* (1), 32–38.

https://doi.org/10.1063/1.882569.

(31) Henry, C. R. Surface Studies of Supported Model Catalysts. *Surf. Sci. Rep.* **1998**, *31* (7–8), 231–233. https://doi.org/10.1016/S0167-5729(98)00002-8.

(32) Zaera, F. Outstanding Mechanistic Questions in Heterogeneous Catalysis. *J. Phys. Chem. B* **2002**, *106* (16), 4043–4052. https://doi.org/10.1021/jp014630e.

(33) Freund, H. J. Clusters and Islands on Oxides: From Catalysis via Electronics and Magnetism to Optics. *Surf. Sci.* **2002**, *500* (1–3), 271–299. https://doi.org/10.1016/S0039-6028(01)01543-6.

(34) Somorjai, G. A.; Frei, H.; Park, J. Y. Advancing the Frontiers in Nanocatalysis, Biointerfaces, and Renewable Energy Conversion by Innovations of Surface Techniques. *J. Am. Chem. Soc.* **2009**, *131* (46), 16589–16605. https://doi.org/10.1021/ja9061954.

(35) Meunier, F. C. Bridging the Gap between Surface Science and Industrial Catalysis. *ACS Nano* **2008**, *2* (12), 2441–2444. https://doi.org/10.1021/nn800787e.

(36) Friedrich, H.; De Jongh, P. E.; Verkleij, A. J.; De Jong, K. P. Electron Tomography for Heterogeneous Catalysts and Related Nanostructured Materials. *Chem. Rev.* **2009**, *109* (5), 1613–1629. https://doi.org/10.1021/cr800434t.

(37) Weckhuysen, B. M. Chemical Imaging of Spatial Heterogeneities in Catalytic Solids at Different Length and Time Scales. *Angew. Chemie - Int. Ed.* **2009**, *48* (27), 4910–4943. https://doi.org/10.1002/anie.200900339.

(38) Bordiga, S.; Groppo, E.; Agostini, G.; Van Bokhoven, J. A.; Lamberti, C. Reactivity of Surface Species in Heterogeneous Catalysts Probed by in Situ X-Ray Absorption

Techniques. *Chem. Rev.* **2013**, *113* (3), 1736–1850.

https://doi.org/10.1021/cr2000898.

(39)   Bañares, M. A. Operando Methodology: Combination of in Situ Spectroscopy and

Simultaneous Activity Measurements under Catalytic Reaction Conditions. *Catal.*

Today **2005**, *100* (1–2), 71–77. https://doi.org/10.1016/j.cattod.2004.12.017.

(40)   Santen R.A., van; Neurock, M. Molecular Heterogeneous Catalysis : A Conceptual and

Computational Approach . Wiley-VCH Verlag : Weinheim 2006.

(41)   Computational Methods in Catalysis and Materials Science . Wiley-VCH Verlag :

Weinheim 2009. https://doi.org/10.1002/9783527625482.

(42)   Hafner, J.; Benco, L.; Bučko, T. Acid-Based Catalysis in Zeolites Investigated by Density-

Functional Methods. *Top. Catal.* **2006**, *37* (1), 41–54. https://doi.org/10.1007/s11244-

006-0003-z.

(43)   Hammer, B.; Nørskov, J. K. B. T.-A. in C. Theoretical Surface Science and Catalysis—

Calculations and Concepts. In *Impact of Surface Science on Catalysis*; Academic Press,

2000; Vol. 45, pp 71–129. https://doi.org/https://doi.org/10.1016/S0360-

0564(02)45013-4.

(44)   Nørskov, J. K.; Bligaard, T.; Rossmeisl, J.; Christensen, C. H. Towards the

Computational Design of Solid Catalysts. *Nat. Chem.* **2009**, *1* (1), 37–46.

https://doi.org/10.1038/nchem.121.

(45)   Hohenberg, P.; Kohn, W. Inhomogeneous Electron Gas. *Phys. Rev.* **1964**, *136* (3B),

B864–B871. https://doi.org/10.1103/PhysRev.136.B864.

(46)   Grimme, S.; Schreiner, P. R. Computational Chemistry: The Fate of Current Methods

and Future Challenges. *Angew. Chemie - Int. Ed.* **2018**, *57* (16), 4170–4176. https://doi.org/10.1002/anie.201709943.

(47)   Bannwarth, C.; Caldeweyher, E.; Ehlert, S.; Hansen, A.; Pracht, P.; Seibert, J.; Spicher, S.; Grimme, S. Extended Tight-Binding Quantum Chemistry Methods. *Wiley Interdiscip. Rev. Comput. Mol. Sci.* **2021**, *11* (2), 1–49. https://doi.org/10.1002/wcms.1493.

(48)   Unke, O. T.; Chmiela, S.; Sauceda, H. E.; Gastegger, M.; Poltavsky, I.; Schütt, K. T.; Tkatchenko, A.; Müller, K. R. Machine Learning Force Fields. *Chem. Rev.* **2021**, *121* (16), 10142–10186. https://doi.org/10.1021/acs.chemrev.0c01111.

(49)   Hourahine, B.; Aradi, B.; Blum, V.; Bonafé, F.; Buccheri, A.; Camacho, C.; Cevallos, C.; Deshaye, M. Y.; Dumitric, T.; Dominguez, A.; Ehlert, S.; Elstner, M.; Van Der Heide, T.; Hermann, J.; Irle, S.; Kranz, J. J.; Köhler, C.; Kowalczyk, T.; Kubař, T.; Lee, I. S.; Lutsker, V.; Maurer, R. J.; Min, S. K.; Mitchell, I.; Negre, C.; Niehaus, T. A.; Niklasson, A. M. N.; Page, A. J.; Pecchia, A.; Penazzi, G.; Persson, M. P.; Řezáč, J.; Sánchez, C. G.; Sternberg, M.; Stöhr, M.; Stuckenberg, F.; Tkatchenko, A.; Yu, V. W. Z.; Frauenheim, T. DFTB+, a Software Package for Efficient Approximate Density Functional Theory Based Atomistic Simulations. *J. Chem. Phys.* **2020**, *152* (12), 124101. https://doi.org/10.1063/1.5143190.

(50)   Van Duin, A. C. T.; Dasgupta, S.; Lorant, F.; Goddard, W. A. ReaxFF: A Reactive Force Field for Hydrocarbons. *J. Phys. Chem. A* **2001**, *105* (41), 9396–9409. https://doi.org/10.1021/jp004368u.

(51)   Pracht, P.; Bohle, F.; Grimme, S. Automated Exploration of the Low-Energy Chemical Space with Fast Quantum Chemical Methods. *Phys. Chem. Chem. Phys.* **2020**, *22* (14),

7169–7192. https://doi.org/10.1039/c9cp06869d.

(52)   Van Den Bossche, M. DFTB-Assisted Global Structure Optimization of 13- and 55-Atom

Late Transition Metal Clusters. *J. Phys. Chem. A* **2019**, *123* (13), 3038–3045.

https://doi.org/10.1021/acs.jpca.9b00927.

(53)   Ricchebuono, A.; Vottero, E.; Piovano, A.; Groppo, E.; Raybaud, P.; Chizallet, C.

Assessing Low-Cost Computational Methods against Structural Properties and Size

Effects of Pt Nanoparticles. *J. Phys. Chem. C* **2023**, *127* (37), 18454–18465.

https://doi.org/10.1021/acs.jpcc.3c02799.

(54)   Vottero, E.; Carosso, M.; Ricchebuono, A.; Jiménez-Ruiz, M.; Pellegrini, R.; Chizallet, C.;

Raybaud, P.; Groppo, E.; Piovano, A. Evidence for H2-Induced Ductility in a Pt/Al2O3

Catalyst. *ACS Catal.* **2022**, *12* (10), 5979–5989.

https://doi.org/10.1021/acscatal.2c00606.

(55)   Sanz-Navarro, C. F.; Åstrand, P.-O.; Chen, D.; Rønning, M.; van Duin, A. C. T.; Jacob, T.;

Goddard, W. A. Molecular Dynamics Simulations of the Interactions between Platinum

Clusters and Carbon Platelets. *J. Phys. Chem. A* **2008**, *112* (7), 1392–1402.

https://doi.org/10.1021/jp074806y.

(56)   Chen, Y.; Cheng, T.; Goddard III, W. A. Atomistic Explanation of the Dramatically

Improved Oxygen Reduction Reaction of Jagged Platinum Nanowires, 50 Times Better

than Pt. *J. Am. Chem. Soc.* **2020**, *142* (19), 8625–8632.

https://doi.org/10.1021/jacs.9b13218.

Chapter 2

Assessing Low-Cost Computational Methods against Structural Properties and Size Effects of Pt nanoparticles

This chapter is based on the reference paper: "Ricchebuono, A. et al., *J. Phys. Chem. C* 2023, 127, 18454–18465"

2.1 Introduction

The importance of metal nanoparticles (NPs) in modern technology has grown exponentially since scientists started studying their properties and engineering during the last century. Pt NPs display unique characteristics (resistance to oxidation, biocidal activity, plasmon resonance, etc.), which made them employed in a great variety of applications: from biosensors to electronics, catalysis and more.[1,2] One of the most interesting features of Pt NPs is their ability to activate and sometimes dissociate many molecules of environmental and industrial relevance, such as H_2, CO, CO_2 and organic compounds.[3,4] The activity enhancement gained by dispersing metal nanoparticles of controlled size on support materials, such as oxides or carbons, has indeed given heterogeneous catalysts based on supported Pt NPs a central role in several catalytic processes,[5] like pollutant removal,[6,7] hydrogenation/dehydrogenation reactions,[8–11] naphtha reforming,[12,13] etc.

The fine understanding of the properties of Pt NPs is challenged by their complex and ductile structure which is very sensitive to the chemical environment (reactants or nature of the support). Usually, Pt NPs display a great variety of sites whose coordination depends on

the NP's shape, size and structural disorder, giving birth to an overlap of contributions and convoluted experimental responses strongly depending on reaction conditions.[14] Hence, the atomic scale determination of these systems requires the use of cutting-edge characterization techniques in combination with state-of-the-art computational chemistry methods.[15–19] The advance of density functional theory (DFT) and the development of high-performance computing (HPC) facilities has led to numerous progresses in the understanding of the properties of Pt NPs through the last decades.[20] For instance, a great variety of shapes has been found for isolated Pt clusters,[21–24] while the interaction of Pt NP's with oxide supports[25–29] and various reactants (such as H_2 or CO) has been investigated for clusters ranging from 2 up to around 200 atoms.[28,30,31]

Nevertheless, one of the frontiers of the field arises from the fact that DFT can be employed for accurate calculations on simple systems featuring up to around a few hundred atoms, but it becomes rapidly too demanding when increasing the number of metallic atoms involved.[32,33] This aspect represents a strong limitation to the development of realistic models, often compelling researchers to rely on simplifications such as reduction of system's size and nano-structure complexity.

The process of building reliable molecular models of metallic NPs comprehends a preliminary step in which many candidate structures have to be screened for a given NP size.[34] During this step, the potential energy surface (PES) has to be explored in order to find the most stable minima that can be relevant and populated at a given temperature.[35,36] Even though various algorithms, such as global optimization[24,37–39] and simulated annealing by *ab initio* molecular dynamics,[21,40–43] can be used to generate and explore candidate structures for metallic clusters, the main bottleneck of this step is the computational method employed to

describe the PES. For example, an exhaustive PES exploration within a full-DFT approach can be carried out only for small and simple systems at a high computational cost. Adopting a multilevel modelling scheme often represents an efficient workaround, envisaging the exploitation of low-cost approximated methods (semiempirical (SE) functionals, force-fields (FF), neural network potentials, etc.) instead of DFT for the exploration of the PES.[23,44] Even though this strategy can massively reduce the computational cost of the process, the approximations on which these methods rely always entail an accuracy loss of some extent. Moreover, the stronger these approximations, the weaker the transferability of the method. Thus, the accuracy of approximated low-cost methods must be thoroughly assessed against reference methods that are proved to be trustable for the systems at issue.

In this chapter, we benchmark the performances of several low-cost computational methods for the computation of structural properties and size effects on Pt nanoparticles of stoichiometry Pt_{13}, Pt_{55}, Pt_{147}, Pt_{309}, Pt_{561}. The semiempirical tested methods are density functional tight binding (DFTB)[45] and three methods belonging to the GFN extended tight binding family: GFN0-xTB,[46] GFN1-xTB[47] and GFN2-xTB,[48] where the acronym "GFN" stands for "geometries, frequencies and noncovalent interactions". The ReaxFF[49,50] reactive force field was tested in the same fashion. DFTB and the ReaxFF are well-known methods that have already been frequently employed in heterogeneous catalysis.[51–58] On the other hand, the recently developed GFN methods were first benchmarked against high-level DFT, wavefunction theory (WFT) and experimental data mainly for organic and metal-organic compounds.[34,46–48] However, their promising applications reported in the last few years[59–62] together with their low computational cost and their atom-specific parametrization make their accuracy worth to be assessed on metal NPs as well.

Due to the lack of clear insight from the literature, our benchmark strategy for this study was built as follows. A small structural dataset containing 14 different Pt_{13} NPs, divided into amorphous and ordered structures, was considered to first test the performances of all the listed methods. The benchmark was performed by assessing their ability to reproduce relative stabilities, thermochemical parameters and structural descriptors (bond lengths, bond angles and radii of gyration) computed at the PBE-dDsC[63,64] level for every NP of the dataset. An analogous approach is adopted for two sets of amorphous NPs of stoichiometry Pt_{13} (54 structures) and Pt_{55} (93 structures) in order to evaluate the particle size effect. The ultimate task of the work will be to propose a cost-effective simulated annealing procedure combining ReaxFF and GFN0-xTB to generate reliable amorphous structures for big sized Pt_x NPs (x = 147, 309, 561). In the last section this route is critically analyzed, pointing out its advantages and limits to overcome.

2.2 Methodology

2.2.1 Computational details

DFT calculations were carried out within the plane-wave formalism, thanks to the VASP[65,66] code (version 5.4.4). The PBE exchange-correlation functional[63] was employed, setting an energy cutoff of 400 eV for Pt_{13}, and Pt_{55}, and 300 eV for Pt_{147}, Pt_{309}, and Pt_{561}. The choice of the PBE functional is due to its computational cost and general applicability,[67] allowing to compute energies and geometries for the biggest NPs considered in this work, coupled with its relevance for simulating Pt and transition metals surfaces in general.[68] The dDsC correction,[69] benchmarked for predicting molecular adsorption at Pt surfaces by Gautier et al.,[70] was added to take into account dispersion interactions, while core electrons were described with the PAW method.[71] To motivate our reference functional choice, we evaluated the performances of PBE, PBE-dDsC and PBEsol[72] on the *Pt_{13} small dataset* (details about the

dataset are given in the next section). The comparison between relative energies computed with the three functionals is presented in Figure 1. The small deviations (below 0.03 eV/atom) observed between the data obtained with the different functionals confirm that the impact of the reference GGA functional lies in the background if compared with the effect of a geometry optimization at SE or FF level. A Gaussian smearing (σ = 0.05 eV) was applied to fasten the convergence of the electronic iterations. The threshold for all the electronic energy minimizations was fixed to 10^{-7} eV. Spin-polarized calculations were performed for Pt_{13} and Pt_{55}. Geometries were optimized with the conjugate-gradient algorithm until the residual forces were below 0.005 eV/Å. Although geometry optimizations of NPs of sizes up to a few hundred of atoms are feasible at PBE level, the same process is thousands of times faster if employing the low-cost methods at issue (Figure 2). Thus, understanding to what extent results obtained with the latter deviate from the PBE reference is crucial to safely exploit this massive gain in computational time.
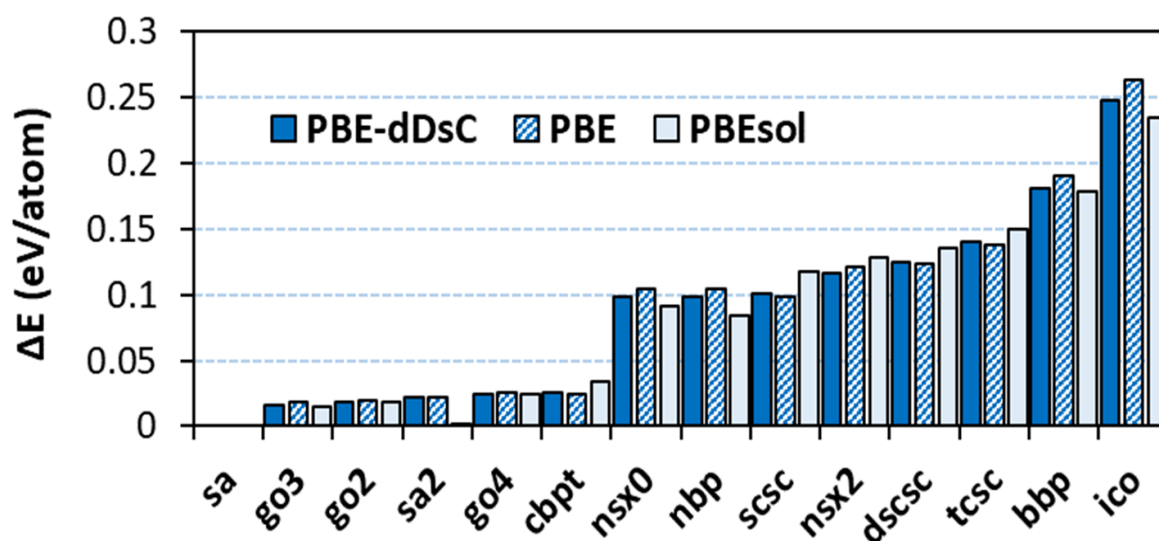
Figure 1. Relative stability (with respect to the global minimum) of all the structures of the Pt_{13} small dataset, ranked according to their electronic energy computed at PBE-dDsC (blue), PBE (striped blue) and PBEsol (light blue) levels.

DFTB calculations were carried out through the DFTB+ code (version 21.1).[45] Electronic energies were computed by setting a self-consistent charge (SCC) tolerance of 2.7 10^{-7} eV, a maximum angular momentum l_{max} = 2 and a Fermi-Dirac smearing featuring an electronic temperature of 500 K, following the settings chosen in ref. 23. Geometries were optimized with the conjugate-gradient algorithm until the residual forces were below 5 10^{-4} eV/Å. The employed Slater-Koster parameters were adopted from ref. 23.

Calculations performed with the GFNn-xTB methods were executed with the xtb code (version 6.4.0).[34] The threshold for the convergence on electronic energies was set to 10^{-6} eV, while geometries were optimized through the ANCOPT algorithm with a convergence criterion of 0.01 eV/Å. We checked that using a tighter convergence criterion does not affect the results reported herein.

ReaxFF calculations were run within version 6.0 of the General Lattice Utility Program (GULP),[73] exploiting a parametrization derived in ref. 74. The latter was made with the final aim of modeling the interaction between Pt clusters and carbon platelets. The convergence criterion for geometry optimizations was set to 0.005 eV/Å.

All the above-mentioned thresholds were chosen in order to avoid negative eigenvalues of the hessian matrix during the computation of harmonic vibrational frequencies. To this purpose, the finite differences method was adopted for the VASP, DFTB+ and xTB code (elongation ± 0.01 Å, ± 5 10^{-5} Å, ± 0.0025 Å, respectively), while analytical derivatives were computed with GULP. The computed vibrational frequencies were post-treated, through the laws of statistical thermodynamics,[75] to extract the vibrational contributions to the following thermodynamic quantities: enthalpy (H_{vib}), entropy (S_{vib}) and

the Zero Point Vibrational Energy (ZPVE). The vibrational contribution to the Gibbs free energy (G_{vib}) at T = 300 K is computed as follows:

$$G_{vib} = H_{vib} - TS_{vib} + ZPVE \tag{1}$$

MD simulations were carried out in an NVT ensemble. ReaxFF MD was performed with the Nosé thermostat[76] and the velocity-Verlet algorithm at different temperatures (details are given in the next section). The employed time-step was 0.5 fs, while the total simulation time was 10 ps. The Berendsen thermostat[77] was employed for GFN0-xTB MD at 2000K, with a time-step of 2 fs and a total simulation time of 50 ps.
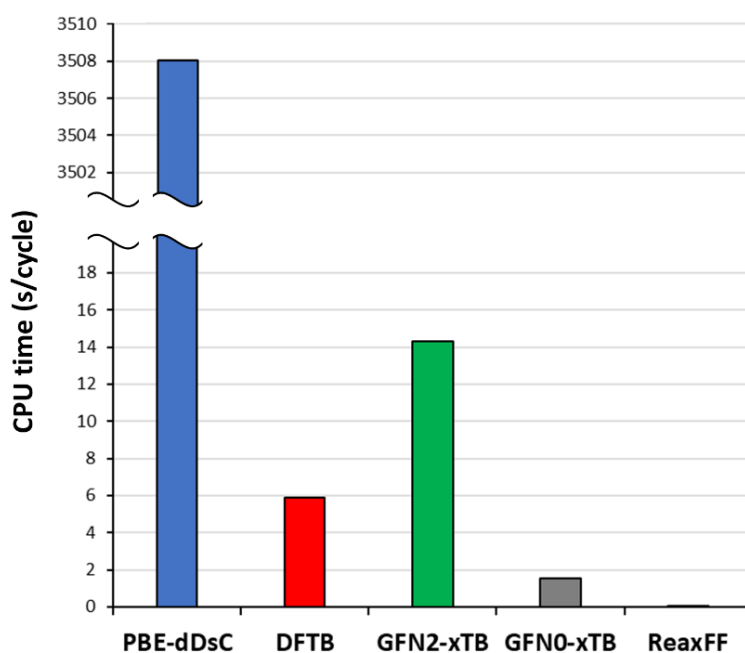
Figure 2. Order of magnitude of the computational cost of the employed for PBE-dDsC (blue), DFTB (red), GFN2-xTB (green), GFN0-xTB (grey), and ReaxFF (pink). The y axis reports the time taken for a single optimization cycle (SCF/non-self-consistent energy evaluation + gradient) computed as a ratio between the total elapsed time and the number of cycles taken to fulfill the optimization. Data are obtained by optimizing the same Pt_{55} structure, on the same number of CPUs (8) of the HPC machine Fram of the Norwegian academic HPC infrastructure (system: Lenovo NeXtScale nx360; CPU type: Intel E5-2683v4 2.1 GHz) with the same optimization thresholds ($\approx$ 0.005 eV/atom).

2.2.2 Datasets and models

The performances of the chosen low-cost methods were evaluated by investigating four structural datasets:

- *Pt$_{13}$ small dataset*: 14 structures divided into ordered and amorphous. Coordinates of structures belonging to this dataset have different origins: the structures cbpt (capped biplanar triangle), nbp (new biplanar), scsc (side-capped simple cubic), dscsc (disordered side-capped simple cubic), tcsc (top-capped simple cubic), bbp (buckled biplanar) and ico (icosahedral) are taken from ref. 21. The structures sa and sa2 are still taken from ref. 21 and differ from the previous ones as they are generated through first-principle simulated annealing (hence the "sa" terminology). The structures go2, go3, go4 are taken from ref. 23 (where "go" stands for "global optimization"). The structures nsx0 and nsx2 were obtained by optimizing at GFN0-xTB and GFN2-xTB level amorphous structures from previous DFT calculations.

- *Pt$_{13}$ amorphous dataset*: 54 amorphous structures (coordinates adopted from ref. 23).

- *Pt$_{55}$ amorphous dataset*: 93 amorphous structures (coordinates adopted from ref. 23).

- *Multi-sized dataset*: 5 amorphous structures of stoichiometry Pt$_{13}$, Pt$_{55}$, Pt$_{147}$, Pt$_{309}$, Pt$_{561}$ (presented in Figure 3) were considered to evaluate the size-dependency of the performances of the tested methods. Pt$_{13}$ and Pt$_{55}$ structures in this dataset correspond to the lowest-energy structures of the *Pt$_{13}$* and *Pt$_{55}$ amorphous datasets*, respectively. Amorphous Pt$_{147}$, Pt$_{309}$, and Pt$_{561}$ were obtained through the amorphization of the ordered cuboctahedral geometry, as schematized in Figure 4A. Cuboctahedral nanoparticles were first cut out of the Pt bulk and subsequently subjected to ReaxFF MD. Different temperatures, ranging from 800 K to 2700 K, were tested to find the minimal temperature to shake cuboctahedral geometries in order to

explore various conformational states. A complete amorphization of the structure was achieved at 2000 K for Pt_{147}, 2500 K for Pt_{309}, and 2700 K for Pt_{561}. The lowest-energy structure of each MD run was quenched at 0 K with ReaxFF, obtaining an amorphous ReaxFF geometry for each stoichiometry. The geometries of the obtained structures were optimized with the low-cost methods, as well as with PBE-dDsC. GFN0-xTB geometries were finally annealed through GFN0-xTB MD, aiming to enhance the accuracy of the generated NP models through higher-level MD. Several candidate low-lying energy conformations per stoichiometry were quenched at 0 K with GFN0-xTB in this case, taking as output only the lowest-energy structure resulting after PBE-dDsC single point energy evaluations. Notably, for this part of the study, we will only compare energies evaluated at our reference level of theory (PBE-dDsC), as will be discussed in section 2.3.3. The energies computed at the GFN0-xTB level are not consideredThe sampling approaches for ReaxFF and GFN0-xTB MD are exemplified in Figure 4B for Pt_{147}.

Pt_{13} Pt_{55} Pt_{147} Pt_{309} Pt_{561}
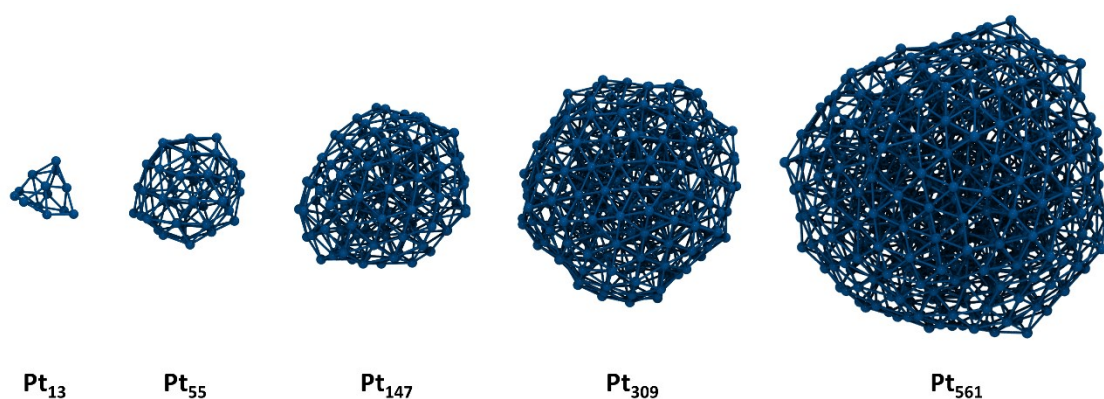
**Figure 3.** Examples of structures of NPs belonging to the multi-sized dataset optimized at PBE-dDsC level at 0 K.

Structures belonging to the *Pt_{13} small dataset* were first optimized at PBE-dDsC level. The thus obtained geometries were further optimized with all the low-cost methods and we evaluated their performances by comparing bond lengths, bond angles, radii of gyration, relative

stabilities and thermochemical parameters computed by the low-cost methods with the reference PBE-dDsC (section 2.3.1). The benchmark on the *Pt$_{13}$ amorphous dataset* and *Pt$_{55}$ amorphous dataset* (section 2.3.2) was carried out analogously, although vibrational frequencies (and thus thermochemical parameters) were not computed. Moreover, GFN1-xTB was not tested on the *Pt$_{13}$* and *Pt$_{55}$ amorphous datasets* due to the poor performances exhibited for the *Pt$_{13}$ small dataset*. As outlined in Figure 4A, all the structures of the *multi-sized dataset* (section 2.3.3) were subjected to a PBE-dDsC single point energy evaluation. Thus, the outcome of the employed multi-level procedure was inspected by analyzing the deviations on PBE-dDsC electronic energies and bond lengths between the low-cost and PBE-dDsC geometries. GFN1-xTB was not employed in this section for the aforementioned reason, while GFN2-xTB was discarded because of the inability of reaching a convergence in SCC calculations for Pt$_{147}$, Pt$_{309}$, and Pt$_{561}$. This work is mainly focused on amorphous NPs since Pt NPs are experimentally known to show a general preference for amorphous morphologies which decreases when increasing the particle size.[78] Notably, after some preliminary test, we testified the inability of the GFN methods to retain cuboctahedral geometries for Pt$_x$ NPs with x > 13.

The graphical visualization and structural manipulation of the NPs was performed with VESTA (version 4.0.0).[79] Images of molecular models were rendered with VMD.[80]
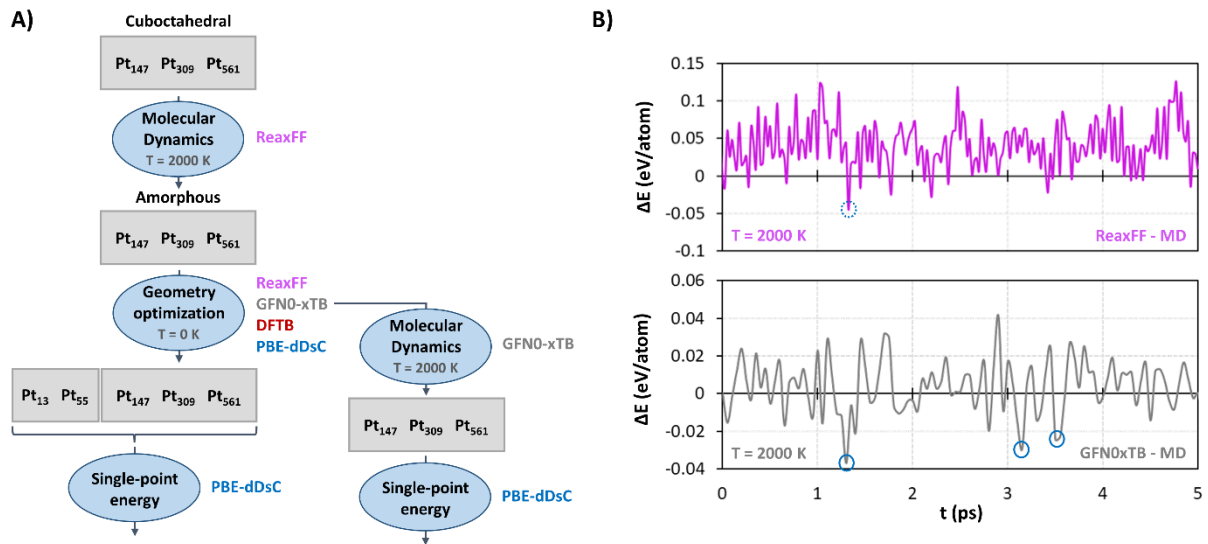
Figure 4. A) Flowchart of the multi-level procedure adopted to build Pt_{147}, Pt_{309}, and Pt_{561} NPs within the *multi-sized* dataset. B) Energy (referred to the starting point) evolution vs simulation time for 5 ps of ReaxFF (pink) and GFN0-xTB (gray) MD for Pt_{147}. The lowest ReaxFF structure (dashed circle) was quenched at 0K with ReaxFF. Among the highlighted lowest-energy GFN0-xTB structures (solid circles), only the most stable conformer according to PBE-dDsC energies was chosen as the output of the procedure.

The kernel density estimate (KDE) plots presented in section 2.3.2 were created with the Python library Seaborn.[81] The KDE plots were built by treating the obtained bond lengths, angles, and radii of gyration extracted for each nanoparticle) as a discrete variable (x). Assuming a definite set of n values for the variable $\boldsymbol{x} = (x_1, x_2, \dots, x_n)$, a probability density function φ can be estimated through the Kernel Density Estimator:

$$\hat{\varphi}_s(x) = \frac{1}{ns} \sum_{i=1}^{n} K(x - x_i) \tag{2}$$

where s is a smoothing parameter and K is the Kernel function. Since the Seaborn library exploits a Gaussian Kernel $K(x) = \frac{1}{\sqrt{2\pi}} e^{-\left(\frac{x^2}{2}\right)}$ to practically compute KDE plots, the estimated probability density function becomes:

$$\hat{\varphi}_s(x) = \frac{1}{ns} \sum_{i=1}^{n} \frac{1}{2\pi} e^{-\frac{1}{2}\left(\frac{x-x_i}{s}\right)^2} \tag{3}$$

where the smoothing parameter s assumes the meaning of a bandwidth tuner for the Gaussians.

2.3 Results and discussion

2.3.1 Pt$_{13}$ small dataset

All the structures optimized at PBE-dDsC level are ranked according to their electronic energy in Figure 5. As outlined in section 2.2, the 14 Pt$_{13}$ NPs are here divided into two classes: "amorphous" and "ordered". While among the structures of the "amorphous" class, the atoms are "randomly" organized in space, the atomic positions in the "ordered" structures are subjected to stricter geometrical constraints. The dispersion-corrected GGA electronic energies suggest that, for the Pt$_{13}$ system, ordered structures are generally less stable than the amorphous ones. This trend is consistent with the fact that the arrangement of atoms in ordered structures is either cut out of the bulk or built to fit specific geometric shapes. On the other hand, most of the amorphous structures (with the exception of sa, the most stable structure, found by simulated annealing)[21] shown here were obtained through a global optimization procedure,[23] that was explicitly devoted to find the most stable geometries for this system. One notable result about this dataset concerns the cuboctahedral geometry, which has been widely employed as a model nanoparticle for many metals due its straightforward extraction from an fcc crystalline lattice.[22,82] According to the analysis of vibrational frequencies, the optimized cuboctahedral structure (ΔE = 0.24 eV/atom with respect to the sa global minimum) displays residual imaginary frequencies corresponding to a compression along the axis normal to the squared facets. A line-minimization was performed to scan the normal coordinate associated with the imaginary frequency, in order to find the

minimum conformation. After the line-minimization procedure, the re-optimized geometry collapsed to the bbp structure, implying the removal of the cuboctahedral Pt_{13} from our dataset. This cuboctahedral structure was kept in ref. 21 without confirming by frequency analysis if it was a true minimum. Nevertheless, the overall energy trend is consistent with the one reported for sa, nbp, bbp, ico, and cub in ref. 21.

Figure 5. Relative stability (with respect to the global minimum) of all the structures of the Pt_{13} small dataset, ranked according to their electronic energy computed at PBE-dDsC level. Amorphous structures are represented in blue, while the ordered ones in orange.

After re-optimizing PBE-dDsC structures with the low-cost methods, a detailed analysis of their performances was achieved by extracting and comparing different features of the NPs: geometries, relative stabilities and thermochemical parameters.

2.3.1.1 Geometries

To represent the geometrical features of each NP, we extracted the Pt-Pt distances between nearest neighbors (Figure 6A), the angles between three nearest neighbors Pt atoms (Figure 6B) and the radius of gyration (R_g, Figure 6C). The errors of the tested low-cost methods for each nanoparticle with respect to the PBE-dDsC reference are reported in Figure 6. Only the errors for the three best performing methods are shown in the main text, due to the poor

results obtained with ReaxFF and GFN1-xTB. Histograms for all the methods are given in Figure

A1.
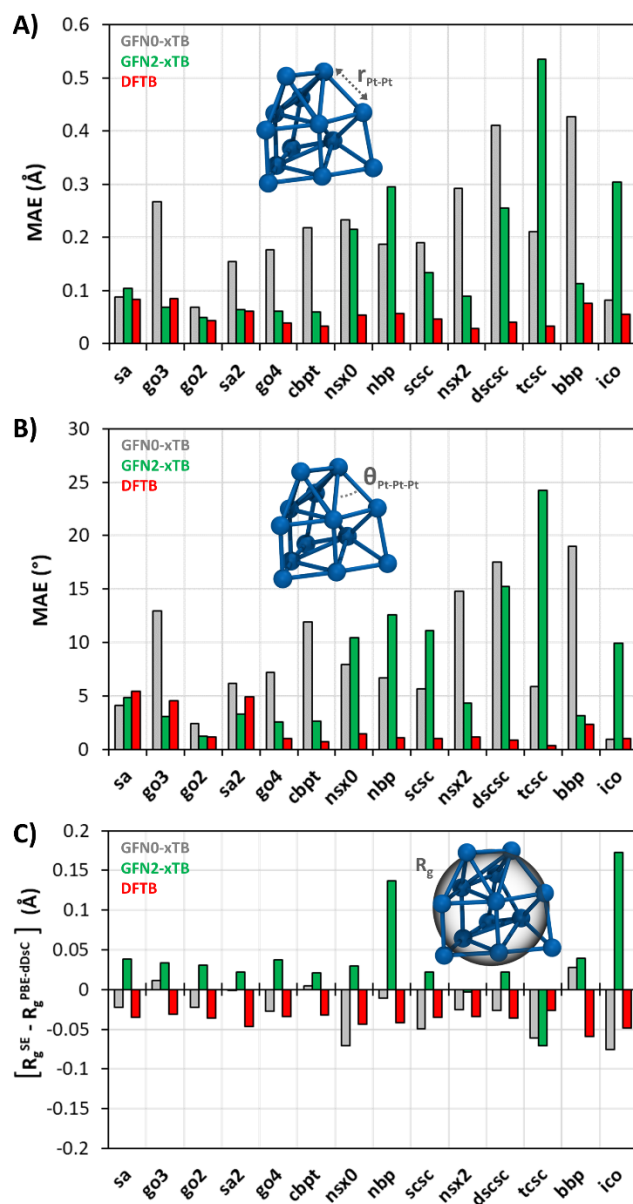
Figure 6. Mean Absolute Error (MAE) for bond lengths (A) and bond angles (B), and the signed deviation from

PBE-dDsC for the gyration radius R_g (C) made by semi-empirical methods (SE): GFN0-xTB (gray), GFN2-xTB (green)

and DFTB (red).

The averaged mean absolute errors (MAEs) computed separately for amorphous and

ordered structures are reported in Table 1. As it emerges both from the histograms in Figure

6 and from Table 1, DFTB outperforms GFN0-xTB and GFN2-xTB in most cases, showing errors below 0.1 Å for bond lengths and generally below 5° for bond angles. GFN2-xTB systematically shows lower errors on amorphous geometries (competing with DFTB), while its performances become poor when evaluated on ordered structures. The results obtained with GFN0 are not undergoing any specific trend. However, it is worth noting that for R_g, GFN0-xTB exhibits the lowest deviation (in absolute value) both for amorphous and ordered structures. Our interpretation of this behavior is that, even though the "local" geometry is not strictly retained from DFT, the global information on the shape of the particle is not completely lost.

Table 1: Averaged errors on bonds, angles and R_g for the small Pt_{13} dataset

	bonds MMAE (Å) [a]			angles MMAE (°) [b]			R_g MAE (Å) [c]		
	GFN0-xTB	GFN2-xTB	DFTB	GFN0-xTB	GFN2-xTB	DFTB	GFN0-xTB	GFN2-xTB	DFTB
Amorphous	0.18	0.09	0.06	7.9	4.2	2.8	0.026	0.028	0.037
Ordered	0.26	0.24	0.05	10.9	10.3	1.1	0.033	0.066	0.040

[a,b] The averaged error on bond lengths and angles is expressed as Mean MAE (MMAE). [c] The average error on R_g is expressed as a MAE. All the quantities are computed separately on amorphous and ordered structures to highlight the morphology-dependent behavior of the tested methods.

2.3.1.2 Relative stabilities

In this section we mean to assess the performances of our low-cost methods on the energetic ranking of the structures belonging to the *Pt_{13} small dataset*. The energies are expressed here as relative stabilities with respect to the global minimum, as it was for Figure 5. For each geometry optimized at PBE-dDsC level, we compare the PBE-dDsC energy with the energy obtained with the chosen low-cost method on the same atomic conformation, thus neglecting the effect of SE geometry optimization in the first place. We express the raw results in the form of histograms (Figure 7, full columns), while we quantify the degree of agreement

between the DFT and SE energies by means of a linear regression analysis, which is performed separately for amorphous and ordered structures. The regression parameters (slope and determination coefficient (R^2)) are compactly given in Table 2, while the relative scatter plots are presented in the panels A, C, E of Figure 8.

Relying on the reported values of R^2, the regression analysis shows itself to be rather inglorious for GFN0-xTB energies, classifying again DFTB as the best performing method (in line with the parametrization of ref. 23), followed by GFN2-xTB. Here, the different behavior for ordered and amorphous structures is evident not only for GFN2-xTB, but also for GFN0-xTB and DFTB, even though for the latter the difference is almost negligible. Despite the poor results of GFN0-xTB, the performances of GFN2-xTB are strongly morphology-dependent, being competitive with DFTB only for the amorphous structures. The generally coarse results of GFN0-xTB are reflected in the histograms of Figure 7B, from which it appears its inability to reproduce the stability trend depicted by PBE-dDsC energies (Figure 7A). While both GFN2-xTB and DFTB are well performing for amorphous structures, they behave differently for the ordered ones: DFTB is slightly underestimating their stability (Figure 7D), while the trend is less uniform for GFN2-xTB (Figure 7C).

At this point, we mean to take into account the effect of geometry optimization at SE level. To this purpose, we carried out an analogous analysis by comparing the PBE-dDsC energy with the energy obtained with the chosen low-cost method on the same NPs after geometry optimization. The corresponding histograms are presented in Figure 7 (striped columns), while the regression parameters are reported in brackets in Table 2 (the relative scatter plots are presented in Figure 9).
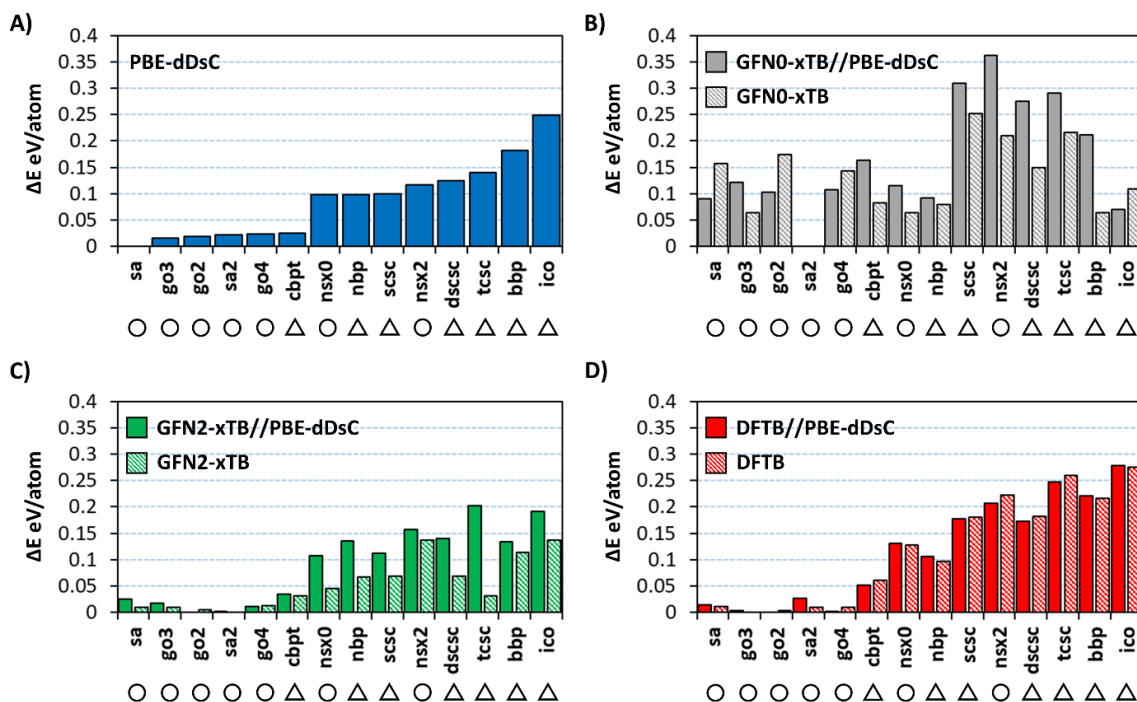
Figure 7. Relative stabilities (with respect to the global minimum) of the structures of the Pt_{13} small dataset, computed with PBE-dDsC (A), GFN0-xTB (B), GFN2-xTB (C) and DFTB (D). Full columns correspond to single point energy evaluations performed on the frozen PBE-dDsC geometry, while striped columns report the SE energy of the same NP after geometry optimization. Circles indicate amorphous structures, while triangles indicate ordered ones.

The value of R^2 is generally decreasing upon geometry optimization with SE methods, which is consistent with the natural action of forces that modify atomic coordinates during geometry optimizations. The case of GFN2-xTB on ordered structures is less trivial. Even though the higher value of R^2 suggests a better correlation between data points, the high slope value (Table 2) indicates a general compression of the energetic range covered by PBE-dDsC, which is reflected in the histograms (Figure 7C). Moreover, the significant difference between relative stabilities of ordered structures before and after GFN2-xTB geometry optimization is consistent with the significant MAE on bond lengths and angles discussed in section 2.3.1.1. DFTB is less sensitive to geometry optimization than the other methods for all structures and provide a more coherent stability trend with respect to PBE-dDsC.

37
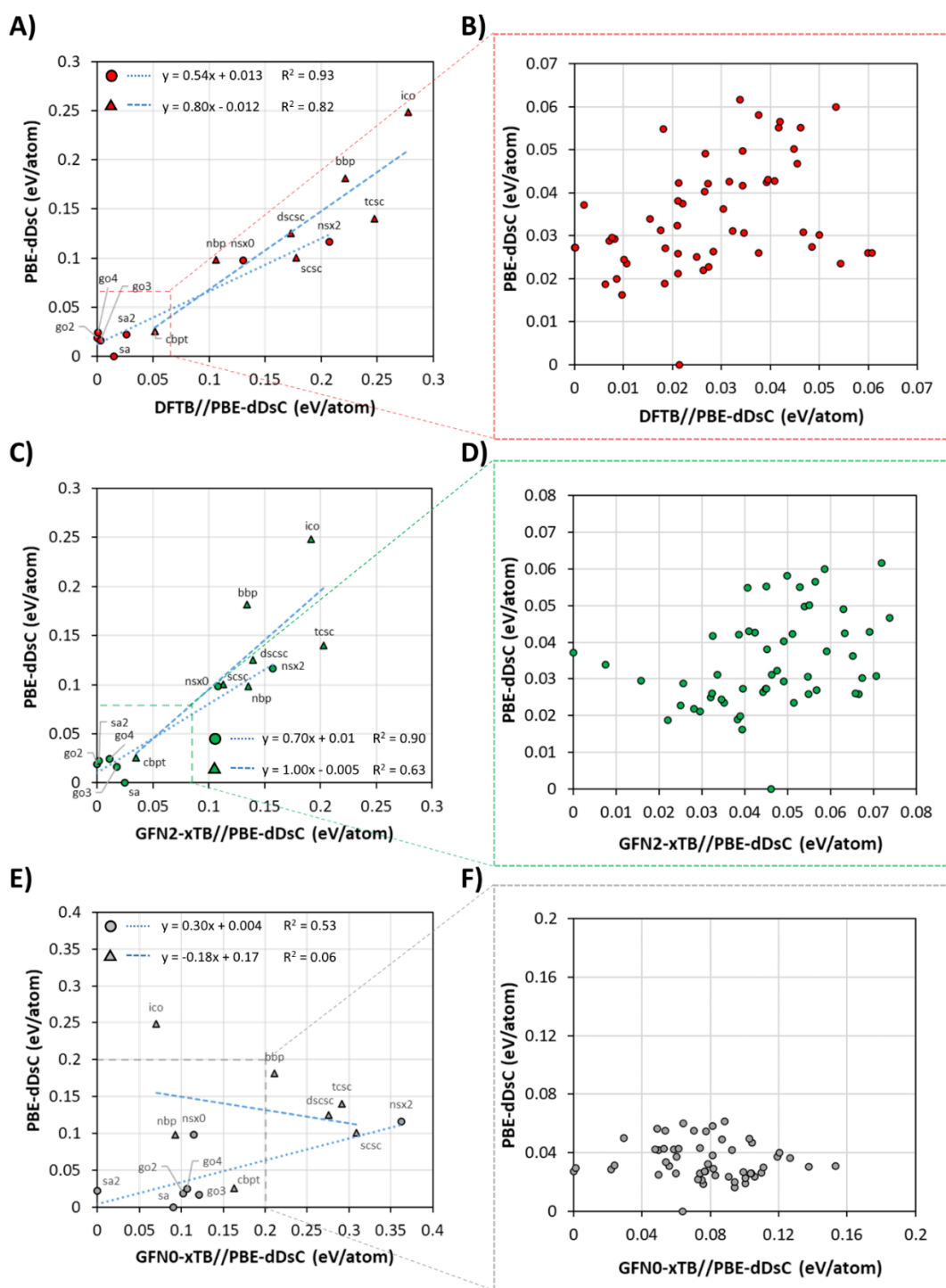
Figure 8. Comparison between PBE-dDsC and "hybrid" semiempirical (SE) energies. Y axis: relative energy of Pt_{13} NPs after geometry optimization at PBE-dDsC level. X axis: single point energy evaluation at SE level (DFTB (A), (B); GFN2-xTB (B), (C); GFN0-xTB (E), (F)), performed on the frozen PBE-dDsC geometry. The plots (A), (C), (E) are referred to structures belonging to the "Pt_{13} small dataset". In these three graphs, the presented linear regression is performed separately for the amorphous (bullets, dotted line) and the ordered (triangles, dashed lines) structures. The plots (B), (D), (F) are referred to structures belonging to the "Pt_{13} amorphous dataset".
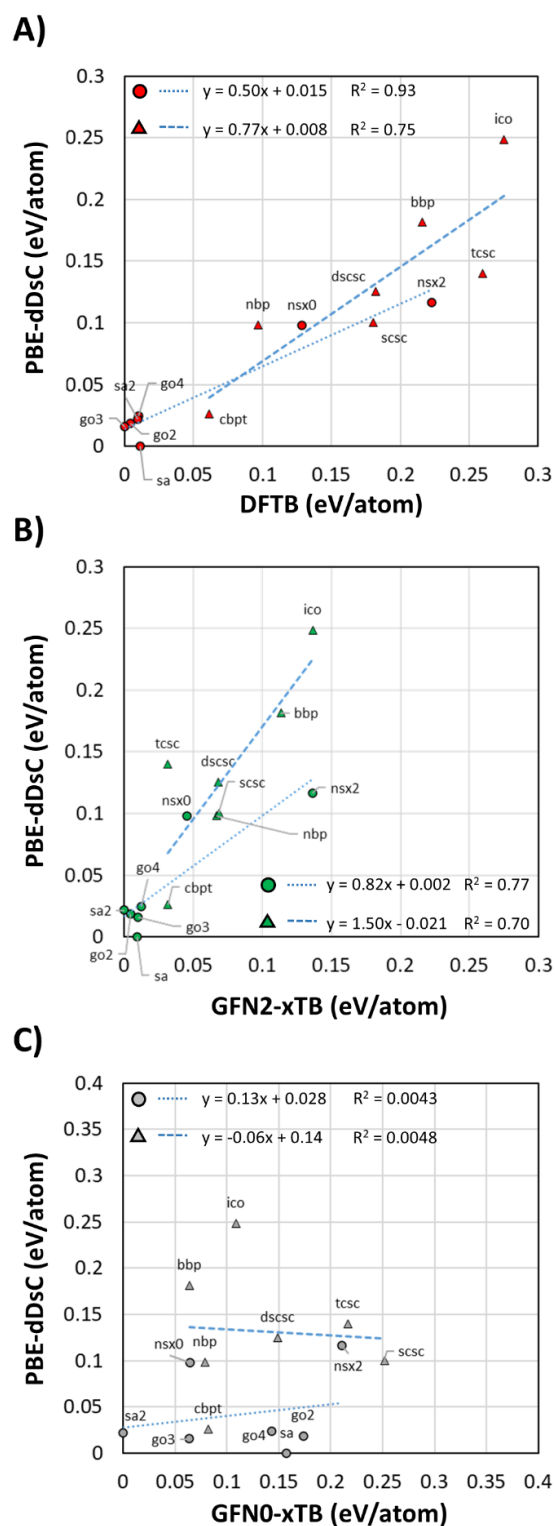
Figure 9. Comparison between PBE-dDsC and semiempirical (SE) energies. Y axis: relative energy of Pt_{13} NPs after geometry optimization at PBE-dDsC level. X axis: relative energy of Pt_{13} NPs after geometry optimization at SE level (DFTB (A); GFN2-xTB (B); GFN0-xTB (C)). The presented linear regression is performed separately for the amorphous (bullets, dotted line) and the ordered (triangles, dashed lines) structures.

Table 2: Determination coefficients and slopes of the regression analysis performed on relative stabilities (PBE-dDsC versus SE energy)

	GFN0-xTB//PBE-dDsC[b] (GFN0-xTB)[a]		GFN2-xTB//PBE-dDsC[d] (GFN2-xTB)[c]		DFTB//PBE-dDsC[f] (DFTB)[e]	
	R^2	slope	R^2	Slope	R^2	slope
Amorphous	0.53 (0.004)	0.30 (0.13)	0.90 (0.77)	0.70 (0.82)	0.93 (0.93)	0.54 (0.50)
Ordered	0.06 (0.005)	-0.18 (-0.06)	0.63 (0.70)	1.00 (1.50)	0.82 (0.75)	0.80 (0.77)

[a,c,e] The regression was performed on relative stabilities computed by SE methods on frozen PBE-dDsC geometries.

[b,d,f] The regression was performed on relative stabilities computed after re-optimization at SE level.

2.3.1.3 Vibrational frequencies and thermochemical parameters

While the previous section checked how the semiempirical methods are able to properly describe the energy minima of the potential energy surface, we now aim at analyzing how these methods describe the fluctuation of the systems in the close vicinity of those energy minima. First, harmonic vibrational frequencies were computed for each structure at the different levels of theory. Information of the unprocessed vibrational frequencies computed with low-cost methods with respect about the deviations to PBE-dDsC is reported in Figure 10.
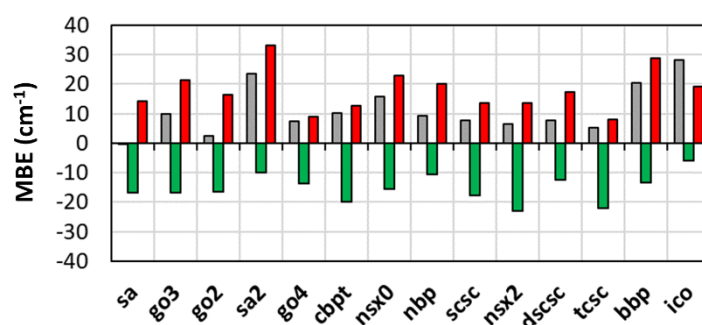
Figure 10. Mean Bias Error (MBE) of GFN0-xTB (gray), GFN2-xTB (green) and DFTB (red) on the computation on the vibrational frequencies. MBE is computed with respect to the benchmark PBE-dDsC.

According to the mean bias errors (MBE) presented in Table 3 and the histograms of Figure 11, deviations on the vibrational enthalpy (H_{vib}) plus ZPVE are found to be negligible compared with the entropic term. Hence, since the vibrational free energy is computed as reported in eq. 1, the error on G_{vib} comes predominantly from the $-TS_{vib}$ term. The main contribution to H_{vib} comes from high-frequency modes,[83] which are most likely associated to close bonding and stretching modes. S_{vib}, on the other hand, is more sensitive to low-frequencies modes, corresponding to concerted movements of the whole NP. Thus, the negligible error on H_{vib} signifies that all the methods are well describing the shape of the potential well associated to high frequency modes and thus, to close bonding, where it is less true for the concerted vibrations. Nevertheless, the magnitude of G_{vib} remains rather small (less than 16 kJ/mol), which implies that the relative stability of all structures is not modified at T = 300 K by vibrational contributions whatever the method used (see Figure A2).

Analyzing the histograms in Figure 11, two main observations can be made: GFN0-xTB shows the smallest deviation from the standard PBE-dDsC and the deviation of GFN2-xTB follows the opposite trend with respect to the other two methods. This behavior indicates that, for low-frequency modes, while DFTB and GFN0-xTB are computing tighter potential wells with respect to PBE-dDsC, the same potential wells computed by GFN2-xTB are looser. This means that GFN2-xTB, in contrast with DFTB and GFN0-xTB, underestimates force constants for vibrations in which the whole nanoparticle is involved.
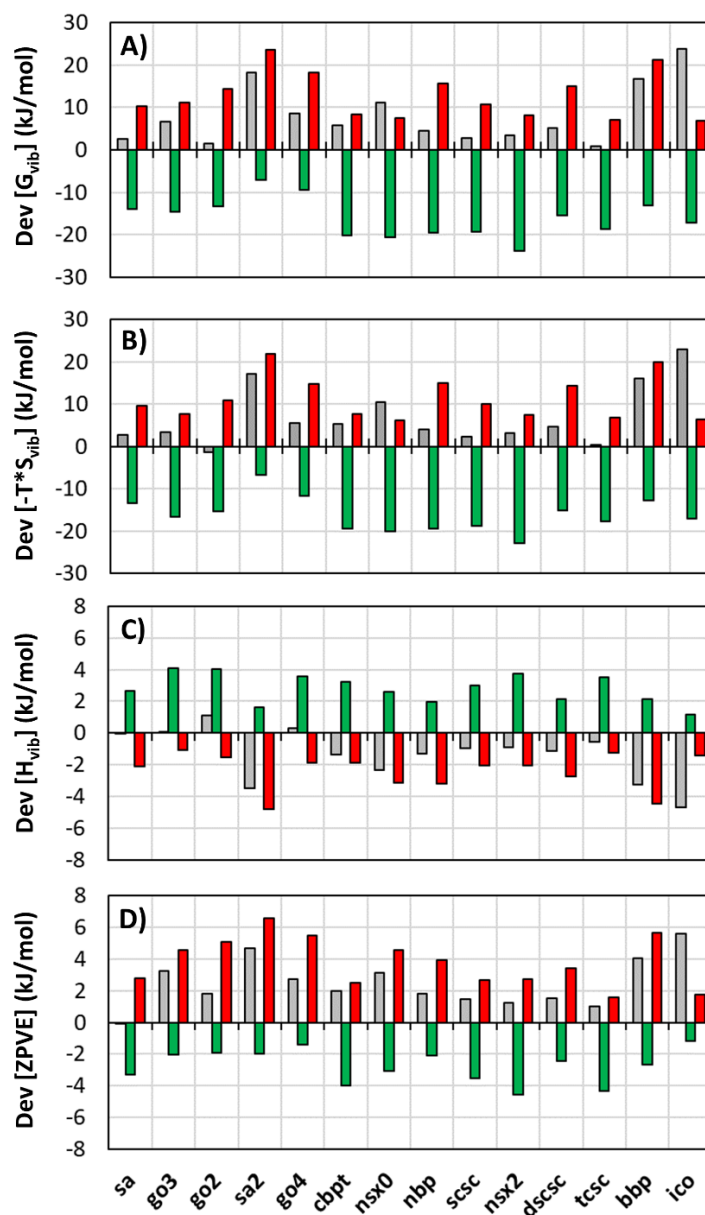
Figure 11. Deviations of GFN0-xTB (gray), GFN2-xTB (green) and DFTB (red) with respect to PBE-dDsC on the computation on the vibrational free energy and entropy (TS_{vib}) at T=300 K. We did not plot Dev [Hvib + ZPVE] since it was fully balanced around 0 and always below 4 kJ/mol.

Table 3: Averaged errors on Gvib, -TSvib, Hvib and ZPVE for the small Pt13 dataset

	MBE [G_{vib}] (kJ/mol)	MBE [$-TS_{vib}$] (kJ/mol)	MBE [H_{vib}] (kJ/mol)	MBE [ZPVE] (kJ/mol)
GFN0-xTB	8.0	6.9	-1.3	2.4
GFN2-xTB	-16.2	-16.2	2.8	-2.7
DFTB	12.7	11.3	-2.4	3.8

2.3.2 Pt$_{13}$ and Pt$_{55}$ amorphous datasets

As described in section 2.2.3, a procedure analogous to the one applied to the *Pt$_{13}$ small dataset* was adopted for the two large datasets of amorphous Pt$_{13}$ and Pt$_{55}$ NPs. All the geometries optimized at PBE-dDsC level were re-optimized with GFN0-xTB, GFN2-xTB, DFTB and ReaxFF. The agreement of the tested methods with the PBE-dDsC reference was evaluated by comparing three geometric descriptors (bond lengths, bond angles and R$_g$) and the relative energies of the structures belonging to the two datasets.

Figure 12 reports the distribution of the signed deviation on bond lengths, bond angles and R$_g$ computed for all the tested low-cost methods, both for the Pt$_{13}$ and Pt$_{55}$ amorphous datasets. Since the signed deviation is a discrete variable in these cases, continuous probability density functions were estimated through the KDE procedure described in section 2.2.2. The KDE plots for each geometric descriptor are computed by employing the same smoothing factor (reported in Table 4), thus legitimating the comparison between the probability density functions of the two datasets.

The differences in the distributions between Pt$_{13}$ and Pt$_{55}$ reveal that the performances of DFTB and GFN0-xTB are generally improving while increasing the particle size: the distributions are getting narrower and shifted towards zero. GFN2-xTB seems to undergo the opposite trend, indeed, the distributions of the deviation for bonds and angles are widening when moving from Pt$_{13}$ to Pt$_{55}$, while the behavior of the deviation on R$_g$ is less clear. The performances of ReaxFF are generally poor and show only a slight improvement for Pt$_{55}$ with respect to Pt$_{13}$. DFTB proves to be the best method, although it causes a small and systematic compression of bond lengths, which is also reflected in the deviation on R$_g$. GFN0-xTB is

43

showing the biggest improvements, becoming competitive with DFTB and outperforming it

for the R_g.
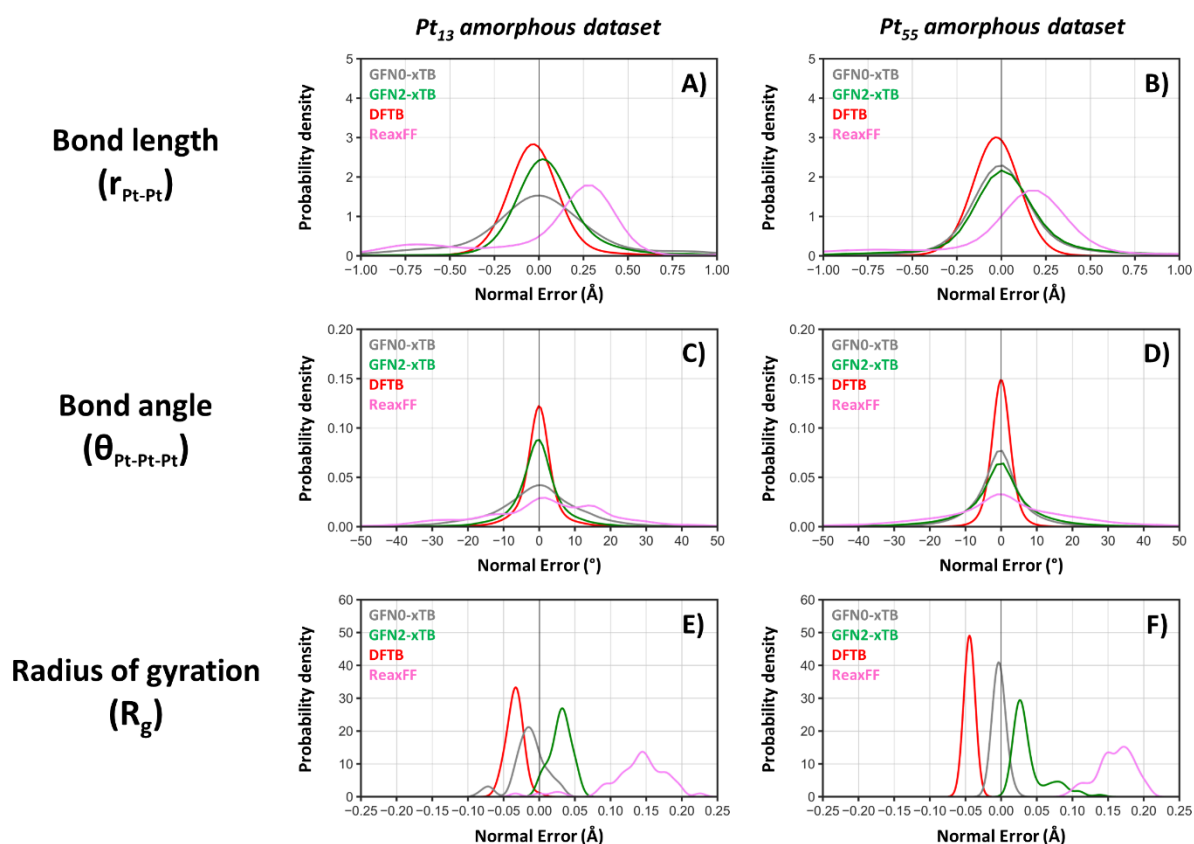
Figure 12. Distribution of the signed deviation on bond lengths (A, B), bond angles (C, D) and radii of gyrations (E, F) for DFTB (red), GFN2-xTB (green), GFN0-xTB (grey) and ReaxFF (pink) with respect to PBE-dDsC values for the Pt_{13} and Pt_{55} amorphous datasets.

The plots reported in Figure 8B, 8D and 8F are conceived to inspect the correlation

between relative energies computed at PBE-dDsC level with relative energies computed with

the tested low-cost methods for the structures belonging to the Pt_{13} amorphous dataset. In

this case, data show that the energy range in which the amorphous isomers of Pt_{13} lie is far

smaller than the accuracy of a GGA functional like PBE. As illustrated in Figure A3, the data

regarding amorphous Pt_{55} NPs exhibit also a very narrow energy fluctuation. Hence, it is

beyond the accuracy level to discuss any correlation between electronic relative energies for these set of amorphous NPs.

Table 4: Adopted smoothing factors for the KDE plots

	bonds (Å)	angles (°)	R_g (Å)
s	0.12	1.8	0.0075

Table 5: Mean values (Å) and standard deviations (Å², reported in brackets) of the error distributions presented in Figure 12

Since the distributions are not perfect gaussians, the reported mean values do not correspond with the maxima of the distributions and the reported variances cannot be linked to the full width at half maximum (FWHM) with the relation: $FWHM = 2\sqrt{2\ln 2}\,\sigma$. This is particularly influent for ReaxFF, for which data are strongly deviating from a gaussian distribution

Bond length ($r_{Pt\text{-}Pt}$)	DFTB	GFN0-xTB	GFN2-xTB	ReaxFF
Pt$_{13}$	-0.027 (0.015)	0.001 (0.120)	0.055 (0.038)	0.093 (0.339)
Pt$_{55}$	-0.030 (0.004)	0.023 (0.055)	0.043 (0.120)	0.063 (0.335)

Bond angle ($\theta_{Pt\text{-}Pt}$)	DFTB	GFN0-xTB	GFN2-xTB	ReaxFF
Pt$_{13}$	-0.245 (23.5)	-0.565 (153.7)	0.458 (50.7)	1.45 (390.8)
Pt$_{55}$	-0.021 (7.03)	-0.620 (67.4)	-0.527 (133.8)	0.787 (380.8)

Radius of Gyration (R_g)	DFTB	GFN0-xTB	GFN2-xTB	ReaxFF
Pt$_{13}$	-0.034 (1 10^{-4})	-0.014 (0.001)	0.030 (2 10^{-4})	0.136 (0.002)
Pt$_{55}$	0.044 (9 10^{-6})	-0.003 (4 10^{-5})	0.040 (7 10^{-4})	0.160 (0.001)

2.3.3 Towards big-sized nanoparticles

Amorphous geometries for nanoparticles of stoichiometry Pt$_{147}$, Pt$_{309}$, Pt$_{561}$ were obtained through the procedure described in section 2.2.2. As a preliminary remark, the relative energies (calculated at PBE-dDsC level) between amorphous and cuboctahedron clusters

show that for sizes smaller than 309 atoms, amorphous clusters are more stable than the cuboctahedral isomers (Figure 13). For a cluster size of 561 atoms, the cuboctahedron becomes more stable. Interestingly, this trend is found in qualitative agreement with the experimental observation showing the predominance of amorphous clusters for sizes smaller than around 250 atoms.[78] Nevertheless, to overcome the limitation of considering cuboctahedral isomers only, such a result should prompt a more systematic theoretical investigation comparing the energies of amorphous clusters found in the present studies with ordered clusters exhibiting much more diverse morphologies (other than cuboctahedral ones).
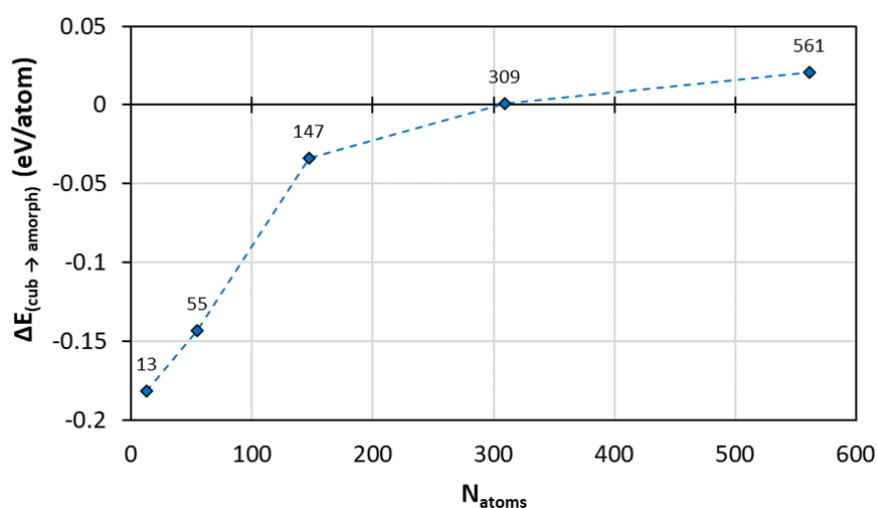
Figure 13. Amorphization energy of Pt_x NPs (x = 13, 55, 147, 309, 561) computed at PBE-dDsC level, intended as energy difference between the electronic energy of amorphous and cuboctahedral geometries for each stoichiometry.

Concerning the only amorphous nanoparticles, We inspected the agreement of the tested low-cost methods with the DFT standard (as well as the performances of XTB MD) by plotting, for each nanoparticle, the deviation between its pure PBE-dDsC energy and its PBE-dDsC energy evaluated as single point on SE or FF geometry. The energy deviation (ΔE) reported in Figure 14A is computed as follows:

$$\Delta E = E_{PBE-dDsC//Low-cost} - E_{PBE-dDsC} \tag{4}$$

Given the strong dependency of the electronic energy on the atomic coordinates, the quantity "ΔE" defined in Eq. 4 is here exploited, together with the mean Pt-Pt distance, to weigh the discrepancy between the benchmark PBE-dDsC structures and the low-cost ones (Figure 14).
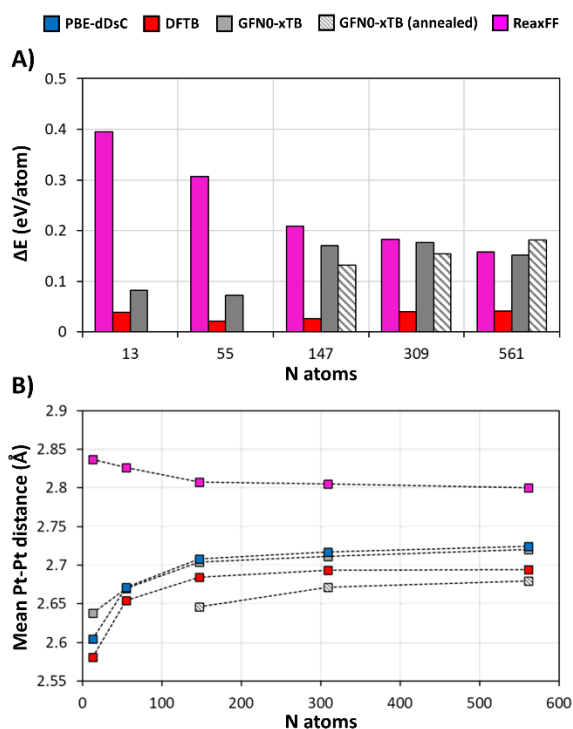
Figure 14. A) Electronic energy difference between the full PBE-dDsC energy and the PBE-dDsC energy evaluated on DFTB (red), GFN0-xTB (grey) or ReaxFF (pink) geometry. The grey stripes represent the difference between the full PBE-dDsC energy and the PBE-dDsC energy evaluated on a geometry annealed with GFN0-xTB molecular dynamics. B) Evolution of the mean Pt-Pt distance with particle size for PBE-dDsC (blue), DFTB (red), GFN0-xTB (gray), annealed GFN0-xTB (striped grey) and ReaxFF (pink) geometries.

The systematic decrease in the deviation (ΔE) of ReaxFF coupled with the increase in the system's size can be at least partially linked to its parametrization, which has been carried out initially on Pt_{100} clusters.[74] However, the energy deviation remains quite large to be exploitable (around 0.16 eV/atom for Pt_{561}). Moreover, ReaxFF completely reverses the canonic relation between the intermetallic distances and NP's size. GFN0-xTB follows the

opposite trend and shows a significantly higher deviation for Pt_{147}, Pt_{309}, Pt_{561} than for Pt_{13} and Pt_{55}. Although this energy deviation is rather comparable to the one observed for ReaxFF, the mean Pt-Pt distance on GFN0-xTB structures shows a good agreement with PBE-dDsC compared with structures optimized with the other low-cost methods. In order to attempt to decrease the ΔE for GFN0-xTB and given the rather low computational cost of GFN0-xTB MD, the GFN0-xTB geometries of Pt_{147}, Pt_{309}, Pt_{561} were further annealed during 50 ps, as explained in section 2.2.2. This additional annealing step succeeded in reducing modestly the ΔE of GFN0-xTB structures for Pt_{147} and Pt_{309} by about 0.03 eV and did not reduce the energy deviation for Pt_{561}. In this latter case, longer MD simulation times are probably required. Even though geometries obtained from GFN0-xTB MD do not provide significant improvements in ΔE (eq. 2, all computed at the PBE-dDsC level) with respect to geometries obtained thanks to ReaxFF for the largest particles, it is still able to provide reliable results for Pt-Pt bond lengths. Unfortunately, the averaged Pt-Pt bond length of annealed GFN0-xTB structures is not straightforwardly comparable with the others, since they are generated through a completely different approach. Finally, DFTB proves itself as the best-performing low-cost method, even though it causes a systematic compression of Pt NPs (Figure 14B). Its low energy deviation (less than 0.05 eV/atom) reported for all the investigated particle sizes states that the good performances exhibited by DFTB for Pt_{13} and Pt_{55} are maintained when increasing the number of atoms up to a few hundred. Since the employed parametrization for DFTB has been carried out solely on Pt_{13} and Pt_{55} clusters,[23] this indicates a good transferability of the set of parameters.

2.4 Conclusions

In this chapter, we assessed the performances of low-cost computational methods for the prediction of structural features and energetics of Pt nanoparticles of stoichiometry Pt_{13}, Pt_{55},

Pt$_{147}$, Pt$_{309}$, Pt$_{561}$. The chosen low-cost methods were the semiempirical DFTB, GFN0-xTB, GFN1-xTB, GFN2-xTB and ReaxFF, while the reference DFT functional was the dispersion-corrected PBE-dDsC. We carried out the benchmark study on four structural datasets, composed by (1) 14 amorphous and ordered Pt$_{13}$ NPs, (2) 54 amorphous Pt$_{13}$ NPs, (3) 93 amorphous Pt$_{55}$ NPs and (4) 5 amorphous NPs of stoichiometry Pt$_x$ (x = 13, 55, 147, 309, 561). In the light of the discussed data, the following conclusions can be drawn.

DFTB is by far the method showing the best performances. Its parametrization, carried out on Pt$_{13}$ and Pt$_{55}$ NPs, grants a good reproduction of properties for NPs of the same size. The good agreement with the DFT standard shown for NPs of bigger sizes also proves the good transferability of the parametrization. The performances of the remaining methods are found to be morphology- and size-dependent. GFN2-xTB produces reasonable results for amorphous Pt$_{13}$ clusters, though not for ordered ones. Moreover, its performances worsen when increasing the cluster's size from 13 to 55, before failing the electronic SCC when further increasing the size of the system. While the agreement between GFN0-xTB and the DFT standard is quite poor for Pt$_{13}$, the method provides a satisfactory prediction of structural features for amorphous Pt$_{55}$ geometries, making it competitive with DFTB. GFN0-xTB is slightly worsening for Pt$_{147}$, Pt$_{309}$ and Pt$_{561}$ with respect to smaller clusters, though it outperforms the other methods on the averaged Pt-Pt bond length. ReaxFF behaves in the opposite way. Starting from considerably poor performances for Pt$_{13}$ and Pt$_{55}$ (both for geometries and energies), its results get better for bigger NPs, becoming competitive with GFN0-xTB for Pt$_{561}$, even though the average Pt-Pt bond length is still not well represented. One last notable conclusion can be drawn about vibrational frequencies: independently from the parametrization and level of theory, all the tested methods show a deviation in the description of vibrational features of Pt$_{13}$. Since the largest part of the error lies on the vibrational entropy,

this indicates a shared intrinsic difficulty in the description of potential wells related to collective vibrations. However, the error on G_{vib} is around 10 kJ/mol for DFTB, and even smaller for GFN0-xTB. Although this is far from being perfect, it still represents a good compromise due to the gain in CPU.

Considering what is here summarized, DFTB turns out to be the most cost-effective method for predicting geometries and energetics of Pt NPs of all the investigated sizes and morphologies. However, since our task is to propose a low-level computational method for fast screening through candidate structures within the "multilevel modelling" of phenomena involving Pt NPs, a few final remarks have to be made. Although DFTB is the best performing method presented in this chapter, both the cheaper GFN0-xTB and ReaxFF should not be entirely discarded. The systematic error structural parameters shown by ReaxFF suggest that a re-optimization of the parametrization could sensibly improve its performances. At the same time, the atom-specific parametrization on which GFN0-xTB relies indeed allows to effortlessly include other atoms into the simulation (while DFTB would require a re-parametrization), thus opening the path to simulations involving adsorbates or nanoalloys.

References

(1)   Xu, Y.; Zhang, B. Recent Advances in Porous Pt-Based Nanostructures: Synthesis and Electrochemical Applications. *Chem. Soc. Rev.* **2014**, *43* (8), 2439–2450. https://doi.org/10.1039/c3cs60351b.

(2)   Khan, M. A. R.; Mamun, M. S. Al; Ara, M. H. Review on Platinum Nanoparticles: Synthesis, Characterization, and Applications. *Microchem. J.* **2021**, *171* (September), 106840. https://doi.org/10.1016/j.microc.2021.106840.

(3)   Chen, A.; Holt-hindle, P. Platinum-Based Nanostructured Materials: Synthesis, Properties, and Applications. *Chem. Rev.* **2010**, *110*, 3767–3804.

(4)   Campelo, J. M.; Luna, D.; Luque, R.; Marinas, J. M.; Romero, A. A. Sustainable Preparation of Supported Metal Nanoparticles and Their Applications in Catalysis. *ChemSusChem* **2009**, *2* (1), 18–45. https://doi.org/10.1002/cssc.200800227.

(5)   Boudart, M. Catalysis by Supported Metals. *Adv. Catal.* **1969**, *20* (C), 153 − 166. https://doi.org/10.1016/S0360-0564(08)60271-0.

(6)   Heck, R. M.; Farrauto, R. J. Automobile Exhaust Catalysts. *Appl. Catal. A Gen.* **2001**, *221* (1), 443–457. https://doi.org/https://doi.org/10.1016/S0926-860X(01)00818-3.

(7)   Gänzler, A. M.; Casapu, M.; Vernoux, P.; Loridant, S.; Cadete Santos Aires, F. J.; Epicier, T.; Betz, B.; Hoyer, R.; Grunwaldt, J. D. Tuning the Structure of Platinum Particles on Ceria In Situ for Enhancing the Catalytic Performance of Exhaust Gas Catalysts. *Angewandte Chemie - International Edition*. 2017, pp 13078–13082. https://doi.org/10.1002/anie.201707842.

(8)   Keppeler, M.; Bräuning, G.; Radhakrishnan, S. G.; Liu, X.; Jensen, C.; Roduner, E. Reactivity of Diatomics and of Ethylene on Zeolite-Supported 13-Atom Platinum Nanoclusters. *Catal. Sci. Technol.* **2016**, *6* (18), 6814–6823.

https://doi.org/10.1039/c6cy00182c.

(9)   Chen, S.; Chang, X.; Sun, G.; Zhang, T.; Xu, Y.; Wang, Y.; Pei, C.; Gong, J. Propane Dehydrogenation: Catalyst Development, New Chemistry, and Emerging Technologies. *Chem. Soc. Rev.* **2021**, *50* (5), 3315–3354. https://doi.org/10.1039/d0cs00814a.

(10)   Docherty, S. R.; Rochlitz, L.; Payard, P. A.; Copéret, C. Heterogeneous Alkane Dehydrogenation Catalysts Investigated via a Surface Organometallic Chemistry Approach. *Chem. Soc. Rev.* **2021**, *50* (9), 5806–5822. https://doi.org/10.1039/d0cs01424a.

(11)   Sattler, J. J. H. B.; Ruiz-Martinez, J.; Santillan-Jimenez, E.; Weckhuysen, B. M. Catalytic Dehydrogenation of Light Alkanes on Metals and Metal Oxides. *Chemical Reviews*. 2014, pp 10613–10653. https://doi.org/10.1021/cr5002436.

(12)   Goodier, J. Springer Handbook of Petroleum Technology. *Ref. Rev.* **2018**, *32* (7/8), 36–36. https://doi.org/10.1108/rr-07-2018-0111.

(13)   Le Goff, P. Y.; Kostka, W.; Ross, J. Catalytic Reforming. In *Springer Handbooks*; 2017; Vol. PartF1, pp 589–616. https://doi.org/10.1007/978-3-319-49347-3_18.

(14)   Piccolo, L. Restructuring Effects of the Chemical Environment in Metal Nanocatalysis and Single-Atom Catalysis. *Catal. Today* **2021**, *373* (April 2020), 80–97. https://doi.org/10.1016/j.cattod.2020.03.052.

(15)   Batista, A. T. F.; Baaziz, W.; Taleb, A. L.; Chaniot, J.; Moreaud, M.; Legens, C.; Aguilar-Tapia, A.; Proux, O.; Hazemann, J. L.; Diehl, F.; Chizallet, C.; Gay, A. S.; Ersen, O.; Raybaud, P. Atomic Scale Insight into the Formation, Size, and Location of Platinum Nanoparticles Supported on γ-Alumina. *ACS Catalysis*. 2020, pp 4193–4204. https://doi.org/10.1021/acscatal.0c00042.

(16)   Vottero, E.; Carosso, M.; Ricchebuono, A.; Jiménez-Ruiz, M.; Pellegrini, R.; Chizallet, C.;

Raybaud, P.; Groppo, E.; Piovano, A. Evidence for H2-Induced Ductility in a Pt/Al2O3 Catalyst. *ACS Catal.* **2022**, *12* (10), 5979–5989. https://doi.org/10.1021/acscatal.2c00606.

(17)   Avanesian, T.; Dai, S.; Kale, M. J.; Graham, G. W.; Pan, X.; Christopher, P. Quantitative and Atomic-Scale View of CO-Induced Pt Nanoparticle Surface Reconstruction at Saturation Coverage via DFT Calculations Coupled with in Situ TEM and IR. *J. Am. Chem. Soc.* **2017**, *139* (12), 4551–4558. https://doi.org/10.1021/jacs.7b01081.

(18)   Sangnier, A.; Genty, E.; Iachella, M.; Sautet, P.; Raybaud, P.; Matrat, M.; Dujardin, C.; Chizallet, C. Thermokinetic and Spectroscopic Mapping of Carbon Monoxide Adsorption on Highly Dispersed Pt/γ-Al2O3. *ACS Catal.* **2021**, *11* (21), 13280–13293. https://doi.org/10.1021/acscatal.1c04262.

(19)   Zhai, H.; Alexandrova, A. N. Fluxionality of Catalytic Clusters: When It Matters and How to Address It. *ACS Catal.* **2017**, *7* (3), 1905–1911. https://doi.org/10.1021/acscatal.6b03243.

(20)   Chizallet, C.; Raybaud, P. Density Functional Theory Simulations of Complex Catalytic Materials in Reactive Environments: Beyond the Ideal Surface at Low Coverage. *Catal. Sci. Technol.* **2014**, *4* (9), 2797–2813. https://doi.org/10.1039/c3cy00965c.

(21)   Hu, C. H.; Chizallet, C.; Toulhoat, H.; Raybaud, P. Structural, Energetic, and Electronic Trends in Low-Dimensional Late-Transition-Metal Systems. *Phys. Rev. B - Condens. Matter Mater. Phys.* **2009**, *79* (19), 1–11. https://doi.org/10.1103/PhysRevB.79.195416.

(22)   Ellaby, T.; Aarons, J.; Varambhia, A.; Jones, L.; Nellist, P.; Ozkaya, D.; Sarwar, M.; Thompsett, D.; Skylaris, C. K. Ideal versus Real: Simulated Annealing of Experimentally Derived and Geometric Platinum Nanoparticles. *J. Phys. Condens. Matter* **2018**, *30* (15).

https://doi.org/10.1088/1361-648X/aab251.

(23) Van Den Bossche, M. DFTB-Assisted Global Structure Optimization of 13- and 55-Atom Late Transition Metal Clusters. *J. Phys. Chem. A* **2019**, *123* (13), 3038–3045. https://doi.org/10.1021/acs.jpca.9b00927.

(24) Yang, Q.; Jiang, G. D.; He, S. G. Enhancing the Performance of Global Optimization of Platinum Cluster Structures by Transfer Learning in a Deep Neural Network. *J. Chem. Theory Comput.* **2023**, *19* (6), 1922–1930. https://doi.org/10.1021/acs.jctc.2c00923.

(25) Raybaud, P.; Chizallet, C.; Mager-Maury, C.; Digne, M.; Toulhoat, H.; Sautet, P. From γ-Alumina to Supported Platinum Nanoclusters in Reforming Conditions: 10 Years of DFT Modeling and Beyond. *J. Catal.* **2013**, *308*, 328–340. https://doi.org/10.1016/j.jcat.2013.08.015.

(26) Mager-Maury, C.; Bonnard, G.; Chizallet, C.; Sautet, P.; Raybaud, P. H2-Induced Reconstruction of Supported Pt Clusters: Metal-Support Interaction versus Surface Hydride. *ChemCatChem* **2011**, *3* (1), 200–207. https://doi.org/10.1002/cctc.201000324.

(27) Hu, C. H.; Chizallet, C.; Mager-Maury, C.; Corral-Valero, M.; Sautet, P.; Toulhoat, H.; Raybaud, P. Modulation of Catalyst Particle Structure upon Support Hydroxylation: Ab Initio Insights into Pd13 and Pt13/γ-Al 2O3. *J. Catal.* **2010**, *274* (1), 99–110. https://doi.org/10.1016/j.jcat.2010.06.009.

(28) Kaiser, S.; Maleki, F.; Zhang, K.; Harbich, W.; Heiz, U.; Tosoni, S.; Lechner, B. A. J.; Pacchioni, G.; Esch, F. Cluster Catalysis with Lattice Oxygen: Tracing Oxygen Transport from a Magnetite (001) Support onto Small Pt Clusters. *ACS Catal.* **2021**, *11* (15), 9519–9529. https://doi.org/10.1021/acscatal.1c01451.

(29) Xu, Y.; Shelton, W. A.; Schneider, W. F. Effect of Particle Size on the Oxidizability of

Platinum Clusters. *J. Phys. Chem. A* **2006**, *110* (17), 5839–5846. https://doi.org/10.1021/jp0547111.

(30)   Laletina, S. S.; Mamatkulov, M.; Shor, E. A.; Kaichev, V. V.; Genest, A.; Yudanov, I. V.; Rösch, N. Size-Dependence of the Adsorption Energy of CO on Pt Nanoparticles: Tracing Two Intersecting Trends by DFT Calculations. *J. Phys. Chem. C* **2017**, *121* (32), 17371–17377. https://doi.org/10.1021/acs.jpcc.7b05580.

(31)   Calle-Vallejo, F.; Sautet, P.; Loffreda, D. Understanding Adsorption-Induced Effects on Platinum Nanoparticles: An Energy-Decomposition Analysis. *J. Phys. Chem. Lett.* **2014**, *5* (18), 3120–3124. https://doi.org/10.1021/jz501263e.

(32)   Grimme, S.; Schreiner, P. R. Computational Chemistry: The Fate of Current Methods and Future Challenges. *Angew. Chemie - Int. Ed.* **2018**, *57* (16), 4170–4176. https://doi.org/10.1002/anie.201709943.

(33)   Aarons, J.; Sarwar, M.; Thompsett, D.; Skylaris, C.-K. Perspective: Methods for Large-Scale Density Functional Calculations on Metallic Systems. *J. Chem. Phys.* **2016**, *145* (22), 220901. https://doi.org/10.1063/1.4972007.

(34)   Bannwarth, C.; Caldeweyher, E.; Ehlert, S.; Hansen, A.; Pracht, P.; Seibert, J.; Spicher, S.; Grimme, S. Extended Tight-Binding Quantum Chemistry Methods. *Wiley Interdiscip. Rev. Comput. Mol. Sci.* **2021**, *11* (2), 1–49. https://doi.org/10.1002/wcms.1493.

(35)   Caldeweyher, E.; Ehlert, S.; Hansen, A.; Neugebauer, H.; Spicher, S.; Bannwarth, C.; Grimme, S. A Generally Applicable Atomic-Charge Dependent London Dispersion Correction. *J. Chem. Phys.* **2019**, *150* (15), 154122. https://doi.org/10.1063/1.5090222.

(36)   Sarwar, M.; Cooper, C.; Briquet, L.; Ukpong, A.; Perry, C.; Jones, G. Atomic-Scale Modelling and Its Application to Catalytic Materials Science. *Johnson Matthey Technol. Rev.* **2015**, *59* (3), 257–283. https://doi.org/10.1595/205651315X687975.

(37)   Heiles, S.; Johnston, R. L. Global Optimization of Clusters Using Electronic Structure Methods. *Int. J. Quantum Chem.* **2013**, *113* (18), 2091–2109. https://doi.org/10.1002/qua.24462.

(38)   Zhai, H.; Ha, M. A.; Alexandrova, A. N. AFFCK: Adaptive Force-Field-Assisted Ab Initio Coalescence Kick Method for Global Minimum Search. *J. Chem. Theory Comput.* **2015**, *11* (5), 2385–2393. https://doi.org/10.1021/acs.jctc.5b00065.

(39)   Fung, V.; Jiang, D. E. Exploring Structural Diversity and Fluxionality of Ptn (n = 10-13) Clusters from First-Principles. *Journal of Physical Chemistry C*. 2017, pp 10796–10802. https://doi.org/10.1021/acs.jpcc.6b11968.

(40)   Chang, C. M.; Chou, M. Y. Alternative Low-Symmetry Structure for 13-Atom Metal Clusters. *Phys. Rev. Lett.* **2004**, *93* (13), 1–4. https://doi.org/10.1103/PhysRevLett.93.133401.

(41)   Li, S.; Li, H.; Liu, J.; Xue, X.; Tian, Y.; He, H.; Jia, Y. Structural and Electronic Properties of Run Clusters (N=2-14) Studied by First-Principles Calculations. *Phys. Rev. B - Condens. Matter Mater. Phys.* **2007**, *76* (4), 1–9. https://doi.org/10.1103/PhysRevB.76.045410.

(42)   Vargas, A.; Santarossa, G.; Iannuzzi, M.; Baiker, A. Fluxionality of Gold Nanoparticles Investigated by Born-Oppenheimer Molecular Dynamics. *Phys. Rev. B - Condens. Matter Mater. Phys.* **2009**, *80* (19), 1–13. https://doi.org/10.1103/PhysRevB.80.195421.

(43)   Pavan, L.; Di Paola, C.; Baletto, F. Sampling the Energy Landscape of Pt13 with Metadynamics. *Eur. Phys. J. D* **2013**, *67*, 24. https://doi.org/10.1140/epjd/e2012-30560-y.

(44)   Pracht, P.; Bohle, F.; Grimme, S. Automated Exploration of the Low-Energy Chemical Space with Fast Quantum Chemical Methods. *Phys. Chem. Chem. Phys.* **2020**, *22* (14), 7169–7192. https://doi.org/10.1039/c9cp06869d.

(45) Hourahine, B.; Aradi, B.; Blum, V.; Bonafé, F.; Buccheri, A.; Camacho, C.; Cevallos, C.; Deshaye, M. Y.; Dumitric, T.; Dominguez, A.; Ehlert, S.; Elstner, M.; Van Der Heide, T.; Hermann, J.; Irle, S.; Kranz, J. J.; Köhler, C.; Kowalczyk, T.; Kubař, T.; Lee, I. S.; Lutsker, V.; Maurer, R. J.; Min, S. K.; Mitchell, I.; Negre, C.; Niehaus, T. A.; Niklasson, A. M. N.; Page, A. J.; Pecchia, A.; Penazzi, G.; Persson, M. P.; Řezáč, J.; Sánchez, C. G.; Sternberg, M.; Stöhr, M.; Stuckenberg, F.; Tkatchenko, A.; Yu, V. W. Z.; Frauenheim, T. DFTB+, a Software Package for Efficient Approximate Density Functional Theory Based Atomistic Simulations. *J. Chem. Phys.* **2020**, *152* (12), 124101. https://doi.org/10.1063/1.5143190.

(46) Pracht, P.; Caldeweyher, E.; Ehlert, S.; Grimme, S. A Robust Non-Self-Consistent Tight-Binding Quantum Chemistry Method for Large Molecules. *ChemRxiv, Cambridge Cambridge Open Engag. 2019* **2019**, *preprint*. https://doi.org/10.26434/chemrxiv.8326202.v1.

(47) Grimme, S.; Bannwarth, C.; Shushkov, P. A Robust and Accurate Tight-Binding Quantum Chemical Method for Structures, Vibrational Frequencies, and Noncovalent Interactions of Large Molecular Systems Parametrized for All Spd-Block Elements (Z = 1-86). *J. Chem. Theory Comput.* **2017**, *13* (5), 1989–2009. https://doi.org/10.1021/acs.jctc.7b00118.

(48) Bannwarth, C.; Ehlert, S.; Grimme, S. GFN2-XTB - An Accurate and Broadly Parametrized Self-Consistent Tight-Binding Quantum Chemical Method with Multipole Electrostatics and Density-Dependent Dispersion Contributions. *J. Chem. Theory Comput.* **2019**, *15* (3), 1652–1671. https://doi.org/10.1021/acs.jctc.8b01176.

(49) Senftle, T. P.; Hong, S.; Islam, M. M.; Kylasa, S. B.; Zheng, Y.; Shin, Y. K.; Junkermeier, C.; Engel-Herbert, R.; Janik, M. J.; Aktulga, H. M.; Verstraelen, T.; Grama, A.; Van Duin, A.

C. T. The ReaxFF Reactive Force-Field: Development, Applications and Future Directions. *npj Comput. Mater.* **2016**, *2* (September 2015). https://doi.org/10.1038/npjcompumats.2015.11.

(50)   Van Duin, A. C. T.; Dasgupta, S.; Lorant, F.; Goddard, W. A. ReaxFF: A Reactive Force Field for Hydrocarbons. *J. Phys. Chem. A* **2001**, *105* (41), 9396–9409. https://doi.org/10.1021/jp004368u.

(51)   Chen, Y.; Cheng, T.; Goddard, W. A. Atomistic Explanation of the Dramatically Improved Oxygen Reduction Reaction of Jagged Platinum Nanowires, 50 Times Better than Pt. *J. Am. Chem. Soc.* **2020**, *142* (19), 8625–8632. https://doi.org/10.1021/jacs.9b13218.

(52)   Shin, Y. K.; Gai, L.; Raman, S.; Van Duin, A. C. T. Development of a ReaxFF Reactive Force Field for the Pt-Ni Alloy Catalyst. *J. Phys. Chem. A* **2016**, *120* (41), 8044–8055. https://doi.org/10.1021/acs.jpca.6b06770.

(53)   Chenoweth, K.; Van Duin, A. C. T.; Persson, P.; Cheng, M. J.; Oxgaard, J.; Goddard, W. A. Development and Application of a ReaxFF Reactive Force Field for Oxidative Dehydrogenation on Vanadium Oxide Catalysts. *J. Phys. Chem. C* **2008**, *112* (37), 14645–14654. https://doi.org/10.1021/jp802134x.

(54)   Zou, C.; Van Duin, A. Investigation of Complex Iron Surface Catalytic Chemistry Using the ReaxFF Reactive Force Field Method. *Jom* **2012**, *64* (12), 1426–1437. https://doi.org/10.1007/s11837-012-0463-5.

(55)   Priyadarsini, A.; Mallik, B. S. Comparative First Principles-Based Molecular Dynamics Study of Catalytic Mechanism and Reaction Energetics of Water Oxidation Reaction on 2D-Surface. *J. Comput. Chem.* **2021**, *42* (16), 1138–1149. https://doi.org/10.1002/jcc.26528.

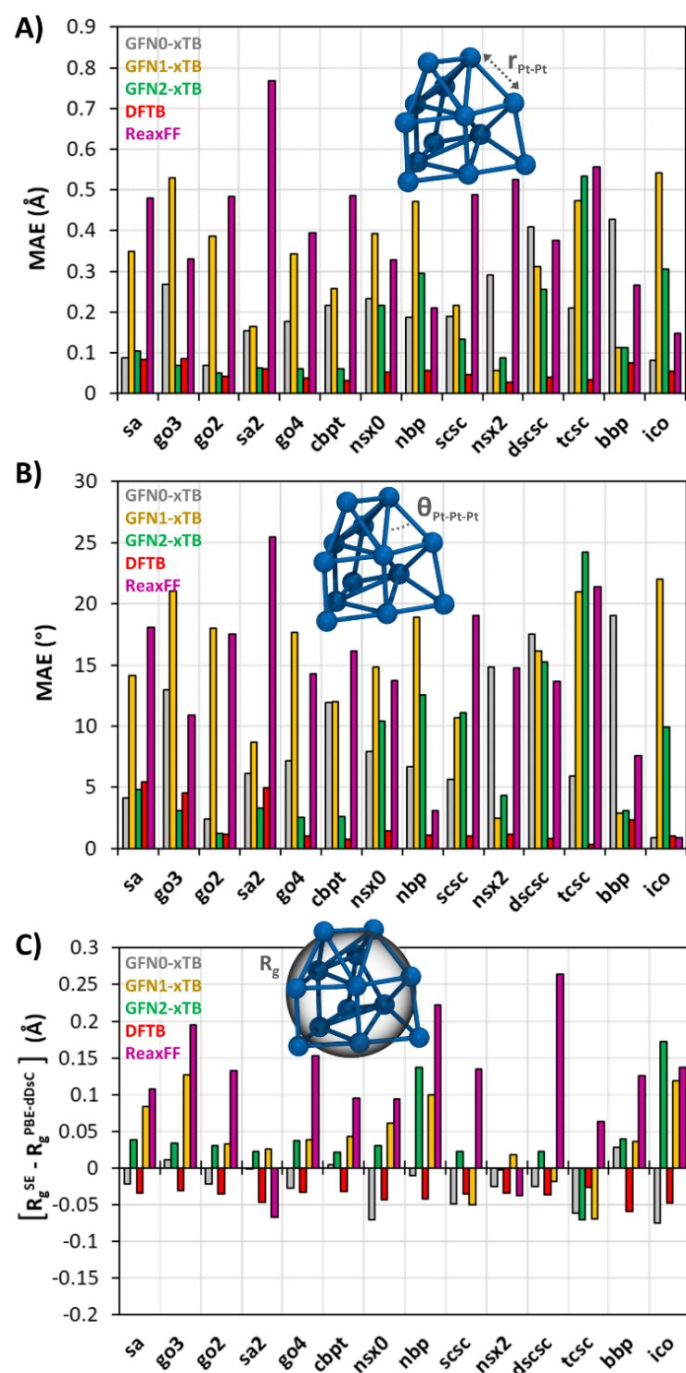(56)   Lourenço, M. P.; Herrera, L. B.; Hostaš, J.; Calaminici, P.; Köster, A. M.; Tchagang, A.;

Salahub, D. R. Automatic Structural Elucidation of Vacancies in Materials by Active Learning. *Phys. Chem. Chem. Phys.* **2022**, *24* (41), 25227–25239. https://doi.org/10.1039/d2cp02585j.

(57)   O'carroll, D.; English, N. J. A DFTB-Based Molecular Dynamics Investigation of an Explicitly Solvated Anatase Nanoparticle. *Appl. Sci.* **2022**, *12* (2). https://doi.org/10.3390/app12020780.

(58)   Liu, X.; Salahub, D. R. Molybdenum Carbide Nanocatalysts at Work in the in Situ Environment: A Density Functional Tight-Binding and Quantum Mechanical/Molecular Mechanical Study. *J. Am. Chem. Soc.* **2015**, *137* (12), 4249–4259. https://doi.org/10.1021/jacs.5b01494.

(59)   Spicher, S.; Bursch, M.; Grimme, S. Efficient Calculation of Small Molecule Binding in Metal-Organic Frameworks and Porous Organic Cages. *J. Phys. Chem. C* **2020**, *124* (50), 27529–27541. https://doi.org/10.1021/acs.jpcc.0c08617.

(60)   Pracht, P.; Grant, D. F.; Grimme, S. Comprehensive Assessment of GFN Tight-Binding and Composite Density Functional Theory Methods for Calculating Gas-Phase Infrared Spectra. *J. Chem. Theory Comput.* **2020**, *16* (11), 7044–7060. https://doi.org/10.1021/acs.jctc.0c00877.

(61)   Kruse, H.; Banáš, P.; Šponer, J. Investigations of Stacked DNA Base-Pair Steps: Highly Accurate Stacking Interaction Energies, Energy Decomposition, and Many-Body Stacking Effects. *J. Chem. Theory Comput.* **2019**, *15* (1), 95–115. https://doi.org/10.1021/acs.jctc.8b00643.

(62)   Cutini, M.; Bechis, I.; Corno, M.; Ugliengo, P. Balancing Cost and Accuracy in Quantum Mechanical Simulations on Collagen Protein Models. *J. Chem. Theory Comput.* **2021**, *17* (4), 2566–2574. https://doi.org/10.1021/acs.jctc.1c00015.

(63)   Perdew, J. P.; Burke, K.; Ernzerhof, M. Generalized Gradient Approximation Made Simple. *Phys. Rev. Lett.* **1996**, *77* (18), 3865–3868. https://doi.org/10.1103/PhysRevLett.77.3865.

(64)   Steinmann, S. N.; Corminboeuf, C. Comprehensive Benchmarking of a Density-Dependent Dispersion Correction. *J. Chem. Theory Comput.* **2011**, *7* (11), 3567–3577. https://doi.org/10.1021/ct200602x.

(65)   Kresse, G.; Hafner, J. Ab Initio Molecular-Dynamics Simulation of the Liquid-Metalamorphous- Semiconductor Transition in Germanium. *Phys. Rev. B* **1994**, *49* (20), 14251–14269. https://doi.org/10.1103/PhysRevB.49.14251.

(66)   Kresse, G.; Furthmüller, J. Efficiency of Ab-Initio Total Energy Calculations for Metals and Semiconductors Using a Plane-Wave Basis Set. *Comput. Mater. Sci.* **1996**, *6* (1), 15–50. https://doi.org/10.1016/0927-0256(96)00008-0.

(67)   Janthon, P.; Kozlov, S. M.; Viñes, F.; Limtrakul, J.; Illas, F. Establishing the Accuracy of Broadly Used Density Functionals in Describing Bulk Properties of Transition Metals. *J. Chem. Theory Comput.* **2013**, *9* (3), 1631–1640. https://doi.org/10.1021/ct3010326.

(68)   Vega, L.; Ruvireta, J.; Viñes, F.; Illas, F. Jacob's Ladder as Sketched by Escher: Assessing the Performance of Broadly Used Density Functionals on Transition Metal Surface Properties. *J. Chem. Theory Comput.* **2018**, *14* (1), 395–403. https://doi.org/10.1021/acs.jctc.7b01047.

(69)   Steinmann, S. N.; Corminboeuf, C. A Generalized-Gradient Approximation Exchange Hole Model for Dispersion Coefficients. *J. Chem. Phys.* **2011**, *134* (4). https://doi.org/10.1063/1.3545985.

(70)   Gautier, S.; Steinmann, S. N.; Michel, C.; Fleurat-Lessard, P.; Sautet, P. Molecular Adsorption at Pt(111). How Accurate Are DFT Functionals? *Phys. Chem. Chem. Phys.*

2015, *17* (43), 28921–28930. https://doi.org/10.1039/c5cp04534g.

(71)   Kresse, G.; Joubert, D. From Ultrasoft Pseudopotentials to the Projector Augmented-Wave Method. *Phys. Rev. B* **1999**, *59* (3), 1758–1775. https://doi.org/10.1103/PhysRevB.59.1758.

(72)   Perdew, J. P.; Ruzsinszky, A.; Csonka, G. I.; Vydrov, O. A.; Scuseria, G. E.; Constantin, L. A.; Zhou, X.; Burke, K. Restoring the Density-Gradient Expansion for Exchange in Solids and Surfaces. *Phys. Rev. Lett.* **2008**, *100* (13), 1–4. https://doi.org/10.1103/PhysRevLett.100.136406.

(73)   Gale, J. D.; Rohl, A. L. The General Utility Lattice Program (GULP). *Mol. Simul.* **2003**, *29* (5), 291–341. https://doi.org/10.1080/0892702031000104887.

(74)   Sanz-Navarro, C. F.; Åstrand, P. O.; Chen, D.; Rønning, M.; Van Duin, A. C. T.; Jacob, T.; Goddard, W. A. Molecular Dynamics Simulations of the Interactions between Platinum Clusters and Carbon Platelets. *J. Phys. Chem. A* **2008**, *112* (7), 1392–1402. https://doi.org/10.1021/jp074806y.

(75)   McDouall, J. J. W. *Computational Quantum Chemistry: Molecular Structure and Properties in Silico*; RSC theoretical and computational chemistry series; RSC Publishing: UK, 2013.

(76)   Nosé, S. An Extension of the Canonical Ensemble Molecular Dynamics Method. *Molecular Physics*. 1986, pp 187–191. https://doi.org/10.1080/00268978600100141.

(77)   Berendsen, H. J. C.; Postma, J. P. M.; Van Gunsteren, W. F.; Dinola, A.; Haak, J. R. Molecular Dynamics with Coupling to an External Bath. *J. Chem. Phys.* **1984**, *81* (8), 3684–3690. https://doi.org/10.1063/1.448118.

(78)   Lambie, S. G.; Weal, G. R.; Blackmore, C. E.; Palmer, R. E.; Garden, A. L. Contrasting Motif Preferences of Platinum and Gold Nanoclusters between 55 and 309 Atoms. *Nanoscale*

Adv. **2019**, *1* (6), 2416–2425. https://doi.org/10.1039/c9na00122k.

(79)   Momma, K.; Izumi, F. VESTA 3 for Three-Dimensional Visualization of Crystal, Volumetric and Morphology Data. *J. Appl. Crystallogr.* **2011**, *44* (6), 1272–1276. https://doi.org/10.1107/S0021889811038970.

(80)   Humphrey, W.; Dalke, A.; Schulten, K. VMD: Visual Molecular Dynamics. *J. Mol. Graph.* **1996**, *14* (1), 33–38. https://doi.org/https://doi.org/10.1016/0263-7855(96)00018-5.

(81)   Waskom, M. Seaborn: Statistical Data Visualization. *J. Open Source Softw.* **2021**, *6* (60), 3021. https://doi.org/10.21105/joss.03021.

(82)   Li, L.; Larsen, A. H.; Romero, N. A.; Morozov, V. A.; Glinsvad, C.; Abild-Pedersen, F.; Greeley, J.; Jacobsen, K. W.; Nørskov, J. K. Investigation of Catalytic Finite-Size-Effects of Platinum Metal Clusters. *J. Phys. Chem. Lett.* **2013**, *4* (1), 222–226. https://doi.org/10.1021/jz3018286.

(83)   McQuarrie, D. A.; Simon, J. D. *Physical Chemistry: A Molecular Approach*; University Science Books: Sausalito, Calif., 1997.

Appendix

Figure A1. Errors made by GFN0-xTB (gray), GFN1-xTB (yellow), GFN2-xTB (green), DFTB (red) and ReaxFF (pink) on the chosen geometric descriptors. The errors are expressed as Mean Average Error (MAE) for bond lengths (A) and bond angles (B), and as the signed deviation from PBE-dDsC for the R_g. The three investigated parameters are highlighted on a molecular model to facilitate their visualization.
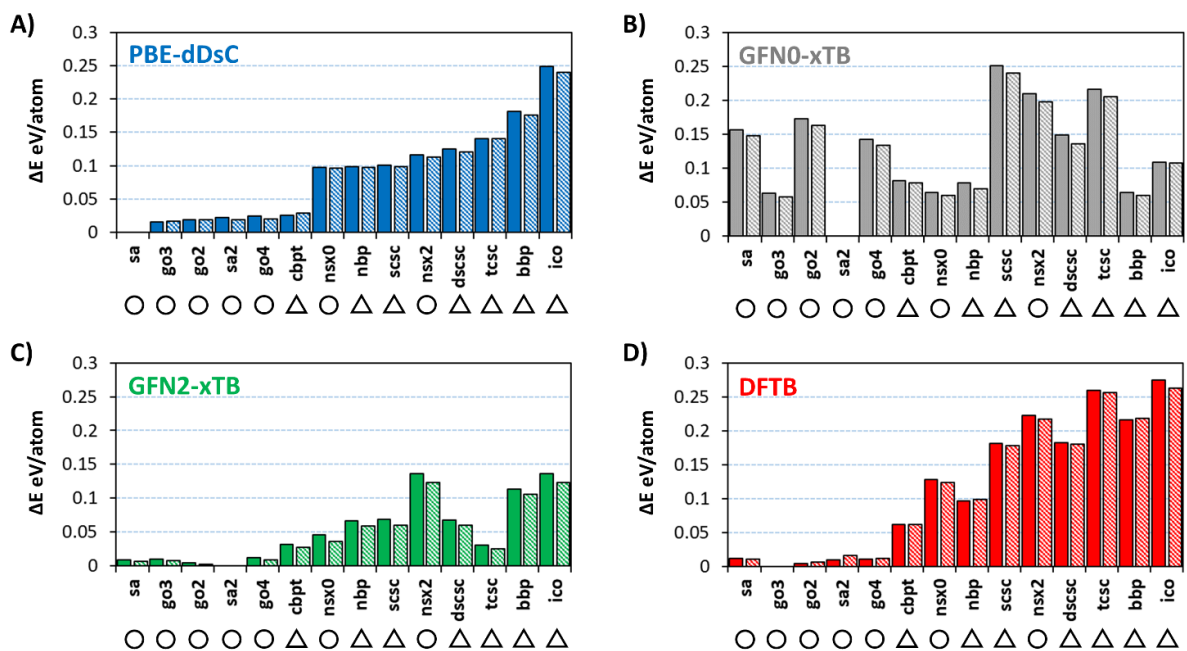
Figure A2. Relative stabilities (with respect to the global minimum) of the structures of the Pt_{13} small dataset, computed with PBE-dDsC (A), GFN0-xTB (B), GFN2-xTB (C) and DFTB (D). Full columns correspond to the only electronic energy, while striped columns are obtained by adding the vibrational free energy (G_{vib}, computed at 300 K) to the former.
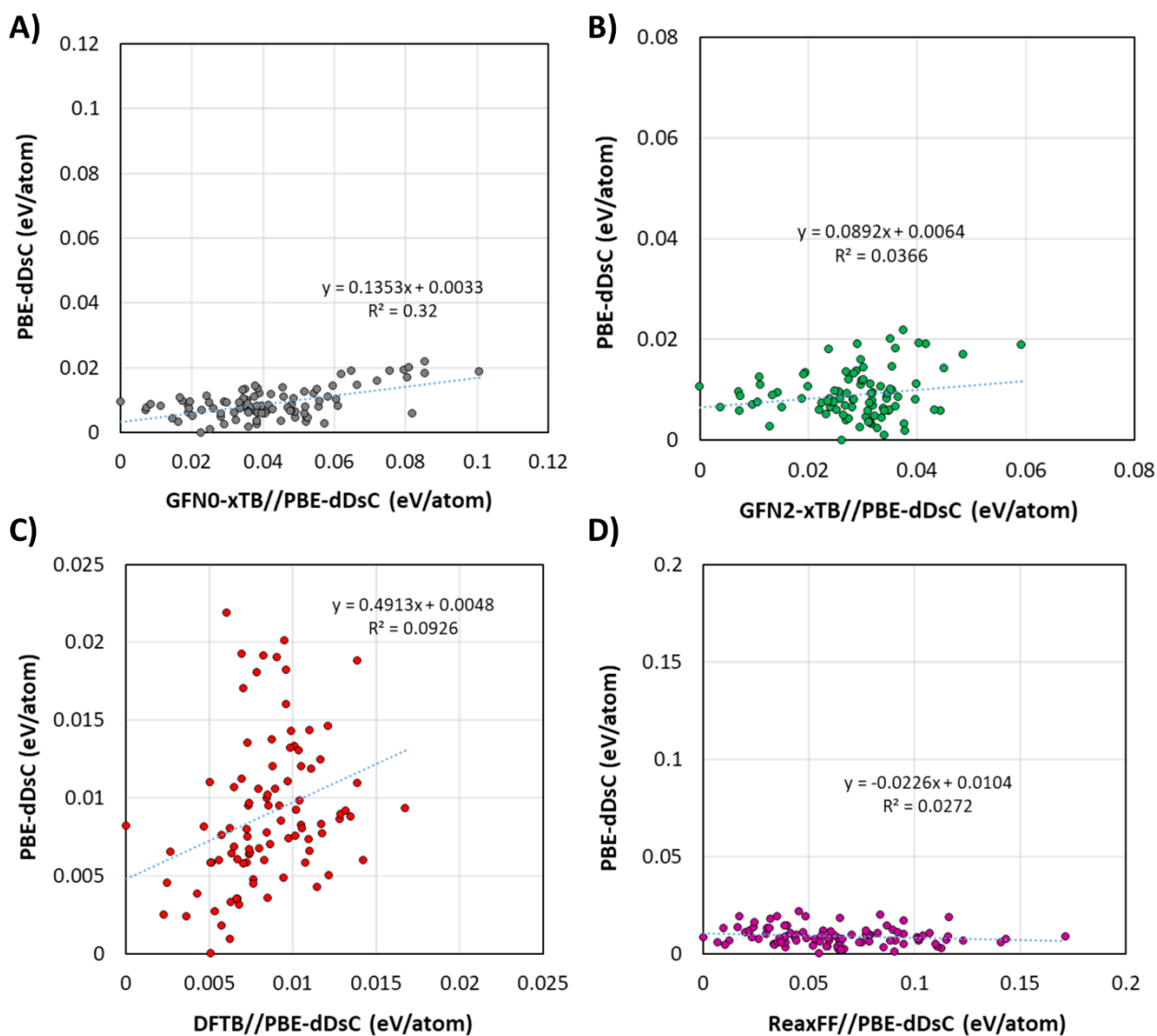
Figure A3. The presented graphs are referred to the Pt_{55} amorphous dataset and are intended to evaluate the correlation between full PBE-dDsC energies and hybrid PBE-dDsC single point energies computed on GFN0-xTB (grey), GFN2-xTB (green), DFTB (red) and ReaxFF (pink) geometries. The interpretation of the graphs is discussed in the main text (sections 2.3.1.2 and 2.3.2).

Chapter 3

Unravelling the CO-induced dynamic behaviour of Al$_2$O$_3$-supported Pd nanoparticles at room temperature

3.1 Introduction

Metal nanoparticles (NPs) have a central role in a variety of technologies and industrial processes and constitute the active phase in many heterogeneous catalysts, which can be addressed as one of the pillars of modern society. Among them, heterogenous catalysts based on supported Pd NPs are widely employed in several industrial processes,[1] both in the liquid[2] and in the gas phase,[3] such as hydrogenation reactions for the synthesis of fine (e.g., pharmaceutical compounds)[4] and bulk chemicals (e.g., terephthalic acid),[5] as well as for photocatalytic applications like pollutant removal[6,7] and hydrogen production.[8] Nowadays it is well recognized that supported metal NPs undergo surface and/or structural modifications under reaction conditions, i.e. in the presence of adsorbates,[9] which can strongly affect their catalytic performance. Identifying these environment-dependent phenomena requires a full characterization of the nature of the surface sites and of their dynamic behaviour when in interaction with adsorbates, which should go far beyond the fundamental surface studies regarding metal NPs as rather invariant entities.[10–12] Accessing this information is not

straightforward and requires coupling multiple cutting edge *in situ* and *operando* techniques, often complemented by DFT calculations.[13–15]

In the last years, thanks to the newest advances in both experimental and computational tools, several evidences of adsorbate-induced phenomena have been reported for various adsorbate-adsorbent systems.[16–20] In this regard, the interaction between Pd NPs and CO is of pivotal importance not only for its catalytic interest (e.g. CO oxidation is often regarded as a model reaction), but also because CO is routinely used as a probe molecule when applying characterization methods based on chemisorption.[21] A few evidences of CO-induced surface phenomena involving Pd NPs have been already reported,[22–25] but in most of the cases the reconstruction occurs much above room temperature and/or in the presence of other reactants, i.e. in conditions similar to those found during the reaction of interest, but far from those commonly adopted for catalyst characterization. To the best of our knowledge, an exhaustive characterization of the dynamic behaviour of Pd NPs under CO atmosphere at room temperature is yet to be reported.

To bridge this gap, in this chapter we present a systematic investigation of the dynamic behaviour of two Pd/Al$_2$O$_3$ catalysts in the presence of CO at room temperature. To this aim, the CO adsorption process was monitored by coupling three complementary experimental techniques, i.e. gas-volumetry, adsorption microcalorimetry and IR spectroscopy, applied in exactly the same experimental conditions. Gas-volumetric measurements provided insight on the relationship between the CO uptake and the equilibrium pressure. A stepped adsorption isotherm was obtained for both samples, similar to what already observed for other classes of materials,[26–29] but never reported so far for Pd-based systems. In the same range of equilibrium pressure, adsorption microcalorimetry showed a re-increase in the differential

heat of adsorption of CO. By monitoring the same phenomenon with IR spectroscopy, we were able to link these two evidences with a sudden change in the relative distribution of the Pd-carbonyls, namely a downfall of bridged carbonyls at (100)-like environments and a simultaneous massive growth of linear carbonyls on defects. These observations, supported by DFT calculations carried out on model Pd crystal facets, are consistent with a reversible corrugation of the Pd(100) facet in the NPs entailing the exposure of novel defective surface sites.

3.2 Experimental & methods

3.2.1 Sample preparation and experimental protocol

The two 5 wt % Pd/Al_2O_3 samples were prepared in the Catalyst Division of Chimet S.p.A. by dispersing the Pd active phase on a high surface area transition alumina (surface area = 121 m^2 g^{-1}; pore volume = 0.43 cm^3 g^{-1}) following a well-established deposition–precipitation approach.[30] After the Pd deposition, one of the two samples was pre-reduced in liquid phase by employing HCOONa as a reducing agent. From now on, we will refer to the unreduced sample as PdAl and to the pre-reduced sample as PdAl(R). Both samples were water-washed and then dried in the oven at 120 °C overnight. The same samples were the object of an extensive experimental multi-technique characterization in the past years as reported in ref. 31. Both catalysts are characterized by a high metal dispersion (D_{PdAl} = 36% and $D_{PdAl(R)}$ = 24%) as measured by pulsed CO chemisorption. SAX measurements report a particle size distribution that, even if peaked at around 1.7 nm for both samples, reveals a contribution of bigger particles for the sample of PdAl(R). The significant exposure of crystalline (100) and (111) facets by the dispersed Pd NPs has been revealed by TEM pictures.

As pointed out in ref. 31,30 the precipitated phase of PdAl presents itself as a mixture of amorphous $Pd(OH)_2$ and crystalline PdO, while in PdAl(R) the pre-reduced Pd(0) phase becomes passivated with a PdO film upon being re-exposed to air. Thus, the samples needed to be further activated and reduced in order to perform CO adsorption measurements on a clean Pd(0) metallic phase. Prior to each measurement, the samples were inserted into dedicated custom cells (details in sessions 2.2, 2.3 and 2.4) and brought up from room temperature (RT) to 120 °C in dynamic vacuum granted by a turbomolecular pump. At this point, the samples were reduced by three cycles of exposure to $\sim$ 120 mbar of H_2 at the same temperature. Water produced during the reduction step was removed by evacuating the sample at 120 °C up to a residual pressure of $\sim 5 \cdot 10^{-4}$ mbar, measured with a Pirani gauge. At this point, the incremental adsorption of CO on the activated samples were monitored with three different techniques (gas-volumetry, adsorption microcalorimetry ad FT-IR spectroscopy) in the same experimental conditions. During all three kind of experiments, small successive doses of CO were put in contact with the samples in isothermal conditions until a first adsorption run was completed (primary adsorption). After a desorption run performed by simply evacuating of the cell, a secondary adsorption run was performed to inspect the reversibility of the process. All the experiments presented in section 3.3 have been repeated from 2 to 3 times to ensure the repeatability of the reported phenomena.

3.2.2 Gas sorption measurements

CO (supplied by Sapio SRL, 99.9998% purity grade) adsorption isotherms were measured at 30 °C in an absolute pressure range spanning from $\sim 1 \cdot 10^{-2}$ mbar to $\sim$ 120 mbar with a high-performance adsorption analyzer (Micromeritics ASAP 2020). Approximately 1 gram of each sample, originally in the powder from, were gently pelletized to prevent powder residues from jumping out of the cell while exposed to sudden pressure changes (which could happen both

during the activation procedure and the measurement itself). Close attention was dedicated to the separation of the pellets from the finer powder. The pellets were then inserted in a custom adsorption cell made in quartz (Figure 1) equipped with connections allowing for vacuum and thermochemical treatment, and a plug-in thermal jacket, as described in ref. 32. The sample temperature was kept constant thanks to a thermostatic fluid continuously flowing through the thermal jacket, connected to an external isothermal liquid bath (Julabo F25-EH). Prior to the measurements each sample was activated through the activation protocol described in section 3.2.1. The exact sample weight was measured after the activation treatment and before the measurement.
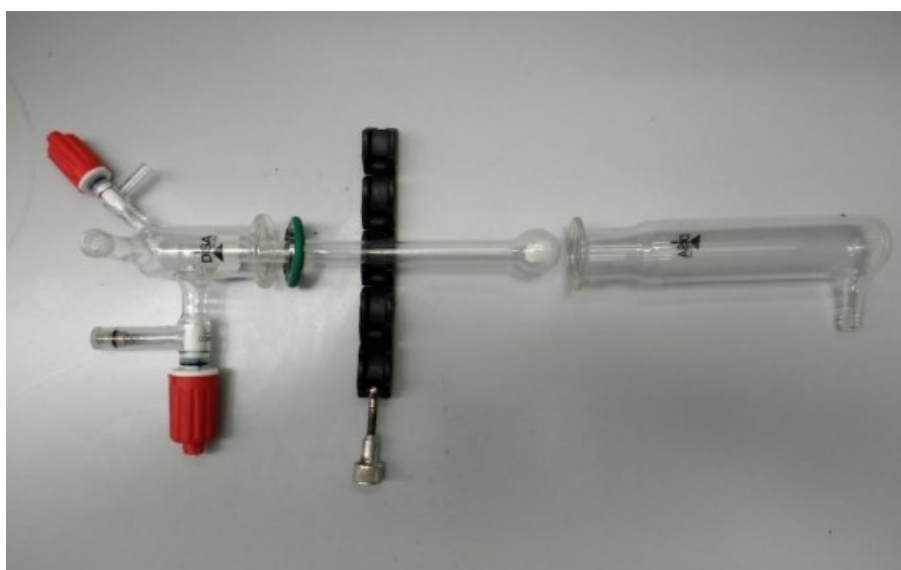
Figure 1. The custom cell that has been employed for volumetric measurements is presented. The cell is composed of a quartz sample container, linked to a valve that can be connected to a vacuum line for thermochemical treatment with different gas-phase reagents. The sample container can be inserted in a thermal jacket that grants precise isothermal conditions thanks to a continuous flow of thermostatic fluid. Italian patent application n°102020000005014 filed on March 9th, 2020 and PCT n. PCT/IB2021/051769 filled on March 3rd, 2021.

3.2.3 Adsorption Microcalorimetry

CO adsorption microcalorimetric data were collected at 30 °C by means of a C80 Calvet heat-flow microcalorimeter (distributed by Setaram) connected to a high-vacuum line, capable of granting a stable pressure as low as $P \leq 1\ 10^{-5}$ mbar in static conditions. For the same reasons explained in section 3.2.2, the samples (approximately 1 g) were pelletized and inserted into a custom quartz calorimetric cell before undergoing the activation procedure and being finally connected to the volumetric-calorimetric apparatus. During the experiment, small incremental CO pulses were manually dosed on the activated catalyst and both the integral heats evolved and the adsorbed amounts were measured for each pulse. The CO pressure in the vacuum line was measured by a Varian Ceramicell transducer gauge (from $\sim 5\ 10^{-2}$ up to $\sim$ 100-120 mbar). The ratio between the amount of heat evolved for each increment and the associated adsorbed quantity is equal to the average value of the differential heat of adsorption in the interval of the adsorbed quantity. For this reason, the plots of differential heat as a function of CO coverage is represented as histograms. By taking the x middle point of each partial column, a consistent measure of the differential heat is achieved.

The extremely accurate measurement of the heat of adsorption (± 0.4 % of accuracy) was achieved thanks to the following scheme: two identical calorimetric cells, one containing the sample, the other (empty) serving as reference, were connected in parallel. Thanks to the differential conception of the apparatus, all side phenomena (i.e., all thermal effects different from the ones due to the adsorbate-adsorbent interactions) were successfully compensated. The heat measured in such a gas-solid open system operating in isothermal conditions represents the enthalpy change ($\Delta_{ads}H$) involved in the adsorption.[33] The completion of the incremental adsorption process coincides with the formation of the liquid-like CO phase on the surface of the catalyst, which occurs when the evolved integral heat coincides with the

heat of vaporization of CO ($\sim$ 6.04 kJ/mol). The corresponding equilibrium pressure ($\sim$ 100-120 mbar) was thus employed as a target pressure to complete the adsorption process in experiments involving the other two techniques.

3.2.4 *In situ* FT-IR spectroscopy

Transmission FT-IR spectra of the adsorbed CO were acquired with a Bruker Invenio R spectrophotometer, equipped with a Mercury Cadmium Telluride (MCT) cryo-detector, at a spectral resolution of 2 cm^{-1}. The background spectrum was recorded on an empty chamber and averaged on 64 scans, while the subsequent spectra were averaged on 32 scans. The samples (approximately 5-10 mg) were pressed into self-supporting thin pellets and inserted in a gold envelop acting as a sample holder. Afterwards, they were activated into a transmission cell made in quartz, equipped with two parallel KBr windows (optical path $\sim$ 2 mm), and measured in the same cell at beam temperature.

In situ experiments were performed in the same way as for adsorption microcalorimetry, though with a slight but unbridgeable difference. To be able to closely follow the adsorption process, it is mandatory to provide very low incremental doses of adsorbate, thus entailing the risk of approaching the limit of sensitivity of the pressure gauge. For microcalorimetry and gas-volumetry this issue was overcome by measuring a great amount of sample ($\sim$ 1 g) per experiment. On the other hand, too thick pellets are not measurable by transmission FT-IR spectroscopy because they completely absorb all the incoming radiation (i.e. zero transmittance). Thus, one is usually forced to work with extremely thin pellets, meaning an amount of sample which is orders of magnitude lower (average weight of $\sim$ 5-10 mg) compared with the other two techniques. For this reason, we were forced to perform the first adsorption steps (up to a total pressure of $\sim$ 10 mbar) by dosing a

10% CO/He mixture in order to gradually follow the early stages of the process. Small incremental CO pulses (from a partial pressure of CO of $\sim 5 \cdot 10^{-3}$ mbar to ~ 100 mbar) were manually dosed on the activated catalyst and one FT-IR spectrum was acquired for each pulse.

3.2.5 Fit of the IR spectra

The series of FT-IR spectra acquired during the primary adsorption of CO on both PdAl and PdAl(R) were the object of a spectral fitting procedure devoted to analyse the behaviour of each type of Pd-carbonyl as a function of the CO coverage by extracting their individual contributions to the whole spectrum throughout a primary adsorption run. IR bands for solids have usually a Gaussian line-shape, while for liquids a Lorentzian function is mostly used. For adsorbed molecular probes, the situation is more ambiguous and should be evaluated case by case.[34] For the present case of the adsorption of CO on Pd, the adsorbate-adsorbent interaction is ruled by π-back donation and the associated average energy (~ 120 kJ/mol) is comparable with the weakest chemical bonds. Thus, we decided to treat the CO molecule as firmly anchored to the solid surface and to represent the single contributions of the Pd-carbonyl types as Gaussian functions. We are aware that the validity of this approximation is expected to decrease with the average strength of the Pd-CO bond (e.g., at the latest stages of the adsorption). Nonetheless, we decided to keep the Gaussian as the only employed functional form and to not take into account any Lorentzian contribution to avoid an overparameterization of the model.

Each IR spectrum was thus fitted as a sum of 6 gaussian components, representing 6 types of Pd-carbonyls: 3 types of linear carbonyls, i.e. on extended surfaces (linear), and on two types of defects characterized by increased under-coordination (defective linear I and defective linear II); one type of two-fold bridged carbonyl (bridged); two types of 3-fold hollow

carbonyls (3-fold hollow I and 3-fold hollow II). Fits were performed by employing the curve_fit function of the scipy.optimize python package. The initial values of the parameters of the gaussian functions (center, amplitude and sigma) were set on the basis of the existing literature[35–38] and were left free to vary during the error minimization according to some constraints, chosen with the goal of reproducing the complex physical chemistry of the system. For example, stricter constrains were adopted at the early stages of the adsorption (featuring low-intensity, wide and non-shifting bands) while looser ones were needed to follow the more complex evolution of the spectra at high coverage.

In a situation like this, when the incremental adsorption of a molecular probe on a multitude of different adsorption sites is monitored with IR spectroscopy, it can be useful to extract the so-called "optical isotherms". These last can be built by plotting a spectroscopic descriptor of the adsorbed quantity (known as the optical coverage (ϑ_{opt})) against the equilibrium pressure at each adsorption step. Here, since we do not have interest in the calculation of the molar absorptivity of the Pd-CO species, ϑ_{opt} is represented by the normalized integrated area of the bands associated with each Pd-CO type and it is defined as follows:

$$A_n^* = \frac{A_{n,i}}{A_{n,max}} \tag{1}$$

where $A_{n,i}$ is the integrated area of the band associated with the *n-th* Pd-CO type at the *i-th* adsorption step, $A_{n,max}$ is the integrated area of the same band at its maximum, and the asterisk means "normalized". Unfortunately, the employment of a 10% mixture CO/He in our FT-IR experiments hampers a correct measurement of the partial equilibrium pressure of CO. In such a situation, we decided to replace the equilibrium pressure with another descriptor of the adsorption progression as a whole, defined as:

$$A^*_{TOT} = \frac{A_{TOT,i}}{A_{TOT,max}} \qquad (2)$$

where $A_{TOT,i}$ is the integrated area of the total fit spectrum at the *i-th* adsorption step and $A_{TOT,max}$ is the integrated area of the total spectrum at its maximum. Even though this approach prevents us from quantitative consideration on the abundance of the different Pd-CO types, it provides a qualitative insight on the evolution of each component during the adsorption process.

3.2.6 Computational details

All DFT calculations in this chapter were carried out within the plane-wave formalism exploiting the VASP[39,40] code (version 5.4.4). The revised version of the PBE functional (RPBE),[41] specifically developed for predicting adsorption energetics for CO on metallic surfaces, has been employed with an energy cutoff of 530 eV. Core electrons were treated according to the PAW formalism.[42] A Methfessel-Paxton smearing of order 2 (σ = 0.06 eV) has been adopted to facilitate the convergence of all the electronic SCF minimizations,[43] for which a threshold of 10^{-6} eV has been set. All the geometries were optimized with the conjugate gradient algorithm until the residual forces were below 0.02 eV/Å.

As outlined in section 3.2.1, the average size of Pd NPs in the investigated samples falls around 1.7 nm, which corresponds to a NP of ∼ 300 atoms in average.[44] Unfortunately, targeting adsorbate-induced phenomena in a system consisting of an explicit NP of this size is unfeasible in a full DFT approach, even avoiding to take into account the contribution of the support. Thus, in our first approximation, we decided to neglect the nano-effects due to the nanometric size of NPs and to approach the problem by considering extended Pd surfaces. This approach is also supported by the fact that NPs in the investigated samples mostly tend to expose well-defined crystal facets.[31] In the light of this consideration, we carried out the

generation of the Pd slabs starting by optimizing the bulk Pd, obtaining a calculated lattice parameter (3.979 Å) in well agreement with experimental data.[45] The cut periodic slabs for each facet consist of a different number of metallic layers, chosen with the aim of guaranteeing a 14 Å thick layer of metallic phase, while the vacuum layer was set to 20 Å. In all cases, the 60% along the z axis of the metallic layer was frozen, leaving the remaining 40% free to evolve upon geometry optimization. In this fashion, 1x1 slabs of the bare Pd(100), Pd(111), Pd(110), Pd(210), Pd(310), Pd(211) and Pd(311) facets were built and CO adsorption in the high-coverage regime was explored for the Pd(100), Pd(111) and Pd(110) facets. Periodic slabs of a 2x2, 4x1 and 5x1 surface multiplicity were built for CO adsorption at the Pd(100) facet in the case of $\theta = 1$, $\theta = 0.75$ and $\theta = 0.8$ respectively, while 1x1 slabs were adopted for CO adsorption at Pd(111) and Pd(110). The exploration of the high CO coverage regime was meant to identify the CO saturation coverage (θ_{sat}), which should correspond to the coverage regime for which experimental observations (discussed in the next section) indicate the occurrence of an unconventional adsorption behavior in the two catalysts. θ_{sat} was here identified according to two criteria: (i) the saturation coverage of CO on a Pd crystal facet should correspond to the minimum of the surface energy of each slab with respect to the coverage itself and (ii) θ_{sat} should correspond to a situation where the CO surface density (ρ_{surf}) does not exceed the limit ρ_{surf} beyond which the Van der Waals radii of adjacent CO molecules get overlapped (i.e. ~ 0.11 Å^{-2}).

The surface free energy of the relaxed Pd facets (Γ_{hkl}), was evaluated according to the following equations:

$$\Gamma_{hkl} = 2\Gamma_{av} - \Gamma_{nr} \tag{3}$$

$$\Gamma_{av} = \frac{G_{slab} - N_{bulk}G_{bulk} - N_{CO}G_{CO}^{gas}}{2A_{slab}} \tag{4}$$

where eq. 3 is necessary to compensate the error arising from the building of asymmetric slabs in which just a fraction of the metallic layers are fully relaxed upon geometry optimization.[46] Γ_{av} is the average surface energy of the asymmetric slab, and G_{slab} and G_{bulk} are the free energies of the considered slab and the bulk Pd (per Pd atom), respectively. G_{slab} and G_{bulk} will be approximated to their corresponding total energies. N_{bulk} is the number of Pd atoms included in the slab unit cell. G_{CO}^{gas} is the free energy of the CO molecule in the gas phase, N_{CO} being the number of adsorbed CO molecules. A_{slab} is the area of one side of the slab. Γ_{nr} is the surface energy of the non-relaxed slab evaluated without adsorbate molecules (at the bulk geometry), defined in a similar way as in eq. 4, with N_{CO} = 0. Notably, given the modest modification (below 300 cm^{-1}) occurring in the CO vibrational frequency upon adsorption, we decided to neglect the effect of the adsorption on the CO vibrational free energy, considering it as an invariant during the adsorption process. Thus, the temperature-dependent free energy of CO in the gas phase has been approximated to:

$$G_{CO}^{gas}(T) = E_{CO} + G_{trasl}(T) + G_{rot}(T) \tag{5}$$

where E_{CO} is the total energy, while $G_{trasl}(T)$ and $G_{rot}(T)$ are the temperature-dependent translational and rotational free energies of the a gas-phase CO molecule. In all calculations the temperature (T) has been set to 303.15 K. The Wulff theorem has been adopted to compute the coverage dependent exposed fraction of each facet on the basis of the corresponding Γ_{hkl}.[47] The graphical visualization and structural manipulation of the slabs, as well as the images rendering, was performed with VESTA (version 4.0.0).[48]

3.3 Results and discussion

3.3.1 Unexpected behaviour in the CO adsorption isotherms and in the CO adsorption heats

Figure 2 shows the primary CO adsorption isotherms for both PdAl (part A) and PdAl(R) (part B) in the whole pressure range investigated. PdAl(R) shows a significantly lower CO uptake with respect to PdAl ($\sim$ 0.08 mmol/g against $\sim$ 0.014 mmol/g, respectively), which is in perfect agreement with what already quantified by pulsed CO chemisorption.[31] Beside this difference, the behaviour of the two adsorption isotherms is the same for the two catalysts and can be described as follows. At the early stages of the adsorption process (light blue points in Figure 2) the two isotherms show a "classic behaviour": the initial sharp increase in the adsorbed quantity as a function of the equilibrium pressure reflects the strong adsorbate-adsorbent interaction occurring between CO and Pd(0) NPs. After this first stage, the slope of the curves starts decreasing as if it was approaching a plateau. At this point, which will be referred as "turning point" in the following (dark blue), as the adsorption run goes on, a second sharp increase in the adsorbed quantity is observed (orange points). This gives birth to a stepped region, which represents an "anomaly" in an adsorption isotherm. After that, the CO adsorbed quantity finally reaches a plateau. This behaviour is suggesting that, in the pressure range corresponding to the stepped region, something is occurring that is making the adsorption process extremely more favoured with respect to the situation found at lower pressures (insets in Figure 2). A similar behaviour was already reported for some classes of materials such as metal organic frameworks (MOF)[26,27] and zeolites,[28,29] and was ascribed to the occurrence of cooperative phenomena between adsorbate and adsorbent phases, such as adsorbate-induced phase transitions and/or framework deformations occurring in the material that make further adsorption events more exergonic than the previous ones. However, this was never reported for Pd NPs so far.
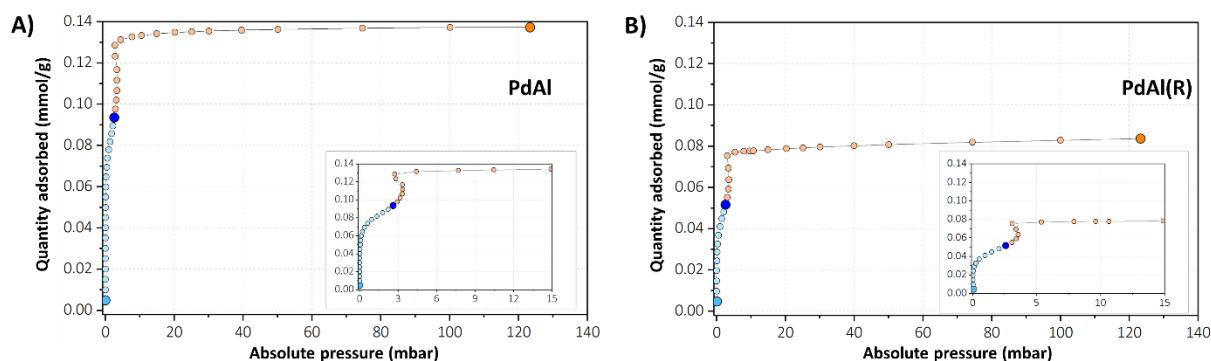
Figure 2. Volumetric isotherms for the adsorption of CO at room temperature on PdAl (part A) and PdAl(R) (part B). Each adsorption isotherm is divided into a pre-step (light blue) and a post-step (light orange) region. The starting (light blue), turning (blue) and final (orange) points are represented as bigger circles. The insets present a magnification of the step region for the two isotherms.

It is worth noticing that a few points collected immediately after the second sharp increase in the adsorbed quantity are observed to fall at higher adsorbed quantity but lower equilibrium pressures with respect to the previous ones. Though this may seem counterintuitive, the reason behind this behaviour resides in the operating mode of the instrument. Indeed, to be able to build an isotherm featuring a dense grid of points even at the very first stages of the adsorption, the instrument does not seek a specific equilibrium pressure to collect a point, but a specific adsorbed amount (which in this cases is set to 0.005 mmol/g). Then, after the isotherm has reached a plateau, a classic equilibrium pressure dosing is reestablished. In the light of this, if some modification in the adsorbent occur that makes the adsorption more favourable for a given point than for the immediately previous one, the behaviour here discussed is consistent.

The primary CO adsorption on both PdAl and PdAl(R) was successively monitored by microcalorimetry. Figure 3 shows the microcalorimetric adsorption isotherms, while Figure 4 shows the differential heat of adsorption (q_{diff}) of CO as a function of its coverage. The general behaviour is qualitatively the same for both catalysts, even though the absolute numbers are

80

different. The first adsorption events are characterized by a differential heat of adsorption of ~ 200 kJ/mol, which is in good agreement with the values reported in the specialized literature and can be ascribed to CO adsorption on defects and to bridged and 3-fold hollow CO on the smallest Pd NPs.[49,50] Then, q_{diff} reaches a plateau at ~ 115 kJ/mol, which indicates that the adsorption process takes place at sites with similar interaction strength, before dropping to the heat of vaporization of CO at 6 kJ/mol. Slightly higher adsorption heat values (by ~ 15 kJ/mol) are registered for PdAl(R) with respect to PdAl. This observation is justified by literature findings, according to which beyond the threshold cluster size of 50-100 atoms, the heat of adsorption of CO is expected to increase with the increasing particle size.[49–52]

Importantly, an unexpected behaviour in the measured q_{diff} is observed for both catalysts exactly in the same pressure range of that found for the adsorption isotherms: instead of decreasing gradually and monotonously upon increasing the coverage, as normally expected for an adsorption process, q_{diff} slightly re-increases at the end of the plateau (dark blue bar), right before the final drop corresponding to CO liquefaction. Using other words, the sum of all the thermal events occurring in correspondence of the dark blue blocks in Figure 4 is more exothermic if compared to the situation found at lower coverage.

Taken together, the observations of an unexpected behaviour in both CO adsorption isotherms and CO adsorption heats strongly suggest the occurrence of some phenomenon involving the adsorbent (Pd NPs), which makes the further adsorption events more favoured than the previous ones.
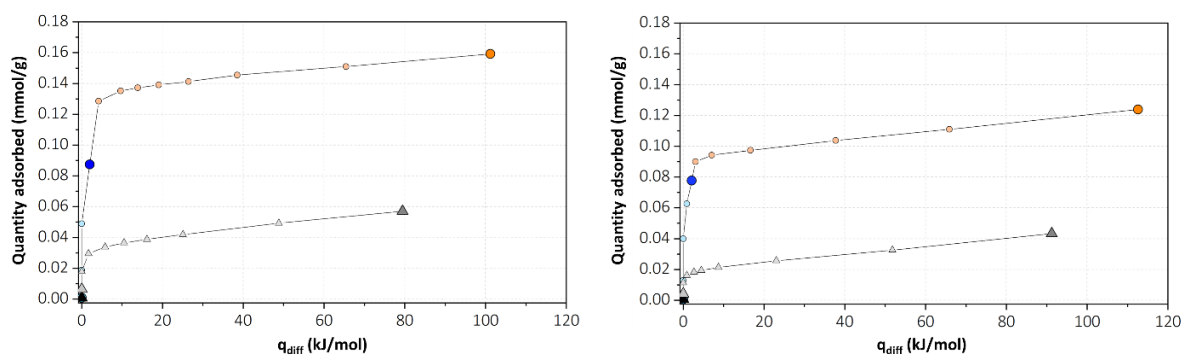
Figure 3. microcalorimetric isotherms for the primary and secondary adsorption of CO on PdAl (part A) and PdAl(R) (part B). Each primary adsorption isotherm is divided into a pre-step (light blue) and a post-step (light orange) region. The starting (black), turning (blue) and final (orange) points are represented as bigger circles. The secondary adsorption isotherms are reported in grey.
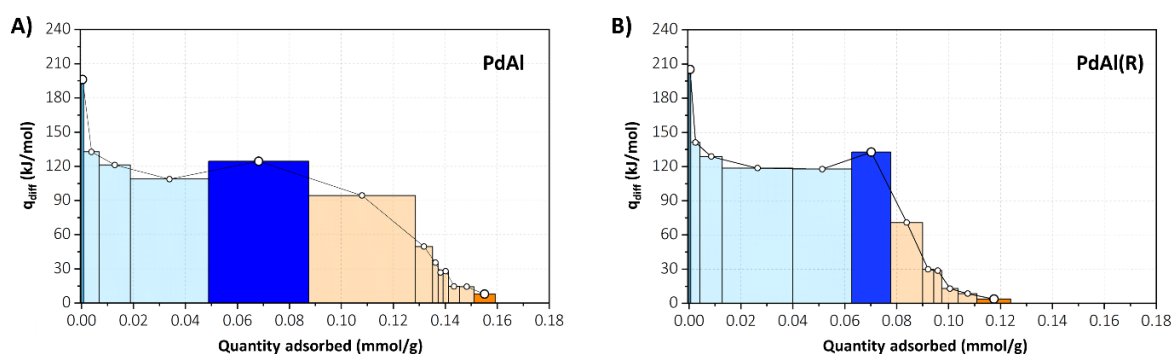
Figure 4. Differential heat of adsorption of CO on PdAl (part A) and PdAl(R) (part B). Each plot is divided into a pre-step (light blue) and a post-step (light orange) region. The mean point of each column, which represents the true measure of the differential heat, is connected to the adjacent one through a straight line to guide the eye. The starting, turning and final points are represented as bigger circles on light blue, blue and orange columns.

3.3.2 Identifying the CO adsorption sites and their dynamics

In order to identify the adsorption sites involved at each adsorption step and to monitor their evolution during the incremental adsorption, we turned our attention to IR spectroscopy, which is known to be extremely sensitive to the nature of the adsorption sites.[13,53,54] Figure 5 shows the sequence of IR spectra collected at increasing CO pulses for the two catalysts. The whole sequences are divided in two parts in order to better visualizing the changes occurring. Generally speaking, since the very beginning, the spectra are characterized by four main

absorption bands, whose assignment can be done straightforwardly according to the literature.[35–38] Band I, at ∼ 2080 cm^{-1} at θ_{min}, is ascribed to linear carbonyls on extended (111) facets; band II, at ∼ 2060 cm^{-1} at θ_{min}, is ascribed to linear carbonyls on defective sites; band III, at ∼ 1975 cm^{-1} at θ_{min}, is ascribed to bridged carbonyls on Pd(100)-like environments; and finally band IV, at ∼ 1915 cm^{-1} at θ_{min}, is ascribed to 3-fold hollow carbonyls on Pd(111)-like environments.
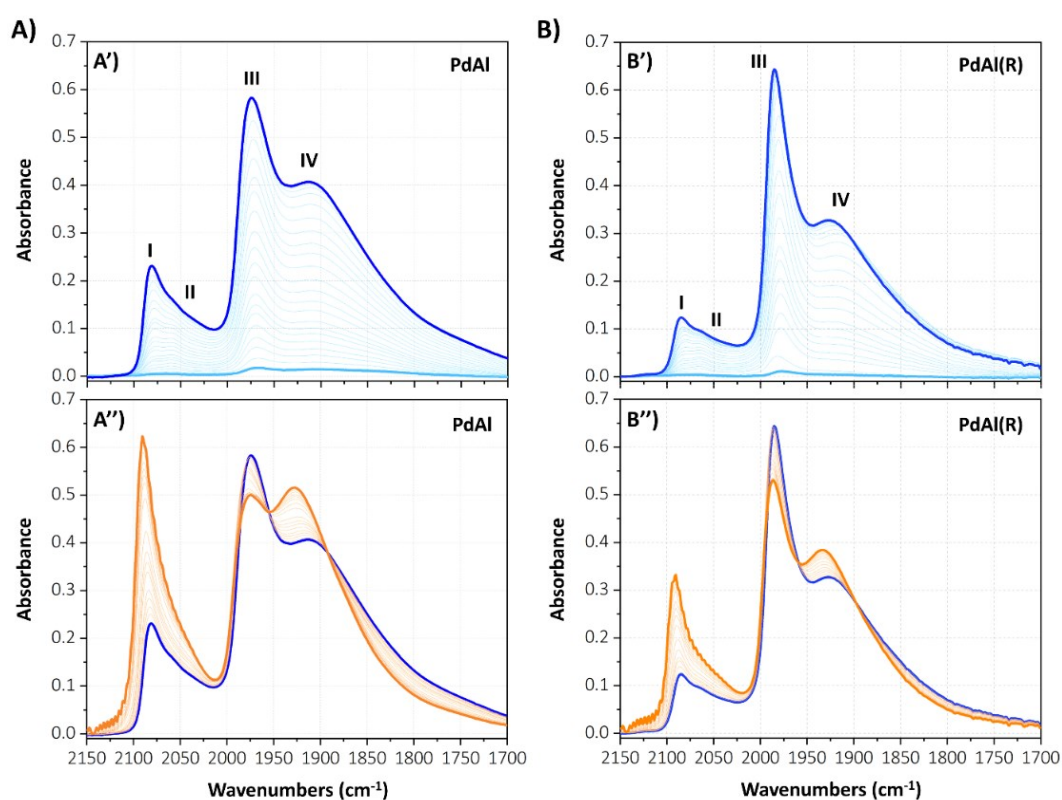
Figure 5. Sequence of *in situ* FT-IR spectra collected while dosing small incremental CO pulses on PdAl (part A) and the PdAl(R) (part B) samples. Bold spectra were collected at a partial CO equilibrium pressure of ∼ 5 10^{-3} mbar (light blue), ∼ 1 mbar (blue) and ∼ 100 mbar (orange). The spectra referring to the low coverage regime are reported in light blue, while the spectra referring to the high coverage regime are reported in orange. All the spectra are reported after subtracting that collected before CO dosage.

At the smallest CO doses (Figure 5A' and Figure 5B'), one should expect isolated CO molecules adsorbing far away from each other. Nevertheless, none of the Pd-CO species is

oscillating at its singleton frequency, which is expected at lower wavenumbers.[35] This observation suggests that, since the lowest coverage, CO is adsorbing on the Pd surface forming islands.[55] All the four absorption bands monotonically grow in intensity upon increasing the CO coverage, without shifting in position, up to a turning point (highlighted in dark blue) that roughly corresponds to the CO pressure range at which both CO adsorption isotherms and heat of adsorption showed an unexpected behaviour. Overpassing this threshold (Figure 5A'' and Figure 5B''): i) bands I and II massively grow in intensity and upward shift by $\sim$ 6-10 cm^{-1} for PdAl(R) and PdAl, respectively; ii) band III considerably decreases in intensity without undergoing any significant shift (< 2 cm^{-1}); iii) band IV keeps on growing, simultaneously shifting at higher wavenumbers. The final IR spectra collected at θ_{max} are the same as those already published in ref. 31. The differences among the two samples, in terms of bands position and relative intensity, reflect the morphological differences of the Pd NPs in the two catalysts. The described behaviour suggests that the two unexpected phenomena registered independently by gas-volumetry and microcalorimetry is associated to a modification of the relative abundance of the carbonyls species at the surface of Pd NPs. To shed more light on this complex behaviour, we adopted a sequential spectral fitting procedure to follow the evolution of each Pd-CO species throughout the adsorption process. Even though four main bands are straightforwardly identifiable in the IR spectra, bands II and IV are characterized by a strong asymmetry due to the presence of a tail at lower wavenumbers. For this reason, not reasonable fits were obtained by including only four components and we had to consider two additional bands: one at around 2040 cm^{-1} ascribable to a second type of defective linear carbonyls and the other at around 1860 cm^{-1} ascribable to a second type of 3-fold hollow carbonyls. Figure 6 shows the most representative results for PdAl, while those for PdAl(R) are reported in Figure 7.
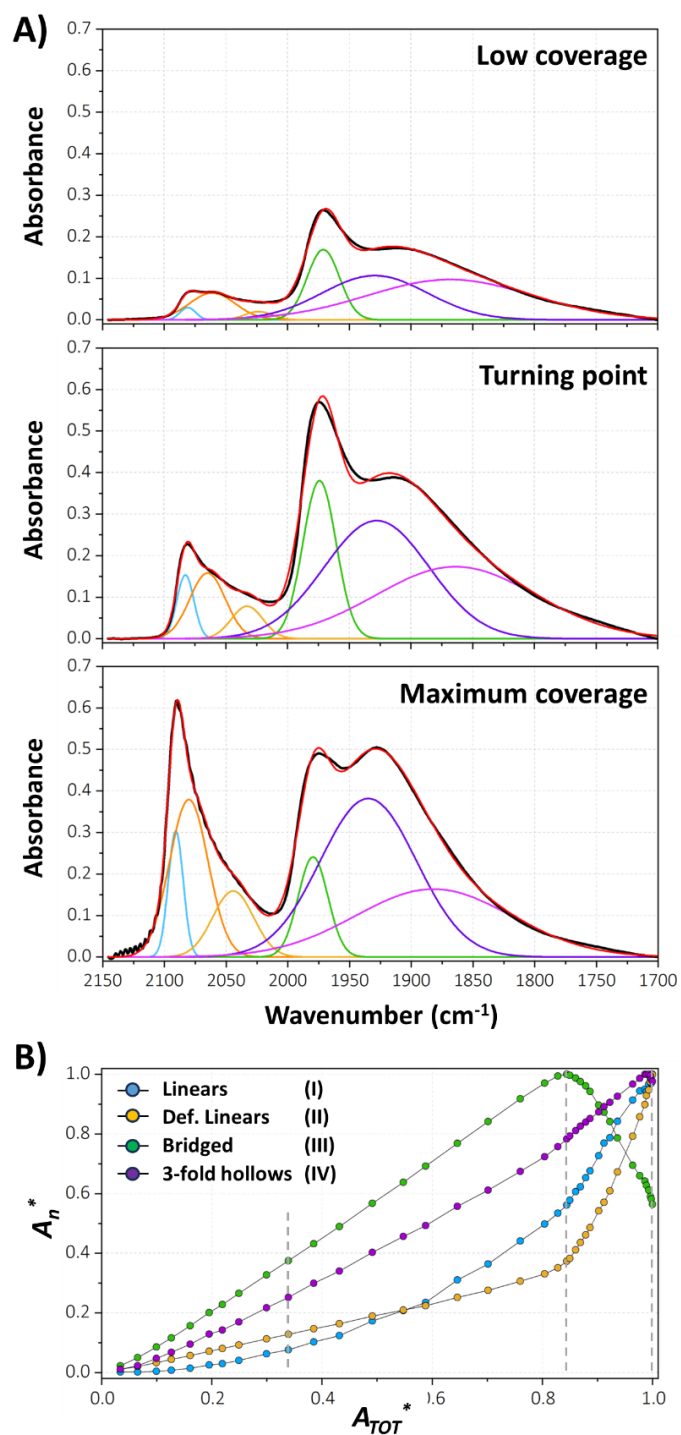
Figure 6. Most representative results of the curve fitting procedure applied to the IR spectra collected for PdAl.

Part A: the single gaussian components relative to linear (cyan), defective linear I (orange), defective linear II

(ochre), bridged (green), 3-fold hollow I (purple) and 3-fold hollow II (pink) carbonyl types are reported, together

with the final fit (red) and the experimental spectrum (black). Part B: The evolution of the respective normalized

integrated areas throughout the whole primary adsorption is plotted against the optical coverage. The three key

points represented by the spectra in panel (A) are highlighted in panel (B) by means of three dashed lines.
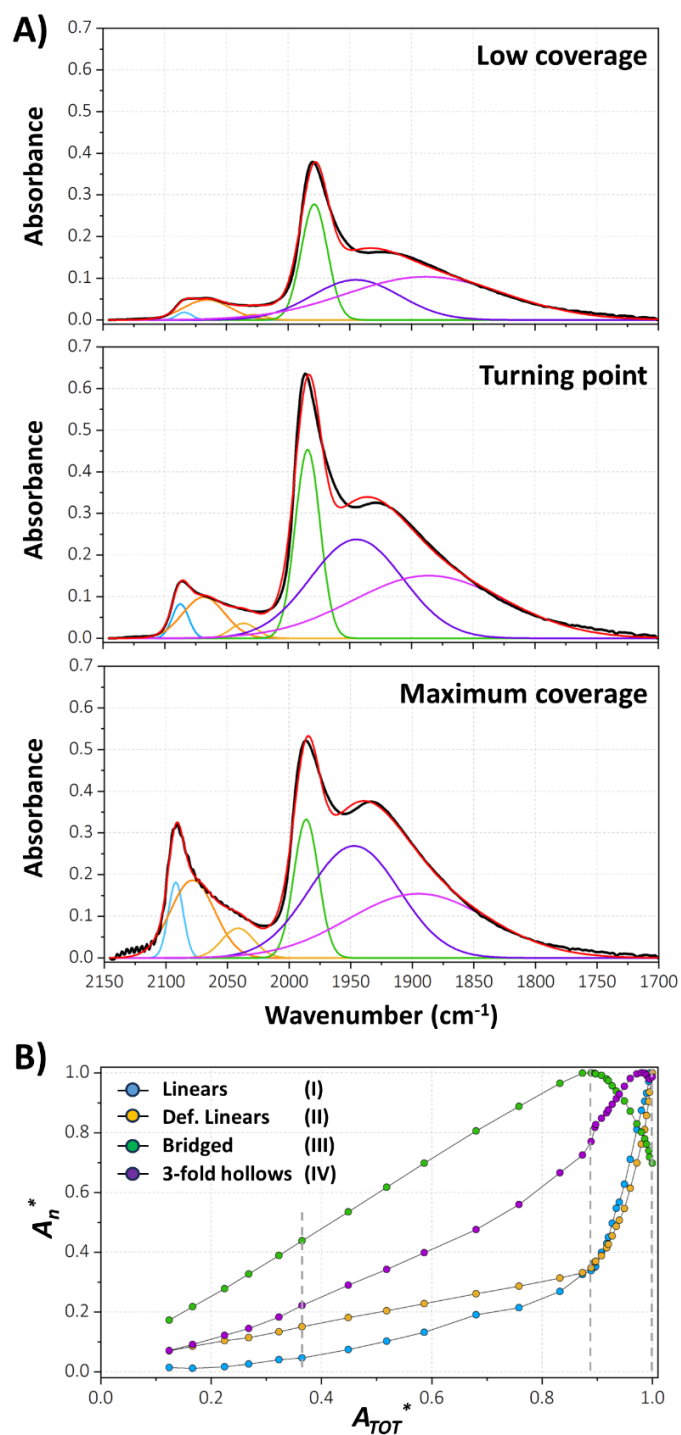
Figure 7. Most representative results of the curve fitting procedure applied to the IR spectra collected for PdAl(R).

Part A: the single gaussian components relative to linear (cyan), defective linear I (orange), defective linear II (ochre), bridged (green), 3-fold hollow I (purple) and 3-fold hollow II (pink) carbonyl types are reported, together with the final fit (red) and the experimental spectrum (black). Part B: The evolution of the respective normalized integrated areas throughout the whole primary adsorption is plotted against the optical coverage. The three key points represented by the spectra in panel (A) are highlighted in panel (B) by means of three dashed lines.

Figure 6A shows the best fits for three representative IR spectra, corresponding to low CO coverage, turning point and maximum CO coverage. The fit (in red) is overlapped to the experimental spectrum (in black) and to the six single components: linear, defective linear I, defective linear II, bridged, 3-fold hollow I and 3-fold hollow II. Figure 6B shows the evolution of the normalized integrated areas of each Pd-CO type (A_n^*) plotted against the normalized integrated area of the total spectrum (A_{TOT}^*). In this plot the contributions of the two linear carbonyls on defects (defective linear I and defective linear II) were summed together, as well as the contributions of the two types of 3-fold hollow carbonyls (3-fold hollow I and 3-fold hollow II). It is evident that in the low CO coverage regime, all the four types of carbonyls monotonously grow with coverage, with bridged (band III) and 3-fold hollow (band IV) carbonyls growing much faster than linear ones (bands I and II). At the turning point, the overall integrated area of band III drastically drops, while that of bands I and II grow at a significantly higher rate than before. The evolution of all the fitted parameters is presented in Figure 8 and Figure 9 for PdAl and PdAl(R), respectively.
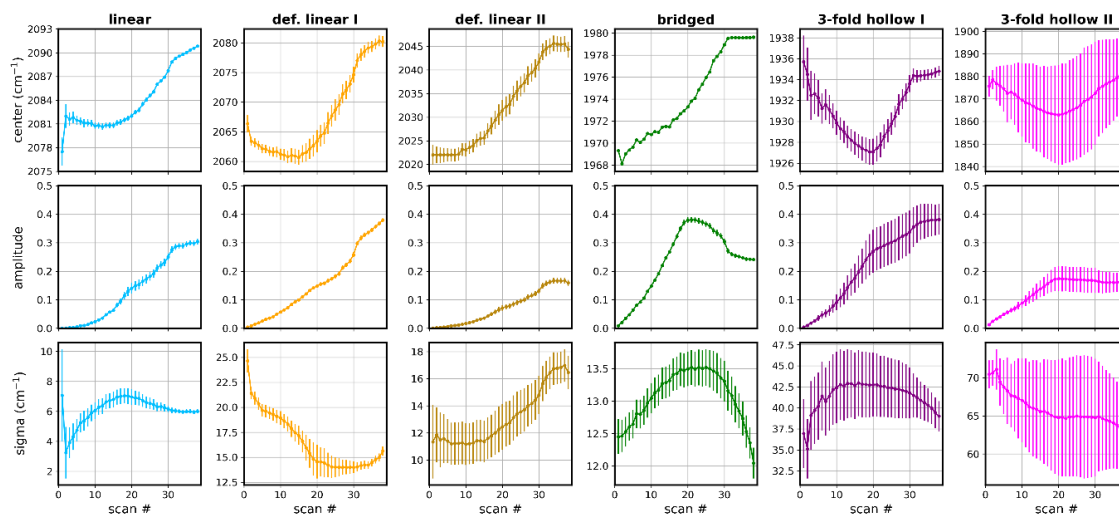
Figure 8. Evolution of the fitted gaussian parameters (center, amplitude and sigma) along the fitting procedure of the primary adsorption of CO on PdAl. The gaussian parameters relative to linear (cyan), def. linear I (orange), def. linear II (ochre), bridged (green), 3-fold hollow I (purple) and 3-fold hollow II (pink) are plotted together with their error bars. The large error generally reported for parameters relative to defective linear and hollow components arise from the strong correlation existing within the two sets of bands.
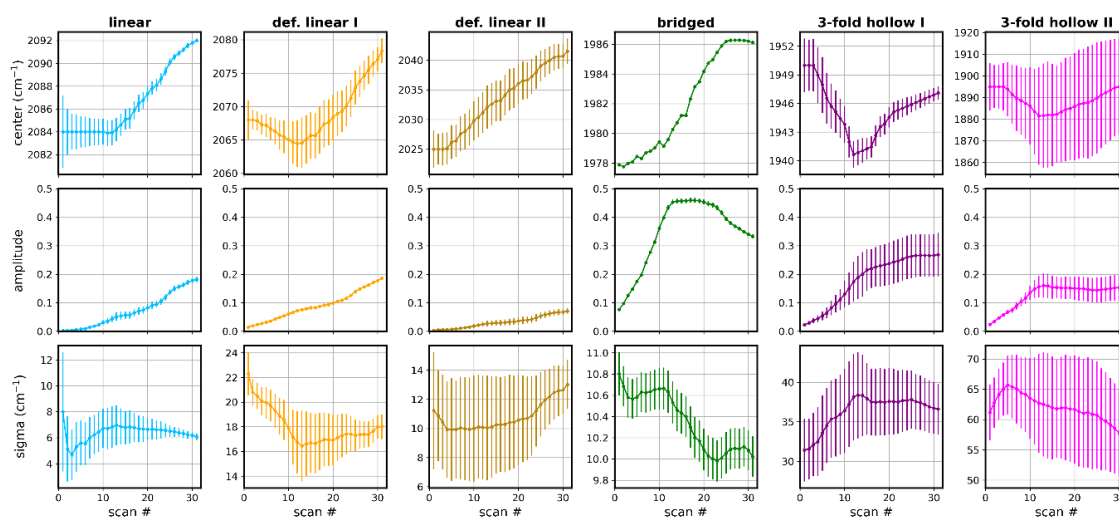
Figure 9. Evolution of the fitted gaussian parameters (center, amplitude and sigma) along the fitting procedure of the primary adsorption of CO on PdAl(R). The gaussian parameters relative to linear (cyan), def. linear I (orange), def. linear II (ochre), bridged (green), 3-fold hollow I (purple) and 3-fold hollow II (pink) are plotted together with their error bars. The large error generally reported for parameters relative defective linear and hollow components arise from the strong correlation existing within the two sets of bands.

The most important contribution of this analysis is pointing out that the massive growth of bands I & II (associated to linear carbonyls) after the turning point is mainly due to band II, i.e. carbonyl species on defective sites. Hence, the drastic decrease in the amount of bridged carbonyls (band III) occurs simultaneously to the increase of linear carbonyls on defective sites. This behaviour, coupled with the above-mentioned volumetric and calorimetric observations, strongly suggests that, once reached the turning coverage, Pd NPs undergo a CO-induced surface reconstruction consisting in a corrugation of the Pd(100) facets entailing the exposure of novel defective sites, characterized by a higher adsorption energy. It is important to notice that such a reconstruction should be an endothermic process. Hence, the overall increase in the heat of CO adsorption measured by microcalorimetry in the reconstruction region indicates that the higher CO adsorption energy at the novel defective sites over-compensates the endothermic heat associated with the reconstruction.

3.3.3 Reversibility of the process

Once completed the primary adsorption, the reversibility of the whole adsorption process was inspected for PdAl: to this aim the reversible fraction of the Pd-CO species was desorbed at room temperature, as reported in Figure 10. This was followed by a secondary adsorption run at the same temperature, which was monitored again with all the three mentioned techniques (Figure 11). All the three techniques agree on that a significant fraction of the Pd-CO species is retained on the surface upon desorption at room temperature, denoting a certain degree of irreversibility in the bonding of CO to the Pd surface. In particular, the volumetric isotherm (grey dots in Figure 11A) indicates that almost 80% of CO remains adsorbed after evacuation at room temperature which, according to IR spectroscopy (Figure 11B, black spectrum in the bottom), correspond to linear carbonyls on defects, bridged and 3-fold hollow CO.
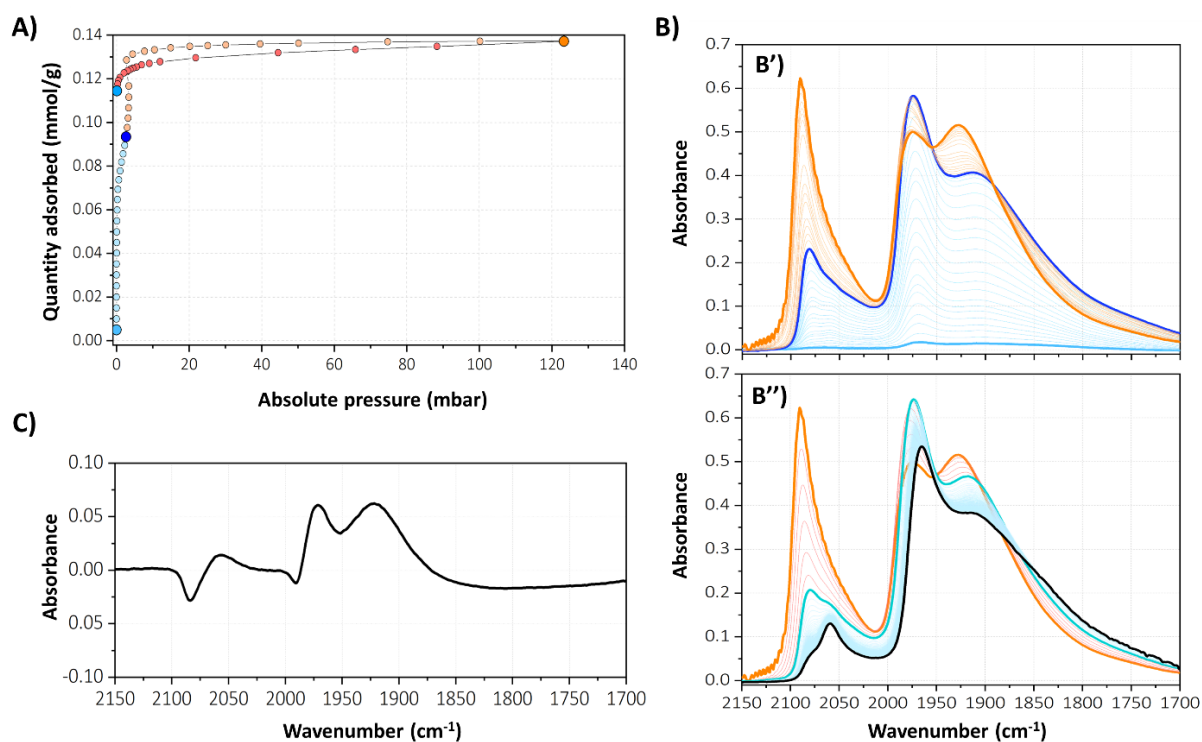
Figure 10. Volumetric isotherm (part A) and FT-IR spectra (part B) for the primary adsorption and desorption of CO on PdAl. Plots of the primary adsorption are represented with the same color code as reported in the previous sections. Data reported in red in panel (A) and (B'') are collected by desorbing CO through subsequent expansions. Spectra from cyan to black in panel (B'') are acquired while evacuating the sample. Panel (C) reports the difference between the spectra corresponding to the maximum amplitude of the bridged band during primary adsorption (B') and desorption (B''). Besides highlighting a mild shift towards lower wavenumber in the bridged band, the difference spectrum spots a slightly higher fraction of defective linear, bridged and 3-fold hollows carbonyls in desorption rather than in adsorption.

The Pd-CO species which are formed during the secondary adsorption are characterized by much milder values of differential heat of adsorption (grey bars in Figure 11C), suggesting that only the weakest sites are being populated throughout the secondary adsorption. However, a close inspection to the IR spectra acquired during the secondary adsorption run (Figure 11B) reveals that a surface reconstruction is taking place also in this case, which leads to a situation that is almost undistinguishable from what is obtained at the end of the first adsorption run, even though it follows a slightly different path (Figure 10C).

Volumetric and calorimetric data look less informative at first sight. The reason is that, as highlighted by FT-IR spectroscopy, the surface reconstruction phenomenon takes place at the very first stages of secondary adsorption. Thus, a step in the adsorbed quantity cannot be detected in the secondary adsorption isotherm. On the other hand, the fact that the first heat of adsorption value measured for the secondary adsorption run is higher than what measured for the plateau over the primary adsorption, supports the claim that a surface reconstruction is taking place at the very beginning of the secondary adsorption process.
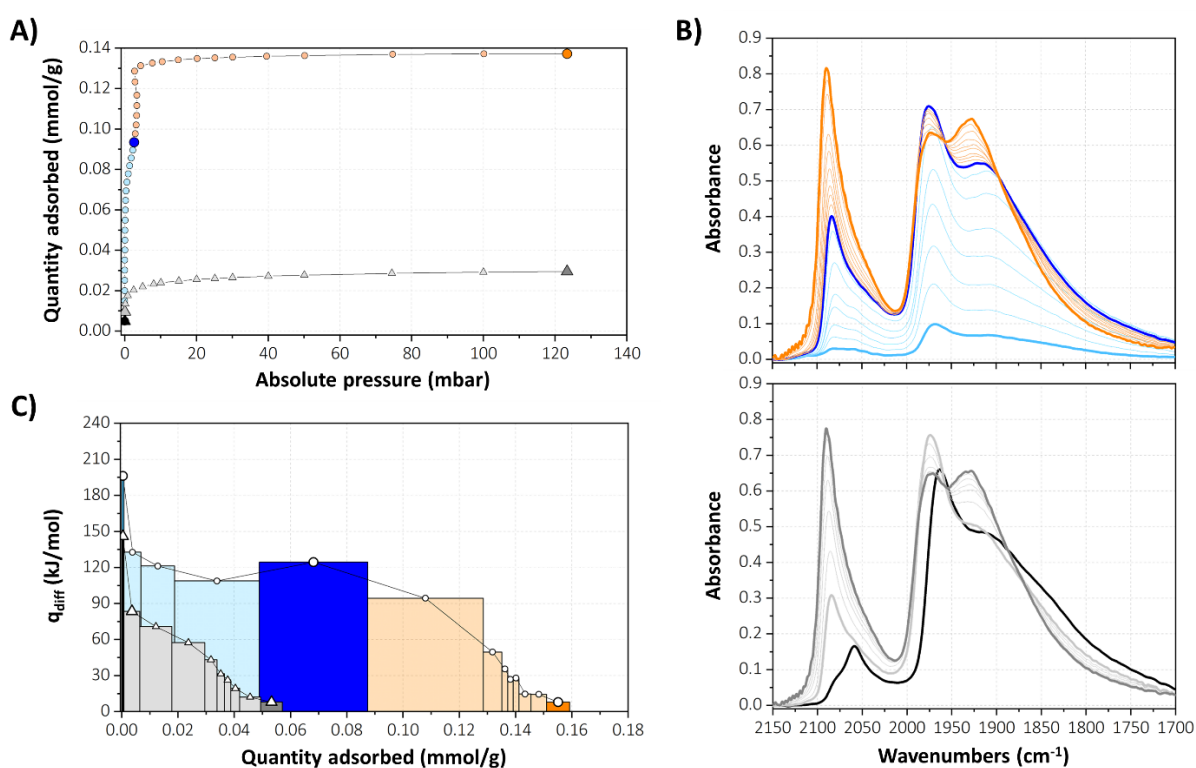
Figure 11. Volumetric isotherms (A), *in situ* FT-IR spectra (B) and heat of adsorption (C) for the primary and secondary adsorption of CO on the PdAl sample. For the three cases, the secondary adsorption is represented in grey (the first step being represented in black), with the turning point represented as a bold light grey spectrum in panel (B) and a bigger light grey triangle in panel (A) and (C). The final point is represented as a bold dark grey spectrum in panel (B) and as a bigger dark grey triangle in panel (A) and (C). Plots for the primary adsorption are represented with the same colour code as reported earlier.
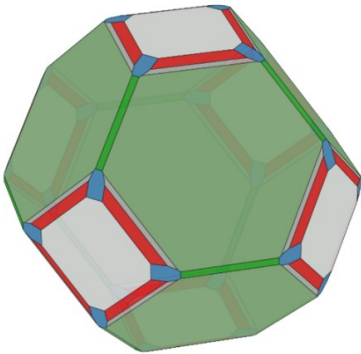
3.3.4 Computational insights

The computed Γ_{hkl} and the relative exposed fractions of the bare Pd(100), Pd(111), Pd(110), Pd(210), Pd(310), Pd(211) and Pd(311) facets are reported in Figure 12 together with the corresponding Wulff construction of the equilibrium shape of a resulting NP. This last, corresponding to a truncated octahedron morphology mainly exposing (100) and (111) facets, is in excellent agreement with the existing literature,[56] thus validating the choice of the functional and the general computational setup. Besides exploring CO adsorption in the high coverage regime for the two most exposed facets (i.e., Pd(100) and Pd(111)), we decided to take into account the effect of CO adsorption on the edges by considering the only Pd(100) facet. In our first approach, the exploration of CO adsorption on higher-index facets has been neglected.

The coverage-dependent ρ_{surf}, free energies of adsorption (G_{ads}) and Γ_{hkl} for the adsorption of CO at different coverages are reported in Table 1 for the three mentioned Pd facets. As outlined in section 3.2.6, the reported values of Γ_{hkl} allow to identify the saturation coverage for the three Pd facets, which turns out to be 0.75 for Pd(100) and Pd(111) and 1 for Pd(110). This finding is consistent with the observations that can be made regarding the corresponding ρ_{surf}. Indeed, the "corrugated" nature of the (110) facet allows CO molecules to adsorb without overlapping their Van der Waals radii already at $\theta = 1$, while lower θ values are required to satisfy this condition on the low-index and flat (100) and (111) facets.

According to the exposed fractions of the three considered facets reported in Figure 6A, the contribution of the Pd(110) facet becomes negligible at θ_{sat}. In the same situation, Figure 6B reports an over-stabilization of the Pd(100) facet with respect to Pd(111) which, unexpectedly, could suggest the occurrence of a surface reconstruction process in which the

exposed Pd(111) facets are converted into Pd(100). However, by looking at the evolution of the Pd(100) slab upon geometry optimization at θ_{sat} (Figure 6C), a beginning of surface corrugation is observed. This suggests that the observed over-stabilization of the Pd(100) facet is due to the corrugation arising from CO adsorption. This last observation supports the claim that the unexpected adsorption behaviour addressed experimentally in the previous sections is due to a CO-induced corrugation of the Pd(100) facets within the catalyst.

(hkl)	Γ_{hkl} (J/m^2)	fraction
(111)	1.11	0.68
(100)	1.28	0.16
(311)	1.32	0.067
(211)	1.28	0.037
(310)	1.37	0.030
(110)	1.34	0.024
(210)	1.41	0.0

Wulff Construction

Figure 12. Surface energies, exposed fractions and corresponding Wulff construction for the considered bare Pd(100), Pd(111), Pd(110), Pd(210), Pd(310), Pd(211) and Pd(311) facets.

Table A1. Notable parameters extracted from the calculations of CO adsorption at Pd (100), Pd(111) and Pd (110) surfaces.

ρ_{surf} is the CO surface density, G_{ads} is the adsorption free energy and Γ_{hkl} is the surface energy as described in section 3.2.6.

(hkl)	θ	ρ_{surf} (Å^{-2})	G_{ads} (kJ/mol)	Γ_{hkl} (J/m^2)
(100)	0.75	0.095	-0.55	0.056
	0.8	0.10	-55.1	0.089
	1	0.13	-75.1	0.456
(111)	0.75	0.11	-68.5	0.079
	1	0.15	-37.6	1.098
(100)	1	0.089	-79.5	0.122

A)	(hkl)	Γ_{hkl} (J/m²)	fraction
	(100)	0.056	0.90
	(111)	0.079	0.10
	(110)	0.122	0.0
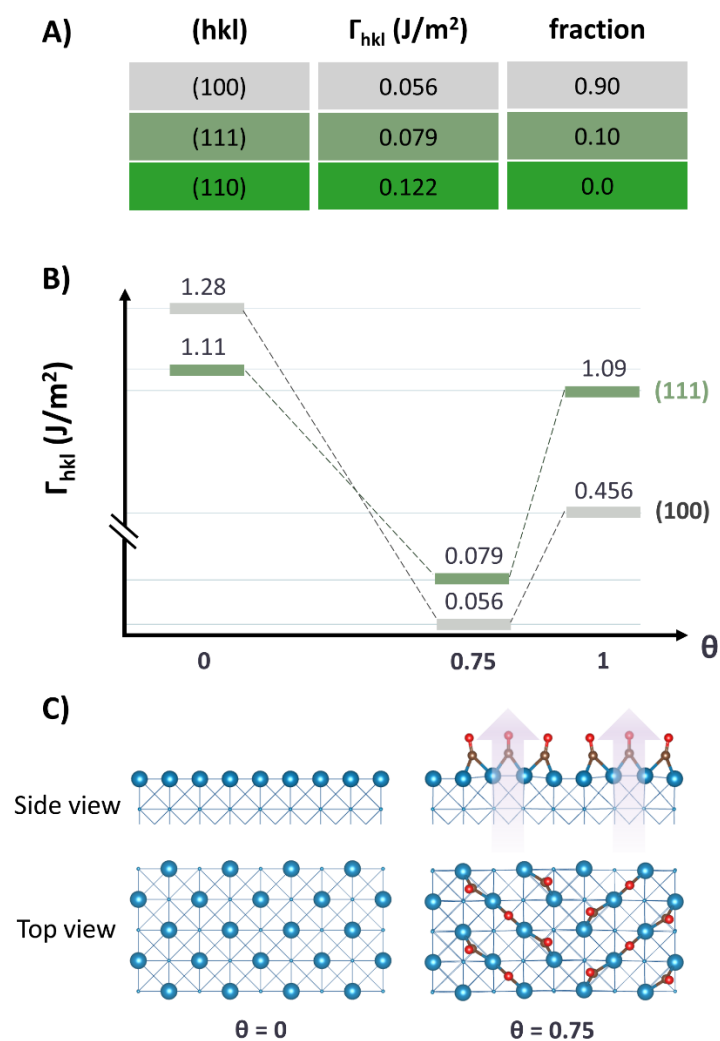
Figure 13. (A) Γ_{hkl} and corresponding exposed fraction for the Pd(100), Pd(111) and Pd(110) facets at CO saturation coverage (i.e. θ = 0.75). (B) Schematic plot of Γ_{hkl} vs θ for the Pd (100) and Pd(111) facets. (C) Side and top view of the Pd(100) slab before (θ = 0) and after being geometry optimized with CO adsorbed at saturation coverage (θ = 0.75). The pink arrows are added to highlight the direction of the corrugation.

3.4 Conclusions

The interaction of CO with Pd NPs is a topic of wide fundamental interest and also high practical relevance. Indeed, Pd-based systems are involved in the catalytic conversion of CO in a variety of valuable chemical compounds, but have a prominent role also in the field of hydrogen purification and pollution abatement. Last, but not least, CO is the most used probe in the characterization of Pd NPs, and it is widely adopted for a rapid and efficient evaluation

of the metal dispersion through pulsed chemisorption methods. It is well assessed that CO adsorption at high temperature, representative of many catalytic reactions, can cause important surface and structural modification in Pd NPs, with evident consequences on the activity and selectivity of the processes. In contrast, the occurrence of such kind of phenomena at milder temperature is by far less documented, despite its importance for a correct interpretation of the characterization data.

In this work, we tried to fill this gap by synergically combining gas-volumetry, adsorption micro-calorimetry and IR spectroscopy, in the atomic-level investigation of the interaction of CO with Al_2O_3-supported Pd NPs, both qualitatively (adsorption modes and sites) and quantitatively (adsorbed quantity and heat of adsorption), as a function of the CO coverage. An anomalous step in the volumetric isotherm was observed for the first time at a relative pressure corresponding approximately to 80% of the maximum coverage. This was accompanied by an unexpected increase in the heat of adsorption. Both observations were correlated with a drastic modification in the relative proportions of adsorbed carbonyls, as revealed by IR spectroscopy. In particular, a massive increase in the amount of linear carbonyls at defect sites was detected, at the expense of bridged carbonyls. These three experimental observations, together, provided a unprecedent insights on a CO-induced surface reconstruction involving the (100) surface and entailing the creation of new, defective, adsorption sites. This was confirmed by preliminary computational simulations, carried out by adopting the infinite slab approach, which predicted that the (100) surface can be corrugated by CO adsorption at the saturation coverage.

As a final conclusion, it is important to notice that the three experimental techniques adopted in this work are nowadays widely available in standard research laboratories, do not

require access to any large-scale facility, but only a rigorous and systematic operation mode. As such, the experimental approach here proposed can be easily extended to other metals and other probes, and has the potential to provide a methodological benchmark in the field of characterization of adsorbate-induced phenomena in supported metal NPs.

References

(1)   Ndolomingo, M. J.; Bingwa, N.; Meijboom, R. Review of Supported Metal Nanoparticles: Synthesis Methodologies, Advantages and Application as Catalysts. *J. Mater. Sci.* **2020**, *55* (15), 6195–6241. https://doi.org/10.1007/s10853-020-04415-x.

(2)   Figueras, F.; Coq, B. Hydrogenation and Hydrogenolysis of Nitro-, Nitroso-, Azo-, Azoxy- and Other Nitrogen-Containing Compounds on Palladium. *J. Mol. Catal. A Chem.* **2001**, *173* (1–2), 223–230. https://doi.org/10.1016/S1381-1169(01)00151-0.

(3)   Duca, D.; Barone, G.; Varga, Z. Hydrogenation of Acetylene-Ethylene Mixtures on Pd Catalysts: Computational Study on the Surface Mechanism and on the Influence of the Carbonaceous Deposits. *Catal. Letters* **2001**, *72* (1–2), 17–23. https://doi.org/10.1023/A:1009089227947.

(4)   Blaser, H. U.; Indolese, A.; Schnyder, A.; Steiner, H.; Studer, M. Supported Palladium Catalysts for Fine Chemicals Synthesis. *J. Mol. Catal. A Chem.* **2001**, *173* (1–2), 3–18. https://doi.org/10.1016/S1381-1169(01)00143-1.

(5)   Pernicone, N.; Cerboni, M.; Prelazzi, G.; Pinna, F.; Fagherazzi, G. An Investigation on Pd/C Industrial Catalysts for the Purification of Terephthalic Acid. *Catal. Today* **1998**, *44* (1–4), 129–135. https://doi.org/10.1016/S0920-5861(98)00183-7.

(6)   Long, X.; Chen, W.; Lei, C.; Xie, Q.; Zhang, F.; Huang, B. Ultrafine Pd Nanoparticles@g-C3N4 for Highly Efficient Dehalogenation of Chlorinated Environmental Pollutant: Structure, Efficacy and Mechanisms. *Sci. Total Environ.* **2021**, *775*. https://doi.org/10.1016/j.scitotenv.2021.145178.

(7)   Selishchev, D.; Svintsitskiy, D.; Kovtunova, L.; Gerasimov, E.; Gladky, A.; Kozlov, D. Surface Modification of TiO2 with Pd Nanoparticles for Enhanced Photocatalytic Oxidation of Benzene Micropollutants. *Colloids Surfaces A Physicochem. Eng. Asp.*

2021, *612* (July 2020), 125959. https://doi.org/10.1016/j.colsurfa.2020.125959.

(8)   Luo, M.; Yao, W.; Huang, C.; Wu, Q.; Xu, Q. Shape-Controlled Synthesis of Pd

Nanoparticles for Effective Photocatalytic Hydrogen Production. *RSC Adv.* **2015**, *5* (51),

40892–40898. https://doi.org/10.1039/c5ra06352c.

(9)   Roldan Cuenya, B.; Behafarid, F. Nanocatalysis: Size- and Shape-Dependent

Chemisorption and Catalytic Reactivity. *Surf. Sci. Rep.* **2015**, *70* (2), 135–187.

https://doi.org/10.1016/j.surfrep.2015.01.001.

(10)   Besenbacher, F.; Chorkendorff, I.; Clausen, B. S.; Hammer, B.; Molenbroek, A. M.;

Nørskov, J. K.; Stensgaard, I. Design of a Surface Alloy Catalyst for Steam Reforming.

Science (80-.). **1998**, *279* (5358), 1913–1915.

https://doi.org/10.1126/science.279.5358.1913.

(11)   Zhdanov, V. P.; Kasemo, B. Mechanism and Kinetics of the NO-CO Reaction on Rh.

Surf. Sci. Rep. **1997**, *29* (2), 31–33. https://doi.org/10.1016/S0167-5729(97)00009-5.

(12)   Yudanov, I. V.; Sahnoun, R.; Neyman, K. M.; Rösch, N.; Hoffmann, J.; Schauermann, S.;

Johánek, V.; Unterhalt, H.; Rupprechter, G.; Libuda, J.; Freund, H. J. CO Adsorption on

Pd Nanoparticles: Density Functional and Vibrational Spectroscopy Studies. *J. Phys.*

Chem. B **2003**, *107* (1), 255–264. https://doi.org/10.1021/jp022052b.

(13)   Groppo, E.; Rojas-Buzo, S.; Bordiga, S. The Role of In Situ/Operando IR Spectroscopy in

Unraveling Adsorbate-Induced Structural Changes in Heterogeneous Catalysis. *Chem.*

Rev. **2023**, *123* (21), 12135–12169. https://doi.org/10.1021/acs.chemrev.3c00372.

(14)   Newton, M. A. Dynamic Adsorbate/Reaction Induced Structural Change of Supported

Metal Nanoparticles: Heterogeneous Catalysis and Beyond. *Chem. Soc. Rev.* **2008**, *37*

(12), 2644–2657. https://doi.org/10.1039/b707746g.

(15)   Chizallet, C.; Raybaud, P. Density Functional Theory Simulations of Complex Catalytic

Materials in Reactive Environments: Beyond the Ideal Surface at Low Coverage. *Catal. Sci. Technol.* **2014**, *4* (9), 2797–2813. https://doi.org/10.1039/c3cy00965c.

(16) Vottero, E.; Carosso, M.; Ricchebuono, A.; Jiménez-Ruiz, M.; Pellegrini, R.; Chizallet, C.; Raybaud, P.; Groppo, E.; Piovano, A. Evidence for H2-Induced Ductility in a Pt/Al2O3 Catalyst. *ACS Catal.* **2022**, *12* (10), 5979–5989. https://doi.org/10.1021/acscatal.2c00606.

(17) Avanesian, T.; Dai, S.; Kale, M. J.; Graham, G. W.; Pan, X.; Christopher, P. Quantitative and Atomic-Scale View of CO-Induced Pt Nanoparticle Surface Reconstruction at Saturation Coverage via DFT Calculations Coupled with in Situ TEM and IR. *J. Am. Chem. Soc.* **2017**, *139* (12), 4551–4558. https://doi.org/10.1021/jacs.7b01081.

(18) Sangnier, A.; Genty, E.; Iachella, M.; Sautet, P.; Raybaud, P.; Matrat, M.; Dujardin, C.; Chizallet, C. Thermokinetic and Spectroscopic Mapping of Carbon Monoxide Adsorption on Highly Dispersed Pt/γ-Al2O3. *ACS Catal.* **2021**, *11* (21), 13280–13293. https://doi.org/10.1021/acscatal.1c04262.

(19) Zhao, P.; Cao, Z.; Liu, X.; Ren, P.; Cao, D. B.; Xiang, H.; Jiao, H.; Yang, Y.; Li, Y. W.; Wen, X. D. Morphology and Reactivity Evolution of HCP and FCC Ru Nanoparticles under CO Atmosphere. *ACS Catal.* **2019**, *9* (4), 2768–2776. https://doi.org/10.1021/acscatal.8b05074.

(20) Roiaz, M.; Falivene, L.; Rameshan, C.; Cavallo, L.; Kozlov, S. M.; Rupprechter, G. Roughening of Copper (100) at Elevated CO Pressure: Cu Adatom and Cluster Formation Enable CO Dissociation. *J. Phys. Chem. C* **2019**, *123* (13), 8112–8121. https://doi.org/10.1021/acs.jpcc.8b07668.

(21) Wanke, S. E. Introduction to Characterization and Testing of Catalysts, by J. R. Anderson and K. C. Pratt 1985, 457 Pages. Academic Press, Sydney, Australia, $119.20

(Canadian). *Can. J. Chem. Eng.* **1988**, *66* (2), 349. https://doi.org/https://doi.org/10.1002/cjce.5450660229.

(22) Zhao, Y.; Tan, X.; Yang, W.; Jia, C.; Chen, X.; Ren, W.; Smith, S. C.; Zhao, C. Surface Reconstruction of Ultrathin Palladium Nanosheets during Electrocatalytic CO2 Reduction. *Angew. Chemie - Int. Ed.* **2020**, *59* (48), 21493–21498. https://doi.org/10.1002/anie.202009616.

(23) Murata, K.; Eleeda, E.; Ohyama, J.; Yamamoto, Y.; Arai, S.; Satsuma, A. Identification of Active Sites in CO Oxidation over a Pd/Al2O3 Catalyst. *Phys. Chem. Chem. Phys.* **2019**, *21* (33), 18128–18137. https://doi.org/10.1039/c9cp03943k.

(24) Raval, R.; Haq, S.; Harrison, M. A.; Blyholder, G.; King, D. A. Molecular Adsorbate-Induced Surface Reconstruction: CO/Pd{110}. *Chem. Phys. Lett.* **1990**, *167* (5), 391–398. https://doi.org/10.1016/0009-2614(90)85019-9.

(25) Jbir, I.; Couble, J.; Khaddar-Zine, S.; Ksibi, Z.; Meunier, F.; Bianchi, D. Individual Heat of Adsorption of Adsorbed CO Species on Palladium and Pd-Sn Nanoparticles Supported on Al2O3 by Using Temperature-Programmed Adsorption Equilibrium Methods. *ACS Catal.* **2016**, *6* (4), 2545–2558. https://doi.org/10.1021/acscatal.5b02749.

(26) Férey, G.; Serre, C. Large Breathing Effects in Three-Dimensional Porous Hybrid Matter: Facts, Analyses, Rules and Consequences. *Chem. Soc. Rev.* **2009**, *38* (5), 1380–1399. https://doi.org/10.1039/b804302g.

(27) Cavallo, M.; Atzori, C.; Signorile, M.; Costantino, F.; Venturi, D. M.; Koutsianos, A.; Lomachenko, K. A.; Calucci, L.; Martini, F.; Giovanelli, A.; Geppi, M.; Crocellà, V.; Taddei, M. Cooperative CO2 Adsorption Mechanism in a Perfluorinated CeIV-Based Metal Organic Framework. *J. Mater. Chem. A* **2023**, *11* (11), 5568–5583. https://doi.org/10.1039/d2ta09746j.

(28)   Sánchez-Gil, V.; Noya, E. G.; Sanz, A.; Khatib, S. J.; Guil, J. M.; Lomba, E.; Marguta, R.;

Valencia, S. Experimental and Simulation Studies of the Stepped Adsorption of

Toluene on Pure-Silica MEL Zeolite. *J. Phys. Chem. C* **2016**, *120* (16), 8640–8652.

https://doi.org/10.1021/acs.jpcc.6b00402.

(29)   Min, J. G.; Luna-Triguero, A.; Byun, Y.; Balestra, S. R. G.; Vicent-Luna, J. M.; Calero, S.;

Hong, S. B.; Camblor, M. A. Stepped Propane Adsorption in Pure-Silica ITW Zeolite.

Langmuir **2018**, *34* (16), 4774–4779. https://doi.org/10.1021/acs.langmuir.8b00628.

(30)   Agostini, G.; Groppo, E.; Piovano, A.; Pellegrini, R.; Leofanti, G.; Lamberti, C.

Preparation of Supported Pd Catalysts: From the Pd Precursor Solution to the

Deposited Pd2+ Phase. *Langmuir* **2010**, *26* (13), 11204–11211.

https://doi.org/10.1021/la1005117.

(31)   Groppo, E.; Agostini, G.; Piovano, A.; Muddada, N. B.; Leofanti, G.; Pellegrini, R.;

Portale, G.; Longo, A.; Lamberti, C. Effect of Reduction in Liquid Phase on the

Properties and the Catalytic Activity of Pd/Al 2O 3 Catalysts. *J. Catal.* **2012**, *287*, 44–

54. https://doi.org/10.1016/j.jcat.2011.11.018.

(32)   MATTEO, C. V. A. C. L. G. S. A KIT FOR VOLUMETRIC MEASUREMENTS OF GAS

ADSORPTION. 2021. https://www.sumobrain.com/patents/WO2021181211A1.html.

(33)   Bolis, V. Fundamentals in Adsorption at the Solid-Gas Interface. Concepts and

Thermodynamics. In *Calorimetry and Thermal Methods in Catalysis*; Auroux, A., Ed.;

Springer Berlin Heidelberg: Berlin, Heidelberg, 2013; pp 3–50.

https://doi.org/10.1007/978-3-642-11954-5_1.

(34)   Bradley, M. S. Curve Fitting in Raman and IR Spectroscopy: Basic Theory of Line

Shapes and Applications; 2007.

(35)   Ozensoy, E.; Goodman, D. W. Vibrational Spectroscopic Studies on CO Adsorption, NO

Adsorption CO + NO Reaction on Pd Model Catalysts. *Phys. Chem. Chem. Phys.* **2004**, *6* (14), 3765–3778. https://doi.org/10.1039/b402302a.

(36)   Groppo, E.; Liu, W.; Zavorotynska, O.; Agostini, G.; Spoto, G.; Bordiga, S.; Lamberti, C.; Zecchina, A. Subnanometric Pd Particles Stabilized inside Highly Cross-Linked Polymeric Supports. *Chem. Mater.* **2010**, *22* (7), 2297–2308. https://doi.org/10.1021/cm903176d.

(37)   Lear, T.; Marshall, R.; Lopez-Sanchez, J. A.; Jackson, S. D.; Klapötke, T. M.; Bäumer, M.; Rupprechter, G.; Freund, H. J.; Lennon, D. The Application of Infrared Spectroscopy to Probe the Surface Morphology of Alumina-Supported Palladium Catalysts. *J. Chem. Phys.* **2005**, *123* (17). https://doi.org/10.1063/1.2101487.

(38)   Surnev, S.; Sock, M.; Ramsey, M. G.; Netzer, P. P.; Wiklund, M.; Borg, M.; Andersen, J. N. CO Adsorption on Pd(111): A High-Resolution Core Level Photoemission and Electron Energy Loss Spectroscopy Study. *Surf. Sci.* **2000**, *470* (1–2), 171–185. https://doi.org/10.1016/S0039-6028(00)00853-0.

(39)   Kresse, G.; Furthmüller, J. Efficiency of Ab-Initio Total Energy Calculations for Metals and Semiconductors Using a Plane-Wave Basis Set. *Comput. Mater. Sci.* **1996**, *6* (1), 15–50. https://doi.org/10.1016/0927-0256(96)00008-0.

(40)   Kresse, G.; Hafner, J. Ab Initio Molecular-Dynamics Simulation of the Liquid-Metalamorphous- Semiconductor Transition in Germanium. *Phys. Rev. B* **1994**, *49* (20), 14251–14269. https://doi.org/10.1103/PhysRevB.49.14251.

(41)   Hammer, B.; Hansen, L. B.; Nørskov, J. K. Improved Adsorption Energetics within Density-Functional Theory Using Revised Perdew-Burke-Ernzerhof Functionals. *Phys. Rev. B* **1999**, *59* (11), 7413–7421. https://doi.org/10.1103/PhysRevB.59.7413.

(42)   Kresse, G.; Joubert, D. From Ultrasoft Pseudopotentials to the Projector Augmented-

Wave Method. *Phys. Rev. B* **1999**, *59* (3), 1758–1775.

https://doi.org/10.1103/PhysRevB.59.1758.

(43)   Methfessel, M.; Paxton, A. T. High-Precision Sampling for Brillouin-Zone Integration in

Metals. *Phys. Rev. B* **1989**, *40* (6), 3616–3621.

https://doi.org/10.1103/PhysRevB.40.3616.

(44)   Agostini, G.; Pellegrini, R.; Leofanti, G.; Bertinetti, L.; Bertarione, S.; Groppo, E.;

Zecchina, A.; Lamberti, C. Determination of the Particle Size, Available Surface Area,

and Nature of Exposed Sites for Silica-Alumina-Supported Pd Nanoparticles: A

Multitechnical Approach. *J. Phys. Chem. C* **2009**, *113* (24), 10485–10492.

https://doi.org/10.1021/jp9023712.

(45)   Kittel, C. *Introduction to Solid State Physics*; John Wiley \& sons, inc, 2005.

(46)   Chizallet, C.; Bonnard, G.; Krebs, E.; Bisson, L.; Thomazeau, C.; Raybaud, P.

Thermodynamic Stability of Buta-1,3-Diene and But-1-Ene on Pd(111) and (100)

Surfaces under H2 Pressure: A DFT Study. *J. Phys. Chem. C* **2011**, *115* (24), 12135–

12149. https://doi.org/10.1021/jp202811t.

(47)   Wulff, G. XXV. Zur Frage Der Geschwindigkeit Des Wachsthums Und Der Auflösung

Der Krystallflächen. **1901**, *34* (1–6), 449–530.

https://doi.org/doi:10.1524/zkri.1901.34.1.449.

(48)   Momma, K.; Izumi, F. VESTA 3 for Three-Dimensional Visualization of Crystal,

Volumetric and Morphology Data. *J. Appl. Crystallogr.* **2011**, *44* (6), 1272–1276.

https://doi.org/10.1107/S0021889811038970.

(49)   Zeinalipour-Yazdi, C. D.; Willock, D. J.; Thomas, L.; Wilson, K.; Lee, A. F. CO Adsorption

over Pd Nanoparticles: A General Framework for IR Simulations on Nanoparticles.

Surf. Sci. **2016**, *646*, 210–220. https://doi.org/10.1016/j.susc.2015.07.014.

(50)   Yudanov, I. V.; Genest, A.; Schauermann, S.; Freund, H. J.; Rösch, N. Size Dependence of the Adsorption Energy of CO on Metal Nanoparticles: A DFT Search for the Minimum Value. *Nano Lett.* **2012**, *12* (4), 2134–2139. https://doi.org/10.1021/nl300515z.

(51)   Fischer-Wolfarth, J. H.; Farmer, J. A.; Flores-Camacho, J. M.; Genest, A.; Yudanov, I. V.; Rösch, N.; Campbell, C. T.; Schauermann, S.; Freund, H. J. Particle-Size Dependent Heats of Adsorption of CO on Supported Pd Nanoparticles as Measured with a Single-Crystal Microcalorimeter. *Phys. Rev. B - Condens. Matter Mater. Phys.* **2010**, *81* (24), 8–11. https://doi.org/10.1103/PhysRevB.81.241416.

(52)   Flores-Camacho, J. M.; Fischer-Wolfarth, J. H.; Peter, M.; Campbell, C. T.; Schauermann, S.; Freund, H. J. Adsorption Energetics of CO on Supported Pd Nanoparticles as a Function of Particle Size by Single Crystal Microcalorimetry. *Phys. Chem. Chem. Phys.* **2011**, *13* (37), 16800–16810. https://doi.org/10.1039/c1cp21677e.

(53)   Lamberti, C.; Zecchina, A.; Groppo, E.; Bordiga, S. Probing the Surfaces of Heterogeneous Catalysts by in Situ IR Spectroscopy. *Chem. Soc. Rev.* **2010**, *39* (12), 4951–5001. https://doi.org/10.1039/C0CS00117A.

(54)   Lear, T.; Marshall, R.; Antonio Lopez-Sanchez, J.; Jackson, S. D.; Klapötke, T. M.; Bäumer, M.; Rupprechter, G.; Freund, H.-J.; Lennon, D. The Application of Infrared Spectroscopy to Probe the Surface Morphology of Alumina-Supported Palladium Catalysts. *J. Chem. Phys.* **2005**, *123* (17), 174706. https://doi.org/10.1063/1.2101487.

(55)   Virnovskaia, A.; Morandi, S.; Rytter, E.; Ghiotti, G.; Olsbye, U. Characterization of Pt,Sn/Mg(Al)O Catalysts for Light Alkane Dehydrogenation by FT-IR Spectroscopy and Catalytic Measurements. *J. Phys. Chem. C* **2007**, *111* (40), 14732–14742. https://doi.org/10.1021/jp074686u.

(56)   Tran, R.; Xu, Z.; Radhakrishnan, B.; Winston, D.; Sun, W.; Persson, K. A.; Ong, S. P.

Surface Energies of Elemental Crystals. *Sci. Data* **2016**, *3* (1), 160080.

https://doi.org/10.1038/sdata.2016.80.

Chapter 4

Probing the micro- and meso-structure of activated carbons with Gas Sorption and Small Angle Neutron Scattering

4.1. Introduction

Activated carbons (ACs) are extremely popular materials, widely employed as catalytic supports or catalysts on their own, adsorbents, storage materials and even components of electrochemical cells.[1–6] Obtained from different carbonaceous precursors (wood, peat, coconut shells, etc.) they can develop a series of pores which remarkably increase their surface area, thanks to the activation process that can be either of physical or chemical nature.[1,5] In physical activations, the precursor is pyrolyzed at high temperature in an inert atmosphere and subsequently activated with weak reactants like water steam or CO_2, while in the latter case the carbonaceous precursor is impregnated with a chemical agent (e.g., $ZnCl_2$ or H_3PO_4) prior to the carbonization step. The thus activated samples can be further modified by post activation treatments,[7–10] for example by oxidation. Both the precursor material and the activation process are known to affect the textural properties,[11,12] as well as the nature and abundance of functional groups, which are fundamental for their chemical properties.[13–15] Despite their popularity, the debate on the micro- and meso-structure of ACs and its impact on the activity of these materials is still open. The reason behind this open question lies in the

highly disordered nature of these materials, coupled with the intrinsic limitations affecting routine techniques employed for their characterization. For example, inferring the Pore Size Distribution (PSD) from gas sorption measurements requires strong assumptions on the pore geometry (routinely assuming a slit-like shape),[16,17] while conventional X-Rays Diffraction (XRD) is blind to the structural organization of these materials, lacking long-range order. In the last decade, the widely accepted model of activated carbons as an ensemble of cross-linked flat graphitic platelets, randomly oriented to create voids (i.e. micropores), has been widely questioned.[16,18–20] The contribution of curved domains could be necessary to explain experimental data from several techniques. For example, the interpretation of the broadening of the XRD peaks in activated carbons as due to the crystallite size shrinking can be indeed combined with the presence of curved domains. Arising from the presence of non-hexagonal rings formed during the activation process, the contribution of curved layers could give the micropore structure a quite different look compared with the conventional model. In this regards, a previous Inelastic Neutron Scattering (INS) study published by our group, did unequivocally show that a model including curved and defective graphitic platelets was essential to reproduce the experimental spectra of several ACs.[14]

Given the limitations of conventional techniques, adding Small Angle Scattering to the puzzle is generally known as suitable for accessing topological information at the required dimensional scale both for crystalline and amorphous samples.[21–23] Moreover, employing Small Angle Neutron Scattering (SANS) over the X-ray analogue (SAXS) has the unique advantage of (1) granting of high sensitivity for the main atoms constituting activated carbons (H and C) and (2) providing information about pore accessibility by gradually filling the pores with a contrast matching agent, like D_2O.[24]

Thus, in this section we present a study in which SANS has been coupled with N_2, Ar and CO_2 sorption in order to shed light on the complex nature of five AC samples of different origin (wood, peat) and activation (steam, HNO_3) on the micro- and mesoscale. Once established Ar as the best suited probe to characterize the porosity of activated carbons by gas sorption, the corresponding PSDs were inferred by means of NL-DFT allowing an accurate measurement of the accessible pore volume. Subsequently, on the basis of the mentioned Ar-PSDs, a SANS experiment employing D_2O as a contrast matching agent has been performed. By coupling data obtained with the two techniques, detailed information concerning the porosity and microstructure of the samples at issues can be accessed, pointing out analogies and differences between the impact of the activation procedure with an unprecedented detail.

4.2. Experimental & methods

4.2.1 Samples

All the ACs investigated in this work are provided by Chimet S.p.A.[25] The experiments were focused on five samples (namely Cwa, Cwa-ox, Cch, Cch-ox and Cpa) of different origin and activation (see Table 1). Three of the carbons (Cwa, Cwa-ox and Cpa) were activated by steam, while Cch and Cch-ox were chemically activated with H_3PO_4. Cwa-ox and Cch-ox were further oxidized with concentrated HNO_3 (67% w/w) at room temperature (RT) for 24 h. All the carbons contain a minor amount of ashes (below 3 wt %).[14] The ACs in Table 1 are the same that have been previously explored with a multi-technique approach by the group in order to assess the identity and amount of functional group at the surface.[15] The possibility to analyse the same set of samples in term of (micro)structure (here) and functionality (before) would permit to rationalize a possible relationship between these two important parameters of ACs.

Table 1. Summary of the synthetic history of the investigated samples

	C_{wa}	C_{wa-ox}	C_{ch}	C_{ch-ox}	C_{pa}
Origin	wood	wood	wood	wood	peat
Activation	physical (steam)	physical (steam)	chemical (H_3PO_4)	chemical (H_3PO_4)	physical (steam)
Oxidation	no	yes	no	yes	no

4.2.2 Gas sorption measurements

Ar and N_2 adsorption isotherms were collected at the liquefaction temperature of each probe molecule (87 K and 77 K, respectively) with a commercial high-performance adsorption analyzer (Micromeritics 3Flex) in the whole p/p_0 range. The samples were analyzed in a designated commercial cell and the temperature was kept constant during the measurement by means of a dewar filled either with liquid Ar or N_2. CO_2 adsorption isotherms were collected at 273 K by means of the high-performance adsorption analyzer Micromeritics ASAP 2020, allowing to cover a p/p_0 range up to ~ 0.03. The samples were analysed in a custom quartz cell (already presented in section 2.2 of Chapter 3) equipped with connections allowing for vacuum and thermochemical treatment, and a plug-in thermal jacket, as described in ref 26. The sample temperature was kept constant thanks to a thermostatic fluid continuously flowing through the thermal jacket, connected to an external isothermal liquid bath (Julabo F25-EH). Prior to any Ar, N_2 and CO_2 measurement, the samples (approximately 60 mg, in the powder form) were evacuated at 120 °C for 2 h by means of a rotary-vane vacuum pump.

The collected isotherms were post treated according to the Brunauer–Emmett–Teller (BET)[27] and Rouquerol[28] theory to evaluate their BET SSA. The Pore Size Distribution (PSD) of each sample was inferred by means of Non Local Density Functional Theory (NL-DFT), within the assumption of slit-shaped pores. For all cases a "Heterogeneous Surface 2D NL-DFT"

model[17] was employed to take into account the heterogeneity of the carbon surface. Insight concerning the pore network was obtained by coupling the NL-DFT analysis of both adsorption and desorption data. Details regarding the isotherm fit can be found in Table A1.

4.2.3 Small Angle Neutron Scattering

4.2.3.1 Contrast matching and experimental protocol

By adapting the master equation of Small Angle Neutron Scattering[29] to a situation corresponding to an ensemble of pores dispersed in a carbonaceous matrix, the scattered intensity from the pores can be written as:

$$I_p(Q) = N_p V_p \left(\rho_c - \rho_p \right)^2 P(Q) S(Q) \tag{1}$$

where N_p and V_p are the number and the volume of the pores, ρ_p and ρ_c are the scattering length densities (SLDs) of the pores and the carbon matrix, $P(Q)$ and $S(Q)$ are the form and the structure factor of the pores.[19] Since the scattered intensity is proportional to the contrast between the SLD of the pores and the carbon matrix, $I_p(Q)$ is maximum when the pores can be considered as empty voids (i.e, in a standard situation). If the pores, or a part of them, are filled with a medium of around the same scattering length density of the carbon matrix, the contribution of the filled pores to $I_p(Q)$ is suppressed, leading to a modification of the SANS pattern of the sample. To fulfill the contrast matching condition, we decided to adopt pure D_2O (SLD of $\sim 6.9 \; 10^{-6} \; Å^{-2}$) as a contrast matching agent. Indeed, since an AC should be slightly less dense than graphite (the latter featuring a SLD of $\sim 7.6 \; 10^{-6} \; Å^{-2}$),[30] the best contrast matching ratio should be achieved with 100% D_2O. Thus, by analyzing each AC at different pore filling levels we were able to gather not only morphological insight on the porosity, but also information on the pore accessibility.

The total volume of the pores of each AC was evaluated from the Ar adsorption isotherms by means of NL-DFT and is reported in Table A2. The five AC samples were activated by heating at 120 °C under dynamic vacuum (final pressure 5 10^{-4} mbar), to remove from the surface as much adsorbed water as possible. The activated samples were transferred into a glovebox and divided into 4 aliquots. One aliquot was left as activated, while the three remaining ones were impregnated with a D_2O amount equal to 1/3, 2/3 and the totality of the micropore volume measured through Ar sorption. The such-prepared samples were inserted into quartz capillaries and sealed under N_2 atmosphere with a photo-crosslinking polymeric glue. The thickness of the employed quartz capillaries was chosen as 2.0 mm to grant a good sensitivity while minimizing multiple scattering. SANS experiments were carried out on the D16 beamline at the ILL in Grenoble (France) with a $\Delta\lambda/\lambda$ = 0.01.[31] Each sample, the empty cell and two references for data normalization (Vanadium and pure D_2O), were analyzed positioning the detector at three different angles (γ) with respect to the incident monochromatic beam (λ = 4.503 Å). γ = 0° was employed to collect the transmitted intensity, while γ = 44° and γ = 90° were employed to collect the scattered intensity respectively in the low- and high-Q regions. This experimental configuration allowed us to collect SANS patterns in a Q region ranging from around 0.03 to 3 Å^{-1}.

An additional preliminary experiment[32] has been carried out on the only Cwa and Cch samples aiming to cover a lower-Q region and thus to explore larger dimensional scales. During the experiment, carried out on the D11 beamline at the same neutron source, the samples (thickness: 3 mm) were analyzed with a fixed beam (λ = 6 Å) to detector angle, which was kept to γ = 0°, where a beam stop was employed to prevent any damage to the detector. By positioning the detector at 1.7, 8 and 38 m from the sample (for the high-, intermediate and

low-Q regions, respectively) this configuration allowed to cover a Q region from around 0.002 to 0.5 Å^{-1}.

4.2.3.2 Morphological models

Three main contributions to the scattered intensity should be observed in a standard SANS pattern of a material exhibiting pure microstructural features:[20]

- A Q^{-4} slope in the low Q range, which corresponds to the Porod's law of scattering by sharp interfaces, that can be ascribed to the macroscopic surface area of the powder grains (I$_{Porod}$);

- The graphite (002) diffraction peak in the wide-angle limit (WANS), related to the carbon microstructure (I$_{WANS}$);

- A contribution in the intermediate Q range caused by the micropores, whose profile depends on the nature of the microporosity (I$_{mp}$).

However, the SANS patterns here presented seem to feature a second contribution in the low Q limit rather than a bare Q^{-4} slope (easily observable in the low-Q plots reported in Figure A1), which could be ascribed both to a family of small carbon grains or to a second family of bigger pores (mesopores). Despite an accurate analysis of this contribution could lead to important information, the here covered Q range is not sufficient to allow a solid fit of the experimental data. Thus, we decided to neglect this effect (avoiding to fit data below ~ 0.06 Å^{-1}) and to model the scattered intensity as a combination of three contributions:

$$I(Q) = I_{Porod} + I_{mp} + I_{WANS} \tag{2}$$

A schematic representation of the contribution of the different structural features of ACs to the total scattered intensity in SANS is given in Figure 1.

Even though the scattering contribution of the carbon grains should be modeled according to the complete Porod's law, in the here presented patterns it should only appear as a Porod's final slope, i.e. like a simple power law. Thus, it has been modeled as follows:

$$I_{Porod} = AQ^{-n} + B \qquad (3)$$

where n is the Porod's exponent (whose value depends on the aspect ratio of the carbon grains), A is a scale factor and B is the flat background.
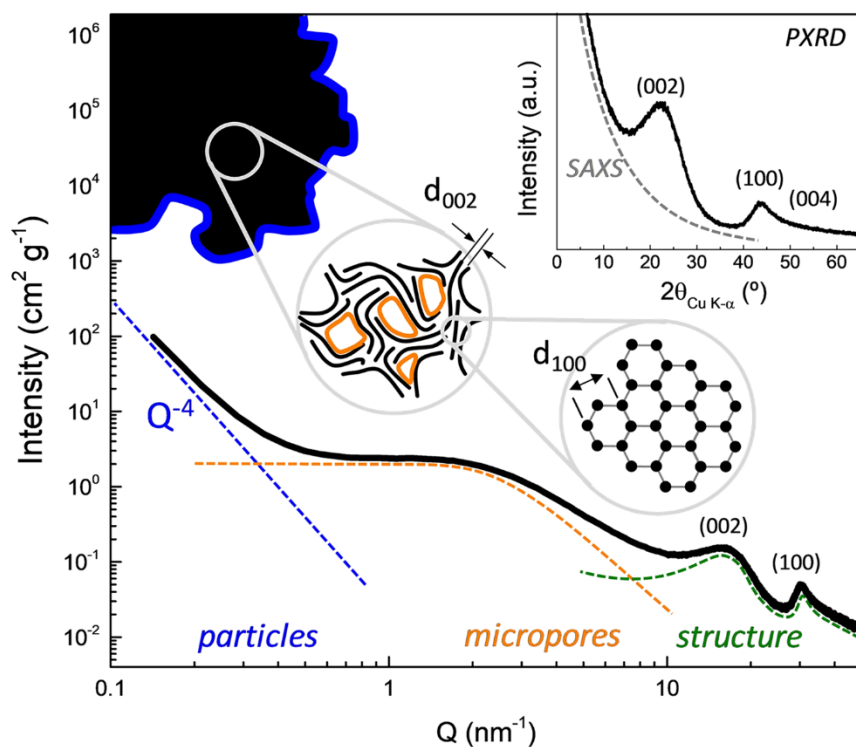
Figure 1. Characteristic SANS pattern in log-log scale of an AC, reported with schematic representations of the microstructural, microporous and macroscopic features, responsible for the scattered intensity in the large, intermediate and low Q ranges, respectively. The inset reports a linear scale representation of the same pattern as a function of the scattering angle 2θ as it is usually done for PXRD patterns. Adapted from ref. 20.

When dealing with AC samples featuring a large pore volume (like the samples here presented), effects due to pore-pore correlations caused by the high pore concentration should be taken into account. In the present work, we adopt the Teubner-Strey model for

microemulsions,[33-35] which describes a situation in which pores tend to locate themselves at an average pore-pore distance, thus making a broad peak appear at $Q_c = 2\pi/d$, d being the average pore-pore distance. This model, already successfully applied to analogous situations, models the scattered intensity of the micropores as:

$$I_{mp} = I_0 \frac{1}{a_2 + c_1 Q^2 + c_2 Q^4} + B \tag{4}$$

Where I_0, a_2, c_1 and c_2 are parameters defined as:

$$I_0 = 8\pi\phi_a(1 - \phi_a)(\Delta\rho)^2 c_2/\xi \tag{5}$$

$$a_2 = \left[1 + \left(\frac{2\pi\xi}{d}\right)^2\right]^2 \tag{6}$$

$$c_1 = -2\xi^2 \left(\frac{2\pi\xi}{d}\right)^2 + 2\xi^2 \tag{7}$$

$$c_2 = \xi^4 \tag{8}$$

where d is the pore-pore distance, ξ is a correlation length representative of the extension of the order, ϕ_a is the volume fraction of one of the two phases and $\Delta\rho$ is the contrast SLD. Within the Teubner-Strey model, a disorder parameter f_a can be defined as:

$$f_a = \frac{\left(1 - \left(\frac{2\pi\xi}{d}\right)^2\right)}{\left(1 + \left(\frac{2\pi\xi}{d}\right)^2\right)} \tag{9}$$

according to this definition, the parameter f_a can assume both positive and negative values, where the more positive is the assumed value, the more disordered will be the described system and vice versa.

Traditional models based on conventional diffraction cannot be applied in the case of WANS peaks of disordered carbons. Since the Lorentzian peak shape has been proven as an

effective functional form to fit the (002) peak of graphite in ACs for SAXS,[20] the same model has been adopted here. Importantly, Lorentzian peak broadening causes intensity not to vanish at low angle, entailing a Q^{-2} behavior at low angle which depends on the origin of the disorder in the carbon's microstructure (nano-crystallinity, crumpled layers, etc.).[20] Thus, the contribution to the scattered intensity in the WANS region has been modeled as:

$$I_{WANS} = A_P Q^{-n} + \frac{A_L}{1 + (|Q - Q_0|\xi)^m} + B \tag{11}$$

where A_P is the Porod's scale factor, n is the Porod's exponent, A_L is the Lorentzian scale factor, m the exponent of Q, ξ the Lorentzian correlation length, and B the flat background.

The non-linear fitting procedure was carried out within the SASview software (https://www.sasview.org/), using the Levenberg–Marquardt algorithm.

4.3 Results and discussion

4.3.1 Choice of the correct probe molecule

In order to identify the best suited probe molecule to assess the porosity of the ACs at issue, preliminary physisorption measurements were carried out on two samples (Cch and Cwa) with three different adsorptive: N_2, Ar and CO_2. For all cases, adsorption isotherms have been collected and the corresponding PSDs were inferred by means of NL-DFT. The results of the analysis are reported in Figure 2. N_2 and Ar adsorption isotherms (Figure 2A, 2C) apparently show minor differences, which are highlighted by the logarithmic scale (linear scale plots are available in Figure A2). Indeed, the BET SSA of the two samples is in agreement between N_2 (Table 2) and Ar (Table 3), with an expected slight overestimation ($\sim 5\%$) by the former.[36]

The PSD inferred from N_2, Ar and CO_2 isotherms for the samples Cwa and Cch, together with their relative cumulative pore volumes, are presented in Figure 2B, 2D. Though N_2 is

widely accepted as the routine probe for estimating the PSD of AC samples,[14,16,17,19,20] its "large" kinetic diameter (around 3.6 Å), its non-spheric shape and its weak quadrupole moment can lead to inaccurate PSDs, especially for ultra-microporous and strong adsorbents. Indeed, PSDs inferred from N_2 isotherms appear significantly different from the ones inferred from Ar isotherms. We attributed this discrepancy to the higher accuracy of the isotherms obtained with Ar, the latter being spheric and a smaller (kinetic diameter around 3.4 Å), less-interacting probe than N_2. Moreover, N_2-PDSs provide a strong overestimation ($\sim$ 80% for Cwa and $\sim$ 50% for Cch) of the total pore volume if compared to Ar (total pore volume values computed with the two probes are reported in Table A2). This observation can be explained in terms of the error arising from the unknown packing of a non-spherical adsorbate like N_2 in the micropores.[28,37] By employing CO_2 as a probe, thanks to its smaller kinetic diameter (around 3.3 Å), we enhanced the resolution on the smallest micropores, pointing out the existence of at least two families of ultra-micropores in each sample. However, CO_2-PSDs do not match perfectly with those obtained with Ar, probably due to the strong interaction existing between a strongly polar molecule like CO_2 and the carbon surface.

The presented analysis proves that, even though the BET SSA computed from N_2 and Ar isotherms is comparable, non-negligible differences appear when PSDs are inferred from the respective isotherms. Thus, we consider Ar sorption as our reference for further experiments.

Table 2. Parameters of the B.E.T. regression analysis for the N_2 adsorption isotherms at 77 K

	B.E.T. SSA (m^2/g)	Error (m^2/g)	C	Q_m (mmol/g)	R^2
Cwa	998	0.7	745	10.2	0.999999
Cch	1596	3.7	89	16.4	0.999984
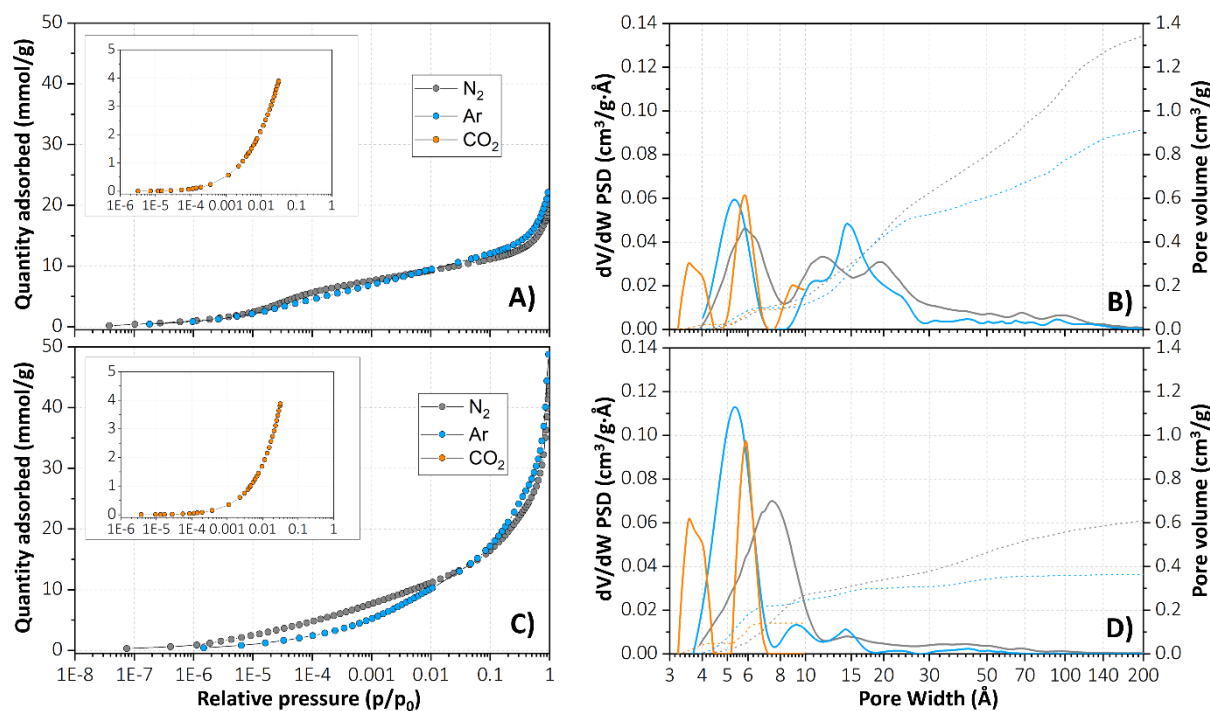
Figure 2. N_2 (grey), Ar (cyan) and CO_2 (orange) logarithmic scale adsorption isotherms (A, C) and corresponding PSDs (B, D) collected for the samples Cwa (A, B) and Cch (C, D) . The CO_2 isotherms in panels (A) and (C) are reported as insets. The width-weighted PSDs (left axis in panel (B) and (D)) are plotted as solid lines, while the corresponding cumulative pore volumes (right axis in panel (B) and (D)) are plotted as dotted lines.

4.3.2 Ar sorption analysis of porosity

After having demonstrated that Ar sorption is required to obtain trustable PSDs of ACs, Ar isotherms were collected for all the 5 samples at issue and the corresponding PSD were inferred. A series of differences between the five ACs can be deduced already from the logarithmic scale adsorption isotherms (Figure 3A, 3C, 3E) and the relative BET SSA (Table 3). Linear scale isotherms are available in Figure A3). The chemically activated samples (Cch and Cch-ox) depict a sensibly higher SSA with respect to the physically activated ones. On the other hand, physically activated ACs show themselves as stronger adsorbents, featuring BET C coefficients of around 500. Moreover, the diminished SSA featured by the oxidized samples (Cwa-ox and Cch-ox) with respect to their precursors (Cwa and Cch) suggests that the oxidation process with HNO_3 is triggering a SSA loss (of approximately 15% and 23%, respectively). By

looking at the comparison between the respective PSDs (Figure 3B for Cwa and Cwa-ox; Figure 3D for Cch and Cch-ox) insight on the nature of this loss can be accessed. Indeed, the oxidizing agent seem to have selectively reduced the abundance of different families of micro and mesopores, dependently on the sample. For the sample Cwa, the oxidation has selectively eroded the family of micropores at 5 Å, while mesopores (especially the three family between 10 and 30 Å) have been affected for the sample Cch. This last observation is consistent with the opposite modification in the C coefficient reported for the two samples upon oxidation: where mainly micropores (responsible for strong adsorption) have been consumed (from Cwa to Cwa-ox), the C coefficient decreases. On the contrary, since the Ar-PSD of Cch-ox seem to report a mild increment of the micro/mesopores ratio with respect to Cch, a slight increment in the C coefficient is observed.

Table 3. Parameters of the B.E.T. regression analysis for the Ar adsorption isotherms at 87 K

	B.E.T. SSA (m^2/g)	Error (m^2/g)	C	Q_m (mmol/g)	R^2
Cwa	948	2	575	11.0	0.999988
Cwa-ox	803	2	507	9.3	0.999990
Cch	1541	7	61	17.9	0.999921
Cch-ox	1182	3	85	13.7	0.999981
Cpa	855	3	446	9.9	0.999971

Lastly, Figure 3F shows a superposition of the PSDs of the unoxidized samples Cwa, Cch and Cpa. The samples Cwa and Cpa (featuring the same activation, but different origin) show a very similar PSD, differing only in the abundance of the micropore family at 5 Å. Even though the chemically activated sample (Cch) shows a less pronounced micropore family, it features an important mesoporous contribution (responsible of the increasement of the cumulative

pore volume from 15 Å up to 200 Å) which is lacking in the PSDs of Cwa and Cpa. This observation is a clear indication that it is the activation process, rather than the origin of the material, which directly determines the porosity of activated carbons.
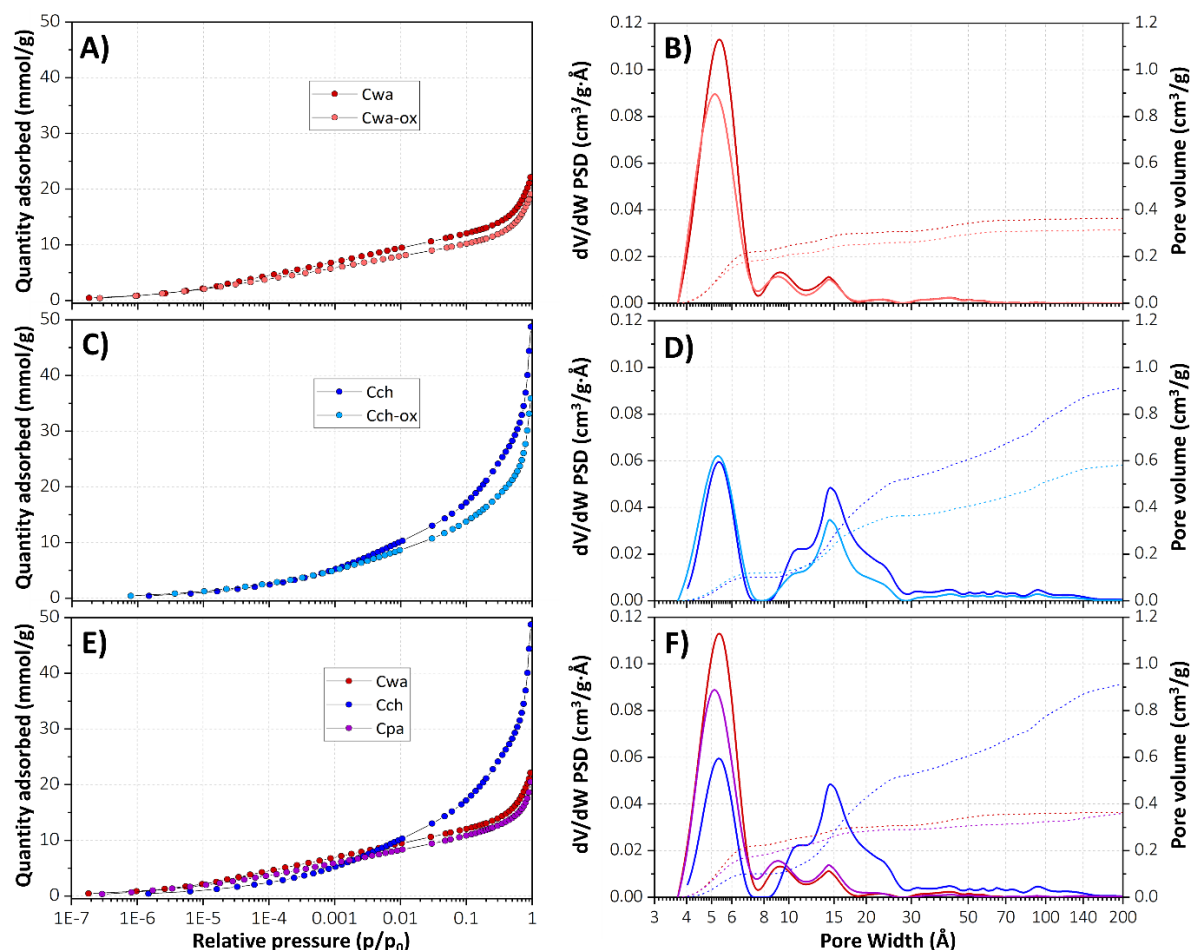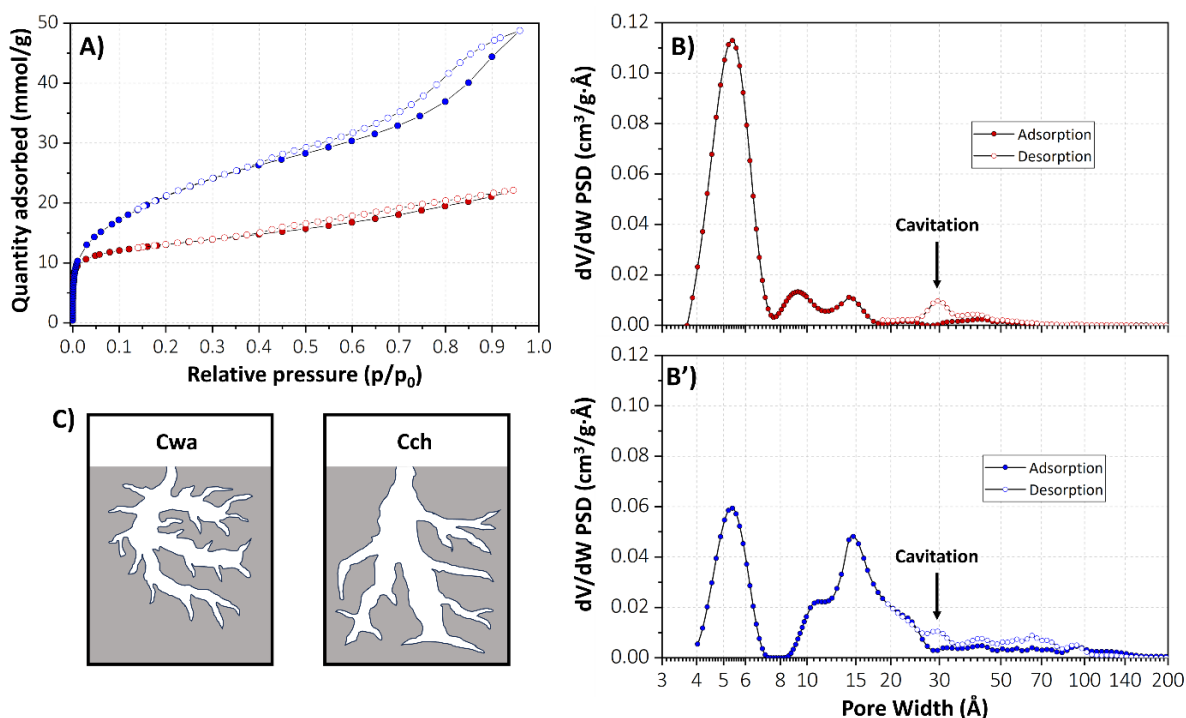

Figure 3. Ar adsorption isotherms (A, C, E) and corresponding PSDs (B, D, F) collected for the samples Cwa (red), Cwa-ox (pink), Cch (blue), Cch-ox (cyan) and Cpa (purple). Panels (A) and (B) report the comparison between Cwa and Cwa-ox, (C) and (D) between Cch and Cch-ox, (E) and (F) between Cwa, Cch and Cpa. The width-weighted PSDs (left axis in panel (B), (D) and (F)) are plotted as solid lines, while the corresponding cumulative pore volumes (right axis in panel (B), (D) and (F)) are plotted as dotted lines.

The linear scale isotherms of the samples Cwa and Cch (representative of the physically and chemically activated samples, respectively) and the relative PSDs evaluated both in adsorption and desorption are reported in Figure 4 (adsorption-desorption PSDs for the other

samples are available in Figure A3). Here, the linear scale is employed to put in evidence the isotherm type, together with the aspect of the desorption branch, pointing out the existence of a hysteresis loop. In both cases, the isotherms can be addressed as a composite Type I + Type II isotherm.[37–39] The Type I adsorption regime evidenced in the low p/p_0 region (up to 0.01 p/p_0) is ascribable to micropore adsorption, while the Type II adsorption regime observed in the rest of the isotherms (way more prominent for Cch rather than Cwa) is typical of meso- and macro-porous adsorbents.[37] This last behaviour is ascribable to samples featuring porosity on multiple dimensional scales (from the micro- to the meso-scale in this case). The difference in the two hysteresis loops, though both are mostly ascribable to the Type H2, confirms the higher mesoporous character of the sample Cch, suggesting a correlation between the chemical activation and the formation of mesopores in ACs.

If the presence of a hysteresis loop in the isotherm indicates the existence of "large" mesopores in the sample, a NL-DFT analysis of the desorption branch (i.e., evaluating the PSD of the sample through desorption data) can provide information regarding their nature and connectivity.[40] In particular, the presence of the artifact peaks in the desorption PSDs (Figure 4B for Cwa and in 3B' for Cch) is representative of the cavitation phenomenon: in not open-ended pores, several studies have shown[41–43] that if the pore neck diameter is smaller than a critical size ($\sim$ 5 - 6 nm), the mechanism of desorption from the larger pores involves the spontaneous nucleation and growth of gas bubbles in the metastable condensed fluid. In ACs samples, a situation like this can be imagined as if mesopores (or just a fraction of them) were accessible only through smaller micropores. A schematic representation of the thus obtained idea of pore connectivity in the two samples is given in Figure 4C.

Figure 4. Ar adsorption and desorption isotherms (A) and the respective PSDs (B, B') for the samples Cwa (red) and Cch (blue). Adsorption data are represented as full dots, while desorption data are represented as empty dots. Panel (C) reports a schematic view of the pore morphology that can be built after the presented Ar sorption analysis.

4.3.3 SANS analysis

The fit of the SANS patterns of the five mentioned samples in the range 0.06 Å^{-1} - 3 Å^{-1} is represented in Figure 5. A selection of notable parameters extracted from the fit is reported in Table 4. As can be proven by the small values of χ^2 (just for the sample Cpa it exceeds 1.5) the fit is in very good agreement with the experimental data, which validates the employed model in the selected Q range. All the fits are coherent with a slope ascribable to the Porod's Law for Q < 0.1 Å^{-1}, a broad peak due to the micropores at 0.2-0.3 Å^{-1} and a Lorentzian peak due to the d_{002} of the stacked graphitic layers at 1.7-1.8 Å^{-1}.

Generally, a Porod's exponent larger than 3 corresponds to a slope regime due to the scattering by interfaces.[29] In this case, being the values of this exponent close to 3, this could

122

correspond to scattering from surface fractals, suggesting that the carbon grains could expose a jagged surface. This last observation is in agreement with a Scanning Electron Microscopy (SEM) investigation presented within a former study of our team (see Figure 1 and the related discussion in ref. 13).

According to the information available at this stage, the only accessible data regarding the pore size of the investigated samples is that it cannot exceed the half of the average pore-pore distance ($\sim$ 30 Å and $\sim$ 50 Å for the physically and chemically activated samples, respectively). These values, indicating a pore size of $\sim$ 25 Å maximum, confirm that only the micropores are responsible for the scattered intensity in this range. The disorder parameter f_a, whose effect on the pore network is exemplified in Figure 5F, is found to be systematically different between samples of chemical ($\sim$ 0.2) and physical activation ($\sim$ -0.3). This suggests that the pores tend to exhibit some degree of short range pore-pore ordering, pointing out the existence of pore-pore repulsion (i.e., the pores tend to be created far away from each other upon activation, rather than agglomerate).[20] The lower degree of order observed for chemically activated samples is consistent with the higher mesoporous character of Cch and Cch-ox, in which the complex micropore-mesopore connectivity could result in increasing the disorder of the system. Summing up, the fact that the pores of the investigated samples can be described as a discontinuous structure with characteristic and quasi-repetitive length scale needs to be reconciled with the widely accepted conception of the slit-like pore in ACs. In this respect, a deeper study is required to understand which form factor could best suit the experimental data, aimed to exploring the suitability of different pore shapes to describe the porosity.
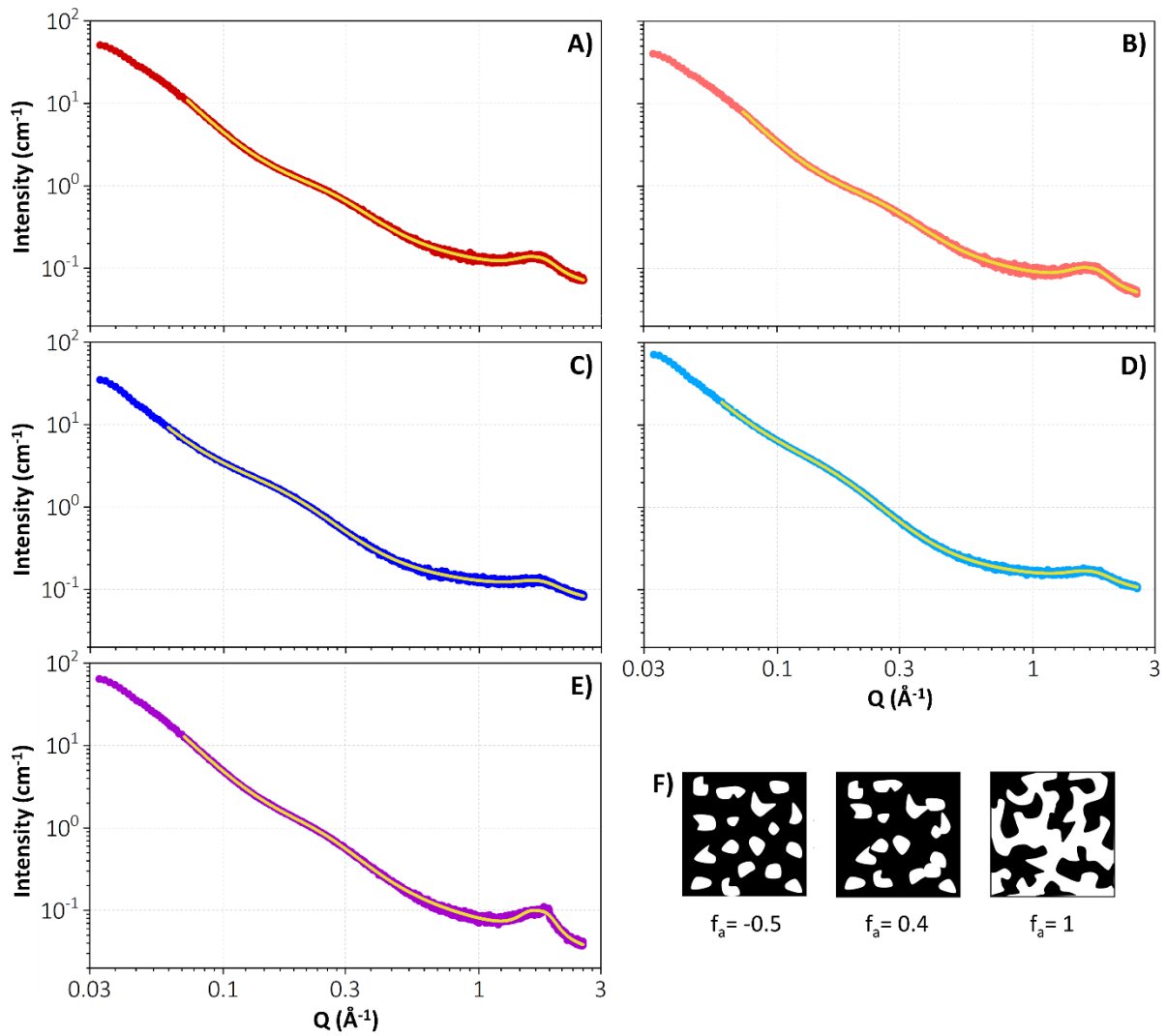
Figure 5. Fit of the SANS patterns of the samples Cwa (A), Cwa-ox (B), Cch (C), Cch-oc (D) and Cpa (E). The calculated pattern is represented as a yellow line, while the experimental data are represented as scatter plots. Panel (F) represents a schematic representation of the micropore arrangement as a function of the order parameter f_a (adapted from ref. 20).

Speaking of the Lorentzian Q range, The reported width of the (002) peak is significantly larger than what reported for graphite ($\sim$ 3.38 Å[30] against an average value of around 3.7 Å for the samples here presented) indicating the disordered nature of the microstructure of the samples. Moreover, as reported in ref. 20, the fully Lorentzian peak shape observed suggests that the broadening is due to the carbon layers curvature rather than to the existence of nano-crystallites. This study is, thus, a further challenge to the traditional

model of pseudo-graphitic nano-crystallites initially proposed by Franklin[44] and still routinely used nowadays to describe the microstructure of the non-graphitic carbons. Since all the studied samples present the same features under this aspect, it seems that a nano-curved layered structure is general feature of ACs, independent on the nature of the activation. Notably, the sample Cpa seem to feature an additional sharp peak in the WANS region (not fitted), which could be probably due to a residual amount of graphite left after the activation step.

Table 4. Morphological and structural parameters deduced from the SANS fit analysis presented in Figure 4.

n_P is the exponent of the porod function in the high-Q range, d is the average pore-pore distance, ξ_{mp} the length beyond which the order of the micropores is lost, f_a the order parameter, r the micropore radius, ξ_L the length beyond which the order in the (002) distance is lost.

	n_P	d (Å)	ξ_{mp} (Å)	f_a	ξ_L (Å)	d_{002} (Å)	χ^2
Cwa	3.2	27.6	5.7	-0.26	2.80	3.76	1.25
Cwa-ox	3.2	28.3	5.7	-0.24	2.78	3.78	1.13
Cch	3.1	50.7	6.5	0.21	2.31	3.71	1.15
Cch-ox	3.0	53.9	7.4	0.14	2.41	3.80	1.23
Cpa	3.1	30.2	6.6	-0.31	3.32	3.67	3.35

To gather further information regarding pore accessibility, contrast matching measurements with D_2O have been performed for all the five samples. Results of the contrast matching experiments for sample Cch are presented in Figure 6. The impregnation of D_2O in just the first fraction of pore volume of the sample (light blue pattern in Figure 5) has led to a shift of the broad peak (I_{mp}) towards lower Q values. This suggests the existence of at least two micropore families, the smaller being completely filled by D_2O and thus its contribution suppressed. Conversely, higher levels of D_2O filling (cyan and grey pattern in Figure 5) has led to a complete suppression of the contribution of the micropores, indicating that the totality of

the pore volume is accessible. However, the analysis of these patterns is still ongoing and thus they will not be discussed further in this section.
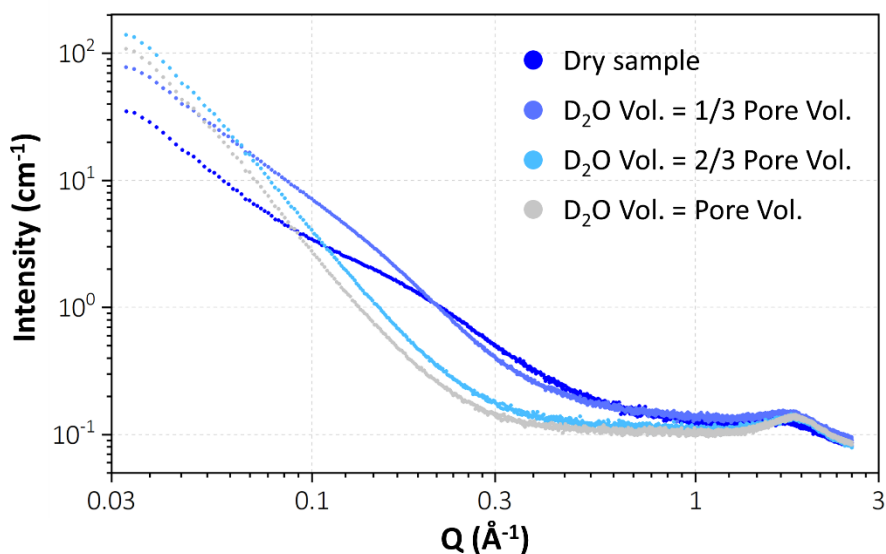
Figure 6. SANS patterns of the sample Cch at different D_2O filling level.

4.4 Conclusions

ACs are a wide class of functional materials, whose popularity is not only confined to catalysis, but extends also to hydrogen storage, electrochemical cells, etc. Since a general agreement on their structural and morphological features on the micro- and meso-scale is yet to be achieved, trying to bridge this gap of knowledge is of extreme importance.

In this chapter, a characterization of the micro-/meso- structure and porosity of five AC samples of different origin and activation has been presented. The study has been carried out through the coupling of two independent techniques (N_2, Ar, CO_2 physisorption and SANS) which have been able to provide key complementary information on the investigated systems. First of all, by carrying out N_2 and Ar physisorption measurements (at 77 and 87 K, respectively) on the two model samples, we have been able to highlight that, despite the good agreement between the BET SSA evaluated with the two probes, N_2 isotherms are not suited to a correct

characterization of the porosity of ACs. Indeed, besides the sensible difference observed in the two PSDs, we reported that N_2 can overestimate the total pore volume of up to 80% with respect to Ar (probably due to its non-spheric and quadrupolar nature). By inferring PSDs from 273K CO_2 isotherms we have been able to point out the existence of diverse families of ultra-micropores in our samples. However, we documented a mild mismatch observed between CO_2- and Ar-PSDs, most likely due to the reactive nature of the former. The following characterization of the ACs porosity through Ar sorption allowed us to document a SSA loss of around 20% entailed by the oxidation process with HNO_3, which we correlated with a selective erosion of different pore families in the two samples (micropores for Cwa and mesopores for Cch). Parallelly, we observed a consistency between PSDs of samples sharing the same activation procedure, regardless of their origin, thus confirming the central role of the activation in determining the porosity of ACs. By a NL-DFT analysis of the desorption branch of Ar-isotherms, we testified the occurrence of the cavitation phenomenon in correspondence of the hysteresis loop, thus pointing to a pore connectivity in which a fraction of mesopores is only accessible through small micropores.

Subsequently, a preliminary analysis of the fit of the SANS patterns collected under inert atmosphere has been discussed. The analysis suggests that the porosity of the investigated samples is ascribable to a discontinuous structure featuring some degree of short-range order, which is different between physically and chemically activated samples (probably due to their different mesoporous character). The peak shape analysis of the stacking (002) peak in the WANS region is consistent with a broadening due to the carbon layers curvature, thus further challenging the idea of ACs as an ensemble of randomly-oriented nano-crystallites. Lastly, even though the analysis of the SANS patterns collected under partial D_2O filling is still at its very first stages, it has already provided promising insights. It is worth noting

127

that, since the kinetic diameter of D_2O is extremely small (2.65 Å), it can have access to the families of ultra-micropores whose existence has been documented is section 3.1 by means of CO_2-PSDs. Given the documented unsuitability of CO_2-PSDs to accurately characterize the ultra-micropores of strong adsorbents rich of surface functional groups like ACs, the existence of an alternative probe useful to provide insights on micropores of this size is crucial. Indeed, the main application of ACs (like hydrogen storage materials and supports for hydrogenation catalysis) involve the adsorption of hydrogen, which, featuring a small kinetic diameter (2.89 Å), is able to access even pores of the smallest sizes.

As outlined in the previous section, the presented fit analysis of the acquired SANS patterns is still at a preliminary stage and will be completed in the incoming months. Among the many challenges that this procedure entails, the most important will be the exploration of different models to take into account the form factor of the micropores. Besides exploiting SANS to provide an independent estimation of the pore size to be compared with what obtained through Ar sorption, this investigation will also allow to assess the suitability of different pore shapes, giving the possibility to challenge the classical slit-like assumption. Since this exploration will entail the application of a huge number of different fitting models, we are planning to adopt an *a posteriori* evaluation of their performances based on the Bayesian inference. Once established a solid fitting procedure, a second challenge will be the fitting the data acquired for the D_2O-filled samples. Though not trivial, this analysis has the potential of providing key information on the pore accessibility on the whole dimensional scale, which could have a non-negligible impact on crucial aspects of material sciences, like hydrogen storage and hydrogenation catalysis.

References

(1)   González-García, P. Activated Carbon from Lignocellulosics Precursors: A Review of the Synthesis Methods, Characterization Techniques and Applications. *Renew. Sustain. Energy Rev.* **2018**, *82* (August 2017), 1393–1414. https://doi.org/10.1016/j.rser.2017.04.117.

(2)   Auer, E.; Freund, A.; Pietsch, J.; Tacke, T. Carbons as Supports for Industrial Precious Metal Catalysts. *Appl. Catal. A Gen.* **1998**, *173* (2), 259–271. https://doi.org/10.1016/S0926-860X(98)00184-7.

(3)   *Carbon Materials for Catalysis*; Serp, P., Figueiredo, J. L., Eds.; Wiley, 2008. https://doi.org/10.1002/9780470403709.

(4)   Fierro, V.; Torné-Fernández, V.; Montané, D.; Celzard, A. Adsorption of Phenol onto Activated Carbons Having Different Textural and Surface Properties. *Microporous Mesoporous Mater.* **2008**, *111* (1–3), 276–284. https://doi.org/10.1016/j.micromeso.2007.08.002.

(5)   Rodríguez-Reinoso, F. Production and Applications of Activated Carbons. In *Handbook of Porous Solids*; Wiley, 2002; Vol. 3, pp 1766–1827. https://doi.org/10.1002/9783527618286.ch24a.

(6)   Sircar, S.; Golden, T. C.; Rao, M. B. Activated Carbon for Gas Separation and Storage. *Carbon N. Y.* **1996**, *34* (1), 1–12. https://doi.org/10.1016/0008-6223(95)00128-X.

(7)   Moreno-Castilla, C.; Carrasco-Marín, F.; Mueden, A. The Creation of Acid Carbon Surfaces by Treatment with (NH4)2S2O8. *Carbon N. Y.* **1997**, *35* (10–11), 1619–1626. https://doi.org/10.1016/S0008-6223(97)00121-8.

(8)   Silva, A. M. T.; Machado, B. F.; Figueiredo, J. L.; Faria, J. L. Controlling the Surface

Chemistry of Carbon Xerogels Using HNO3-Hydrothermal Oxidation. *Carbon N. Y.*

2009, *47* (7), 1670–1679. https://doi.org/10.1016/j.carbon.2009.02.022.

(9)   Bhatnagar, A.; Hogland, W.; Marques, M.; Sillanpää, M. An Overview of the

Modification Methods of Activated Carbon for Its Water Treatment Applications.

Chem. Eng. J. **2013**, *219*, 499–511. https://doi.org/10.1016/j.cej.2012.12.038.

(10)   Rodrigues, R.; Gonçalves, M.; Mandelli, D.; Pescarmona, P. P.; Carvalho, W. A. Solvent-

Free Conversion of Glycerol to Solketal Catalysed by Activated Carbons Functionalised

with Acid Groups. *Catal. Sci. Technol.* **2014**, *4* (8), 2293–2301.

https://doi.org/10.1039/c4cy00181h.

(11)   Girgis, B. S.; Yunis, S. S.; Soliman, A. M. Characteristics of Activated Carbon from

Peanut Hulls in Relation to Conditions of Preparation. *Mater. Lett.* **2002**, *57* (1), 164–

172. https://doi.org/10.1016/S0167-577X(02)00724-3.

(12)   Miguel, G. S.; Fowler, G. D.; Dall'Orso, M.; Sollars, C. J. Porosity and Surface

Characteristics of Activated Carbons Produced from Waste Tyre Rubber. *J. Chem.*

Technol. Biotechnol. **2002**, *77* (1), 1–8. https://doi.org/10.1002/jctb.518.

(13)   Lazzarini, A.; Piovano, A.; Pellegrini, R.; Leofanti, G.; Agostini, G.; Rudić, S.; Chierotti,

M. R.; Gobetto, R.; Battiato, A.; Spoto, G.; Zecchina, A.; Lamberti, C.; Groppo, E. A

Comprehensive Approach to Investigate the Structural and Surface Properties of

Activated Carbons and Related Pd-Based Catalysts. *Catal. Sci. Technol.* **2016**, *6* (13),

4910–4922. https://doi.org/10.1039/c6cy00159a.

(14)   Vottero, E.; Carosso, M.; Jiménez-Ruiz, M.; Pellegrini, R.; Groppo, E.; Piovano, A. How

Do the Graphenic Domains Terminate in Activated Carbons and Carbon-Supported Metal Catalysts? *Carbon N. Y.* **2020**, *169*, 357–369. https://doi.org/10.1016/j.carbon.2020.07.033.

(15) Vottero, E.; Carosso, M.; Pellegrini, R.; Piovano, A.; Groppo, E. Assessing the Functional Groups in Activated Carbons through a Multi-Technique Approach. *Catal. Sci. Technol.* **2022**, *12* (4), 1271–1288. https://doi.org/10.1039/d1cy01751a.

(16) Prehal, C.; Grätz, S.; Krüner, B.; Thommes, M.; Borchardt, L.; Presser, V.; Paris, O. Comparing Pore Structure Models of Nanoporous Carbons Obtained from Small Angle X-Ray Scattering and Gas Adsorption. *Carbon N. Y.* **2019**, *152*, 416–423. https://doi.org/10.1016/j.carbon.2019.06.008.

(17) Jagiello, J.; Olivier, J. P. Carbon Slit Pore Model Incorporating Surface Energetical Heterogeneity and Geometrical Corrugation. *Adsorption* **2013**, *19* (2–4), 777–783. https://doi.org/10.1007/s10450-013-9517-4.

(18) Harris, P. J. F. Fullerene-like Models for Microporous Carbon. *J. Mater. Sci.* **2013**, *48* (2), 565–577. https://doi.org/10.1007/s10853-012-6788-1.

(19) Kurig, H.; Russina, M.; Tallo, I.; Siebenbürger, M.; Romann, T.; Lust, E. The Suitability of Infinite Slit-Shaped Pore Model to Describe the Pores in Highly Porous Carbon Materials. *Carbon N. Y.* **2016**, *100* (2016), 617–624. https://doi.org/10.1016/j.carbon.2016.01.061.

(20) Saurel, D.; Segalini, J.; Jauregui, M.; Pendashteh, A.; Daffos, B.; Simon, P.; Casas-Cabanas, M. A SAXS Outlook on Disordered Carbonaceous Materials for Electrochemical Energy Storage. *Energy Storage Mater.* **2019**, *21* (May), 162–173.

https://doi.org/10.1016/j.ensm.2019.05.007.

(21) Wu, Z.; Xing, X. Small Angle X-Ray Scattering and Its Applications. In *Synchrotron Radiation Applications*; WORLD SCIENTIFIC, 2017; pp 225–285. https://doi.org/doi:10.1142/9789813227675_0007.

(22) Fratzl, P. Small-Angle Scattering in Materials Science - A Short Review of Applications in Alloys, Ceramics and Composite Materials. *J. Appl. Crystallogr.* **2003**, *36* (3 I), 397–404. https://doi.org/10.1107/S0021889803000335.

(23) Hollamby, M. J. Practical Applications of Small-Angle Neutron Scattering. *Phys. Chem. Chem. Phys.* **2013**, *15* (26), 10566–10579. https://doi.org/10.1039/c3cp50293g.

(24) Hammouda, B. Insight into the SANS Technique. *Natl. Inst. Stand. Technol.* **2008**, 1–717.

(25) Pellegrini, R.; Leofanti, G.; Agostini, G.; Groppo, E.; Rivallan, M.; Lamberti, C. Pd-Supported Catalysts: Evolution of Support Porous Texture along Pd Deposition and Alkali-Metal Doping. *Langmuir* **2009**, *25* (11), 6476–6485. https://doi.org/10.1021/la900084p.

(26) MATTEO, C. V. A. C. L. G. S. A KIT FOR VOLUMETRIC MEASUREMENTS OF GAS ADSORPTION. 2021. https://www.sumobrain.com/patents/WO2021181211A1.html.

(27) Brunauer, S.; Emmett, P. H.; Teller, E. Adsorption of Gases in Multimolecular Layers. *J. Am. Chem. Soc.* **1938**, *60* (2), 309–319. https://doi.org/10.1021/ja01269a023.

(28) Rouquerol, J.; Llewellyn, P.; Rouquerol, F. Is the BET Equation Applicable to Microporous Adsorbents? *Stud. Surf. Sci. Catal.* **2007**, *160*, 49–56. https://doi.org/10.1016/s0167-2991(07)80008-5.

(29) Hammouda, B. Probing Nanoscale Structures – the sans Toolbox; 2008.

(30) Mileeva, Z.; Ross, D. K.; Wilkinson, D.; King, S. M.; Ryan, T. A.; Sharrock, H. The Use of Small Angle Neutron Scattering with Contrast Matching and Variable Adsorbate Partial Pressures in the Study of Porosity in Activated Carbons. *Carbon N. Y.* **2012**, *50* (14), 5062–5075. https://doi.org/10.1016/j.carbon.2012.06.046.

(31) Piovano, A.; Ricchebuono, A.; Vottero, E.; Cristiglio, V. Micropore Structure of Activated Carbon of Different Origin. *Inst. Laue-Langevin* **2023**. https://doi.org/https://doi.ill.fr/10.5291/ILL-DATA.TEST-3271.

(32) Piovano, A.; Ricchebuono, A.; Schweins, R. Unrevealing the Meso- and Micro-Structure of Activated Carbons for Catalysis. *Inst. Laue-Langevin* **2021**. https://doi.org/https://doi.ill.fr/10.5291/ILL-DATA.EASY-970.

(33) Teubner, M.; Strey, R. Origin of the Scattering Peak in Microemulsions. *J. Chem. Phys.* **1987**, *87* (5), 3195–3200. https://doi.org/10.1063/1.453006.

(34) Schubert, K. V.; Strey, R.; Kline, S. R.; Kaler, E. W. Small Angle Neutron Scattering near Lifshitz Lines: Transition from Weakly Structured Mixtures to Microemulsions. *J. Chem. Phys.* **1994**, *101* (6), 5343–5355. https://doi.org/10.1063/1.467387.

(35) Endo, H.; Mihailescu, M.; Monkenbusch, M.; Allgaier, J.; Gompper, G.; Richter, D.; Jakobs, B.; Sottmann, T.; Strey, R.; Grillo, I. Effect of Amphiphilic Block Copolymers on the Structure and Phase Behavior of Oil-Water-Surfactant Mixtures. *J. Chem. Phys.* **2001**, *115* (1), 580–600. https://doi.org/10.1063/1.1377881.

(36) Datar, A.; Yoon, S.; Lin, L. C.; Chung, Y. G. Brunauer–Emmett–Teller Areas from Nitrogen and Argon Isotherms Are Similar. *Langmuir* **2022**, *38* (38), 11631–11640.

https://doi.org/10.1021/acs.langmuir.2c01390.

(37)   Thommes, M.; Kaneko, K.; Neimark, A. V.; Olivier, J. P.; Rodriguez-Reinoso, F.;

Rouquerol, J.; Sing, K. S. W. Physisorption of Gases, with Special Reference to the

Evaluation of Surface Area and Pore Size Distribution (IUPAC Technical Report). *Pure*

Appl. Chem. **2015**, *87* (9–10), 1051–1069. https://doi.org/10.1515/pac-2014-1117.

(38)   Lowell, S.; Shields, J. E.; Thomas, M. A.; Thommes, M. *Characterization of Porous*

Solids and Powders: Surface Area, Pore Size and Density; Particle Technology Series;

Springer Netherlands: Dordrecht, 2004; Vol. 16. https://doi.org/10.1007/978-1-4020-

2303-3.

(39)   Sing, K. S. W. Reporting Physisorption Data for Gas/Solid Systems with Special

Reference to the Determination of Surface Area and Porosity (Recommendations

1984). *Pure Appl. Chem.* **1985**, *57* (4), 603–619.

https://doi.org/10.1351/pac198557040603.

(40)   Schlumberger, C.; Thommes, M. Characterization of Hierarchically Ordered Porous

Materials by Physisorption and Mercury Porosimetry—A Tutorial Review. *Adv. Mater.*

Interfaces **2021**, *8* (4). https://doi.org/10.1002/admi.202002181.

(41)   Thommes, M.; Cychosz, K. A. Physical Adsorption Characterization of Nanoporous

Materials: Progress and Challenges. *Adsorption* **2014**, *20* (2–3), 233–250.

https://doi.org/10.1007/s10450-014-9606-z.

(42)   Monson, P. A. Understanding Adsorption/Desorption Hysteresis for Fluids in

Mesoporous Materials Using Simple Molecular Models and Classical Density

Functional Theory. *Microporous Mesoporous Mater.* **2012**, *160*, 47–66.

https://doi.org/10.1016/j.micromeso.2012.04.043.

(43)   Landers, J.; Gor, G. Y.; Neimark, A. V. Density Functional Theory Methods for

Characterization of Porous Materials. *Colloids Surfaces A Physicochem. Eng. Asp.* **2013**,

437, 3–32. https://doi.org/10.1016/j.colsurfa.2013.01.007.

(44)   Franklin, R. E.; A, P. R. S. L. Crystallite Growth in Graphitizing and Non-Graphitizing

Carbons. *Proc. R. Soc. London. Ser. A. Math. Phys. Sci.* **1951**, *209* (1097), 196–218.

https://doi.org/10.1098/rspa.1951.0197.

Appendix
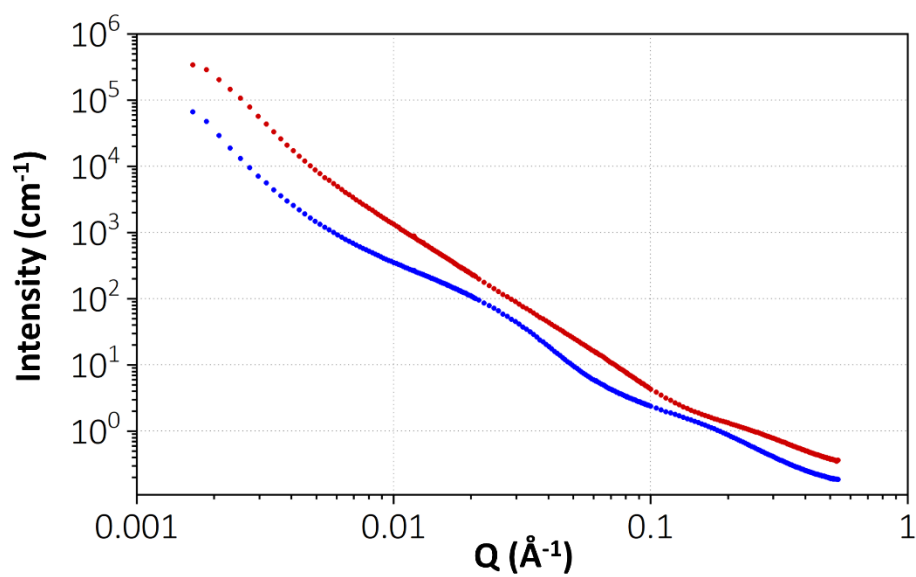
Figure A1. Low-Q SANS patterns of the samples Cwa (red) and Cch (blue) collected on the D11 beamline at the ILL. The measurements were affected by multiple scattering in the low-Q region due to the excessive thickness of the samples, which hampers a fine discussion on the obtained results.

Table A1. Root Mean Square Error (RMSE) and Regularization (R) values obtained from the NL-DFT fit of the N_2, Ar and CO_2 isotherms.

|	N_2		Ar				CO_2	
	R	RMSE (mmol/g)	R_{ads}	$RMSE_{ads}$ (mmol/g)	R_{des}	$RMSE_{des}$ (mmol/g)	R	RMSE (mmol/g)
Cwa	0.1	0.057	0.2	0.028	0.316	0.037	0.1	0.018
Cch	0.1	0.103	0.2	0.057	0.316	0.059	0.1	0.008
Cwa-ox			0.2	0.016	0.316	0.034		
Cch-ox			0.2	0.037	0.316	0.052		
Cpa			0.2	0.020	0.316	0.030		
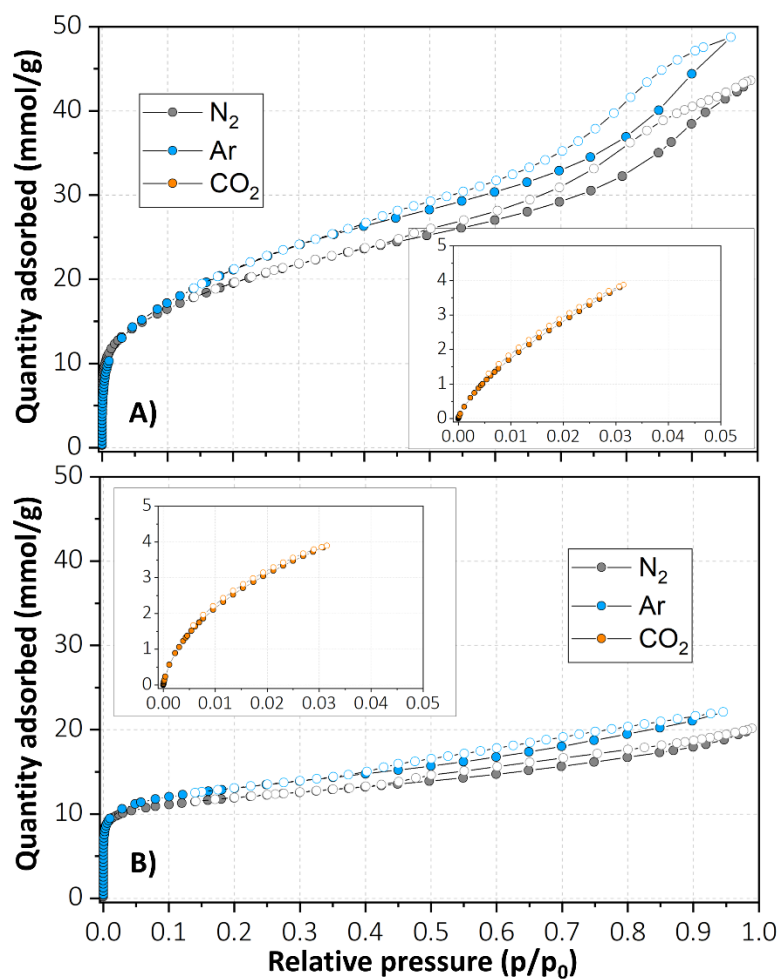
Figure A2. N_2 (grey), Ar (cyan) and CO_2 (orange) adsorption and desorption isotherms collected for the samples Cwa (A) and Cch (B). The CO_2 isotherms are reported as insets. Adsorption data are reported as full dots, desorption data as empty dots.

Table A2. Total Pore Volume of the five AC samples measured from Ar-PSDs.

	Cwa	Cwa-ox	Cch	Cch-ox	Cpa
Total Pore Volume (N_2) (cm³/g)	0.66	- - -	1.42	- - -	- - -
Total Pore Volume (Ar) (cm³/g)	0.36	0.31	0.93	0.58	0.36
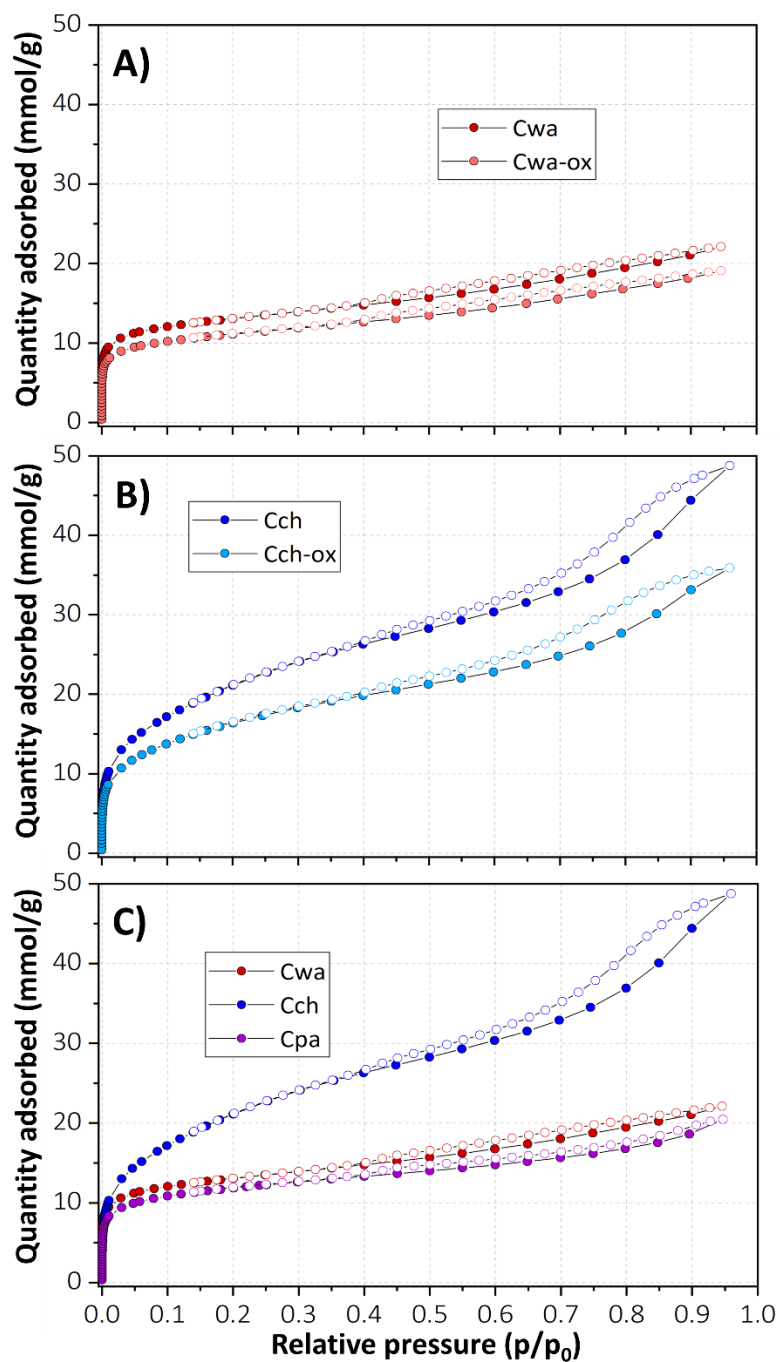
Figure A3. Ar adsorption and desorption isotherms collected for the samples Cwa (red), Cwa-ox (pink), Cch (blue), Cch-ox (cyan) and Cpa (purple). The panels report the comparison between Cwa and Cwa-ox (A), between Cch and Cch-ox (B), and between Cwa, Cch and Cpa (C). Adsorption data are reported as full dots, desorption data as empty dots.
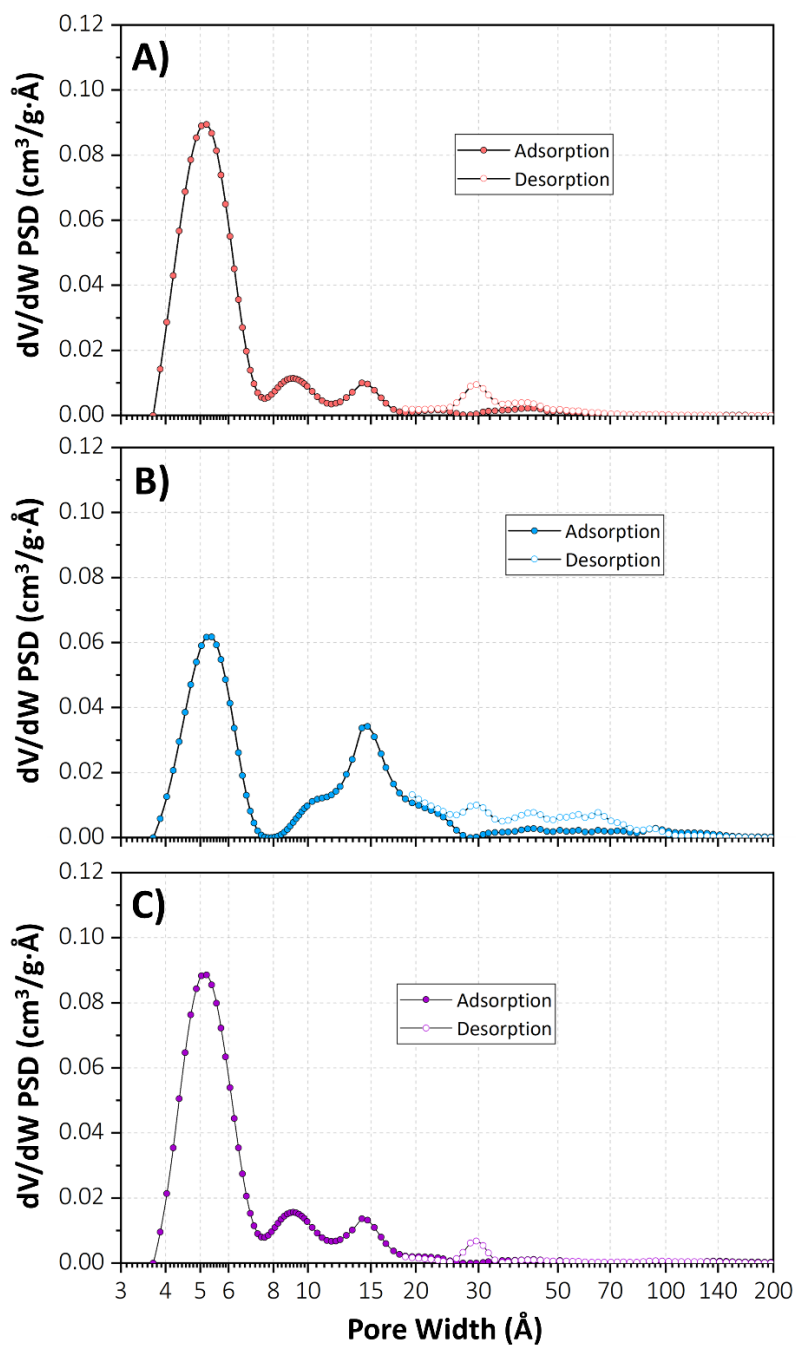
Figure A3. Ar adsorption and desorption PSDs inferred for the samples Cwa-ox (A), Cch-ox (B) and Cpa (C). Adsorption data are reported as full dots, desorption data as empty dots.

Chapter 5

General conclusions and perspectives

This thesis work is a result of a long-lasting collaboration between the University of Torino, the Institute Laue Langevin (ILL) in Grenoble (F) and the Chimet S.p.A. company, which in the last 20 years has contributed to several important advances in the field of characterization of heterogeneous catalysts based on supported metal nanoparticles, mainly Pd and Pt. Through the years, the key to this success has been always the wise application of a multi-technique approach to the same set of catalysts, in which multiple experimental methodologies have been employed together to unravel the properties of these complex systems at a molecular scale. The most important part of my PhD's work has been devoted to extending this paradigm to new experimental methods and, for the first time in this research group, to couple experiments with computational simulation. The latter have been conducted in the frame of a collaboration with the IFP Energies Nouvelles of Lyon, which granted me the possibility of spending 6 months onsite during the 2021/2022 academic year. There, I had the possibility to learn how to apply advanced computational tools to the simulation of the atomistic properties of metal NPs under the supervision of Dr. Céline Chizallet, thus adding molecular modelling to the panel of employed techniques.

This work is also a paradigmatic example of a multi-scale investigation. Indeed, the scale and the complexity of the targeted systems grow from Chapter 2, where a full

computational study on isolated Pt NPs is presented, to Chapter 3, in which real Pd/Al$_2$O$_3$ catalysts are addresses focusing on their interaction with adsorbates. Lastly, Chapter 4 is focused on the properties of activated carbons, addressing their structure and porosity from the micro- to the meso-scale.

In these years, I have been able to explore and, finally, master an unusual amount of experimental techniques, both in the laboratories of the Chemistry Department at the University of Turin and at several large-scale facilities (ESRF and ILL in Grenoble, F, and SLS in Villigen, CH), as follows.

- **FT-IR spectroscopy (of adsorbed molecules).** It is a vibrational spectroscopy extremely sensitive to vibrations entailing an oscillation of the dipole moment of the oscillators (e.g., functional groups and chemical bonds) at issue. Application of FT-IR spectroscopy in the mid-infrared (4200 − 200 cm^{-1}) region allows to monitor the surface of the catalysts through the perturbation inferred to molecular probes upon adsorption. In this sense, FT-IR spectroscopy is an indirect technique for the characterization of heterogeneous catalysts, which can grant insight on complex surface phenomena, even under reaction conditions.

- **Gas-volumetry.** Gas adsorption monitored by volumetric measurements is still one of the most employed techniques in the characterization of materials. In the case of physisorption of inert probes it allows assessing textural properties and porosity, by covering the complete range of micro- (pore width < 2 nm), meso- (pore width: 2–50 nm), and to some extent even macropores (pore width > 50 nm). In this respect, a central role is covered by the inference of the Pore Size Distribution from the experimental adsorption isotherms (by means, for example, of NL-DFT). In the case of

chemisorption, gas-volumetry can be adopted to gather quantitative information on the surface of the catalysts.

- **Adsorption microcalorimetry.** This technique allows a quantitative measurement of the heat evolved when a fluid (gas or vapour) gets in contact with the surface of a material, which is intimately related to the nature and energy of the interaction between adsorbed species and the surface itself. In this way, adsorption microcalorimetry can provide knowledge of the energetics of chemical and physical events occurring at catalytic interfaces, as well as of the associated thermodynamic parameters, contributing to a deeper understanding of the underlying phenomena.

- **Small Angle Neutron Scattering (SANS).** SANS is a small angle scattering technique, which grants access to topological information at the micro- and meso-scale both for crystalline and amorphous samples. In this frame, it can be exploited to extract information concerning the morphology of solid materials, allowing to take into account non-traditional descriptors of porosity. Working with neutrons has the peculiarity of (1) granting a high sensitivity for "light" atoms like H and C (complementary to x-ray scattering) and (2) allowing a study of pore accessibility by adopting the contrast matching technique (i.e., filling the accessible pores with a fluid featuring the same Scattering Length Density of the material matrix).

- **Inelastic Neutron Scattering (INS).** INS spectroscopy is an unconventional vibrational spectroscopy which, thanks to the employment of neutrons, is not subject to any selection rule. In this sense, it provides a complementary alternative to IR spectroscopy since it allows to detect vibrations of molecules and functional groups that do not entail oscillations in the dipole moment. Given its enhanced sensitivity towards the atomic

and molecular hydrogen, it allows to monitor the vibrations of metal hydrides, thus allowing to deepen the comprehension of their complex catalytic behaviour.

- **High-energy X-ray Diffraction (XRD) and Pair Distribution Function (PDF).** Powder XRD is a useful tool to characterize catalytic materials, since it can provide information regarding the long-range order of the atoms in the sample. By exploiting a high brilliance x-ray source (like most existing synchrotrons) the sensitivity gain that can be provided by the most advanced facilities is so high that adsorbate-induced structural modifications in metal NPs of a few nanometres can be observed. When high-energy X-ray total scattering data are collected, a PDF analysis can be performed. This method is an emerging structural characterization tool with the potential to provide valuable insights into a broad range of problems in heterogeneous catalysis. The method yields atomic scale structural information with crystallographic resolution, without the need for long-range order, which is implicit in conventional Bragg diffraction. Accordingly, it can be used to study the nanoscale systems and/or the defect-rich materials often involved in heterogeneous catalysis.

- **X-ray Absorption Spectroscopy (XAS).** Among the methods that can provide insight on the structural environment and electronic properties of active sites in catalytic materials, synchrotron-based XAS has become one of the techniques of choice due to its excellent spatial, temporal, and energy resolutions. In the extended X-ray absorption fine structure (EXAFS) region, information about the local structural environment of the X-ray absorbing atom is extracted from the fine structure oscillations of the absorption coefficient. The X-ray absorption near-edge structure (XANES) portion of the XAS signal contains, instead, information about the electronic structure, density of unoccupied states, and bonding geometry around the absorbing atom. Since XAS does

not require long-range order and it can be employed to monitor adsorbate-induced structural changes in heterogeneous catalysts, it is considerable as a complementary technique with respect to the PDF analysis of total x-ray scattering.

The last three techniques have been the subject of several beamtimes throughout the years of my PhD and the collected data are not reported in this thesis. I have been a pioneer in my research group to apply some of these techniques to the investigation of catalysts based on supported metal NPs, and this implied a certain induction time before achieving a full understanding of their underlying rules.

On the computational side, I had the opportunity to explore a manifold of computational methods and approaches, allowing me to acquire knowledge on performing calculations at different levels of theory (from high to low), in the spirit of "multilevel modelling". The different levels of theory explored in this thesis work are listed as follows.

- **Density Functional Theory (DFT).** DFT is a computational method derived in the frame of quantum mechanics (QM) employed in modern research to investigate the electronic and/or nuclear structure of many-body systems (e.g., atoms, molecules, and condensed phases). Unlike the more complex Wavefunction Theories (WFT), DFT computes the electronic energy of a system as a functional of the electron density bypassing the computation of the electron wavefunction. This feature, making DFT a more affordable computational tool than WFT without a dramatic loss in accuracy, is the reason why it is routinely employed to compute high-accuracy molecular properties for the complex systems typical of heterogeneous catalysis.

- **Semi-empirical (SE) methods.** Computational methods based on quantum mechanics (such as DFT and WFT) can be simplified as some quantities, that should be calculated

through the resolution of complex integrals and equations, can be substituted by empirical parameters. The thus obtained SE methods usually benefit of a sensible computational speedup, but, being weaker models than QM methods, pay the fee of a reduced accuracy and transferability.

- **Molecular mechanics (MM).** Molecular Mechanics is a computational method that computes the Potential Energy Surface of a particular arrangement of atoms using parametric equations derived using classical physics. These sets of equations, together with their parameters, are known as a force-fields (FF). Given the strong approximation level and the usually high number of parameters composing each FF, MM methods are weaker and less transferable methods if compared with SE ones. However, given their extremely low computational cost, they usually find application in treating extremely complex systems or in high-throughput studies.

By synergically combining this huge number of experimental techniques and computational methods, this PhD work has been able to shed some light on three fundamental aspects of the modern research about heterogeneous catalysis by supported metal NPs, offering at the same time interesting perspective for the near future.

1. The applicability of low-cost methods to the simulation of metal NPs. The performances of a series of low-cost computational methods have been assessed on Pt NPs of size up to 561 atoms against a robust DFT reference, clarifying their applicability to these systems with its advantages and limitations. In the future, this research branch could be further explored by moving to other metals, nanoalloys and, compatibly with the next developments in the available computational tools, to the simulation of even more complex and bigger systems.

2. The adsorbate-induced ductility of metal NPs. A CO-induced corrugation of the Pd(100) facets, occurring at high CO coverage and at room temperature, has been documented for the first time on Pd/Al$_2$O$_3$ catalysts, thanks to the coupling of three experimental techniques (CO chemisorption, adsorption microcalorimetry and *in situ* FT-IR spectroscopy) with DFT calculations. Additional molecular dynamics simulations should be performed to boost the solidity of the presented computational insights. This experimental/computational approach can be easily extended to other metals and other probes, and has the potential to provide a methodological benchmark in the field of characterization of adsorbate-induced phenomena in supported metal NPs.

3. The micro- and meso-structure of activated carbons. A characterization of both the microstructure and porosity of different activated carbons has been pursued by coupling N$_2$, Ar and CO$_2$ physisorption with SANS. The presented preliminary analysis further challenges both the traditional assumptions of the slit-shaped pore model and of the activated carbons microstructure as composed by an ensemble of randomly assembled graphitic nano-crystallites. Lastly, through a refinement of the analysis of the collected SANS data, we will be able to complement Ar sorption with accurate topological information on the morphology of both the pores and the carbon domains, as well as on pore accessibility thanks to D$_2$O contrast matching. Extracting all these data from the SANS patterns will involve a delicate fitting procedure, devoted to separate and analyze the contributions of carbon particles, micropores and structural peaks of the carbon matrix. Since this will involve the employment of several fitting models, we will evaluate their performances *a posteriori* by performing a statistic analysis based on the Bayesian inference.

147

Publications

ROYAL SOCIETY
OF CHEMISTRY

PAPER

Check for updates

Gas phase *vs.* liquid phase: monitoring H₂ and CO adsorption phenomena on Pt/Al₂O₃ by IR spectroscopy

Michele Carosso,[a] Thibault Fovanna,[b] Alberto Ricchebuono,[a] Eleonora Vottero, [iD][a]
Maela Manzoli, [iD][c] Sara Morandi, [iD][a] Riccardo Pellegrini,[d] Andrea Piovano, [iD][e]
Davide Ferri [iD] *[b] and Elena Groppo [iD] *[a]

The adsorption phenomena occurring at the surface of a highly-dispersed Pt/Al₂O₃ catalyst for hydrogenation reactions were thoroughly investigated in the gas-phase by transmission IR spectroscopy and in the liquid-phase by ATR–IR spectroscopy. The reduction of Pt/Al₂O₃ in H₂ with the formation of Pt–hydrides and adsorption of CO were used as case studies for the comparison of the two different environments under otherwise similar experimental conditions. We found that compared to gas-phase, the selected solvent (cyclohexane) greatly affects the reducibility of Pt. Incomplete reduction under the adopted liquid-phase conditions was demonstrated by the formation of carbonate species at very low CO coverage. Moreover, cyclohexane competes with the adsorbates (H₂ as well as CO) for the occupancy of the available surface sites, thus affecting the shape, position and relative intensity of the infrared signals corresponding to the surface Pt–H and Pt–CO species and leading to an overall lower H and/or CO coverage. Our spectroscopic data show also that the presence of the solvent is crucial in maintaining the Pt nanoparticles in partially H-solvated state even in a H₂-free environment. This evidence might have important implications with respect to the catalyst reactivity and stability.

1. Introduction

Platinum based catalysts are massively employed in industrial processes involving hydrogenation reactions, such as in the synthesis of specialty chemicals and drugs.[1–4] This is largely due to the superior ability of platinum in splitting molecular hydrogen into its atomic form.[5,6] Understanding the nature and the behaviour of the platinum hydride (Pt–H) species under reaction conditions is crucial to design more efficient and profitable catalysts. However, characterizing the phenomena occurring at the surface of supported metal nanoparticles is one of the main challenges in surface science, due to the combination of many factors, among which are the intrinsic complexity of metal nanoparticles[7–13] and their dynamic behaviour in the presence of adsorbates.[14–24] In this context, the H₂@Pt system was extensively investigated both theoretically[15,16,21,24–28] and

experimentally, especially by means of X-ray absorption spectroscopy (XAS),[13,14,17,18,22,25,29–36] IR spectroscopy[37–43] and inelastic neutron scattering (INS) spectroscopy.[44–48] While XAS provides direct information on the structural and electronic changes experienced by nanometric Pt particles in the presence of hydrogen, vibrational spectroscopies have the capability to discern between different Pt–H surface species, since the Pt–H vibration is sensitive to even small changes in the coordination geometry.

In such a scenario, some of us were involved in a systematic investigation of the hydride species formed over an industrial Pt/Al₂O₃ catalyst as a function of the H-coverage in the gas-phase, exploiting a multi-technique approach comprising INS, FT-IR and synchronous DRIFT/XAS/MS.[49] INS, being extremely sensitive towards vibrational modes involving hydrogen motion and almost silent towards all other elements, allowed the detection of the vibrational fingerprints of multi-coordinated Pt–H species under high H-coverage conditions, which are not visible by FT-IR spectroscopy because they fall in the spectral region dominated by the vibrational modes of the alumina framework. By comparison, because the threshold of absorption of MgO is at lower energy, multi-folded hydrides were observed on Pt/MgO.[50] By *operando* DRIFT/XAS/MS we were able to distinguish with an unprecedented level of detail

[a] Department of Chemistry, INSTM and NIS Centre, University of Torino, via Quarello 15/A, I-10135 Torino, Italy. E-mail: elena.groppo@unito.it
[b] Paul Scherrer Institut, 5232 Villigen PSI, Switzerland. E-mail: davide.ferri@psi.ch
[c] Department of Drug Science and Technology, INSTM and NIS Centre, University of Torino, via Pietro Giuria 9, I-10125 Torino, Italy
[d] Chimet SpA – Catalyst Division, via di Pescaiola 74, I-52041, Viciomaggio Arezzo, Italy
[e] Institut Laue-Langevin (ILL), 71 avenue des Martyrs, 38000 Grenoble, France

at least four different species of linear Pt–hydrides characterized by different adsorption strengths and local environment, and to follow their interconversion into multi-coordinated Pt–H species upon changing the H-coverage.[49] This phenomenon was correlated with a structural and electronic reconstruction of the Pt nanoparticles, in good agreement with theoretical predictions.[15,16,21,24,25,27] It should be mentioned for the sake of clarity that the assignment of the IR signals in the 2100–1700 cm^{-1} to Pt–H species rather than to adsorbed CO is unambiguously confirmed by identical experiments with D_2, which shifts them to the 1600–1200 cm^{-1} region.[49]

Industrial reactions are often carried out in a liquid solvent and the transferability of the results obtained in the gas-phase to liquid-phase cannot be assumed *a priori*. In order to close the gap of knowledge between gas-phase and liquid-phase conditions, similar experiments should be performed in the presence of a solvent. Unfortunately, the reports dealing with the vibrational characterization of Pt–hydrides at a solid–liquid interface are rare,[43] likely because of technical limitations.[51] In the liquid phase, the absorption bands related to the solvent can be orders of magnitude more intense than those associated with the adsorbed species. In this context, attenuated total reflection IR (ATR-IR) spectroscopy offers interesting opportunities.[52] The catalyst can be deposited as a thin layer on the ATR crystal and contacted with the solvent. By exploiting this geometry, the amount of liquid sampled by the IR radiation is very small and most of the information is retrieved from the catalyst surface.[53–59] Nevertheless only very few studies dealing with a detailed characterization of Pt-based catalysts in organic solvents and/or water are available,[60] and they mainly focused on the use of CO as a molecular probe.[61–63] As a further consequence of the lack of studies in liquid-phase environment a systematic comparison between gas-phase and liquid-phase experiments performed on the same catalyst is rare.[94]

In this work, we bridged this gap of knowledge in the characterization of surface phenomena occurring at solid–gas and solid–liquid interfaces, by thoroughly investigating a highly-dispersed Pt/Al$_2$O$_3$ catalyst during H_2 and CO adsorption using transmission IR spectroscopy for the gas-phase and ATR-IR spectroscopy for the liquid-phase.

2. Experimental

2.1 Catalyst synthesis and preliminary characterization

The 5 wt% Pt/Al$_2$O$_3$ catalyst was prepared in the laboratories of the Catalyst Division of Chimet S.p.A., adopting a high-surface-area transitional alumina as a support (specific surface area = 116 m^2 g^{-1}; pore volume = 0.41 cm^3 g^{-1}) and following a proprietary deposition–precipitation method similar to the one reported by Kaprielova *et al.*[64] After preparation, the sample was carefully washed with water and dried at 120 °C overnight. The nominal Pt dispersion (D = 63%) was determined by a H_2/O_2 titration method.[65] As previously reported,[49] HR-TEM micrographs showed very

small and homogeneously distributed Pt nanoparticles, with an almost spherical shape and a regular size. A representative HR-TEM micrograph is reported in Fig. 1A, while Fig. 1B shows the particle size distribution obtained from the analysis of more than 700 particles. The average value (1.4 ± 0.4 nm) is in good agreement with the dispersion determined by H_2/O_2 titration, and was previously confirmed also by EXAFS data analysis.[49] Temperature programmed reduction (TPR) was performed to evaluate the reducibility of the Pt phase. The main reduction peak (Fig. 1C), which is due to the Pt^{2+} → Pt^0 reduction, starts at a temperature as low as −30 °C, reaches its maximum around 55 °C and ends around 130 °C. The integrated area below the peak delivers the overall hydrogen consumed in the process: it accounts for a Pt/H ratio of 3.6, indicating that the majority of the Pt phase was in the PtO$_2$ form in the pristine catalyst.

2.2 Methods

2.2.1 IR experiments in gas-phase. For the H_2 adsorption experiment, about 10 mg of undiluted Pt/Al$_2$O$_3$ were pressed into a self-supported pellet and placed inside a commercial FT-IR reactor cell (AABSPEC, no. 2000-A multimode), which allows sample activation and collection of FT-IR spectra under controlled temperature and atmosphere. In our previous work[49] we demonstrated that the large dead volume of the cell allows exchanging the gas composition at a low rate, thus permitting to follow the intermediate steps in the dynamic behavior of the Pt nanoparticles as a function of the gas concentration. On the other hand, the large internal volume makes the gas flow dynamics poorly predictable. The catalyst was heated up to 70 °C (heating rate 5 °C min^{-1}) under an inert stream (N$_2$, 50 mL min^{-1}) and left at this temperature for *ca.* 30 min in order to desorb most of the physisorbed water before collecting a FT-IR spectrum. Then, the catalyst was contacted at the same temperature with a N$_2$/H$_2$ flow (50 mL min^{-1}, 10 vol% H$_2$) and FT-IR spectra were acquired every 10 s for about 10 min until saturation of the signals of surface hydride species. Finally, the gas flow composition was changed back to pure N$_2$ to monitor the H_2 desorption step: FT-IR spectra were collected continuously for approximately 70 min.

The CO adsorption experiment was performed in static conditions. The self-supported pellet was inserted into a gold envelope and successively placed inside a homemade quartz cell equipped with KBr windows, allowing for the sample activation in the 25–700 °C range and successive measurements at room temperature, in the 10^{-4}–10^3 mbar pressure range. The sample was heated up to 70 °C in dynamic vacuum and left at this temperature up to a final vacuum of 10^{-4} mbar. Successive reduction was performed by dosing an excess of H_2 (equilibrium pressure of p_{H_2} = 100 mbar, 2 times × 15 min) over the sample, followed by a final dynamic vacuum treatment down to 10^{-4} mbar. A FT-IR spectrum was collected at room temperature before contacting the sample at room temperature with pulses of a
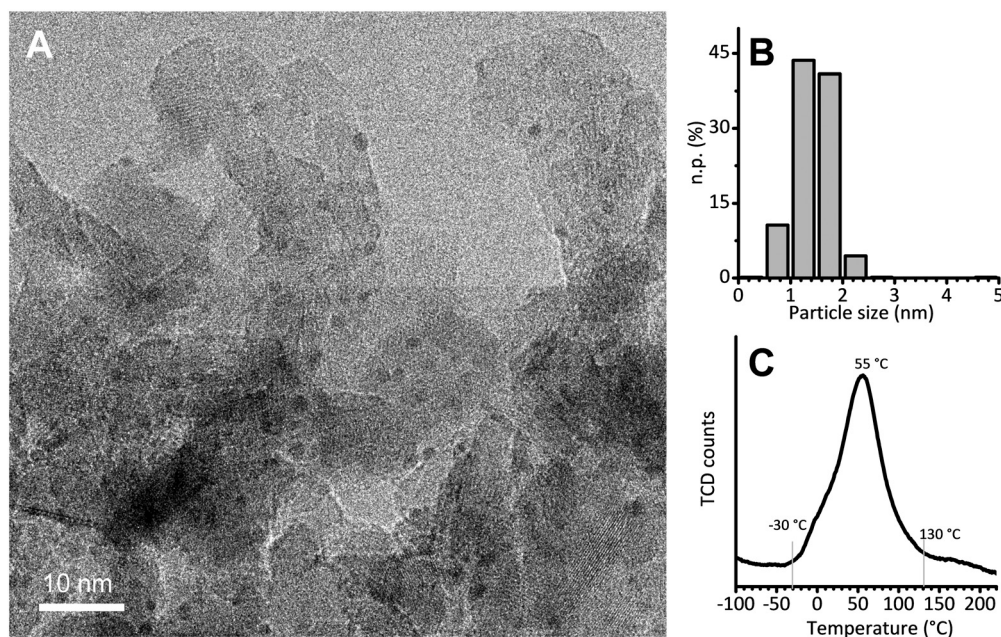
Fig. 1 (A) Representative HR-TEM micrograph of Pt/Al$_2$O$_3$ (instrumental magnification 200 000X). (B) Corresponding particle size distribution determined by analysing more than 700 particles. (C) H$_2$-TPR.

10 vol% CO/He mixture up to an equilibrium pressure of $p_{He/CO}$ = 30 mbar. An IR spectrum was collected at each pulse.

For the experiments in gas-phase the FT-IR spectra were collected with a Bruker Invenio IR spectrometer equipped with a MCT detector by averaging 32 scans at 2 cm^{-1} resolution.

2.2.2 IR experiments in liquid-phase. For the *in situ* ATR-IR experiments, a slurry of the Pt/Al$_2$O$_3$ powder catalyst (*ca.* 10 mg) in Milli-Q water (*ca.* 1 mL) was dropped on the ZnSe internal reflection element (IRE; 90 × 10 × 10 mm) and dried overnight in a fume hood. The dried catalyst layer was then inserted into a horizontal ATR-IR cell working in continuous flow and whose temperature was regulated using a recirculating water bath. Cyclohexane was selected as the solvent, because it does not exhibit major absorptions in the spectral region of interest and it is considered relatively innocent, contrary to other solvents *e.g.* alcohols.[66,67] For the H$_2$ adsorption experiment, the catalyst was heated up to 70 °C under a continuous flow of Ar-saturated cyclohexane using a peristaltic pump (Ismatec) and left at 70 °C for 5 min. A first spectrum was collected and used as background. Then, the sample was contacted at the same temperature with H$_2$-saturated cyclohexane. ATR-IR spectra were recorded every minute for 60 min before switching the flow to Ar-saturated cyclohexane in order to investigate the stability of the adsorbates.

For the CO adsorption experiment, the catalyst layer was reduced in H$_2$ at 70 °C as described above, then cooled to room temperature in Ar-saturated cyclohexane and contacted with cyclohexane saturated with a 5 vol% CO/Ar mixture.

ATR-IR spectra were recorded continuously every minute for 60 min.

All the measurements were performed with a Bruker Vertex70 spectrometer equipped with a MCT detector and a commercial ATR mirror unit. The ATR-IR spectra were collected by accumulating 20 scans at 4 cm^{-1} resolution.

3. Results and discussion

3.1 Pt–Hydrides formation and dynamics upon reducing the H-coverage

Fig. 2A shows the sequence of IR spectra collected during gas-phase reduction of Pt/Al$_2$O$_3$ at 70 °C in the region characteristic for the v(Pt–H) vibrational modes of linear Pt–H species. For the sake of clarity, this experiment is equivalent to the one reported in our previous work,[49] but performed at 70 °C instead of 120 °C in order to allow for a direct comparison with the experiments in the liquid phase. As soon as the catalyst was contacted by the N$_2$/H$_2$ flow, the growth of bands in the v(OH) and δ(OH) region (not shown) testified the formation of H$_2$O that was accompanied by the simultaneous appearance of a few weak bands in the v(Pt–H) region. According to the literature[37–43] and following our previous work,[49] band I at 2115 cm^{-1} (which is detectable only in the presence of gaseous H$_2$) is attributed to a weakly adsorbed hydride. Bands II and III at 2045 and 1990 cm^{-1} (the latter appearing as a shoulder of the former) are assigned to strongly adsorbed hydrides differing in terms of their local environment. Finally, the weaker bands IVa and IVb at about 1865 and 1740 cm^{-1} are assigned to interfacial Pt–H species, *i.e.* linear hydrides formed at Pt atoms in direct interaction with the alumina support. The assignments are
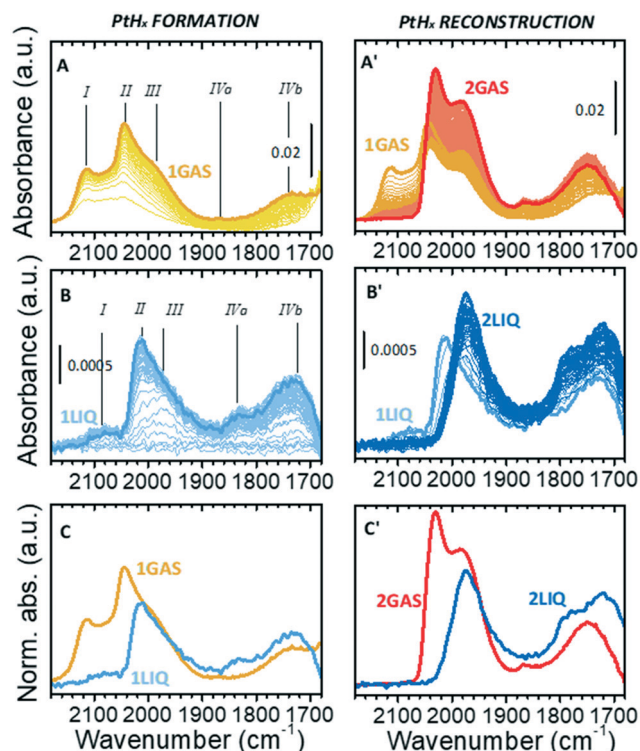
Fig. 2 (A) Evolution of the IR spectra in the region characteristic of the v(Pt–H) vibrational modes for linear Pt–H species during the gas-phase reduction of Pt/Al$_2$O$_3$ in N$_2$/H$_2$ at 70 °C. Spectrum 1GAS was collected after 10 min in N$_2$/H$_2$ flow. (A′) Evolution of the IR spectra during the successive H$_2$ desorption in N$_2$ flow at 70 °C, up to the maximum intensities of the v(Pt–H) bands. Spectrum 2GAS was collected after about 1 h in desorption conditions. (B) and (B′) are the same as (A) and (A′) for the ATR-IR experiment performed in liquid phase. Spectrum 1LIQ was collected after about 1 h in hydrogenation conditions, while spectrum 2LIQ after about 1 h in inert conditions. (C) Comparison of the final spectra reported in (A) and (B). (C′) Comparison of the final spectra reported in (A′) and (B′).

summarized in Table 1. All the five bands gradually intensified over time almost at the same rate and reached a steady condition after about 10 min (spectrum 1GAS). At that point H$_2$ was removed from the flow, and the desorption process was monitored (Fig. 2A′). Band I rapidly disappeared,

while the other bands evolved in a counterintuitive way. The intensity of bands II and III passed through a minimum and then rose, while that of bands IVa and IVb increased constantly. These v(Pt–H) bands reached their maximum intensity after about 1 h (spectrum 2GAS) and then they all vanished rapidly, following the observations reported in our previous work.[49]

This counterintuitive behavior is the same observed for the same sample measured in the presence of H$_2$ at 120 °C, that was explained with a reconstruction of the hydrogenated Pt nanoparticles driven by a change in the H-coverage.[49] Several theoretical models predict the occurrence of this phenomenon for Pt particles of subnanometric and nanometric size, which is also in accordance with experimental structural data obtained by XAS.[15,16,21,24,25,27,34] According to theoretical models, at high H-coverage Pt$_{13}$ nanoparticles adopt preferentially a cuboctahedral geometry poorly interacting with the support because they are H-solvated, mainly by multi-folded hydrides which are not visible by IR spectroscopy. Upon decreasing the H-coverage, the Pt$_{13}$ nanoparticles reconstruct into a biplanar geometry strongly interacting with the support, which is accompanied by a conversion of multi-folded hydrides into linear ones, thus explaining the intensification of the v(Pt–H) bands in the IR spectrum.

Fig. 2B and B′ show the results of the same experiment performed in liquid phase. The evident similarity to the gas-phase experiment allows us to translate the assignment of the observed signals to Pt–H species (Table 1). Focusing the attention on the hydrides formation step (Fig. 2B), from a qualitative perspective the ATR-IR spectra possess the same profile of those collected in the gas-phase (Fig. 2A), but there are important differences in the position, relative intensity and temporal evolution of the bands. Band I was barely present in cyclohexane (2088 cm^{-1}); band II was less intense and red-shifted by *ca.* 25 cm^{-1}; band IVa was more evident and red-shifted by *ca.* 30 cm^{-1}, while bands III and IVb remained unaffected. Moreover, the five bands did not grow simultaneously as observed in the gas-phase experiment: band III was the first one to appear, followed by band II. In general, the kinetics of hydrides formation in the liquid-

Table 1 Assignment of the vibrational modes of Pt–hydride and Pt–carbonyl species on Pt/Al$_2$O$_3$ in the gas-phase experiment as well as in cyclohexane. The reported frequencies (in cm^{-1}) of PtH$_x$ refer to 1GAS and 1LIQ spectra of Fig. 2A and B. The reported frequencies of Pt–carbonyls refer to the maximum CO-coverage obtained under the conditions adopted in this work (Fig. 4)

Linear Pt–hydrides, v(Pt–H)				
	Species I	Species II	Species III	Species IVa and IVb
Gas-phase	2115	2045	1990	1865 and 1740
Cyclohexane	2088	2020	1990	1835 and 1740

Pt–Carbonyls, v(Pt–CO)					
	Linear Pt–carbonyls			Multi-folded Pt–carbonyls		
	Terrace sites (L1)	Edge sites (L2)	Corner sites (L3)	Bridged on terraces (B1)	Bridged on edges (B2)	3-Fold (B3)
Gas-phase	2088	2070	2010	1878	1830	1790
Cyclohexane	2080	2060	—	1862	1818	—

phase was slower than in the gas-phase, likely as a consequence of the low H_2 concentration in cyclohexane, which is dictated by its solubility, and its higher diffusion limitation from the liquid-phase onto the catalyst surface than in the gas-phase. A direct comparison of the two final spectra collected in the presence of H_2 is provided in Fig. 2C.

The differences between gas-phase and liquid-phase experiments are even larger when looking at the evolution of the IR spectra during the desorption step in cyclohexane (Fig. 2B′). Band I rapidly disappeared, while band II was quickly converted into band III within a few minutes as indicated by the formation of an isosbestic point at 1988 cm^{-1}. At longer time, only a constant drift in the baseline was observed without further evolution in the position and/or intensity of the bands. The kinetics involved is very different from that observed in the gas-phase: the conversion of species II into species III is very fast and the spectra do not change further even after a very prolonged treatment in Ar-saturated solvent, while in the gas-phase the increase in intensity of species II and III is much slower. The final spectrum (2LIQ) is compared in Fig. 2C′ to that corresponding to the maximum intensity of the v(Pt–H) bands obtained under gas-phase conditions (spectrum 2GAS). The complete absence of band II in the ATR-IR spectrum is the major difference between the two experiments. It is important to notice that, within the time interval investigated, the Pt–H bands did not disappear, in contrast to what was observed in the gas-phase and already reported in our previous work.[49] This indicates that cyclohexane stabilizes the Pt nanoparticles in a hydrogenated form even in absence of hydrogen, preventing their reconstruction.

The set of data reported in Fig. 2 reveals that the presence of the solvent alters the relative distribution of the Pt–H species with respect to the gas-phase situation, both during the Pt oxide reduction and during the H_2 desorption steps. We find at least two possible explanations for this behavior, which are not mutually exclusive: i) in the presence of the solvent, the overall H-coverage is lower than in gas-phase, either because the solvent competes with hydrogen in the occupancy of the adsorption sites and/or because the morphology of the Pt nanoparticles is different in the two cases; ii) under these conditions, in liquid-phase Pt is not completely reduced, which also leads to an overall lower H-coverage. In support of hypothesis i) it must be noticed that the evolution of the ATR-IR spectra in liquid-phase during the desorption step is very much similar to what occurs during the catalytic hydrogenation of toluene in vapour-phase,[49] and is ascribed to a competitive adsorption between hydrogen and toluene. In support of hypothesis ii) there is the experimental evidence that the Pt phase is indeed not fully reduced in liquid-phase at 70 °C (as demonstrated in the following section).

Another relevant effect of the solvent is the stabilization of the Pt nanoparticles in a H-solvated form even in the absence of H_2. This appears particularly relevant during reaction. In

the case the reaction environment becomes poor in H_2, the solvent can disfavour hydrogen desorption and decrease the rate of the morphologic reconstruction the Pt nanoparticles experience in the gas phase.[16,21,22,24,25,27] We speculate that in this situation, the catalyst could sustain a reaction for longer time.
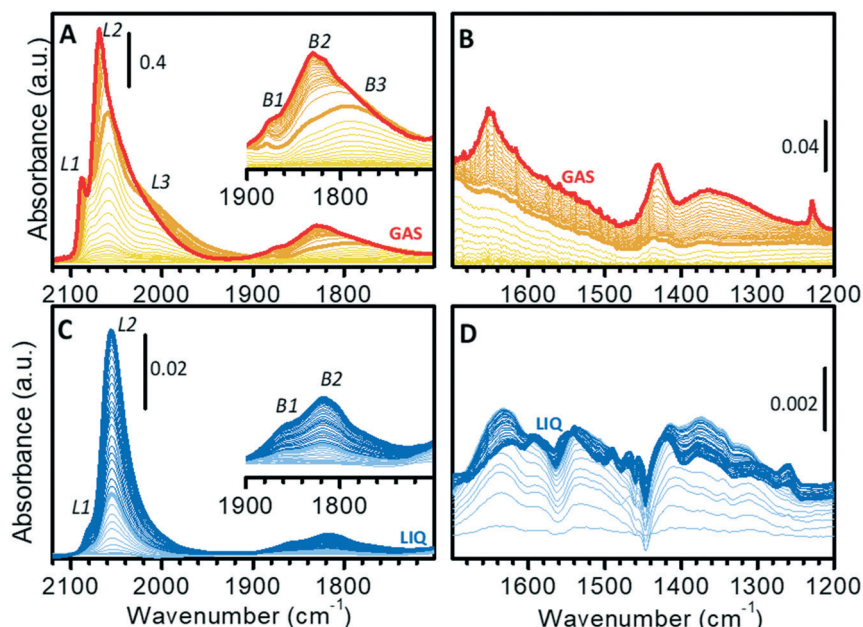
3.2 CO adsorption at room temperature

The surface properties of the Pt nanoparticles were successively investigated by means of CO adsorption at room temperature, which is one of the most utilized methods for the characterization of metal surfaces and of metal nano-particles.[68–84] Fig. 3 shows the sequence of transmission IR spectra collected upon progressive CO adsorption on Pt/Al$_2$O$_3$ in the gas-phase (Fig. 3A and B) and in the liquid-phase (Fig. 3C and D) in two different spectral regions, namely the v(CO) region (Fig. 3A and C) and the region characteristic of surface carbonates (Fig. 3B and D).

The sequence of IR spectra collected upon increasing the CO coverage (θ_{CO}) in gas-phase is complex. More in detail, a total of six bands was observed in the v(CO) region (Fig. 3A), which shift in position and grow at a different rate upon increasing the CO partial pressure. Bands in the 2100–1900 cm^{-1} region (L1, L2 and L3) are characteristic of linear Pt–carbonyls, while those in 1900–1700 cm^{-1} (B1, B2 and B3) are characteristic of multi-coordinated Pt–carbonyls. These bands can be assigned on the basis of surface science studies,[68–73] as well as of the abundant literature on CO adsorption over Pt-based heterogeneous catalysts[75,77–80] as follows (Table 1).

– Band L1 at 2077 cm^{-1} at low θ_{CO} and at 2088 cm^{-1} at high θ_{CO}, is attributed to CO linearly adsorbed at terrace sites.[73–76,85]

– Band L2 at 2060 cm^{-1} at low θ_{CO} and at 2070 cm^{-1} at high θ_{CO}, is due to CO adsorbed at the particles edges.[73,85–89]

– The very broad band L3 centered at *ca.* 2010 cm^{-1}, which does not shift with θ_{CO}, is ascribed to CO adsorbed at particles corners/kinks.[85,87]

– Band B1 at 1878 cm^{-1} and band B2 at *ca.* 1830 cm^{-1}, which are almost insensitive to θ_{CO}, are assigned to bridged carbonyls on terraces and edges, respectively.[86,88–90]

– The broad band B3 at *ca.* 1790 cm^{-1} is attributed to 3-fold coordinated CO at hollow sites.[62,80,86,90,91]

A rapid inspection of the spectra as a whole suggests a predominance of defects (edges and corners/kinks) rather than extended terraces, as expected because of the very high metal dispersion.

When analyzing the whole sequence of spectra as a function of θ_{CO} in a narrower spectral range, additional relevant information can be obtained. After the very first small pulses of CO, L1 and L2 were the first bands to appear, immediately followed by L3; bands due to bridged species appeared later. Upon increasing θ_{CO}, all the bands intensified, but did not shift until $P_{He/CO}$ of about 2 mbar (bold orange spectrum in Fig. 3A). At this point, band L1 stopped growing and blue-shifted, band L2 blue-shifted while

This journal is © The Royal Society of Chemistry 2022

Catal. Sci. Technol., 2022, **12**, 1359–1367 | **1363**

Fig. 3 (A) FT-IR spectra of CO adsorbed at room temperature on Pt/Al_2O_3 (activated and reduced at 70 °C in gas-phase) in the $\nu(CO)$ region and (B) in the 1700–1200 cm^{-1} region, where the bands typical for surface carbonates are observed. The bold orange spectrum in (A) and (B) ($P_{He/CO}$ = 2 mbar) is the last one before observing the upward shift of bands L1 and L2 (see text). (C) ATR-IR spectra of CO adsorbed at room temperature on Pt/Al_2O_3 (activated and reduced at 70 °C in liquid-phase) in the presence of cyclohexane in the $\nu(CO)$ region and (D) in the 1700–1200 cm^{-1} region. The bold light blue spectrum in (C) and (D) is that where the bands in 1700–1200 cm^{-1} region are maximized. The insets in (A) and (C) show a magnification of the 1900–1700 cm^{-1} region.

still growing and band L3 slightly attenuated. In the region of multi-folded carbonyls, bands B1 and B3 did not grow further, while band B2 became dominant. The blue-shift of bands L1 and L2 is explained in terms of a strong dipole–dipole coupling interaction between adjacent CO molecules at high θ_{CO}. The attenuation of band L3 and the simultaneous intensification of band L2 is well explained by the "transfer of intensity" concept proposed by Hollins:[92] in the presence of strong dipole–dipole coupling involving more than one adsorbed species, a transfer of intensity may take place from a band at lower frequency to a band at higher frequency.

It is worth mentioning that, at the same time, in the 1700–1200 cm^{-1} region (Fig. 3B) a few bands started growing at *ca.* 1650, 1440 and 1230 cm^{-1}. These bands are readily assigned to the $\nu(CO)$ and $\delta(OH)$ vibrational modes of a family of bicarbonates typically formed on alumina activated at low temperature.[93] Interestingly, bicarbonates formed only when θ_{CO} was high enough to determine a coupling interaction among adsorbed CO (from bold orange spectra in Fig. 3B). We hypothesize that they are the result of disproportionation of two neighboring adsorbed CO molecules, which give CO_2 (stabilized as bicarbonate at the partially hydrated surface of alumina) and adsorbed carbon. As a final observation, the fact that carbonate formation was not observed at low θ_{CO} confirms that the Pt phase was completely reduced, despite the low reduction temperature (70 °C). With reference to the TPR curve of Fig. 1C, this means that full reduction of the Pt–oxide phase can be

achieved in the gas-phase even below 130 °C, provided that the reduction time is sufficiently long.

Fig. 3C and D show the results of a similar experiment performed in the liquid-phase, where the spectra were collected as a function of exposure time of the catalyst to a flow of CO-saturated cyclohexane. In this case, the gradual increase in θ_{CO} is also affected by the diffusion of CO from the solvent to the catalyst. In the $\nu(CO)$ region (Fig. 3C), the evolution of the spectra was much simpler than in the gas-phase. Contrary to what observed in gas-phase, the $\nu(CO)$ bands intensified at the same rate and did not shift until reaching saturation (Fig. 3C). This indicates that when the catalyst is in the liquid environment under these experimental conditions, dipole–dipole coupling between adsorbed CO molecules is not favored and thus the overall θ_{CO} is much lower than in the absence of the solvent. Nevertheless, these spectra are not the same as those collected in gas-phase at very low θ_{CO}, the most striking difference being the almost total absence of bands L3 and B3. In the carbonates region (broad signals in the 1700–1200 cm^{-1} region; Fig. 3D) the spectra are more complex than in gas-phase and the appearance of carbonate species already in the early stages of CO adsorption reveals the occurrence of a rich chemistry. Observation of carbonates as soon as CO reached the sample is a strong indication that the Pt phase was not fully reduced after the reduction at 70 °C in the liquid-phase. CO reduced this fraction of oxidized Pt with the consequent production of CO_2, which is stabilized by the alumina support as carbonate (light blue spectra in Fig. 3D).

1364 | *Catal. Sci. Technol.*, 2022, **12**, 1359–1367

This journal is © The Royal Society of Chemistry 2022

This demonstrates that H_2-reduction at 70 °C was less efficient in the presence of cyclohexane than in the gas-phase. The poor solubility of H_2 in cyclohexane is a possible explanation, but we cannot exclude that the geometry of the ATR-IR cell, in which the solvent mostly by-passes the catalyst layer, could also play an important role. Formation of carbonates was completed after a few minutes, while Pt–carbonyls kept growing for longer time. Finally, it is worth noticing that in the liquid-phase experiment the simultaneous growth of carbonates and carbonyls as well as the shiftless growth of signals of carbonyls indicate that disproportionation of CO and the consequent formation of carbonates did not occur, thus confirming that disproportionation requires two vicinal adsorbed CO molecules as it was observed in the spectra collected in gas-phase.

Fig. 4 compares the IR spectra collected at the maximum θ_{CO} in the two experiments in the gas-phase and in the liquid-phase. It is evident that the spectrum of CO adsorbed on Pt/Al_2O_3 in cyclohexane is simpler than that of CO adsorbed in the gas-phase, with only two bands in the region of linear carbonyls, and two bands in the region of bridged carbonyls. Bands L1 and L2 are observed at 2080 and 2060 cm^{-1} in the liquid phase experiment, which are the values expected for linearly adsorbed CO on terraces and edges when isolated; moreover, the relative intensity of band L1 is much lower than in spectrum GAS and bands L3 and B3 are absent. All these observations suggest that the adsorption sites located at the flat domains of the nanoparticles (bands L1 and B3), as well as on corners/kinks (band L3), are less accessible to CO in the presence of the solvent, which forces CO to adsorb prevalently at the edges (bands L2 and B2). This suggests that in the presence of the solvent there are less sites available for CO adsorption, most likely because the solvent competes with CO for adsorption on the Pt surface.[68]

Finally, we should note that we have performed a purely qualitative study. We do not have yet the elements to compare quantitatively the coverages of CO and hydrides in th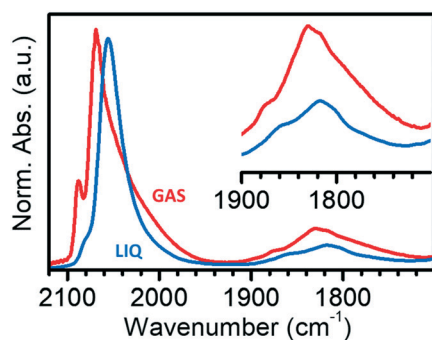e two different environments. We have to consider that a direct comparison of the intensities associated with adsorbed CO species in the gas and in the liquid phases cannot be performed, because of the different environment, optical geometries of the experiments and CO-coverage (likely lower in liquid-phase because of the competitive effect of the solvent). In order to proceed to a reliable quantitative prediction, the degree of the CO-coverage under the adopted experimental conditions, the metal surface area and the relative proportion of the different families of binding sites, as well as their energetics and the extinction coefficients of all the adsorbed species, should be known exactly. The data presented here allows us to qualitatively describe the surface sites available at the Pt nanoparticles and to predict which sites are favored in the liquid environment by comparing the differences in the relative intensities in the two cases.

4. Conclusions

In this work, we aimed at bridging the gap of knowledge of the adsorption phenomena occurring at the solid–gas and the solid–liquid interfaces. To this end, we investigated the adsorption of H_2 and CO over an industrial Pt/Al_2O_3 catalyst using transmission IR spectroscopy in gas-phase and ATR-IR spectroscopy in the liquid-phase.

We found that reduction by H_2 at 70 °C is less efficient in the presence of the solvent (in this case, cyclohexane) than in the gas-phase, probably due to the poor H_2 solubility in cyclohexane and/or to the particular geometry of the spectroscopy cell used to analyze the solid–liquid interface. Contrary to gas-phase case, the solvent stabilizes the Pt nanoparticles in a partially hydrogenated form even in the absence of H_2, preventing their complete reconstruction. Not only the Pt–H species stability is affected, but also their relative distribution. This suggests that the solvent competes with H_2 for the occupation of the surface sites, thus determining an overall lower H_2 coverage. Competition between the solvent and the adsorbing molecule was also observed in the case of CO. A careful comparison of the transmission and ATR-IR spectra of adsorbed CO allowed us to conclude that the adsorption sites located at the terraces as well as on kinks are less accessible to CO in the presence of the solvent. Therefore, CO adsorbs prevalently at the edges of the Pt nanoparticles. This different behavior may bear important implications for the reactivity of the Pt nanoparticles in heterogeneously catalyzed reactions in the gas- and in the liquid-phase.

Conflicts of interest

There are no conflicts to declare.

Acknowledgements

Fig. 4 IR spectra of CO adsorbed at room temperature on Pt/Al_2O_3 activated and reduced at 70 °C in gas-phase (GAS) and in liquid-phase (LIQ) in the ν(CO) region. The inset reports a magnification of the 1900–1700 cm^{-1} region of multi-coordinated carbonyls. Spectra GAS and LIQ were arbitrarily normalized to the intensity of band L2.

References

1 R. L. Augustine, *Heterogeneous Catalysis for the Synthetic Chemist*, Dekker, New York, 1995.

2 G. M. Loudon, *Organic Chemistry*, Benjamin/Cummings Pub. Co., Menlo Park, 2nd edn, 1988.

3 S. Nishimura, *Handbook of Heterogeneous Catalytic Hydrogenation for Organic Synthesis*, Wiley, Chichester, 2001.

4 P. N. Rylander, *Best Synthetic Methods: Hydrogenation Methods*, Academic Press, London, 1985.

5 M. Che, *Catal. Today*, 2013, **218–219**, 162–171.

6 A. Zecchina and S. Califano, Chapter 1 – From the Onset to the First Large-Scale Industrial Processes, in *The Development of Catalysis: A History of Key Processes and Personas in Catalytic Science and Technology*, ed. I. John, Wiley & Sons, 2017, ch. 1, pp. 1–57, DOI: 10.1002/9781119181286.

7 A. I. Frenkel, M. W. Small, J. G. Smith, R. G. Nuzzo, K. O. Kvashnina and M. Tromp, *J. Phys. Chem. C*, 2013, **117**, 23286–23294.

8 A. I. Frenkel, C. W. Hills and R. G. Nuzzo, *J. Phys. Chem. B*, 2001, **105**, 12689–12703.

9 J.-D. Grunwaldt and B. S. Clausen, *Top. Catal.*, 2002, **18**, 37–43.

10 M. A. Newton, B. Jyoti, A. J. Dent, S. G. Fiddy and J. Evans, *Chem. Commun.*, 2004, 2382–2383, DOI: 10.1039/b405694a.

11 G. Agostini, R. Pellegrini, G. Leofanti, L. Bertinetti, S. Bertarione, E. Groppo, A. Zecchina and C. Lamberti, *J. Phys. Chem. C*, 2009, **113**, 10485–10492.

12 R. Arrigo, K. Badmus, F. Baletto, M. Boeije, M. Bowker, K. Brinkert, A. Bugaev, V. Bukhtiyarov, M. Carosso, R. Catlow, R. Chanerika, P. R. Davies, W. Dononelli, H. J. Freund, C. Friend, S. Gallarati, B. Gates, A. Genest, E. K. Gibson, J. Hargreaves, S. Helveg, H. Huang, G. Hutchings, N. Irvine, R. Johnston, S. Lai, C. Lamberti, J. Macginley, D. Marchant, T. Murayama, R. Nome, Y. Odarchenko, J. Quinson, S. Rogers, A. Russell, S. Said, P. Sermon, P. Shah, S. Simoncelli, K. Soulantica, F. Spolaore, B. Tooze, L. Torrente-Murciano, A. Trunschke, D. Willock and J. Zhang, *Faraday Discuss.*, 2018, **208**, 339–394.

13 J. H. Kang, L. D. Menard, R. G. Nuzzo and A. I. Frenkel, *J. Am. Chem. Soc.*, 2006, **128**, 12068–12069.

14 M. W. Small, S. I. Sanchez, N. S. Marinkovic, A. I. Frenkel and R. G. Nuzzo, *ACS Nano*, 2012, **6**, 5583–5595.

15 L.-L. Wang and D. D. Johnson, *J. Am. Chem. Soc.*, 2007, **129**, 3658–3664.

16 C. Mager-Maury, G. Bonnard, C. Chizallet, P. Sautet and P. Raybaud, *ChemCatChem*, 2011, **3**, 200–207.

17 O. S. Alexeev, F. Li, M. D. Amiridis and B. C. Gates, *J. Phys. Chem. B*, 2005, **109**, 2338–2349.

18 E. Bus and J. A. van Bokhoven, *Phys. Chem. Chem. Phys.*, 2007, **9**, 2894–2902.

19 L. Li, L.-L. Wang, D. D. Johnson, Z. Zhang, S. I. Sanchez, J. H. Kang, R. G. Nuzzo, Q. Wang, A. I. Frenkel, J. Li, J. Ciston, E. A. Stach and J. C. Yang, *J. Am. Chem. Soc.*, 2013, **135**, 13062–13072.

20 S. I. Sanchez, L. D. Menard, A. Bram, J. H. Kang, M. W. Small, R. G. Nuzzo and A. I. Frenkel, *J. Am. Chem. Soc.*, 2009, **131**, 7040–7054.

21 W. Zhao, C. Chizallet, P. Sautet and P. Raybaud, *J. Catal.*, 2019, **370**, 118–129.

22 C. Dessal, A. Sangnier, C. Chizallet, C. Dujardin, F. Morfin, J. L. Rousset, M. Aouine, M. Bugnet, P. Afanasiev and L. Piccolo, *Nanoscale*, 2019, **11**, 6897–6904.

23 L. Piccolo, *Catal. Today*, 2021, **373**, 80–97.

24 C. Chizallet and P. Raybaud, *Catal. Sci. Technol.*, 2014, **4**, 2797–2813.

25 A. Gorczyca, V. Moizan, C. Chizallet, O. Proux, W. Del Net, E. Lahera, J.-L. Hazemann, P. Raybaud and Y. Joly, *Angew. Chem., Int. Ed.*, 2014, **53**, 12426–12429.

26 G. Sun, A. N. Alexandrova and P. Sautet, *J. Chem. Phys.*, 2019, **151**, 1–15.

27 P. Raybaud, C. Chizallet, H. Toulhoat and P. Sautet, *Phys. Chem. Chem. Phys.*, 2012, **14**, 16773–16774.

28 G. S. Erfani, S. Hong and T. S. Rahman, *J. Phys. Chem. C*, 2019, **123**, 16893–16901.

29 F. W. Lytle, P. S. P. Wei, R. B. Greegor, G. H. Via and J. H. Sinfelt, *J. Chem. Phys.*, 1979, **70**, 4849–4855.

30 M. Vaarkamp, J. T. Miller, F. S. Modica and D. C. Koningsberger, *J. Catal.*, 1996, **163**, 294–305.

31 D. E. Ramaker, B. L. Mojet, M. T. Garriga Oostenbrink, J. T. Miller and D. C. Koningsberger, *Phys. Chem. Chem. Phys.*, 1999, **1**, 2293–2302.

32 A. L. Ankudinov, J. J. Rehr, J. J. Low and S. R. Bare, *Phys. Rev. Lett.*, 2002, **89**, 139702-1.

33 D. C. Koningsberger, M. K. Oudenhuijzen, J. De Graaf, J. A. Van Bokhoven and D. E. Ramaker, *J. Catal.*, 2003, **216**, 178–191.

34 M. K. Oudenhuijzen, J. A. van Bokhoven, J. T. Miller, D. E. Ramaker and D. C. Koningsberger, *J. Am. Chem. Soc.*, 2005, **127**, 1530–1540.

35 E. Bus, J. T. Miller, A. J. Kropf, R. Prins and J. A. van Bokhoven, *Phys. Chem. Chem. Phys.*, 2006, **8**, 3248–3258.

36 E. Bus, J. T. Miller and J. A. van Bokhoven, *J. Phys. Chem. B*, 2005, **109**, 14581–14587.

37 J. P. Candy, P. Fouilloux and M. Primet, *Surf. Sci.*, 1978, **72**, 167–176.

38 L. T. Dixon, R. Barth and J. W. Gryder, *J. Catal.*, 1975, **37**, 368–375.

39 D. D. Eley, D. M. Moran and C. H. Rochester, *Trans. Faraday Soc.*, 1968, **64**, 2168–2180.

40 W. A. Pliskin and R. P. Eischens, *Z. Phys. Chem.*, 1960, **24**, 11–23.

41 M. Primet, J. M. Basset, M. V. Mathieu and M. Prettre, *J. Catal.*, 1973, **28**, 368–375.

42 T. Szilagyi, *J. Catal.*, 1990, **121**, 223–227.

43 D. Paleček, G. Tek, J. Lan, M. Iannuzzi and P. Hamm, *J. Phys. Chem. Lett.*, 2018, **9**, 1254–1259.

44 P. Albers, E. Auer, K. Ruth and S. F. Parker, *J. Catal.*, 2000, **196**, 174–179.

45 P. W. Albers, M. Lopez, G. Sextl, G. Jeske and S. F. Parker, *J. Catal.*, 2004, **223**, 44–53.

46 H. Asada, T. Toya, H. Motohashi, M. Sakamoto and Y. Hamaguchi, *J. Chem. Phys.*, 1975, **63**, 4078–4079.

47 S. F. Parker, C. D. Frost, M. Telling, P. Albers, M. Lopez and K. Seitz, *Catal. Today*, 2006, **114**, 418–421.

48 A. J. Renouprez and H. Jobic, *J. Catal.*, 1988, **113**, 509–516.

49 M. Carosso, E. Vottero, A. Lazzarini, S. Morandi, M. Manzoli, K. A. Lomachenko, M. J. Ruiz, R. Pellegrini, C. Lamberti, A. Piovano and E. Groppo, *ACS Catal.*, 2019, **9**, 7124–7136.

50 J.-P. Candy, P. Fouilloux and M. Primet, *Surf. Sci.*, 1978, **72**, 167–176.

51 D. Ferri, Toward operando infrared spectroscopy of heterogeneous catalysts, in *Heterogeneous catalysts: Emerging techniques for design, characterization and applications*, ed. A. U. W. Y. Teoh, Y. H. Ng and P. Sit, Wiley-VCH GmbH, 2021, pp. 311–338, DOI: 10.1002/9783527813599.ch18.

52 T. Bürgi and A. Baiker, *Adv. Catal.*, 2006, **50**, 227–283.

53 T. Bürgi, R. Wirz and A. Baiker, *J. Phys. Chem. B*, 2003, **107**, 6774–6781.

54 G. M. Hamminga, G. Mul and J. A. Moulijn, *Chem. Eng. Sci.*, 2004, **59**, 5479–5485.

55 A. Pintar, R. Malacea, C. Pinel, G. Fogassy and M. Besson, *Appl. Catal., A*, 2004, **264**, 1–12.

56 J. E. Rekoske and M. A. Barteau, *Ind. Eng. Chem. Res.*, 1995, **34**, 2931–2939.

57 Z. Wang, M. L. Larsson, M. Grahn, A. Holmgren and J. Hedlund, *Chem. Commun.*, 2004, 2888–2889, DOI: 10.1039/b410314a.

58 D. Ferri and A. Baiker, *Top. Catal.*, 2009, **52**, 1323–1333.

59 C. Boulho, E. K. Gibson, M. I. McAllister, R. Moss and D. Lennon, *Top. Catal.*, 2020, **63**, 386–393.

60 R. He, R. R. Davda and J. A. Dumesic, *J. Phys. Chem. B*, 2005, **109**, 2810–2820.

61 S. D. Ebbesen, B. L. Mojet and L. Lefferts, *J. Catal.*, 2007, **246**, 66–73.

62 D. Ferri, T. Bürgi and A. Baiker, *J. Phys. Chem. B*, 2001, **105**, 3187–3195.

63 I. Ortiz-Hernandez, D. J. Owens, M. R. Strunk and C. T. Williams, *Langmuir*, 2006, **22**, 2629–2639.

64 K. M. Kaprielova, O. A. Yakovina, I. I. Ovchinnikov, S. V. Koscheev and A. S. Lisitsyn, *Appl. Catal., A*, 2012, **449**, 203–214.

65 J. E. Benson and M. Boudart, *J. Catal.*, 1965, **4**, 704–710.

66 M. Carosso, E. Vottero, S. Morandi, M. Manzoli, D. Ferri, T. Fovanna, R. Pellegrini, A. Piovano and E. Groppo, *ChemCatChem*, 2021, **13**, 900–908.

67 J. B. Brazier, B. N. Nguyen, L. A. Adrio, E. M. Barreiro, W. P. Leong, M. A. Newton, S. J. A. Figueroa, K. Hellgardt and K. K. M. Hii, *Catal. Today*, 2014, **229**, 95–103.

68 A. Crossley and D. A. King, *Surf. Sci.*, 1977, **68**, 528–538.

69 B. E. Heyden and A. M. Bradshaw, *Surf. Sci.*, 1983, **125**, 787–802.

70 B. E. Hayden, K. Kretzschmar, A. M. Bradshaw and R. G. Greenler, *Surf. Sci.*, 1985, **149**, 394–406.

71 A. M. Bradshaw and F. M. Hoffmann, *Surf. Sci.*, 1978, **72**, 513–535.

72 G. Ertl, M. Neumann and K. M. Streit, *Surf. Sci.*, 1977, **64**, 393–410.

73 R. K. Brandt, M. R. Hughes, L. P. Bourget, K. Truszkowska and R. G. Greenler, *Surf. Sci.*, 1993, **286**, 15–25.

74 P. Pillonel, S. Derrouiche, A. Bourane, F. Gaillard, P. Vernoux and D. Bianchi, *Appl. Catal., A*, 2005, **278**, 223–231.

75 S. K. Cheah, V. P. Bernardet, A. A. Franco, O. Lemaire and P. Gelin, *J. Phys. Chem. C*, 2013, **117**, 22756–22767.

76 T. Avanesian, S. Dai, M. J. Kale, G. W. Graham, X. Pan and P. Christopher, *J. Am. Chem. Soc.*, 2017, **139**, 4551–4558.

77 J. A. Anderson, F. K. Chong and C. H. Rochester, *J. Mol. Catal. A: Chem.*, 1999, **140**, 65–80.

78 R. Barth, R. Pitchai, R. L. Anderson and X. E. Verykios, *J. Catal.*, 1989, **116**, 61–70.

79 P. Bazin, O. Saur, J. C. Lavalley, M. Daturi and G. Blanchard, *Phys. Chem. Chem. Phys.*, 2005, **7**, 187–194.

80 D. M. Haaland, *Surf. Sci.*, 1987, **185**, 1–14.

81 F. Zaera, *ChemCatChem*, 2012, **4**, 1525–1533.

82 T. Elgayyar, R. Atwi, A. Tuel and F. C. Meunier, *Catal. Today*, 2021, **373**, 59–68.

83 C. Lentz, S. P. Jand, J. Melke, C. Roth and P. Kaghazchi, *J. Mol. Catal. A: Chem.*, 2017, **426**, 1–9.

84 I. Jbir, A. Paredes-Nunez, S. Khaddar-Zine, Z. Ksibir, F. Meunier and D. Bianchi, *Appl. Catal., A*, 2015, **505**, 309–318.

85 F. Coloma, J. M. Coronado, C. H. Rochester and J. A. Anderson, *Catal. Lett.*, 1998, **51**, 155–162.

86 A. Bourane, O. Dulaurent and D. Bianchi, *J. Catal.*, 2000, **196**, 115–125.

87 J. Rasko, *J. Catal.*, 2003, **217**, 478–486.

88 J. Xu and J. T. Yates Jr., *J. Chem. Phys.*, 1993, **99**, 725–732.

89 J. Xu and J. T. Yates Jr., *Surf. Sci.*, 1995, **327**, 193–201.

90 B. E. Hayden and A. M. Bradshaw, The Adsorption of CO on Pt(111) Studied by Infrared-Reflection-Adsorption Spectroscopy, in *Stud. Surf. Sci. Catal.*, ed. C. R. Brundle and H. Morawitz, Elsevier, 1983, vol. 14, p. 51.

91 N. P. Lebedeva, A. Rodes, J. M. Feliu, M. T. M. Koper and R. A. van Santen, *J. Phys. Chem. B*, 2002, **106**, 9863–9872.

92 P. Hollins, *Surf. Sci. Rep.*, 1992, **16**, 51–94.

93 C. Morterra and G. Magnacca, *Catal. Today*, 1996, **27**, 497–532.

94 S. D. Ebbesen, B. L. Mojet and L. Lefferts, *Langmuir*, 2006, **22**, 1079–1085.

This journal is © The Royal Society of Chemistry 2022

Catal. Sci. Technol., 2022, **12**, 1359–1367 | **1367**

Evidence for H$_2$-Induced Ductility in a Pt/Al$_2$O$_3$ Catalyst

Eleonora Vottero,* Michele Carosso, Alberto Ricchebuono, Monica Jiménez-Ruiz, Riccardo Pellegrini, Céline Chizallet, Pascal Raybaud, Elena Groppo, and Andrea Piovano

ACCESS | Metrics & More | Article Recommendations | Supporting Information

ABSTRACT: Focusing on a highly dispersed 5 wt % Pt/Al$_2$O$_3$ catalyst for industrial hydrogenation and dehydrogenation reactions, we employ inelastic neutron scattering (INS) spectroscopy to obtain the vibrational fingerprint of the hydrogenous species formed under different H$_2$ equilibrium pressure and temperature. The INS profiles are interpreted on the basis of systematic DFT simulations on 26 different Pt$_x$H$_y$/γ-Al$_2$O$_3$ models, indicating that the INS spectra are a unique fingerprint of the Pt$_x$H$_y$/γ-Al$_2$O$_3$ model morphology, size (x), H-coverage (y), and typology of Pt−H species. We fit the experimental INS spectrum of Pt/Al$_2$O$_3$ measured under higher H-coverage conditions with a linear combination of the simulated spectra. We find that 47% of the spectrum can be ascribed to Pt$_{55}$H$_y$/γ-Al$_2$O$_3$ clusters completely solvated by H atoms (y = 81 and 91) and in weak interaction with the support, followed by the disordered Pt$_{34}$H$_{54}$/γ-Al$_2$O$_3$ model (36%) and by the smaller Pt$_{13}$H$_{32}$/γ-Al$_2$O$_3$ one (18%). These results are in good agreement with the particle size distribution previously determined by TEM and confirmed by XAS. A second INS spectrum collected under lower H-coverage conditions exhibits the typical features of less hydrogenated Pt$_x$H$_y$ models in stronger interaction with the γ-Al$_2$O$_3$ support, as well as bands associated with the formation of −OH species at the support by H-spillover. Overall, our study reveals the relevance of combined INS and DFT analysis to quantify the versatile atomic scale's properties of Pt/Al$_2$O$_3$ catalyst in terms of cluster morphology, size, typology of Pt−H species, and cluster/support interaction depending on the H-coverage, providing important insights about their behavior under hydrogenation conditions.

KEYWORDS: *platinum nanoparticles, hydrogenation, inelastic neutron scattering, density functional theory, nanoparticles ductility*
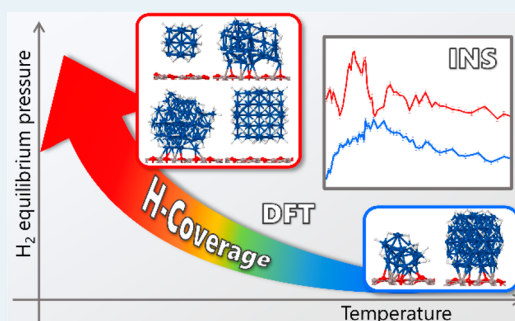
1. INTRODUCTION

Heterogeneous catalysts based on supported platinum nanoparticles are pivotal in the production process of many fine and bulk chemicals, including the catalytical reforming of gasoline,[1,2] the hydrogenation and dehydrogenation of organic substrates[3−7] or the oxidation of hydrocarbons and CO,[8−10] and also for their applications in fuel cells[11] or in the purification of exhaust gases.[12,13] The exceptional catalytic activity of platinum for hydrogenation reactions relies on its ability to activate and dissociate the H$_2$ molecule with the subsequent formation of surface platinum hydride species, which are those involved in the hydrogenation of the substrate. Although platinum has been employed in such catalytic processes since the onset of heterogeneous catalysis, many features such as the nature of the Pt−H species, the Pt−H stoichiometry,[14−16] their behavior under reaction conditions, the influence of the support, or the identification of the most active species in a given reaction are not yet fully understood, stimulating further investigations, which are not only of academic interest but also relevant for industrial applications.[17,18]

Experimental and theoretical evidence pointing out the ductility of supported Pt nanoparticles (i.e., their tendency to undergo a structural reconstruction, as a consequence of the

ability of the material to deform without breaking) as a function of reaction conditions such as the temperature and the H$_2$ partial pressure are accumulating over the years. The matter was largely addressed by means of density functional theory (DFT) simulations in refs 19 and 20, in which the most stable structures for Pt$_{13}$ nanoclusters on γ-Al$_2$O$_3$ surfaces under different temperatures and equilibrium H$_2$ pressures ($P(\text{H}_2)_{eq}$) were investigated by means of *ab initio* molecular dynamics. The simulations performed on dehydrated γ-Al$_2$O$_3$ surface models[19] indicated that high temperature and low $P(\text{H}_2)_{eq}$ favor a biplanar geometry strongly anchored to the support, while a decrease in the temperature and/or an increase of $P(\text{H}_2)_{eq}$ trigger a morphological reconstruction to a cuboctahedric Pt cluster which, eventually, get completely solvated by H atoms weakening the interaction with the support. Concomitantly with the reconstruction from a
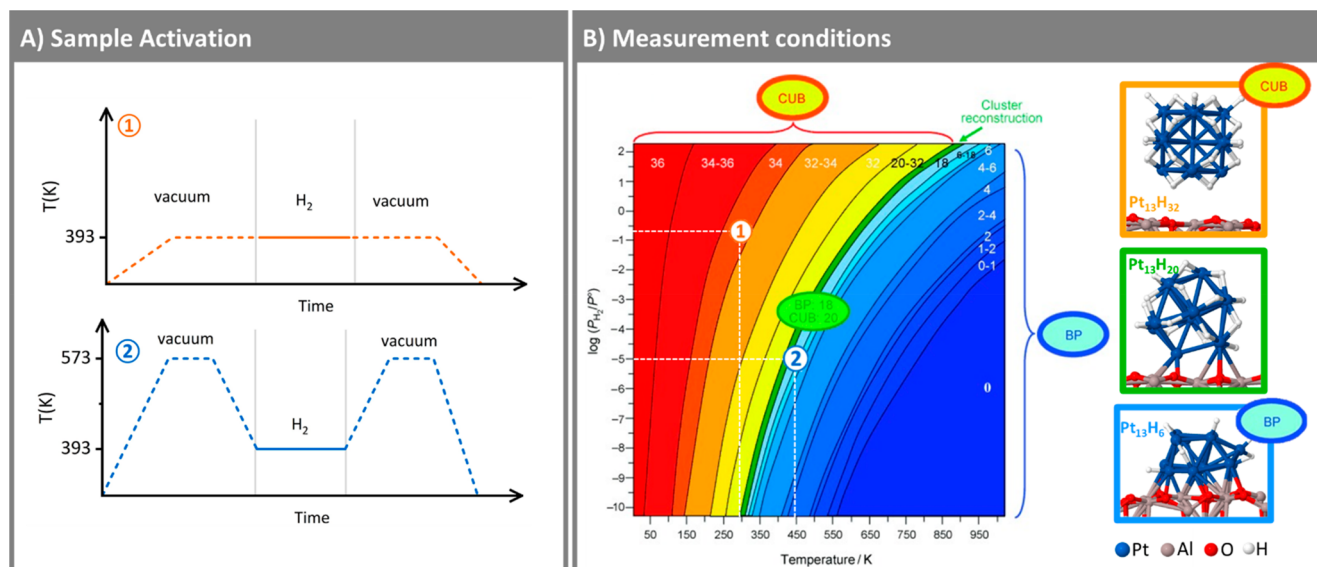
Figure 1. (A) Schematic description of the catalyst activation procedure prior the INS measurements for experiments (1) and (2). (B) Thermodynamic diagram displaying the most stable morphology and H-coverage for $Pt_{13}/\gamma\text{-}Al_2O_3(100)$ models as a function of the temperature and of the $P(H_2)_{eq}$, as calculated in ref 19. Representative geometries for the biplanar (BP), reconstructing and cuboctahedric (CUB) geometries are shown. Circles (1) and (2) indicate the temperature and $P(H_2)_{eq}$ at which H_2 was dosed during the first and second experiment. Adapted with permission from ref 19. Copyright 2011 Wiley-VCH.

biplanar to a cuboctahedric structure, a conversion of top Pt–H species (in which H is bonded to a single Pt atom) into multifolded Pt–H species was also predicted. This inter-conversion between top and multibridged Pt–H species and the ductility of supported Pt nanoparticles in the presence of H_2 was also pointed out by other computational studies on Pt_x nanoparticles (x up to 44) also considering isolated clusters or other supports.[21−25]

Experimental evidence is also cumulating, with several instances provided by Fourier Transform Infrared spectroscopy (FT-IR),[26] X-ray absorption spectroscopy (XAS),[20,26,27] transmission electron microscopy (TEM),[28] or H_2 temperature-programmed desorption (H_2-TPD).[29] In this respect, some of us have recently investigated the modifications undergone by a Pt/Al_2O_3 catalyst when varying the hydrogenation conditions by simultaneous XAS-DRIFT-MS measurements performed under *operando* conditions.[26] When reducing the H_2 concentration, a progressive modification of the coordination number and of the Pt–Pt bond distances was observed, indicating the occurrence of a structural change in the Pt nanoparticles. Four different top Pt–H species were detected at the Pt nanoparticles surface, whose amount initially increased when reducing the H_2 concentration up to a maximum, after which they completely disappeared. This counterintuitive behavior was attributed to the conversion of multifolded Pt–H species (not visible by IR techniques because they are obscured by the intense vibrational modes of the Al_2O_3 support) into top ones (which instead are detected by IR), as predicted by DFT calculations.

To access the complete vibrational spectrum of Pt–H species, inelastic neutron scattering (INS) spectroscopy coupled with advanced DFT simulations is mandatory.[30−32] This method is well-known for providing detailed information about all the H-containing species in several classes of samples[33] in the form of vibrational spectra. This is possible thanks to the lightweight and the high neutron scattering cross-section of ^1H nuclei, as well as to the absence of selection rules,

which make INS particularly sensitive toward all the vibrational modes involving H atoms. The potential of this coupled approach was recently shown in the work of Parker et al.,[34] who compared the INS spectrum of an unsupported $Pt_{44}H_{80}$ tetradecahedron model with the experimental spectra of hydrogen on Pt black and of a few Pt-based catalysts on different supports and with different metal loading and particle size. However, the effects of the support and of the Pt nanoparticle size, shape, and the H-coverage were never systematically investigated either computationally or experimentally. In the present work, we systematically simulated the INS spectra of a large pool of $Pt_xH_y/\gamma\text{-}Al_2O_3$ models ($13 \leq x \leq 55$), and we compared them with the experimental INS spectra of a highly dispersed Pt/Al_2O_3 catalyst under two markedly different H-coverage conditions. We obtained a complete description of the H_2-induced dynamics of Al_2O_3-supported Pt nanoparticles as a function of the temperature and of the $P(H_2)_{eq}$, pointing out details concerning the H atoms' coordination mode, the Pt clusters morphology and size, as well as the impact of the support.

2. EXPERIMENTAL AND METHODS

2.1. Sample Preparation. The 5 wt % Pt/Al_2O_3 catalyst was prepared by the Catalyst Division of Chimet S.p.A. following a deposition−precipitation proprietary protocol similar to that reported by Kaprielova et al.[35] using a high surface area transition alumina (SSA = 116 m^2g^{-1}; pore volume = 0.41 cm^3g^{-1}) as the support. After the Pt deposition, the sample was water-washed and then dried at 120 °C overnight. The same sample was the object of an extensive experimental investigation in the past years as reported in ref 26. The catalyst is characterized by a high metal dispersion (D = 63%) as determined by means of the H_2/O_2 titration method[15] and confirmed by both TEM and XAS.[26] The analysis of TEM pictures over more than 700 particles indicated a narrow size distribution corresponding to 1.4 ± 0.4 nm.

2.2. Inelastic Neutron Scattering (INS) Spectroscopy. Two INS experiments were performed on the Pt/Al$_2$O$_3$ catalyst under different P(H$_2$)$_{eq}$ and temperature conditions.[36,37] In the following, the two experiments will be labeled as (1) and (2). Prior to both the INS measurements, the sample was degassed in dynamic vacuum up to 10^{-3} mbar in order to remove physisorbed water, then reduced in H$_2$ atmosphere, and finally further outgassed in order to remove the water and the residual H atoms adsorbed on the Pt clusters which may have been generated during the reduction step. The effective removal of these residual Pt−H species was verified by comparing the INS spectrum of the reduced Pt/Al$_2$O$_3$ catalyst with that of the bare Al$_2$O$_3$ support after degassing at 393 K, as shown in Figure S1 in the Supporting Information. The two INS spectra are almost identical, indicating that there are no residual Pt−H species or, if present, they are below the spectral sensitivity. The sample activation preceding the INS measurements in the two experiments presented some differences, as schematically shown in Figure 1a: for experiment (1), both the outgassing and reduction steps were performed at a temperature of 393 K. For experiment (2), instead, the outgassing steps were performed at 573 K and the reduction in H$_2$ at 393 K. In both cases, the sample outgassing steps were performed at a significantly higher temperature than the measurement temperature, in order to avoid any further removal of the hydroxyl group at the surface of the alumina during the measurement which, in turn, would result in changes in the spectral features. All the subsequent sample handling was performed inside a glovebox in order to prevent any contamination with moisture and catalyst reoxidation.

Both experiments were performed on the IN1-Lagrange instrument[38] at the ILL in Grenoble, France, which allows measuring energy transfer values up to 4000 cm^{-1} (500 meV) with an energy resolution of $\Delta E/E = 2\%$. All the spectra were collected in the 90−2900 cm^{-1} range of energy transfer by using the Si311 and Cu220 monochromators. For both the experiments, the sample was inserted into an aluminum cell mounted on a gas injection stick and connected to a gas injection device with calibrated volumes.

The two experiments were designed to investigate the sample under different H-coverage conditions, higher for experiment (1) than for experiment (2). Figure 1B locates the two experiments in the P(H$_2$)$_{eq}$-T thermodynamic diagram, which displays the expected most stable morphologies and H-coverages for the case of Pt$_{13}$H$_y$/γ-Al$_2$O$_3$(100) system as calculated in ref 19. The two chosen points in the diagram correspond to very different DFT-predicted H-coverage levels (Pt$_{13}$H$_{34}$ for experiment (1) and Pt$_{13}$H$_{6-18}$ for (2)) but also different morphologies (cuboctahedric geometry for experiment (1), and biplanar for (2)).[19] It has to be noted that some differences in the thermodynamic plot are expected when passing from the Pt$_{13}$H$_y$ clusters to larger Pt$_x$H$_y$ nanoparticles: for instance, analogous simulations on Pt−H species over extended Pt(111) and Pt(100) surface (representative of large Pt particles) pointed out an easier removal of Pt−H species in comparison with Pt$_{13}$H$_y$.[19] Considering this and the fact that our catalyst exhibits a particle size distribution of 1.4 ± 0.4 nm, our analysis included models with larger sizes than Pt$_{13}$, as explained in section 2.3.

Experiment (1) consisted in measuring the sample under vacuum and at room temperature in the presence of a 160 mbar equilibrium pressure of H$_2$, which was reached with incremental H$_2$ doses. The measurements were performed at 25 K with the use of a CCR (closed cycle refrigerator) cryostat. Experiment (2) posed some additional challenges, since lower P(H$_2$)$_{eq}$ and higher temperatures were required to be able to access a significantly lower level of H coverage than in experiment (1). In fact, keeping the same temperature as in experiment (1) and simply decreasing P(H$_2$)$_{eq}$ would not have been as effective in decreasing the H-coverage, as shown in Figure 1B. Hence, for this experiment the sample was measured under vacuum and in the presence of a smaller amount of H$_2$ at a temperature of 450 K. The dosed H$_2$ was almost completely adsorbed by the sample, making the residual equilibrium pressure not detectable by our equipment. However, the amount of H$_2$ was calculated by applying the perfect gas law, being all the volumes known, and corresponds to a H:Pt ratio of 0.76. Both the gas dosing and the measurement were conducted at the same temperature of 450 K without removing the sample stick from the instrument. This was possible thanks to a new heating insert setup inside the CCR cryostat now available on the IN1-Lagrange instrument. Previous test measurements on this same sample demonstrated that measuring the INS spectra at temperature higher than 25 K (up to 573 K) does not cause a deterioration of the signal but only a change in the background profile at low energy transfer values that is due to the variation in the population of the vibrational energy levels. To compare the spectra measured during experiment (2) with those measured at cryogenic temperature during experiment (1), the former were corrected by the corresponding Bose−Einstein factor. Further details on this procedure and the original uncorrected spectra are reported in the Supporting Information, section S2.

2.3. Computational Details. The experimental INS spectra were interpreted on the basis of DFT simulations on Pt$_x$H$_y$/γ-Al$_2$O$_3$ model systems. All the structural and vibrational simulations were performed with the VASP package,[39,40] by employing the PBE functional[41] and the projector augmented wave (PAW) pseudopotentials,[42] with a cutoff energy of 400 eV and a convergence criterion for SCF cycles of 10^{-6} eV. The models consist in slabs of a dehydroxylated γ-Al$_2$O$_3$(100) surface or of partially hydroxylated γ-Al$_2$O$_3$(110) surface (following refs 43−46), upon which Pt$_x$H$_y$ nanoparticles at various H-coverages and for various sizes (x = 13, 34, 38, 55) were supported. The sizes chosen for these Pt clusters correspond to the range of sizes measured by TEM (1.4 ± 0.4 nm),[26] as shown in Table S2 in the Supporting Information. Hereafter, we will use the shorted notation Pt$_x$H$_y$/γ-Al$_2$O$_3$(100) and Pt$_x$H$_y$/γ-Al$_2$O$_3$(110) to refer to models supported on the two different γ-Al$_2$O$_3$ surfaces, without indicating explicitly the hydroxylation degree anymore. Some complementary calculations have also been run on hydrogenated Pt(111) and Pt(100) surfaces considering previous analysis reported in[19] and described in more detail in section S7 in the Supporting Information.

The most stable structures of the Pt$_{13}$H$_y$ models at various H-coverages on the two γ-Al$_2$O$_3$ surfaces were previously obtained by means of velocity scale molecular dynamics calculations followed by a quenching procedure as described in refs 19,20, while the larger models were obtained in the present work by static optimization because of computational cost. Further computational details over the simulated models are reported in section S3 of the Supporting Information. Overall, 26 INS spectra of Pt$_x$H$_y$/γ-Al$_2$O$_3$(100) and Pt$_x$H$_y$/γ-Al$_2$O$_3$(110) models were computed. For all the systems, the geometry optimization and frequency calculations (finite

differences, elongation ±0.01 Å) were performed, and finally the obtained outputs were elaborated with the software aCLIMAX[47] to simulate the corresponding INS spectra. Considering the relatively low amount of Pt−H species in the sample and on the basis of our previous experience,[48] we only included the $0 \rightarrow 1$ transition in the calculated INS spectra. For the analysis of the data in experiment (1) we also performed a linear combination fit analysis: more details about this procedure are described in the Supporting Information, section S4.

3. RESULTS AND DISCUSSION

3.1. Experimental INS Spectra. The INS spectra of the bare Pt/Al$_2$O$_3$ catalyst activated following procedures (1) and (2) are compared in Figure 2A. They are dominated by the
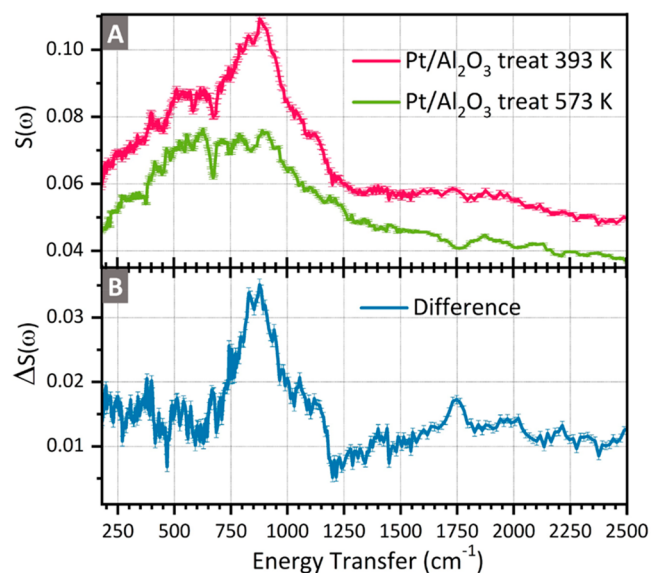
Figure 2. Experimental INS spectra of the Pt/Al$_2$O$_3$ catalyst activated following procedures (1) and (2) (A) and their difference, highlighting the spectral profile of the −OH groups at the alumina support which are removed in the 393−573 K activation temperature range (B).

signals relative to the H-containing species in the sample, which are assigned exclusively to the −OH groups at the alumina surface (since no residual Pt−H signals are expected, as justified in section 2.2). More precisely, the very broad band ranging between 200 and 1200 cm^{-1} is attributed in the literature to various bending and deformation modes of the −OH groups at the Al$_2$O$_3$ surface.[49] According to the theoretical calculations performed in this work on the γ-Al$_2$O$_3$(110) supported models, also the riding modes of Al$_2$O$_3$ (i.e., vibrational modes of the Al$_2$O$_3$ surface enhanced in intensity by the presence of the bonded −OH groups) contribute to this spectral range. All those vibrational modes combine to a large extent, with the Al$_2$O$_3$ riding modes contributing mainly to low energy transfer values and the deformation and bending modes of the surface −OH groups to higher ones, but without a clear delimitation between them. Since the −OH groups are progressively removed as the treatment temperature increases,[45,46,50] the difference between the two spectra (Figure 2B) is straightforwardly assigned to the surface hydroxyl groups loss between the temperature of 393 and 573 K during the sample activation.

Figure 3A,C compare the INS spectra of the Pt/Al$_2$O$_3$ samples in vacuum and in the presence of H$_2$ following the protocols described for experiment (1) and (2), respectively. Following H$_2$ introduction, the spectra are still dominated by the characteristic features of the hydroxyl species at the Al$_2$O$_3$ surface, but the difference spectra (Figure 3B,D) pointed out the appearance of new bands which are attributed to the formation of new hydrogenous species, including Pt−H species at the surface of the Pt nanoparticles.[26] The intensity of the difference spectrum is greater for experiment (1) than for experiment (2), as expected since the higher $P(\text{H}_2)_{\text{eq}}$ and the lower temperature favored the formation of a larger amount of Pt−H species. The difference spectra obtained in the two cases also exhibit clearly different spectral profiles, characterized in experiment (1) by a main band centered at about 550 cm^{-1} and other weaker bands in the 800−1550 cm^{-1} range, and in experiment (2) by a much broader signal centered at about 750 cm^{-1}.

3.2. Theoretical INS Spectra. In order to precisely assign the experimentally observed Pt−H vibrations, we systematically simulated the INS spectra of 26 different Pt$_x$H$_y$/γ-Al$_2$O$_3$ models. To ease their interpretation, the spectral contributions of top, 2-fold bridge, 3-fold hollow, and interfacial Pt−H species were separated. Representative examples of each typology of Pt−H species are illustrated in Figure 4A (also displaying their typical Pt−H distances). On this basis, it was possible to assign the vibrational modes involving each class of Pt−H species to specific frequency ranges and to analyze the spectral differences among the models, as summarized in Figure 4B.

The contributions between 250 and 800 cm^{-1} correspond to the bending modes of all the Pt−H species vibrating together. These modes are strongly coupled, and only for the highest symmetry models (Pt$_{13}$H$_{32-36}$ or Pt$_{55}$H$_{91}$) is it possible to partially distinguish between the bending modes of top Pt−H species (spanning over the 500−580 cm^{-1} range) and of bridge species (covering the 530−710 cm^{-1} interval). The energy transfer range 800−1600 cm^{-1} is dominated by the stretching modes of the multifolded Pt−H species. The ν(Pt−H) of 3-fold hollow species is observed in the 850−1300 cm^{-1} range, while the asymmetric and symmetric stretching modes of 2-fold bridged species fall in the 800−1200 cm^{-1} and 1200−1600 cm^{-1} ranges, respectively. Finally, the ν(Pt−H) mode of top species contributes within the 2050−2380 cm^{-1} range.

For bridge Pt−H species, larger asymmetry in bond lengths corresponds to ν(Pt−H) modes spread over a larger interval of frequencies. In most cases, very asymmetric Pt−H bond lengths were observed when the Pt atom is directly bonded to the support. These Pt−H species exhibit Pt−H−Pt bond lengths which pose them in an intermediate position between pure bridge and top species and, for this reason, they were labeled as top-bridge species (see Figure 4A, right as an example). These species exhibit stretching modes within the 1600−1800 cm^{-1} interval, the more asymmetric the bond, the higher the stretching frequency. Top sites facing the support can also exhibit a peculiar elongation of the Pt−H bond, often above 1.60 Å instead of the usual 1.57−1.58 Å value (Figure 4A, central), which corresponds to a shift of the stretching mode at a frequency lower than 2000 cm^{-1}. These interfacial Pt−H species are favored in close proximity to low-coordinated pentahedral Al^{3+} sites at the support surface, with H−Al distances of about 2 Å. For both interfacial top and top-bridge Pt−H species, the effect of the support is stronger
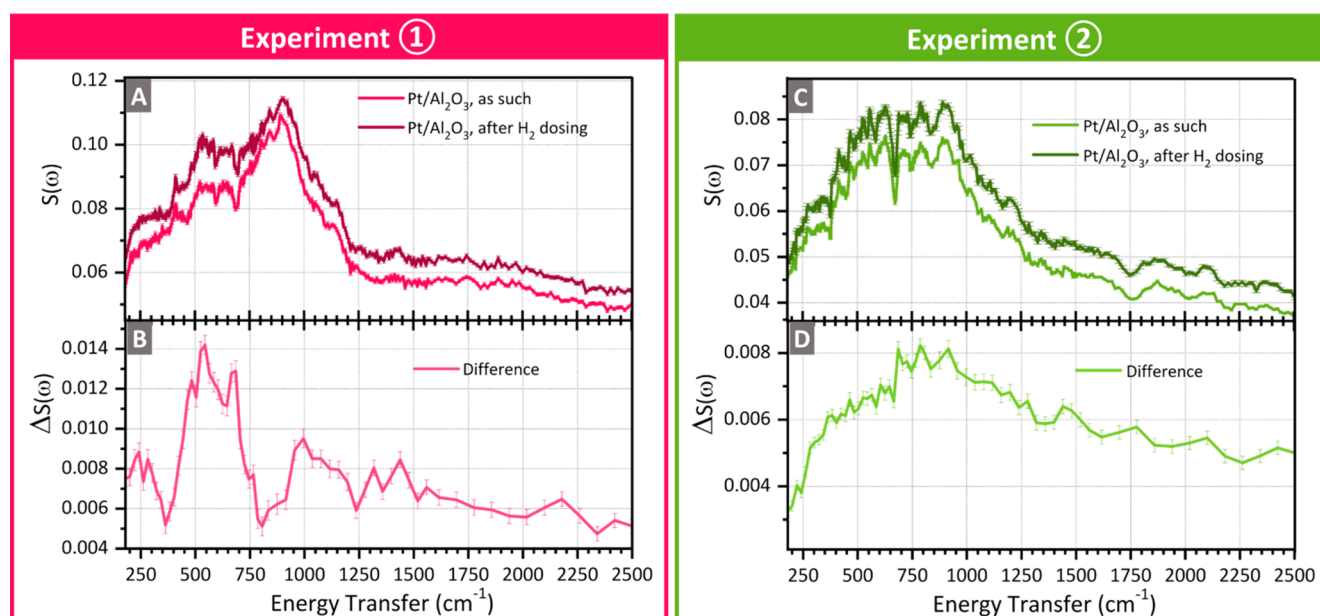
Figure 3. (A) experimental INS spectra of Pt/Al$_2$O$_3$ activated according to procedure (1) and of the same sample after dosing H$_2$ up to a $P(\mathrm{H}_2)_{eq} =$ 160 mbar at room temperature. (B) Difference between the two spectra shown in panel A. (C) Experimental INS spectra of Pt/Al$_2$O$_3$ activated according to procedure (2) and of the same sample after dosing a low amount of H$_2$ (resulting in a negligible residual pressure and to a H:Pt ratio of 0.76) at a temperature of 450 K. Both the spectra have been corrected for the temperature effect. (D) Difference between the two spectra shown in panel C. In panels B and D, the subtraction was performed over 5-points rebinned spectra in order to reduce the error bars.

when the Pt nanoparticles are placed on the completely dehydroxylated γ-Al$_2$O$_3$(100) surface than on the partially hydroxylated γ-Al$_2$O$_3$(110). More detailed examples of the spectral features of top-bridge and interfacial top Pt–H species, together with the values for the Pt–H and H–Al distances involved, are shown in section S5 in the Supporting Information.

A selection of the simulated INS spectra is shown in Figure 5, while the others are shown in the Supporting Information, section S6. The effects of increasing the Pt nanoparticles' size (from left to right) and of the H-coverage (from top to bottom) are highlighted. In all the cases, the simulated spectra have been also decomposed into the contributions of top, 2-fold bridge, and 3-fold hollow Pt–H species. All the vibrational modes are highly collective, meaning that each of them simultaneously involves several Pt–H species over the whole nanoparticle. This makes the final simulated spectra a unique fingerprint depending on the model shape, size, total H-coverage and typology of Pt–H species formed at the surface of the Pt nanoparticles. In addition, the absolute intensity of the INS spectra is able to provide information about the amount of H present in the model, as the integrated area of the spectra linearly scales with the H-content (analogously to what was pointed out in the past on other classes of samples).[51]

The effect of increasing the H-coverage and of the consequent morphological reconstruction[19] on the INS spectra of Pt$_{13}$H$_y$/γ-Al$_2$O$_3$(100) models can be observed in Figure 5A–C. The first model (Figure 5A) consists in a biplanar structure in strong interaction with the support and featuring a comparable number of bridge and top Pt–H species. Its INS spectrum is dominated by a very broad group of bands corresponding to the $\delta(\mathrm{Pt-H})$ modes, with a maximum at about 400 cm^{-1}. As a consequence of the irregular shape of the model and of the variable lengths of the Pt–H bonds, the frequencies of the $\nu(\mathrm{Pt-H})$ are very spread over a large

interval of frequencies. The effect of the support on the interfacial Pt–H species is highlighted by the presence of bands in the 1800–2000 cm^{-1} range, as commented above. The simulated spectrum drastically changes when the reconstruction to a cuboctahedral structure is initiated (Pt$_{13}$H$_{20}$ in Figure 5B), both as a consequence of the morphological modification and of the conversion of top Pt–H species into bridge ones, resulting in bands spanning over much narrower frequency intervals (500–800 cm^{-1} for the $\delta(\mathrm{Pt-H})$ modes and 800–1600 cm^{-1} for the $\nu(\mathrm{Pt-H})$ ones). Similar features are retained for the completely reconstructed model in cuboctahedral geometry (Figure 5C), where the main changes arise from the formation of new top Pt–H species upon the complete H-solvation of the nano-particle (contributing in the 2000–2250 cm^{-1} range). Analogous trends were observed for the Pt$_{13}$H$_y$/γ-Al$_2$O$_3$(110) models (Figure S8 in the Supporting Information), with the most significant spectral differences arising from the lack of top-bridge and interfacial top Pt–H features.

By moving from left to right in Figure 5, it is instead possible to evaluate the effect of the change in shape and size of the hydrogenated Pt nanoparticle on the INS spectra. Model Pt$_{34}$H$_{54}$ (Figure 5D) features a quite irregular geometry, resulting in a spectrum where the $\delta(\mathrm{Pt-H})$ and the $\nu(\mathrm{Pt-H})$ bands of both bridge and top species span over a large frequency interval. Only one and very asymmetrical hollow Pt–H site is present. From Pt$_{38}$H$_{72}$ onward, the considered models are large enough to expose well-recognizable facets. Indeed, model Pt$_{38}$H$_{72}$ (Figure 5E) corresponds to a truncated octahedron structure exposing quite large hexagonal Pt(111) facets and smaller squared Pt(100) ones, while the Pt$_{55}$H$_y$ models (Figure 5F–H) were optimized starting from a cuboctahedron structure exposing triangular Pt(111) facets and squared Pt(100) ones. The exposed facets are shown more clearly in Figure S7 in the Supporting Information. As bridge
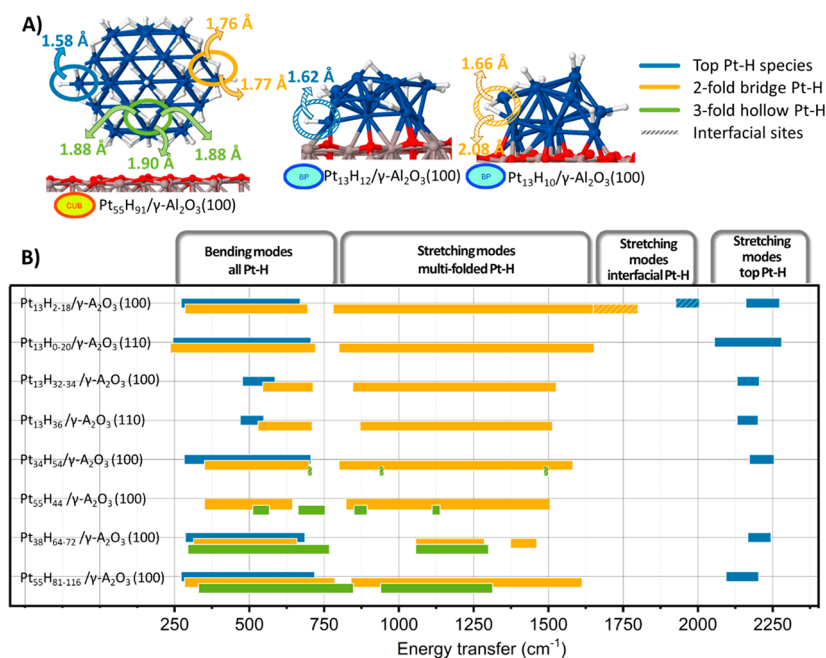
Figure 4. (A) Representative geometry of top (blue), 2-fold bridge (yellow), 3-fold hollow (green), and interfacial (lined pattern) Pt−H species. The typical bond lengths for each of these Pt−H species are also reported. (B) Summary of the characteristic position of the INS signals for the different types of Pt−H species in the simulated models. The general assignment into stretching and bending for top, bridge, hollow, and interfacial Pt−H is also indicated.
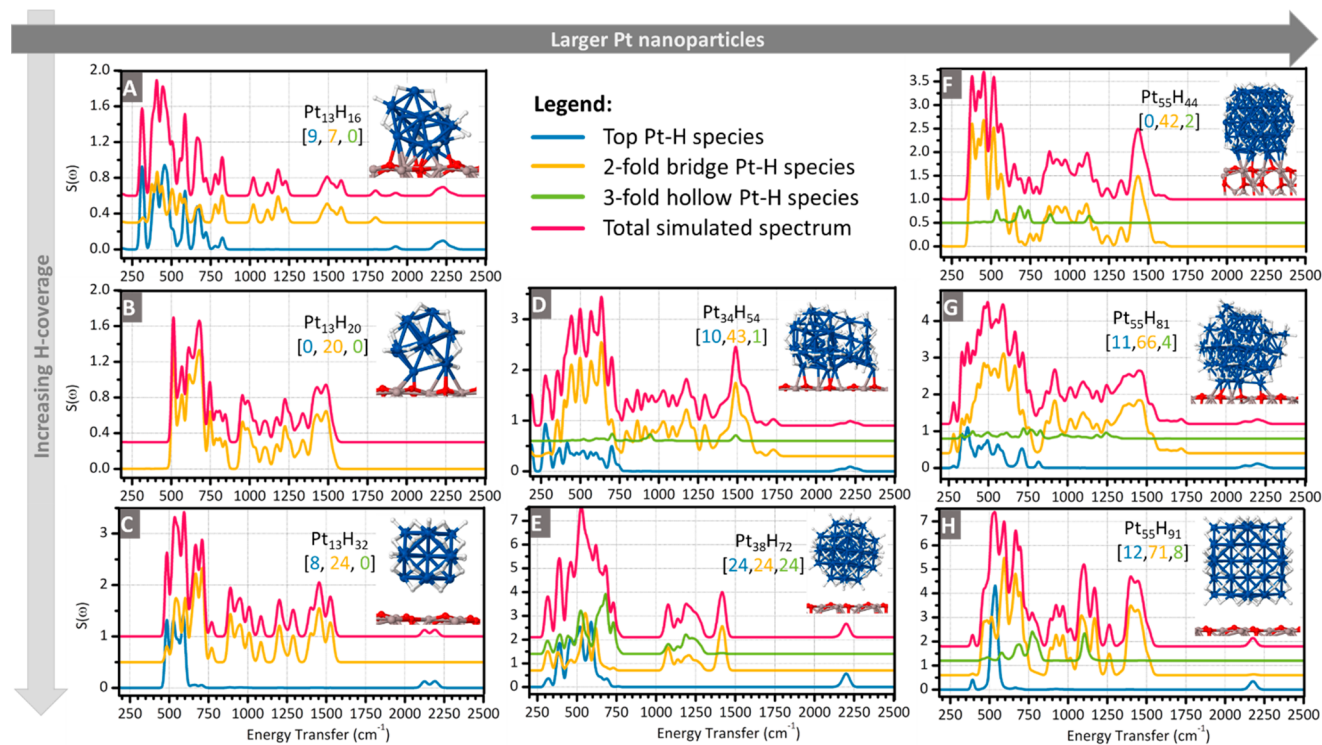
Figure 5. Simulated INS spectra for a selection of Pt_xH_y/γ-$Al_2O_3(100)$ models, featuring different sizes, morphologies, and H-coverages. The shown models correspond to (A) $Pt_{13}H_{16}$, (B) $Pt_{13}H_{20}$, (C) $Pt_{13}H_{32}$, (D) $Pt_{34}H_{54}$, (E) $Pt_{38}H_{72}$, (F) $Pt_{55}H_{44}$, (G) $Pt_{55}H_{81}$, (H) $Pt_{55}H_{91}$. The spectra are decomposed into the contributions of top (blue), 2-fold bridge (orange) and 3-fold hollow (green) Pt−H species. The geometry of the models corresponding to each spectrum are reported, together with their Pt_xH_y stoichiometry and the number of top, bridge, and hollow Pt−H species present in the model in the form [top, bridge, hollow].

species are the most stable on the Pt(100) surface[52] and fcc hollow ones are the most stable on the Pt(111) one,[53] the number of bridge and hollow Pt−H species in the optimized geometries vary greatly depending on the most exposed facets

in the model. Top Pt−H species is preferentially located at the edges and corners between the faces. The simulation of a $Pt_{55}H_{91}$ model with icosahedral shape was also attempted, but its geometry collapsed onto a distorted cuboctahedron both in
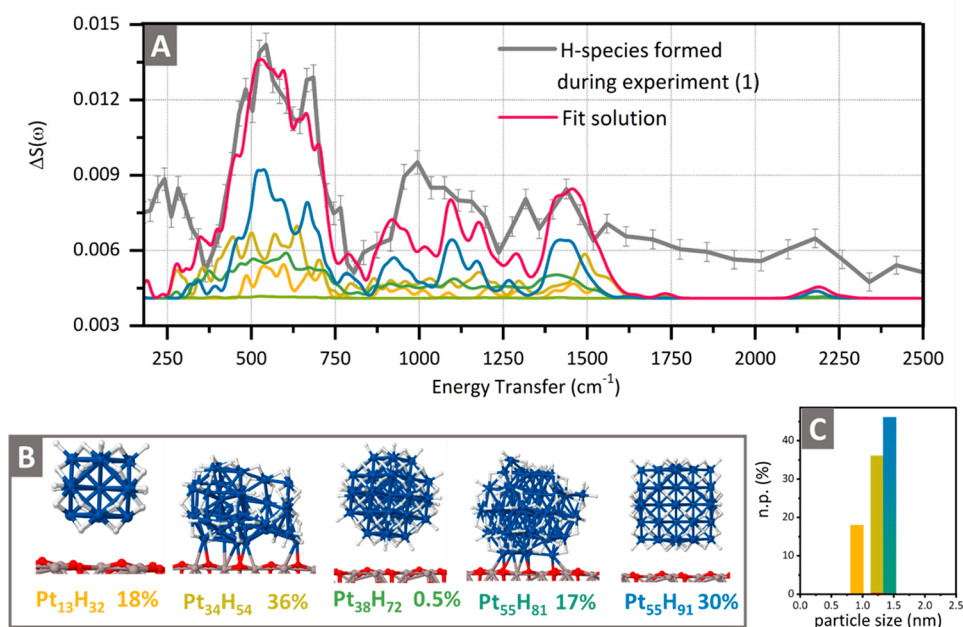
Figure 6. (A) Experimental INS difference spectrum containing the fingerprint of the Pt−H species formed at Pt/Al$_2$O$_3$ at high H-coverage compared with the best linear combination fit performed with the simulated spectra of Pt$_{13}$H$_{32}$, Pt$_{34}$H$_{54}$, Pt$_{38}$H$_{72}$, Pt$_{55}$H$_{81}$, and the two Pt$_{55}$H$_{91}$ models on the dehydroxylated γ-Al$_2$O$_3$ (100) surface. (B) Models included in the fit and their weight in the final solution. (C) Corresponding simulated Pt nanoparticles size distribution.

the preliminary optimization performed on the isolated nanoparticle and on the one including the support, suggesting that an icosahedral habit does not correspond to an energetic minimum for small hydrogenated Pt nanoparticles. The spectrum of the truncated octahedron Pt$_{38}$H$_{72}$ model (Figure 5E) exhibits a large δ(Pt−H) band spanning over the 250−750 cm^{-1} interval and a relatively narrow spectral region corresponding to the ν(Pt−H) of multifolded species between 1000 and 1500 cm^{-1}. The Pt$_{55}$H$_y$ models instead (Figure 5F−H), corresponding to larger cuboctahedral-based geometries, exhibit spectra characterized by a progressive shift of the δ(Pt−H) region from lower to higher frequencies as the H-coverage increases, with the ν(Pt−H) of multifolded species spanning over the whole 800−1600 cm^{-1} interval. In many respects, the two groups of cuboctahedral models Pt$_{55}$H$_y$ and Pt$_{13}$H$_y$ show similar spectral profiles, while the truncated octahedra Pt$_{38}$H$_y$ result readily distinguishable. Also in this case, very symmetric structures can be optimized only at the highest H-coverage levels.

Finally, in addition to those Pt$_x$H$_y$/γ-Al$_2$O$_3$ models, the INS spectra of bridged Pt−H species at the extended Pt(100) surface and the top and hollow ones at the Pt(111) surface were also simulated. The obtained spectra are shown and commented in the Supporting Information, section S7.

Generalizing the observations summarized above, the simulated INS spectra arise from the combination of multiple factors, among which are the following: (i) the ratio between top, bridge, and hollow Pt−H species; (ii) their relative position; (iii) the shape of the model, (iv) its size, and (v) its interaction with the support, in a way that makes each INS spectrum the fingerprint of the corresponding model. It is important to notice that the proposed assignments are in generally good agreement with those proposed in the past not only for INS spectra[30,31] but also for other vibrational spectra (such as FT-IR[26] or EELS[52]), as well as with other computational simulations.[34] However, most of the assign-

ments in the literature were based on measurements on extended Pt surfaces or simulations on isolated Pt clusters. In this regard, our results provide a picture closer to the real catalyst under H$_2$ atmosphere, since they also take into account the modifications introduced by the support and the effects of the size, shape, and H-coverage of the Pt nanoparticles.

3.3. Comparison between Experiments and Simulations. *3.3.1. Higher H-Coverage Conditions.* On the basis of the information collected from the simulated INS spectra presented in section 3.2, we proceeded with the interpretation of the difference experimental INS spectrum containing the fingerprint of the Pt−H species formed during experiment (1) (Figure 3B). None of the models is able to completely describe the experimental spectrum alone: indeed, Pt/Al$_2$O$_3$ is characterized by a more heterogeneous nature than any of the considered models in terms of nanoparticles size, shape, and interaction with the support. For this reason, a linear combination fit analysis of the experimental spectrum with the simulated ones was performed. In order to ensure the robustness of the fit calculation, we had to limit the number of simulated functions to be included, which were selected on the basis of the best agreement with the experimental spectrum to be fitted. Following the procedure explained in more detail in section S4 in the Supporting Information, five models were included: Pt$_{13}$H$_{32}$, Pt$_{34}$H$_{54}$, Pt$_{38}$H$_{72}$, Pt$_{55}$H$_{81}$ and Pt$_{55}$H$_{91}$, which are in good agreement with the observed TEM sizes (as explained in section S3 in the Supporting Information). According to the linear combination fit analysis reported in Figure 6, the following interpretations can be proposed:

(1) The main model contributing to the fit is the irregular model Pt$_{34}$H$_{54}$ (accounting for 36%), followed by the cuboctahedral based models Pt$_{55}$H$_{91}$ and Pt$_{55}$H$_{81}$ (30% and 17%) and then by the smaller cuboctahedron Pt$_{13}$H$_{32}$ (18%).

(2) All the models included into the fit are characterized by a H:Pt ratio larger than 1. However, the model with the highest H-coverage ($Pt_{55}H_{116}$, see Supporting Information, Figure S6D) is characterized by remarkably different spectral features, suggesting that the H-coverage reached during this experiment was not the highest possible.

(3) In all the included models, the Pt nanoparticle shows a weak interaction with the support, in particular the cuboctahedral $Pt_{13}H_{32}$ and $Pt_{55}H_{91}$ models. The fit highlights that both regular geometries (such as $Pt_{13}H_{32}$ and $Pt_{55}H_{91}$) and less regular ones (such as $Pt_{55}H_{81}$ and, even more so, $Pt_{34}H_{54}$) are needed to describe the experimental spectrum. Among the regular shapes, cuboctahedra such as $Pt_{13}H_y$ and $Pt_{55}H_y$ models are favored over the $Pt_{38}H_y$ truncated octahedron, whose occurrence according to the fit is lower than 1%.

(4) It was not possible to discriminate between nanoparticles supported on the two considered γ-Al_2O_3 surfaces (dehydroxylated (100) one or partially hydroxylated (110)) as the spectral features corresponding to the two sets of models were extremely similar, in particular for nanoparticles in very weak interaction with the support (compare Figure 5A−C with Figure S8 in the Supporting Information).

Quite remarkably, the particle size distribution suggested by the linear combination fit analysis (Figure 6C) is in very good accordance with that determined experimentally by means of TEM and confirmed by XAS.[26]

Although the best linear combination fit reproduces most of the experimental bands, some spectral regions (in particular around 250, 1000, and 1300 cm^{-1}) are not well described. Since the spectral features are strongly related to the shape and size of the nanoparticle, the main possible source for this residual discrepancy could be attributed to the lack of diversity in the considered nanoparticle morphology, size, and/or H-coverage in our simulations set. One possibility is given by Pt−H species formed over more extended Pt(100) and Pt(111) surfaces, which could be exposed by the largest nanoparticles in the sample (although rare, nanoparticles as large as 2.5−3.0 nm were detected by TEM[26]). For exploring this possibility, the INS spectra of bridged Pt−H species on the Pt(100) extended surface, and top and hollow Pt−H at the Pt(111) one were also considered (Supporting Information, section S7). On the basis of those simulations, the missing signal at 250 cm^{-1} may be attributed to top Pt−H species at extended Pt(111) surfaces, while hollow Pt−H species at Pt(111) surfaces might be responsible of the signal at 1000 cm^{-1}. The possible attribution to other H containing species instead, such as new −OH species formed at the support, is presently considered improbable because the spectral ranges do not match, as shown in Figure S11 in the Supporting Information.

3.3.2. Lower H-Coverage Conditions. In the case of the INS spectra measured during experiment (2), the amount of new hydrogenous species formed upon dosing H_2 was significantly lower than in experiment (1), resulting in a difference signal which was too weak and broad to perform a quantitative evaluation. However, a qualitative assignment was still possible by comparing the available experimental and simulated data, as summarized in Figure 7. First of all, the most intense signal at about 800 cm^{-1} exhibits a remarkable similarity to that reported in Figure 2B and ascribed to surface
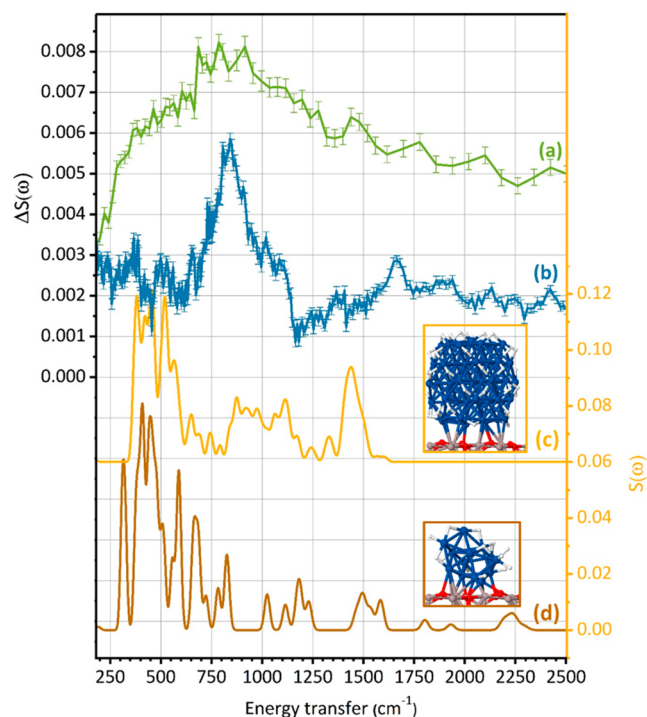
Figure 7. Comparison among: (a) the differential INS spectrum containing the spectral fingerprint of the species formed on Pt/Al_2O_3 during experiment (2) (same as in Figure 3D); (b) differential INS spectrum ascribed to surface −OH species removed in the temperature range 393−573 K (same as in Figure 2B, scaled by a factor 6 for a better comparison); (c) simulated spectrum of the low-coverage $Pt_{55}H_{44}/\gamma$-Al_2O_3(100) model, and (d) simulated spectrum of $Pt_{13}H_{16}/\gamma$-Al_2O_3(100). The geometries of the two models are shown for clarity, and the intensities of the simulated spectra were normalized to the number of H atoms in the respective models.

−OH groups. This suggests that at a significant part of the new H-containing species formed during this experiment are due to the formation of new surface −OH groups, as a result of H-spillover.[54,55] The presence of this signal in the difference spectra of experiment (2), and not of experiment (1), could be a consequence of the different activation procedures followed in the two experiments (Figure 1A). Indeed, in the present experiment, the sample was activated at a significantly higher temperature (573 vs 393 K), and thus a larger fraction of surface −OH groups was lost during activation. According to previous DFT calculations,[45,46,56,57] the γ-Al_2O_3(110) lateral surface is the most sensitive to −OH group loss within this interval of treatment temperature, while the (100) is almost completely dehydroxylated in this range. Furthermore, previous reports concluded that exposed low-coordinated Al^{3+} sites are necessary for the occurrence of H-spillover[54] and that this typology of highly reactive sites exists on the γ-Al_2O_3(110) surface and stabilizes H-species upon high temperature treatment.[56,58] More generally, such defective sites may also exist on the edges of alumina platelets as recently shown.[59] On these premises, we hypothesize that the H-spillover process observed in our experiment is related to the formation of new −OH groups at the Al_2O_3 (110) surface. However, we cannot exclude that the observed difference arose because of kinetics reasons. In fact, H_2 was dosed at a significantly higher temperature in experiment (2) than in (1) (450 vs 300 K). Furthermore, in (2) the whole measurement

was performed at that same temperature, while in (1) the sample was quenched at 25 K prior to the measurement. Thus, H-spillover could have been kinetically favored during experiment (2) and not during (1).

The signal at lower energy transfer (centered at about 450 cm^{-1}), instead, falls in the range typical for $\delta(Pt-H)$ modes, in particular for models characterized by a H:Pt ratio close to 1 or lower and exhibiting a strong interaction with the γ-Al_2O_3 support. As an example, the structures and the simulated spectra for $Pt_{55}H_{44}$ and $Pt_{13}H_{16}$ are shown in Figure 7c,d. The broad tail in the experimental INS spectrum at energy transfer values higher than 950 cm^{-1} is also compatible with the signals of $\nu(Pt-H)$ of bridge and hollow Pt−H species. In particular, the signal at about 1475 cm^{-1} strongly resembles the profile of both the simulated spectra shown in Figure 7.

Overall, these qualitative observations are in accordance with the thermodynamic calculations on $Pt_{13}H_y$ clusters[19,20] that, at the temperature and $P(H_2)_{eq}$ conditions here adopted, predicted a H coverage in the range $Pt_{13}H_{6-18}$, confirming that it is possible to distinguish between low and high H-coverage in supported Pt_xH_y nanoparticles from their INS spectra.

4. CONCLUSIONS

The reactive adsorption of H_2 with Pt nanoparticles on transition alumina is predicted to trigger significant changes in the nanoparticles morphology and in their interaction with the support as a function of temperature and $P(H_2)_{eq}$.[19,20] Although a few experimental studies by XAS and IR spectroscopy confirm the theoretical predictions, direct experimental evidence on all the types of surface Pt−H species and on their interconversion during Pt nanoparticles reconstruction are still limited. Herein, we addressed this challenge by analyzing the behavior of an industrial highly dispersed 5 wt % Pt/Al_2O_3 catalyst characterized by a narrow particle size distribution under hydrogenation conditions by means of INS spectroscopy combined with DFT simulations.

Two experiments were conducted under different H_2 pressure and T conditions, corresponding to higher H-coverages for experiment (1) than for experiment (2). Albeit the weak intensity of the difference INS spectra, the high sensitivity of modern spectrometers allowed us to obtain the INS fingerprints of the hydrogenous species generated under these two conditions. The two experimental spectra were interpreted on the basis of DFT and INS spectra simulations on 26 Pt_xH_y/γ-Al_2O_3 models.[19,20] Remarkable variations were observed as a function particle sizes (x), H-coverages (y/x), and morphologies, revealing that INS spectroscopy is able to provide a fine description of the Pt/Al_2O_3 system under different hydrogenation conditions. Two relevant γ-Al_2O_3 surfaces at different hydroxylation states were also considered: the completely dehydroxylated (100) surface and the partially hydroxylated (110) one (following refs 43,45,46). It was found that the type of support surface does not affect significantly the simulated INS spectra of the Pt−H species.

For experiment (1), the INS spectrum was satisfactorily fitted with a linear combination of a few simulated spectra corresponding to Pt nanoparticles characterized by a H:Pt ratio much larger than 1 and by a weak interaction with the alumina support. The analysis also pointed out that the best solution favors a particle size in the $Pt_{34}H_y$-$Pt_{55}H_y$ range, in good agreement with that determined by TEM and confirmed by XAS.[26] In addition, it allowed us to conclude the coexistence of

both irregular morphologies, such as $Pt_{34}H_{54}$, and very symmetric ones, such as $Pt_{55}H_{91}$. Also among the regular morphologies, cuboctahedra are strongly favored over truncated octahedra shapes. Some complementary contributions are suspected to originate from Pt−H species located on more extended Pt(111) surface present on a few larger Pt nanoparticles. Furthermore, it has to be noticed how the weakening of the interaction with the support upon complete solvation might also increase the probability for nanoparticles sintering, with possible consequences concerning the catalyst longevity and deactivation.

As for experiment (2) instead, the spectral interpretation was more challenging because of the very weak intensity and broadness of the difference spectrum. We were however able to proceed with a qualitative assignment: the spectral features of the newly formed hydrogenous species are compatible with the formation of new hydroxyls at the support surface, likely as a consequence of H-spillover from the metal nanoparticles to the support, and with the characteristic spectral features of Pt_xH_y nanoparticles with a H:Pt ratio close or lower than 1 and in strong interaction with the support, such as for the $Pt_{55}H_{44}$ or the $Pt_{13}H_{16}$ models.

Overall, our data confirm that Pt nanoparticles undergo important changes in terms of morphology, degree of interaction with the support and types of Pt−H species (top, bridge, hollow) formed as a function of the hydrogenation conditions (temperature and $P(H_2)_{eq}$), providing unprecedented vibrational spectra describing the variety of Pt−H species involved in the hydrogenation reactions. The present study is consistent with previously reported theoretical and experimental data, being at the same time able to make a further step in the description of the complexity and heterogeneity of real Pt/Al_2O_3 systems. While previous studies were mostly obtained from simulations and/or experiments performed on Pt surfaces or on isolated cluster systems, the present one is the first systematic investigation quantifying the effect of the particle size, morphology, and H-coverage by INS. It also shows a direct evidence of the occurrence of H-spillover, when the catalyst in preactivated at sufficiently high temperature to significantly reduce the density of −OH groups at the Al_2O_3 surface. Finally, we demonstrated the capability of INS spectroscopy, coupled with DFT simulation, to discriminate among Pt_xH_y nanoparticles stabilized under different experimental conditions.

As we underlined in the Introduction, Pt/Al_2O_3 are key catalysts widely used in numerous catalytic processes where dihydrogen is a crucial coreactant used during the activation process or during reaction. In all cases, H_2 partial pressure must be optimally tuned to control the process selectivity. Hence, from a catalytic standpoint, the results obtained in the present study translate into significant insights into the behavior of Pt/Al_2O_3 catalysts upon reductive H_2 atmosphere, the available reactive Pt−H species and their modification upon change in the temperature or the $P(H_2)_{eq}$. Beyond that, our study also provides a solid starting point to further investigate the ductility of the Pt active phase in the presence of reactants and under reaction conditions.

■ ASSOCIATED CONTENT

Ⓢ Supporting Information

The Supporting Information is available free of charge at https://pubs.acs.org/doi/10.1021/acscatal.2c00606.

Additional material concerning the experiment INS spectra and their data analysis, the simulated Pt_xH_y/γ-Al_2O_3 models and the corresponding calculated INS spectra (PDF)

■ AUTHOR INFORMATION

Corresponding Author

Eleonora Vottero — *Department of Chemistry, INSTM and NIS Centre, University of Torino, I-10135 Torino, Italy; Institut Laue-Langevin (ILL), 38042 Grenoble, France;* orcid.org/0000-0002-0183-0669; Email: eleonora.vottero@unito.it

Authors

Michele Carosso — *Department of Chemistry, INSTM and NIS Centre, University of Torino, I-10135 Torino, Italy*

Alberto Ricchebuono — *Department of Chemistry, INSTM and NIS Centre, University of Torino, I-10135 Torino, Italy*

Monica Jiménez-Ruiz — *Institut Laue-Langevin (ILL), 38042 Grenoble, France;* orcid.org/0000-0002-9856-807X

Riccardo Pellegrini — *Chimet SpA - Catalyst Division, I-52041 Viciomaggio Arezzo, Italy*

Céline Chizallet — *IFP Energies nouvelles, BP3-69360 Solaize, France;* orcid.org/0000-0001-5140-8397

Pascal Raybaud — *IFP Energies nouvelles, BP3-69360 Solaize, France;* orcid.org/0000-0003-4506-5062

Elena Groppo — *Department of Chemistry, INSTM and NIS Centre, University of Torino, I-10135 Torino, Italy;* orcid.org/0000-0003-4153-5709

Andrea Piovano — *Institut Laue-Langevin (ILL), 38042 Grenoble, France;* orcid.org/0000-0002-5005-6307

Complete contact information is available at:
https://pubs.acs.org/10.1021/acscatal.2c00606

Notes

The authors declare no competing financial interest.

■ REFERENCES

(1) Gjervan, T.; Prestvik, R.; Holmen, A. Catalytic Reforming. In *Basic Principles in Applied Catalysis*; Baerns, M., Ed.; Springer Berlin Heidelberg: Berlin, Heidelberg, 2004; pp 125−158.

(2) le Goff, P.-Y.; Kostka, W.; Ross, J. Catalytic Reforming. In *Springer Handbook of Petroleum Technology*, 2nd ed.; Hsu, C. S.; Robinson, P., Eds.; Springer: New York, 2017; pp 589−616.

(3) Bartok, M. Heterogeneous Catalytic Enantioselective Hydrogenation of Activated Ketones. *Curr. Org. Chem.* **2006**, *10* (13), 1533−1567.

(4) Sattler, J. J. H. B.; Ruiz-Martinez, J.; Santillan-Jimenez, E.; Weckhuysen, B. M. Catalytic Dehydrogenation of Light Alkanes on Metals and Metal Oxides. *Chem. Rev.* **2014**, *114* (20), 10613−10653.

(5) Chen, S.; Chang, X.; Sun, G.; Zhang, T.; Xu, Y.; Wang, Y.; Pei, C.; Gong, J. Propane dehydrogenation: catalyst development, new chemistry, and emerging technologies. *Chem. Soc. Rev.* **2021**, *50* (5), 3315−3354.

(6) Docherty, S. R.; Rochlitz, L.; Payard, P.-A.; Copéret, C. Heterogeneous alkane dehydrogenation catalysts investigated via a surface organometallic chemistry approach. *Chem. Soc. Rev.* **2021**, *50* (9), 5806−5822.

(7) Keppeler, M.; Bräuning, G.; Radhakrishnan, S. G.; Liu, X.; Jensen, C.; Roduner, E. Reactivity of diatomics and of ethylene on zeolite-supported 13-atom platinum nanoclusters. *Catal. Sci. Technol.* **2016**, *6* (18), 6814−6823.

(8) Kahlich, M. J.; Gasteiger, H. A.; Behm, R. J. Kinetics of the Selective CO Oxidation in H_2-Rich Gas on Pt/Al_2O_3. *J. Catal.* **1997**, *171* (1), 93−105.

(9) Gélin, P.; Primet, M. Complete oxidation of methane at low temperature over noble metal based catalysts: a review. *Appl. Catal., B* **2002**, *39* (1), 1−37.

(10) Sangnier, A.; Genty, E.; Iachella, M.; Sautet, P.; Raybaud, P.; Matrat, M.; Dujardin, C.; Chizallet, C. Thermokinetic and Spectroscopic Mapping of Carbon Monoxide Adsorption on Highly Dispersed Pt/γ-Al_2O_3. *ACS Catal.* **2021**, *11* (21), 13280−13293.

(11) Ren, X.; Lv, Q.; Liu, L.; Liu, B.; Wang, Y.; Liu, A.; Wu, G. Current progress of Pt and Pt-based electrocatalysts used for fuel cells. *Sustainable Energy Fuels* **2020**, *4* (1), 15−30.

(12) Heck, R. M.; Farrauto, R. J. Automobile exhaust catalysts. *Appl. Catal. A: Gen.* **2001**, *221* (1), 443−457.

(13) Gänzler, A. M.; Casapu, M.; Vernoux, P.; Loridant, S.; Cadete Santos Aires, F. J.; Epicier, T.; Betz, B.; Hoyer, R.; Grunwaldt, J.-D. Tuning the Structure of Platinum Particles on Ceria In Situ for Enhancing the Catalytic Performance of Exhaust Gas Catalysts. *Angew. Chem., Int. Ed.* **2017**, *56* (42), 13078−13082.

(14) Gruber, H. L. Chemisorption studies on supported platinum. *J. Phys. Chem.* **1962**, *66* (1), 48−54.

(15) Benson, J. E.; Boudart, M. Hydrogen-oxygen titration method for the measurement of supported platinum surface areas. *J. Catal.* **1965**, *4* (6), 704−710.

(16) Vannice, M. A.; Benson, J. E.; Boudart, M. Determination of surface area by chemisorption: Unsupported platinum. *J. Catal.* **1970**, *16* (3), 348−356.

(17) Zaera, F. New Challenges in Heterogeneous Catalysis for the 21st Century. *Catal. Lett.* **2012**, *142* (5), 501−516.

(18) Boudart, M.; Aldag, A.; Benson, J. E.; Dougharty, N. A.; Girvin Harkins, C. On the specific activity of platinum catalysts. *J. Catal.* **1966**, *6* (1), 92−99.

(19) Mager-Maury, C.; Bonnard, G.; Chizallet, C.; Sautet, P.; Raybaud, P. H_2-Induced Reconstruction of Supported Pt Clusters: Metal-Support Interaction versus Surface Hydride. *ChemCatChem.* **2011**, *3* (1), 200−207.

(20) Gorczyca, A.; Moizan, V.; Chizallet, C.; Proux, O.; Del Net, W.; Lahera, E.; Hazemann, J.-L.; Raybaud, P.; Joly, Y. Monitoring Morphology and Hydrogen Coverage of Nanometric Pt/γ-Al_2O_3 Particles by In Situ HERFD-XANES and Quantum Simulations. *Angew. Chem., Int. Ed.* **2014**, *53* (46), 12426−12429.

(21) Wang, L.-L.; Johnson, D. D. Shear Instabilities in Metallic Nanoparticles: Hydrogen-Stabilized Structure of Pt_{37} on Carbon. *J. Am. Chem. Soc.* **2007**, *129* (12), 3658−3664.

(22) Wei, G.-F.; Liu, Z.-P. Restructuring and Hydrogen Evolution on Pt Nanoparticle. *Chem. Sci.* **2015**, *6* (2), 1485−1490.

(23) Oudenhuijzen, M. K.; van Bokhoven, J. A.; Miller, J. T.; Ramaker, D. E.; Koningsberger, D. C. Three-Site Model for Hydrogen Adsorption on Supported Platinum Particles: Influence of Support Ionicity and Particle Size on the Hydrogen Coverage. *J. Am. Chem. Soc.* **2005**, *127* (5), 1530−1540.

(24) Sun, G.; Sautet, P. Metastable Structures in Cluster Catalysis from First-Principles: Structural Ensemble in Reaction Conditions and Metastability Triggered Reactivity. *J. Am. Chem. Soc.* **2018**, *140* (8), 2812−2820.

(25) Timoshenko, J.; Lu, D.; Lin, Y.; Frenkel, A. I. Supervised Machine-Learning-Based Determination of Three-Dimensional Structure of Metallic Nanoparticles. *J. Phys. Chem. Lett.* **2017**, *8* (20), 5091−5098.

(26) Carosso, M.; Vottero, E.; Lazzarini, A.; Morandi, S.; Manzoli, M.; Lomachenko, K. A.; Ruiz, M. J.; Pellegrini, R.; Lamberti, C.; Piovano, A.; Groppo, E. Dynamics of Reactive Species and Reactant-Induced Reconstruction of Pt Clusters in Pt/Al_2O_3 Catalysts. *ACS Catal.* **2019**, *9* (8), 7124−7136.

(27) Vaarkamp, M.; Miller, J. T.; Modica, F. S.; Koningsberger, D. C. On the Relation between Particle Morphology, Structure of the Metal-Support Interface, and Catalytic Properties of Pt/γ-Al_2O_3. *J. Catal.* **1996**, *163* (2), 294−305.

(28) Cabié, M.; Giorgio, S.; Henry, C. R.; Axet, M. R.; Philippot, K.; Chaudret, B. Direct Observation of the Reversible Changes of the

Morphology of Pt Nanoparticles under Gas Environment. *J. Phys. Chem. C* **2010**, *114* (5), 2160−2163.

(29) Yakovina, O. A.; Lisitsyn, A. S. Probing the H₂-Induced Restructuring of Pt Nanoclusters by H₂-TPD. *Langmuir* **2016**, *32* (46), 12013−12021.

(30) Albers, P.; Auer, E.; Ruth, K.; Parker, S. F. Inelastic Neutron Scattering Investigation of the Nature of Surface Sites Occupied by Hydrogen on Highly Dispersed Platinum on Commercial Carbon Black Supports. *J. Catal.* **2000**, *196* (1), 174−179.

(31) Parker, S. F.; Frost, C. D.; Telling, M.; Albers, P.; Lopez, M.; Seitz, K. Characterisation of the adsorption sites of hydrogen on Pt/C fuel cell catalysts. *Catal. Today* **2006**, *114* (4), 418−421.

(32) Yamazoe, S.; Yamamoto, A.; Hosokawa, S.; Fukuda, R.; Hara, K.; Nakamura, M.; Kamazawa, K.; Tsukuda, T.; Yoshida, H.; Tanaka, T. Identification of hydrogen species on Pt/Al₂O₃ by in situ inelastic neutron scattering and their reactivity with ethylene. *Catal. Sci. Technol.* **2021**, *11* (1), 116−123.

(33) Parker, S. F.; Lennon, D.; Albers, P. W. Vibrational Spectroscopy with Neutrons: A Review of New Directions. *Appl. Spectrosc.* **2011**, *65* (12), 1325−1341.

(34) Parker, S. F.; Mukhopadhyay, S.; Jiménez-Ruiz, M.; Albers, P. W. Adsorbed States of Hydrogen on Platinum: A New Perspective. *Chem.—Eur. J.* **2019**, *25* (26), 6496−6499.

(35) Kaprielova, K. M.; Yakovina, O. A.; Ovchinnikov, I. I.; Koscheev, S. V.; Lisitsyn, A. S. Preparation of platinum-on-carbon catalysts via hydrolytic deposition: Factors influencing the deposition and catalytic properties. *Appl. Catal., A* **2012**, *449*, 203−214.

(36) Piovano, A.; Giovanni, A.; Michele, C.; Groppo, E.; Monica, J. R.; Carlo, L.; Andrea, L.; Manzoli, M.; Morandi, S.; Pellegrini, R.; Vottero, E. *Data from: Study of the Pt-hydride formation and spillover effect on Pt/Al₂O₃ and Pt/C catalysts*; Institut Laue-Langevin (ILL), 2016, DOI: 10.5291/ILL-DATA.7-05-466.

(37) Vottero, E.; Carosso, M.; Jimenez Ruiz, M.; Manzoli, M.; Piovano, A. *Data from: Dynamics of Pt-H species on an industrial Pt/Al₂O₃ catalyst as a function of hydrogenation temperature*; Institut Laue-Langevin (ILL), 2021, DOI: 10.5291/ILL-DATA.7-05-514.

(38) Ivanov, A.; Jimenéz-Ruiz, M.; Kulda, J. IN1-LAGRANGE - the new ILL instrument to explore vibration dynamics of complex materials. *J. Phys.: Conf. Ser.* **2014**, *554*, 012001.

(39) Kresse, G.; Hafner, J. Ab initio molecular-dynamics simulation of the liquid-metal-amorphous-semiconductor transition in germanium. *Phys. Rev. B* **1994**, *49* (20), 14251−14269.

(40) Kresse, G.; Furthmüller, J. Efficient iterative schemes for ab initio total-energy calculations using a plane-wave basis set. *Phys. Rev. B* **1996**, *54* (16), 11169−11186.

(41) Perdew, J. P.; Burke, K.; Ernzerhof, M. Generalized Gradient Approximation Made Simple. *Phys. Rev. Lett.* **1996**, *77* (18), 3865−3868.

(42) Kresse, G.; Joubert, D. From ultrasoft pseudopotentials to the projector augmented-wave method. *Phys. Rev. B* **1999**, *59* (3), 1758−1775.

(43) Hu, C. H.; Chizallet, C.; Mager-Maury, C.; Corral-Valero, M.; Sautet, P.; Toulhoat, H.; Raybaud, P. Modulation of catalyst particle structure upon support hydroxylation: Ab initio insights into Pd₁₃ and Pt₁₃/γ-Al₂O₃. *J. Catal.* **2010**, *274* (1), 99−110.

(44) Krokidis, X.; Raybaud, P.; Gobichon, A.-E.; Rebours, B.; Euzen, P.; Toulhoat, H. Theoretical Study of the Dehydration Process of Boehmite to γ-Alumina. *J. Phys. Chem. B* **2001**, *105* (22), 5121−5130.

(45) Digne, M.; Sautet, P.; Raybaud, P.; Euzen, P.; Toulhoat, H. Hydroxyl Groups on γ-Alumina Surfaces: A DFT Study. *J. Catal.* **2002**, *211* (1), 1−5.

(46) Digne, M.; Sautet, P.; Raybaud, P.; Euzen, P.; Toulhoat, H. Use of DFT to achieve a rational understanding of acid-basic properties of γ-alumina surfaces. *J. Catal.* **2004**, *226* (1), 54−68.

(47) Ramirez-Cuesta, A. J. aCLIMAX 4.0.1, The new version of the software for analyzing and interpreting INS spectra. *Comput. Phys. Commun.* **2004**, *157* (3), 226−238.

(48) Vottero, E.; Carosso, M.; Jiménez-Ruiz, M.; Pellegrini, R.; Groppo, E.; Piovano, A. How do the graphenic domains terminate in

activated carbons and carbon-supported metal catalysts? *Carbon* **2020**, *169*, 357−369.

(49) McInroy, A. R.; Lundie, D. T.; Winfield, J. M.; Dudman, C. C.; Jones, P.; Parker, S. F.; Lennon, D. The interaction of alumina with HCl: An infrared spectroscopy, temperature-programmed desorption and inelastic neutron scattering study. *J. Catal.* **2006**, *114* (4), 403−411.

(50) Lagauche, M.; Larmier, K.; Jolimaitre, E.; Barthelet, K.; Chizallet, C.; Favergeon, L.; Pijolat, M. Thermodynamic Characterization of the Hydroxyl Group on the γ-Alumina Surface by the Energy Distribution Function. *J. Phys. Chem. C* **2017**, *121* (31), 16770−16782.

(51) Albers, P. W.; Pietsch, J.; Krauter, J.; Parker, S. F. Investigations of activated carbon catalyst supports from different natural sources. *Phys. Chem. Chem. Phys.* **2003**, *5* (9), 1941−1949.

(52) Zemlyanov, D. Y.; Smirnov, M. Y.; Gorodetskii, V. V. HREELS characterization of hydrogen adsorption states on the Pt(100)-(hex) and (1 × 1) surfaces. *Catal. Lett.* **1997**, *43* (3), 181−187.

(53) Olsen, R. A.; Kroes, G. J.; Baerends, E. J. Atomic and molecular hydrogen interacting with Pt(111). *J. Chem. Phys.* **1999**, *111* (24), 11155−11163.

(54) Karim, W.; Spreafico, C.; Kleibert, A.; Gobrecht, J.; VandeVondele, J.; Ekinci, Y.; van Bokhoven, J. A. Catalyst support effects on hydrogen spillover. *Nature* **2017**, *541* (7635), 68−71.

(55) Spreafico, C.; Karim, W.; Ekinci, Y.; van Bokhoven, J. A.; VandeVondele, J. Hydrogen Adsorption on Nanosized Platinum and Dynamics of Spillover onto Alumina and Titania. *J. Phys. Chem. C* **2017**, *121* (33), 17862−17872.

(56) Arrouvel, C.; Toulhoat, H.; Breysse, M.; Raybaud, P. Effects of PH₂O, PH₂S, PH₂ on the surface properties of anatase-TiO₂ and γ-Al₂O₃: a DFT study. *J. Catal.* **2004**, *226* (2), 260−272.

(57) Pigeon, T.; Chizallet, C.; Raybaud, P. Revisiting γ-alumina surface models through the topotactic transformation of boehmite surfaces. *J. Catal.* **2022**, *405*, 140−151.

(58) Wischert, R.; Laurent, P.; Copéret, C.; Delbecq, F.; Sautet, P. γ-Alumina: The Essential and Unexpected Role of Water for the Structure, Stability, and Reactivity of "Defect" Sites. *J. Am. Chem. Soc.* **2012**, *134* (35), 14430−14449.

(59) Batista, A. T. F.; Wisser, D.; Pigeon, T.; Gajan, D.; Diehl, F.; Rivallan, M.; Catita, L.; Gay, A.-S.; Lesage, A.; Chizallet, C.; Raybaud, P. Beyond γ-Al₂O₃ crystallite surfaces: The hidden features of edges revealed by solid-state ¹H NMR and DFT calculations. *J. Catal.* **2019**, *378*, 140−143.

Article

Assessing Low-Cost Computational Methods against Structural Properties and Size Effects of Pt nanoparticles

Alberto Ricchebuono,* Eleonora Vottero, Andrea Piovano, Elena Groppo, Pascal Raybaud, and Céline Chizallet*

Read Online

ACCESS | Metrics & More | Article Recommendations | SI Supporting Information

ABSTRACT: An evaluation of the performances of several known low-cost methods for the reproduction of structural features of differently sized Pt nanoparticles (NPs) is presented. The full density functional theory PBE-dDsC functional (within the plane-wave formalism) was employed to benchmark the semiempirical tight-binding DFTB and GFNn-xTB (n = 0, 1, 2) and the reactive force-field ReaxFF. Performances were evaluated by comparing several size-dependent features (such as relative stabilities, structural descriptors, and vibrational features) computed with the different methods. Various structures (ordered and amorphous) and sizes (from Pt_{13} to Pt_{561}) were considered in the datasets. ReaxFF molecular dynamics (MD) was employed to achieve the amorphization of cuboctahedral Pt_{147}, Pt_{309}, and Pt_{561} geometries, which were subsequently optimized with both the low-cost methods and the DFT reference, within a multilevel modeling approach. The structures were further annealed with GFN0-xTB MD. While DFTB performs quite well over all the selected structures, GFN2-xTB and the cheaper GFN0-xTB show a general predilection for amorphous geometries. The performances of GFN2-xTB are found to worsen with the increasing size of the system, while ReaxFF and GFN0-xTB undergo the opposite trend. We suggest that the semiempirical DFTB (and within certain limitations GFN0-xTB and ReaxFF) could be suited for fast screening through amorphous big-sized Pt NPs.
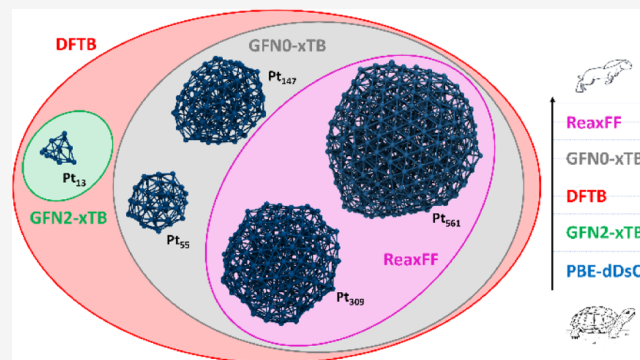
1. INTRODUCTION

The importance of metal nanoparticles (NPs) in modern technology has grown exponentially since scientists started studying their properties and engineering during the last century. Pt NPs display unique characteristics (resistance to oxidation, biocidal activity, plasmon resonance, etc.), which made them employable in a great variety of applications: from biosensors to electronics, catalysis, and more.[1,2] One of the most interesting features of Pt NPs is their ability to activate and sometimes dissociate many molecules of environmental and industrial relevance, such as H_2, CO, CO_2 and organic compounds.[3,4] The activity enhancement gained by dispersing metal nanoparticles of controlled size on support materials, such as oxides or carbons, has indeed given heterogeneous catalysts based on supported Pt NPs a central role in several catalytic processes,[5] like pollutant removal,[6,7] hydrogenation/dehydrogenation reactions,[8−11] naphtha reforming,[12,13] etc.

The fine understanding of the properties of Pt NPs is challenged by their complex and ductile structure, which is very sensitive to the chemical environment (reactants or nature of the support). Usually, Pt NPs display a great variety of sites whose coordination depends on the NP's shape, size, and structural disorder, 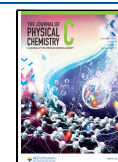giving birth to an overlap of contributions and convoluted experimental responses strongly depending on reaction conditions.[14] Hence, the atomic scale determination of these systems requires the use of cutting-edge characterization techniques in combination with state-of-the-art computational chemistry methods.[15−19] The advance of density functional theory (DFT) and the development of high-performance computing (HPC) facilities has led to numerous progresses in the understanding of the properties of Pt NPs through the last decades.[20] For instance, a great variety of shapes has been found for isolated Pt clusters,[21−24] while the interaction of Pt NP's with oxide supports[25−29] and various reactants (such as H_2 or CO) has been investigated for clusters ranging from 2 up to around 200 atoms.[28,30,31]

Nevertheless, one of the frontiers of the field arises from the fact that DFT can be employed for accurate calculations on simple systems featuring up to around a few hundred atoms,

but it becomes rapidly too demanding when increasing the number of metallic atoms involved.[32,33] This aspect represents a strong limitation to the development of realistic models, often compelling researchers to rely on simplifications such as reduction of system's size and of nanostructure complexity.

The process of building reliable molecular models of metallic NPs comprehends a preliminary step in which many candidate structures have to be screened for a given NP size.[34] During this step, the potential energy surface (PES) has to be explored in order to find the most stable minima that can be relevant and populated at a given temperature.[35,36] Even though various algorithms, such as global optimization[24,37−39] and simulated annealing by *ab initio* molecular dynamics,[21,40−43] can be used to generate and explore candidate structures for metallic clusters, the main bottleneck of this step is the computational method employed to describe the PES. For example, an exhaustive PES exploration within a full-DFT approach can be carried out only for small and simple systems at a high computational cost. Adopting a multi-level modeling scheme often represents an efficient workaround, envisaging the exploitation of low-cost approximated methods (semiempirical (SE) functionals, force-fields (FF), neural network potentials, etc.) instead of DFT for the exploration of the PES.[23,44] Even though this strategy can massively reduce the computational cost of the process, the approximations on which these methods rely always entail an accuracy loss to some extent. Moreover, the stronger these approximations are, the weaker the transferability of the method. Thus, the accuracy of approximated low-cost methods must be thoroughly assessed against reference methods that are proven to be trustable for the systems at issue.

In this paper, we benchmark the performances of several low-cost computational methods for the computation of structural properties and size effects on Pt nanoparticles of stoichiometry Pt_{13}, Pt_{55}, Pt_{147}, Pt_{309}, and Pt_{561}. The semi-empirical tested methods are density functional tight binding (DFTB)[45] and three methods belonging to the GFN extended tight binding family: GFN0-xTB,[46] GFN1-xTB,[47] and GFN2-xTB,[48] where the acronym "GFN" stands for "geometries, frequencies and noncovalent interactions". The ReaxFF[49,50] reactive force field was tested in the same fashion. DFTB and the ReaxFF are well-known methods that have already been frequently employed in heterogeneous catalysis.[51−58] On the other hand, the recently developed GFN methods were first benchmarked against high-level DFT, wave function theory (WFT), and experimental data mainly for organic and metal−organic compounds.[34,46−48] However, their promising applications reported in the past few years[59−62] together with their low computational cost and their atom-specific parametrization make their accuracy worth to be assessed on metal NPs as well.

Due to the lack of clear insight from the literature, our benchmark strategy for this study was built as follows. A small structural dataset containing 14 different Pt_{13} NPs, divided into amorphous and ordered structures, was considered to first test the performances of all the listed methods. The benchmark was performed by assessing their ability to reproduce relative stabilities, thermochemical parameters and structural descriptors (bond lengths, bond angles, and radii of gyration) computed at the PBE-dDsC[63,64] level for every NP of the dataset. An analogous approach is adopted for two sets of amorphous NPs of Pt_{13} (54 structures) and Pt_{55} (93 structures) stoichiometry, in order to evaluate the particle size effect. The ultimate task of the work will be to propose a cost-effective simulated annealing procedure combining ReaxFF and GFN0-xTB to generate reliable amorphous structures for large Pt_x NPs (x = 147, 309, 561). In the last section, this route is critically analyzed, pointing out its advantages and limits to overcome.

2. METHODOLOGY

2.1. Computational Details. DFT calculations were carried out within the plane-wave formalism, thanks to the VASP[65,66] code (version 5.4.4). The PBE exchange−correlation functional[63] was employed, setting an energy cutoff of 400 eV for Pt_{13} and Pt_{55} and 300 eV for Pt_{147}, Pt_{309}, and Pt_{561}. The choice of the PBE functional is due to its computational cost and general applicability,[67] allowing us to compute energies and geometries for the biggest NPs considered in this work, coupled with its relevance for simulating Pt and surfaces of transition metals in general.[68] The dDsC correction,[69] benchmarked for predicting molecular adsorption at Pt surfaces by Gautier et al.,[70] was added to take into account dispersion interactions, while core electrons were described with the PAW method.[71] To motivate our reference functional choice, we evaluated the performances of PBE, PBE-dDsC and PBEsol[72] on the Pt_{13}*small dataset* (details about the dataset are given in the next section). The comparison between relative energies computed with the three functionals is presented in Figure S1 of the Supporting Information. The small deviations (below 0.03 eV/atom) observed between the data obtained with the different functionals confirm that the impact of the reference GGA functional lies in the background if compared with the effect of a geometry optimization at the SE or FF level. A Gaussian smearing (σ = 0.05 eV) was applied to accelerate the convergence of the electronic iterations. The threshold for all the electronic energy minimizations was fixed to 10^{-7} eV. Spin-polarized calculations were performed for Pt_{13} and Pt_{55}. Geometries were optimized with the conjugate-gradient algorithm until the residual forces were below 0.005 eV/Å. Although geometry optimizations of NPs of sizes up to a few hundred of atoms are feasible at the PBE level, the same process is thousands of times faster if employing the low-cost methods at issue (Figure S2). Thus, understanding to what extent results obtained with the latter deviate from the PBE reference is crucial to safely exploit this massive gain in computational time.

DFTB calculations were carried out through the DFTB+ code (version 21.1).[45] Electronic energies were computed by setting a self-consistent charge (SCC) tolerance of 2.7×10^{-7} eV, a maximum angular momentum l_{max} = 2 and a Fermi−Dirac smearing featuring an electronic temperature of 500 K, following the settings chosen in ref 23. Geometries were optimized with the conjugate-gradient algorithm until the residual forces were below 5×10^{-4} eV/Å. The employed Slater−Koster parameters were adopted from ref 23.

Calculations performed with the GFNn-xTB methods were executed with the xTB code (version 6.4.0).[34] The threshold for convergence on electronic energies was set to 10^{-6} eV, while geometries were optimized through the ANCOPT algorithm with a convergence criterion of 0.01 eV/Å. We checked that using a tighter convergence criterion does not affect the results reported herein.

ReaxFF calculations were run within version 6.0 of the General Lattice Utility Program (GULP),[73] exploiting a parametrization derived in ref 74. The latter was made with the final aim of modeling the interaction between Pt clusters

and carbon platelets. The convergence criterion for geometry optimizations was set to 0.005 eV/Å.

All of the above-mentioned thresholds were chosen in order to avoid negative eigenvalues of the Hessian matrix during the computation of harmonic vibrational frequencies. To this purpose, the finite differences method was adopted for the VASP, DFTB+, and xTB code (elongation ± 0.01 Å, $\pm 5 \times 10^{-5}$ Å, ± 0.0025 Å, respectively), while analytical derivatives were computed with GULP. The computed vibrational frequencies were post-treated, through the laws of statistical thermodynamics,[75] to extract the vibrational contributions to the following thermodynamic quantities: enthalpy (H_{vib}), entropy (S_{vib}), and the Zero Point Vibrational Energy (ZPVE). The vibrational contribution to the Gibbs free energy (G_{vib}) at $T = 300$ K is computed as follows:

$$G_{vib} = H_{vib} - TS_{vib} + ZPVE \qquad (1)$$

MD simulations were carried out in the *NVT* ensemble. ReaxFF MD was performed with the Nosé thermostat[76] and the velocity-Verlet algorithm at different temperatures (details are given in the next section). The employed time-step was 0.5 fs, while the total simulation time was 10 ps. The Berendsen thermostat[77] was employed for GFN0-xTB MD at 2000 K, with a time-step of 2 fs and a total simulation time of 50 ps.

2.2. Datasets and Models. The performances of the chosen low-cost methods were evaluated by investigating four structural datasets (coordinates in XYZ format of PBE-dDsC structures for each data set are given in the Supporting Information):

- *Pt$_{13}$small dataset*: 14 structures divided into ordered and amorphous

  Coordinates of structures belonging to this dataset have different origins: the structures cbpt (capped biplanar triangle), nbp (new biplanar), scsc (side-capped simple cubic), dscsc (disordered side-capped simple cubic), tcsc (top-capped simple cubic), bbp (buckled biplanar), and ico (icosahedral) are taken from ref 21. The structures sa and sa2 are still taken from ref 21 and differ from the previous ones as they are generated through first-principles simulated annealing (hence the "sa" terminology). The structures go2, go3, and go4 are taken from ref 23 (where "go" stands for "global optimization"). The structures nsx0 and nsx2 were obtained by optimizing at GFN0-xTB and GFN2-xTB level amorphous structures from previous DFT calculations.

- *Pt$_{13}$amorphous dataset*: 54 amorphous structures (coordinates adopted from ref 23)

- *Pt$_{55}$amorphous dataset*: 93 amorphous structures (coordinates adopted from ref 23)

- *Multi-sized dataset*: 5 amorphous structures of stoichiometry Pt$_{13}$, Pt$_{55}$, Pt$_{147}$, Pt$_{309}$, Pt$_{561}$ (presented in Figure 1) considered to evaluate the size-dependency of the performances of the tested methods.

  Pt$_{13}$ and Pt$_{55}$ structures in this dataset correspond to the lowest-energy structures of the *Pt$_{13}$* and *Pt$_{55}$amorphous datasets*, respectively. Amorphous Pt$_{147}$, Pt$_{309}$, and Pt$_{561}$ were obtained through the amorphization of the ordered cuboctahedral geometry, as schematized in Figure 2A. Cuboctahedral nanoparticles were first cut out of the Pt bulk and subsequently subjected to ReaxFF MD. Different temperatures, ranging from 800 to 2700 K, were tested to find the
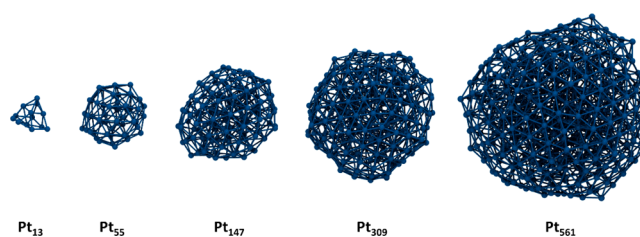

Figure 1. Examples of structures of NPs belonging to the multi-sized dataset optimized at the PBE-dDsC level at 0 K.

minimal temperature to shake cuboctahedral geometries in order to explore various conformational states. A complete amorphization of the structure was achieved at 2000 K for Pt$_{147}$, 2500 K for Pt$_{309}$, and 2700 K for Pt$_{561}$. The lowest-energy structure of each MD run was quenched at 0 K with ReaxFF, obtaining an amorphous ReaxFF geometry for each stoichiometry. The geometries of the obtained structures were optimized with the low-cost methods, as well as with PBE-dDsC. GFN0-xTB geometries were finally annealed through GFN0-xTB MD, aiming to enhance the accuracy of the generated NP models through higher-level MD. Several candidate low-lying energy conformations per stoichiometry were quenched at 0 K with GFN0-xTB in this case, taking as output only the lowest-energy structure resulting after PBE-dDsC single point energy evaluations. Notably, for this part of the study, we will only compare energies evaluated at our reference level of theory (PBE-dDsC), as will be discussed in section 3.3. The energies computed at the GFN0-xTB level are not considered. The sampling approaches for ReaxFF and GFN0-xTB MD are exemplified in Figure 2B for Pt$_{147}$.

Structures belonging to the *Pt$_{13}$small dataset* were first optimized at the PBE-dDsC level. The thus obtained geometries were further optimized with all the low-cost methods, and we evaluated their performances by comparing bond lengths, bond angles, radii of gyration, relative stabilities, and thermochemical parameters computed by the low-cost methods with the reference PBE-dDsC (section 3.1). The benchmark on the *Pt$_{13}$amorphous dataset* and *Pt$_{55}$amorphous dataset* (section 3.2) was carried out analogously, although vibrational frequencies (and thus thermochemical parameters) were not computed. Moreover, GFN1-xTB was not tested on the *Pt$_{13}$* and *Pt$_{55}$amorphous datasets* due to the poor performances exhibited for the *Pt$_{13}$small dataset*. As outlined in Figure 2A, all the structures of the *multi-sized dataset* (section 3.3) were subjected to a PBE-dDsC single point energy evaluation. Thus, the outcome of the employed multi-level procedure was inspected by analyzing the deviations on PBE-dDsC electronic energies and bond lengths between the low-cost and PBE-dDsC geometries. GFN1-xTB was not employed in this section for the aforementioned reason, while GFN2-xTB was discarded because of the inability to reach a convergence in SCC calculations for Pt$_{147}$, Pt$_{309}$, and Pt$_{561}$. This work is mainly focused on amorphous NPs since Pt NPs are experimentally known to show a general preference for amorphous morphologies which vanishes when increasing the particle size.[78] Notably, after some preliminary tests, we testified the inability of
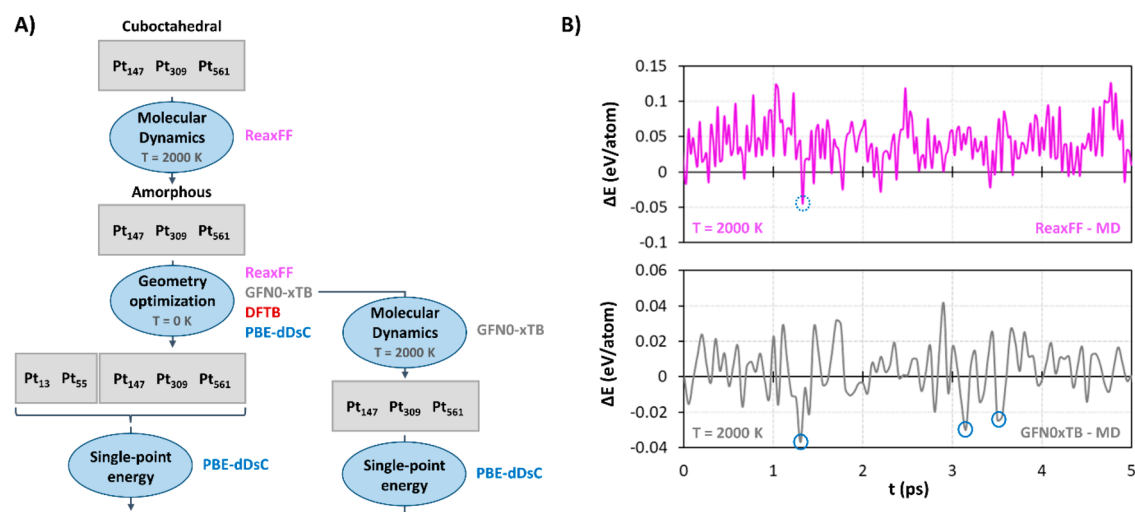
Figure 2. (A) Flowchart of the multi-level procedure adopted to build Pt_{147}, Pt_{309}, and Pt_{561} NPs within the *multi-sized dataset*. (B) Energy (referred to the starting point) evolution versus simulation time for 5 ps of ReaxFF (pink) and GFN0-xTB (gray) MD for Pt_{147}. The lowest ReaxFF structure (dashed circle) was quenched at 0 K with ReaxFF. Among the highlighted lowest-energy GFN0-xTB structures (solid circles), only the most stable conformer according to PBE-dDsC energies was chosen as the output of the procedure.
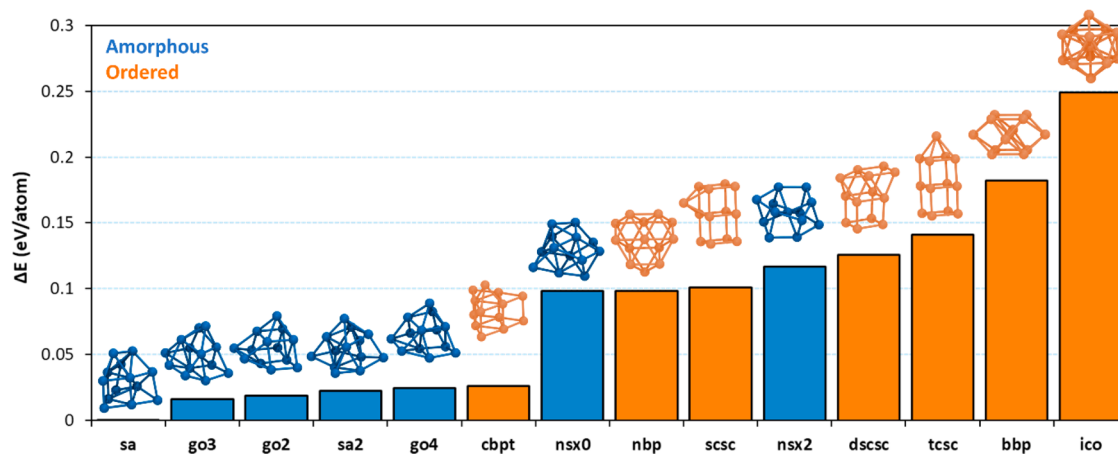
Figure 3. Relative stability (with respect to the global minimum) of all the structures of the Pt_{13} small dataset, ranked according to their electronic energy computed at PBE-dDsC level. Amorphous structures are represented in blue, while ordered ones are in orange.

the GFN methods to retain cuboctahedral geometries for Pt_x NPs with $x > 13$.

The graphical visualization and structural manipulation of the NPs was performed with VESTA (version 4.0.0).[79] Images of molecular models were rendered with VMD.[80] The kernel density estimate (KDE) plots presented in section 3.2 were created with the Python library Seaborn.[81]

3. RESULTS AND DISCUSSION

3.1. Pt_{13} Small Dataset. All of the structures optimized at the PBE-dDsC level are ranked according to their electronic energy in Figure 3. As outlined in section 2, the 14 Pt_{13} NPs are divided into two classes: "amorphous" and "ordered". While among the structures of the "amorphous" class, the atoms are "randomly" organized in space, the atomic positions in the "ordered" structures are subjected to stricter geometrical constraints. The dispersion-corrected GGA electronic energies suggest that for the Pt_{13} system ordered structures are generally less stable than the amorphous ones. This trend is consistent with the fact that the arrangement of atoms in ordered structures is either cut out of the bulk or built to fit specific

geometric shapes. On the other hand, most of the amorphous structures (with the exception of sa, the most stable structure, found by simulated annealing)[21] shown here were obtained through a global optimization procedure[23] that was explicitly devoted to find the most stable geometries for this system.

One notable result about this dataset concerns the cuboctahedral geometry, which has been widely employed as a model nanoparticle for many metals due its straightforward extraction from an fcc crystalline lattice.[22,82] According to the analysis of vibrational frequencies, the optimized cuboctahedral structure ($\Delta E = 0.24$ eV/atom with respect to the sa global minimum) displays residual imaginary frequencies corresponding to compression along the axis normal to the squared facets. A line minimization was performed to scan the normal coordinate associated with the imaginary frequency in order to find the minimum conformation. After the line-minimization procedure, the reoptimized geometry collapsed to the bbp structure, implying the removal of the cuboctahedral Pt_{13} from our dataset. This cuboctahedral structure was kept in ref 21 without confirming by frequency analysis if it was a true

minimum. Nevertheless, the overall energy trend is consistent with the one reported for sa, nbp, bbp, ico, and cub in ref 21.

After reoptimizing PBE-dDsC structures with the low-cost methods, a detailed analysis of their performances was achieved by extracting and comparing different features of the NPs: geometries, relative stabilities, and thermochemical parameters.

3.1.1. Geometries. To represent the geometrical features of each NP, we extracted the Pt–Pt distances between nearest neighbors (Figure 4A), the angles between three nearest
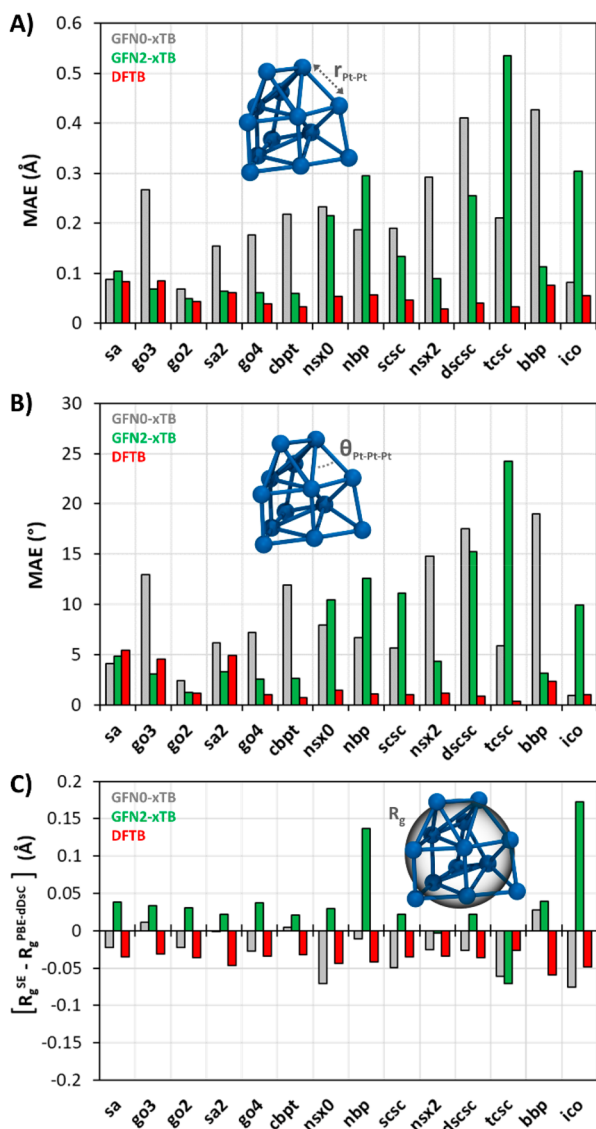
Figure 4. Mean Absolute Error (MAE) for bond lengths (A) and bond angles (B) and the signed deviation from PBE-dDsC for the gyration radius R_g (C) made by semiempirical methods (SE): GFN0-xTB (gray), GFN2-xTB (green), and DFTB (red).

neighbors Pt atoms (Figure 4B) and the radius of gyration (R_g, Figure 4C). The errors of the tested low-cost methods for each nanoparticle with respect to the PBE-dDsC reference are reported in Figure 4. Only the errors for the three best performing methods are shown in the main text due to the poor results obtained with ReaxFF and GFN1-xTB. Histograms for all the methods are given in Figure S3.

The averaged mean absolute errors (MAEs) computed separately for amorphous and ordered structures are reported in Table 1. As emerges both from the histograms in Figure 4 and from Table 1, DFTB outperforms GFN0-xTB and GFN2-xTB in most cases, showing errors below 0.1 Å for bond lengths and generally below 5° for bond angles. GFN2-xTB systematically shows lower errors on amorphous geometries (competing with DFTB), while its performances become poor when evaluated on ordered structures. The results obtained with GFN0 are not undergoing any specific trend. However, it is worth noting that for R_g, GFN0-xTB exhibits the lowest deviation (in absolute value) for both amorphous and ordered structures. Our interpretation of this behavior is that, even though the "local" geometry is not strictly retained from DFT, the global information on the shape of the particle is not completely lost.

3.1.2. Relative Stabilities. In this section, we aim to assess the performances of our low-cost methods on the energetic ranking of the structures belonging to the *Pt$_{13}$small* dataset. The energies are expressed here as relative stabilities with respect to the global minimum, as was done for Figure 3. For each geometry optimized at the PBE-dDsC level, we compare the PBE-dDsC energy with the energy obtained with the chosen low-cost method on the same atomic conformation, thus neglecting the effect of SE geometry optimization in the first place. We express the raw results in the form of histograms (Figure 5, full columns), while we quantify the degree of agreement between the DFT and SE energies by means of a linear regression analysis, which is performed separately for amorphous and ordered structures. The regression parameters (slope and determination coefficient (R^2)) are compactly given in Table 2, while the relative scatter plots are presented in panels A, C and E of Figure S4.

Relying on the reported values of R^2, the regression analysis shows itself to be rather inglorious for GFN0-xTB energies, classifying again DFTB as the best performing method (in line with the parametrization of ref 23), followed by GFN2-xTB. Here, the different behavior for ordered and amorphous structures is evident not only for GFN2-xTB but also for GFN0-xTB and DFTB, even though for the latter the difference is almost negligible. Despite the poor results of GFN0-xTB, the performances of GFN2-xTB are strongly morphology-dependent, being competitive with those of DFTB only for the amorphous structures. The generally coarse results of GFN0-xTB are reflected in the histograms of Figure 5B, from which it appears its inability to reproduce the stability trend depicted by PBE-dDsC energies (Figure 5A). While both GFN2-xTB and DFTB perform well for amorphous structures, they behave differently for the ordered ones: DFTB is slightly underestimating their stability (Figure 5D), while the trend is less uniform for GFN2-xTB (Figure 5C).

At this point, we mean to take into account the effect of geometry optimization at the SE level. To this purpose, we carried out an analogous analysis by comparing the PBE-dDsC relative energy with the relative energy obtained with the chosen low-cost method on the same NPs after geometry optimization. The corresponding histograms are presented in Figure 5 (striped columns), while the regression parameters are reported in brackets in Table 2 (the relative scatter plots are presented in Figure S5).

The value of R^2 generally decreases upon geometry optimization with SE methods, which is consistent with the

Table 1. Averaged Errors on Bonds, Angles and R_g for the Small Pt_{13} Dataset

	bonds MMAE (Å)[a]			angles MMAE (deg)[a]			R_g MAE (Å)[b]		
	GFN0-xTB	GFN2-xTB	DFTB	GFN0-xTB	GFN2-xTB	DFTB	GFN0-xTB	GFN2-xTB	DFTB
Amorphous	0.18	0.09	0.06	7.9	4.2	2.8	0.026	0.028	0.037
Ordered	0.26	0.24	0.05	10.9	10.3	1.1	0.033	0.066	0.040

[a]The averaged error on bond lengths and angles is expressed as Mean MAE (MMAE). [b]The average error on R_g is expressed as a MAE. All the quantities are computed separately on amorphous and ordered structures to highlight the morphology-dependent behavior of the tested methods.
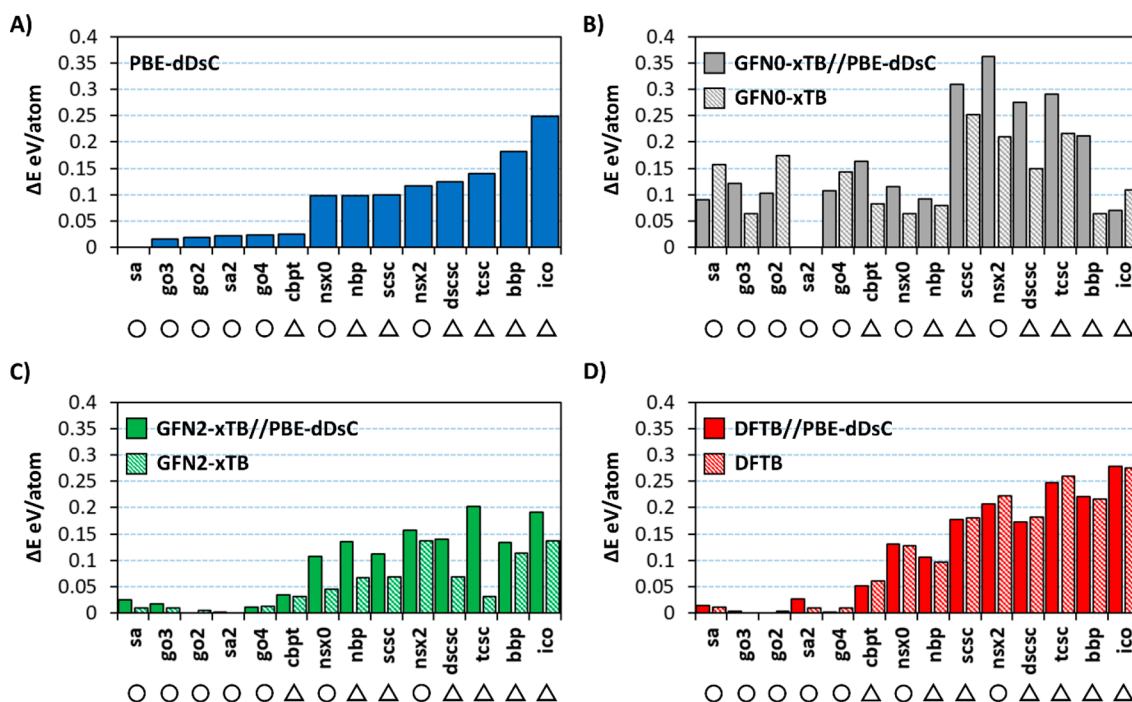

Figure 5. Relative stabilities (with respect to the global minimum) of the structures of the Pt_{13} small dataset, computed with PBE-dDsC (A), GFN0-xTB (B), GFN2-xTB (C), and DFTB (D). Full columns correspond to single point energy evaluations performed on the frozen PBE-dDsC geometry, while striped columns report the SE energy of the same NP after geometry optimization. Circles indicate amorphous structures, while triangles indicate ordered ones.

Table 2. Determination Coefficients and Slopes of the Regression Analysis Performed on Relative Stabilities (PBE-dDsC versus SE Energy)

	GFN0-xTB//PBE-dDsC[a] (GFN0-xTB)[b]		GFN2-xTB//PBE-dDsC[a] (GFN2-xTB)[b]		DFTB//PBE-dDsC[a] (DFTB)[b]	
	R^2	Slope	R^2	Slope	R^2	Slope
Amorphous	0.53 (0.004)	0.30 (0.13)	0.90 (0.77)	0.70 (0.82)	0.93 (0.93)	0.54 (0.50)
Ordered	0.06 (0.005)	−0.18 (−0.06)	0.63 (0.70)	1.00 (1.50)	0.82 (0.75)	0.80 (0.77)

[a]The regression was performed on relative stabilities computed by SE methods on frozen PBE-dDsC geometries. [b]The regression was performed on relative stabilities computed after reoptimization at SE level.

natural action of forces that modify atomic coordinates during geometry optimizations. The case of GFN2-xTB on ordered structures is less trivial. Even though the higher value of R^2 suggests a better correlation between data points, the high slope value (Table 2) indicates a general compression of the energetic range covered by PBE-dDsC, which is reflected in the histograms (Figure 5C). Moreover, the significant difference between the relative stabilities of ordered structures before and after GFN2-xTB geometry optimization is consistent with the significant MAE on bond lengths and angles discussed in section 3.1.1. DFTB is less sensitive to geometry optimization than the other methods for all structures and provides a more coherent stability trend with respect to PBE-dDsC.
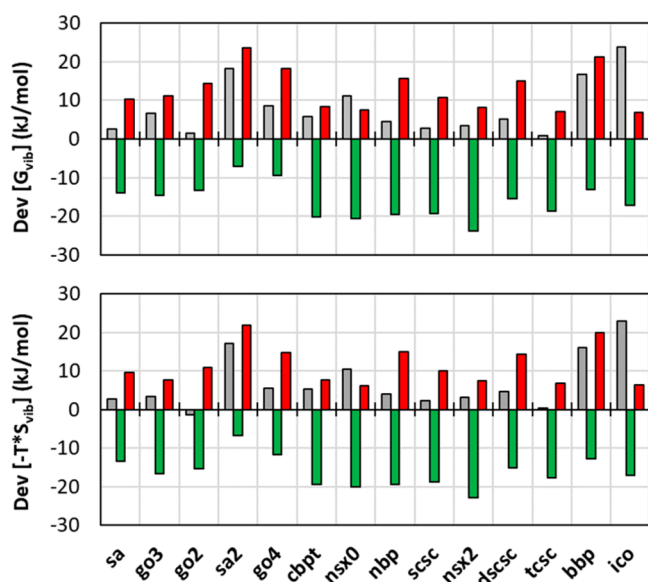
3.1.3. Vibrational Frequencies and Thermochemical Parameters. While the previous section checked how the semiempirical methods are able to identify the energy minima of the potential energy surface, we now aim to analyze how these methods describe the fluctuation of the systems in the close vicinity of those energy minima. First, harmonic vibrational frequencies were computed for each structure at different levels of theory. Information about the deviations of the unprocessed vibrational frequencies computed with low-cost methods with respect to PBE-dDsC can be found in Figure S6.

According to the mean bias errors (MBE) presented in Table 3 and the histograms of Figure 6 and Figure S7, deviations on the vibrational enthalpy (H_{vib}) plus ZPVE are found to be negligible compared with the entropic term.

Table 3. Averaged Errors on G_{vib}, $-TS_{vib}$, H_{vib}, and ZPVE for the Small Pt_{13} Dataset

	MBE [G_{vib}] (kJ/mol)	MBE [$-TS_{vib}$] (kJ/mol)	MBE [H_{vib}] (kJ/mol)	MBE [ZPVE] (kJ/mol)
GFN0-xTB	8.0	6.9	−1.3	2.4
GFN2-xTB	−16.2	−16.2	2.8	−2.7
DFTB	12.7	11.3	−2.4	3.8

Figure 6. Deviations of GFN0-xTB (gray), GFN2-xTB (green), and DFTB (red) with respect to PBE-dDsC on the computation on the vibrational free energy and entropy (TS_{vib}) at $T = 300$ K. We did not plot Dev [Hvib + ZPVE] since it was fully balanced around 0 and always below 4 kJ/mol.

Hence, since the vibrational free energy is computed as reported in eq 1, the error on G_{vib} comes predominantly from the $-TS_{vib}$ term. The main contribution to H_{vib} comes from high-frequency modes,[83] which are most likely associated with close bonding and stretching modes. S_{vib}, on the other hand, is more sensitive to low-frequency modes, corresponding to concerted movements of the whole NP. Thus, the negligible error on H_{vib} signifies that all the methods are well describing the shape of the potential well associated with high-frequency modes and thus to close bonding, where it is less true for the concerted vibrations. Nevertheless, the magnitude of G_{vib} remains rather small (less than 16 kJ/mol), which implies that the relative stability of all structures is not modified at $T = 300$ K by vibrational contributions whatever the method used (Figure S8).

Analyzing the histograms in Figure 6, two main observations can be made: GFN0-xTB shows the smallest deviation from the standard PBE-dDsC and the deviation of GFN2-xTB follows the opposite trend with respect to the other two methods. This behavior indicates that for low-frequency modes, while DFTB and GFN0-xTB are computing tighter potential wells with respect to PBE-dDsC, the same potential wells computed by GFN2-xTB are looser. This means that GFN2-xTB, in contrast to DFTB and GFN0-xTB, underestimates force constants for vibrations in which the whole nanoparticle is involved.

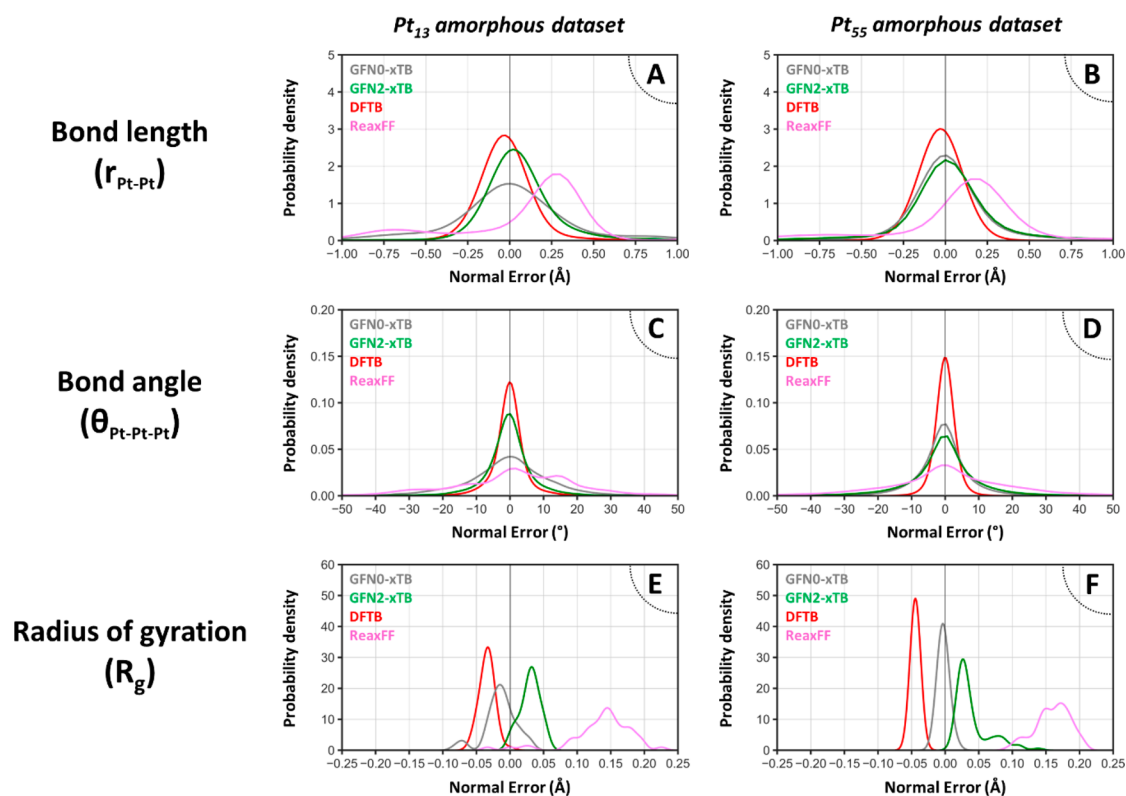**3.2. Pt₁₃ and Pt₅₅ Amorphous Datasets.** As described in section 2.2, a procedure analogous to the one applied to the

Pt_{13}*small dataset* was adopted for the two large datasets of amorphous Pt_{13} and Pt_{55} NPs. All the geometries optimized at PBE-dDsC level were reoptimized with GFN0-xTB, GFN2-xTB, DFTB, and ReaxFF. The agreement of the tested methods with the PBE-dDsC reference was evaluated by comparing three geometric descriptors (bond lengths, bond angles, and R_g) and the relative energies of the structures belonging to the two datasets.

Figure 7 reports the distribution of the signed deviation on bond lengths, bond angles, and R_g computed for all the tested low-cost methods, for both the Pt_{13} and Pt_{55} amorphous datasets. Since the signed deviation is a discrete variable in these cases, continuous probability density functions were estimated through the Kernel Density Estimation (KDE) procedure, with the Seaborn library[81] available in the Python code. The KDE plots for each geometric descriptor are computed by employing the same smoothing factor, thus legitimating the comparison between the probability density functions of the two datasets. Additional information about the computation of KDE plots can be found in section S7 of the Supporting Information.

The differences in the distributions between Pt_{13} and Pt_{55} reveal that the performances of DFTB and GFN0-xTB are generally improving while increasing the particle size: the distributions are getting narrower and shifted toward zero. GFN2-xTB seems to undergo the opposite trend; indeed, the distributions of the deviation for bonds and angles are widening when moving from Pt_{13} to Pt_{55}, while the behavior of the deviation on R_g is less clear. The performances of ReaxFF are generally poor and show only a slight improvement for Pt_{55} with respect to Pt_{13}. DFTB proves to be the best method, although it causes a small and systematic compression of bond lengths, which is also reflected in the deviation on R_g. GFN0-xTB is showing the biggest improvements, becoming competitive with DFTB and outperforming it for R_g.

The plots reported in Figure S4B, S4D, and S4F are conceived to inspect the correlation between relative energies computed at PBE-dDsC level with relative energies computed with the tested low-cost methods for the structures belonging to the Pt_{13} amorphous dataset. In this case, data show that the energy range in which the amorphous isomers of Pt_{13} lie is far smaller than the accuracy of a GGA functional such as PBE. As illustrated in Figure S9, the data regarding amorphous Pt_{55} NPs exhibit also a very narrow energy fluctuation. Hence, it is beyond the accuracy level to discuss any correlation between electronic relative energies for these sets of amorphous NPs.

3.3. Towards Big-Sized Nanoparticles. Amorphous geometries for nanoparticles of stoichiometry Pt_{147}, Pt_{309}, and Pt_{561} were obtained through the procedure described in section 2.2. As a preliminary remark, the relative energies (calculated at PBE-dDsC level) between amorphous and cuboctahedron clusters show that for clusters smaller than 309 atoms, amorphous clusters are more stable than the cuboctahedral isomers (Figure S10). For a cluster size of 561 atoms, the cuboctahedron becomes more stable. Interestingly, this trend is found in qualitative agreement with the experimental observation showing the predominance of amorphous clusters for sizes smaller than ∼250 atoms.[78] Nevertheless, to overcome the limitation of considering only cuboctahedral isomers, such a result should prompt a more systematic theoretical investigation comparing the energies of amorphous clusters found in the present studies with ordered clusters exhibiting much more diverse morphologies (other than

Figure 7. Distribution of the signed deviation on bond lengths (A, B), bond angles (C, D), and radii of gyrations (E, F) for DFTB (red), GFN2-xTB (green), GFN0-xTB (gray), and ReaxFF (pink) with respect to PBE-dDsC values for the Pt_{13} and Pt_{55} amorphous datasets.

cuboctahedral ones). Concerning only the amorphous nanoparticles, we inspected the agreement of the tested low-cost methods with the DFT standard (as well as the performances of xTB MD) by plotting, for each nanoparticle, the deviation between its pure PBE-dDsC energy and its PBE-dDsC energy evaluated as single point on SE or FF geometry. The energy deviation (ΔE) reported in Figure 8A is computed as follows:

$$\Delta E = E_{PBE\text{-}dDsC \,//\, Low\text{-}cost} - E_{PBE\text{-}dDsC} \qquad (2)$$

Given the strong dependency of the electronic energy on the atomic coordinates, the quantity "ΔE" defined in eq 2 is exploited here, together with the mean Pt−Pt distance, to weigh the discrepancy between the benchmark PBE-dDsC structures and the low-cost ones (Figure 8).

The systematic decrease in the deviation (ΔE) of ReaxFF coupled with the increase in the system's size can be at least partially linked to its parametrization, which has been carried out initially on Pt_{100} clusters.[74] However, the energy deviation remains quite large to be exploitable (around 0.16 eV/atom for Pt_{561}). Moreover, ReaxFF completely reverses the canonic relationship between the intermetallic distances and the NP's size. GFN0-xTB follows the opposite trend and shows a significantly higher deviation for Pt_{147}, Pt_{309}, and Pt_{561} than for Pt_{13} and Pt_{55}. Although this energy deviation is rather comparable with the one observed for ReaxFF, the mean Pt−Pt distance on GFN0-xTB structures shows good agreement with PBE-dDsC compared with structures optimized with the other low-cost methods. In order to attempt to decrease the ΔE for GFN0-xTB and in light of the rather low computational cost of GFN0-xTB MD, the GFN0-xTB geometries of Pt_{147}, Pt_{309}, and Pt_{561} were further annealed during 50 ps, as explained in section 2.2. This additional
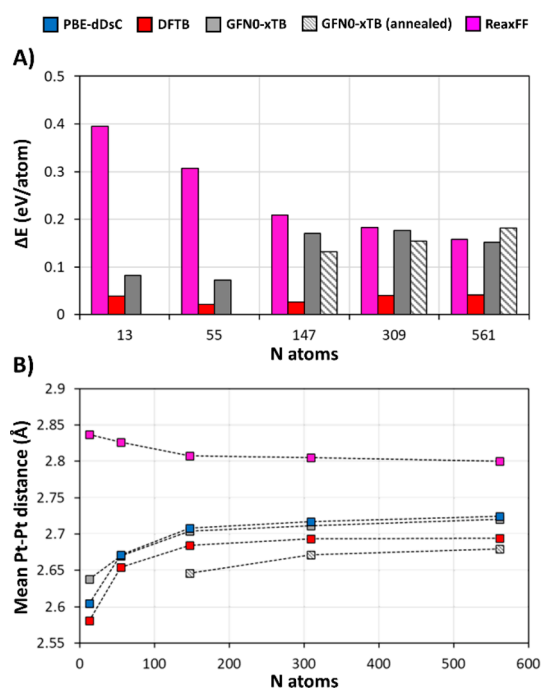
Figure 8. (A) Electronic energy difference between the full PBE-dDsC energy and the PBE-dDsC energy evaluated on DFTB (red), GFN0-xTB (gray), or ReaxFF (pink) geometry. The gray stripes represent the difference between the full PBE-dDsC energy and the PBE-dDsC energy evaluated on a geometry annealed with GFN0-xTB molecular dynamics. (B) Evolution of the mean Pt−Pt distance with particle size for PBE-dDsC (blue), DFTB (red), GFN0-xTB (gray), annealed GFN0-xTB (striped gray), and ReaxFF (pink) geometries.

annealing step succeeded in modestly reducing the ΔE of GFN0-xTB structures for Pt_{147} and Pt_{309} by about 0.03 eV and did not reduce the energy deviation for Pt_{561}. In this latter case, longer MD simulation times are probably required. Even though geometries obtained from GFN0-xTB molecular dynamics do not provide significant improvements in ΔE (eq 2, all computed at the PBE-dDsC level) with respect to geometries obtained thanks to ReaxFF for the largest particles, GFN0-xTB molecular dynamics is still able to provide reliable results for Pt–Pt bond lengths. Unfortunately, the averaged Pt–Pt bond length of annealed GFN0-xTB structures is not straightforwardly comparable with the others since they are generated through a completely different approach. Finally, DFTB proves itself as the best-performing low-cost method, even though it causes a systematic compression of Pt NPs (Figure 8B). Its low energy deviation (less than 0.05 eV/atom) reported for all of the investigated particle sizes states that the good performances exhibited by DFTB for Pt_{13} and Pt_{55} are maintained when increasing the number of atoms up to a few hundred. Since the employed parametrization for DFTB has been carried out solely on Pt_{13} and Pt_{55} clusters,[23] this indicates a good transferability of the set of parameters.

4. CONCLUSIONS

In this work, we assessed the performances of low-cost computational methods for the prediction of structural features and energetics of Pt nanoparticles of stoichiometry Pt_{13}, Pt_{55}, Pt_{147}, Pt_{309}, and Pt_{561}. The chosen low-cost methods were the semiempirical DFTB, GFN0-xTB, GFN1-xTB, GFN2-xTB, and ReaxFF, while the reference DFT functional was the dispersion-corrected PBE-dDsC. We carried out the benchmark study on four structural datasets, composed of (1) 14 amorphous and ordered Pt_{13} NPs, (2) 54 amorphous Pt_{13} NPs, (3) 93 amorphous Pt_{55} NPs, and (4) 5 amorphous NPs of stoichiometry Pt_x (x = 13, 55, 147, 309, 561). In the light of the discussed data, the following conclusions can be drawn.

DFTB is by far the method showing the best performances. Its parametrization, carried out on Pt_{13} and Pt_{55} NPs, grants good reproduction of properties for NPs of the same size. The good agreement with the DFT standard shown for NPs of bigger sizes also proves the good transferability of the parametrization. The performances of the remaining methods are found to be morphology- and size-dependent. GFN2-xTB produces reasonable results for amorphous Pt_{13} clusters, though not for ordered ones. Moreover, its performances worsen when increasing the cluster's size from 13 to 55, before failing the electronic SCC when further increasing the size of the system. While the agreement between GFN0-xTB and the DFT standard is quite poor for Pt_{13}, the method provides a satisfactory prediction of structural features for amorphous Pt_{55} geometries, making it competitive with DFTB. GFN0-xTB is slightly worsening for Pt_{147}, Pt_{309}, and Pt_{561} with respect to smaller clusters, though it outperforms the other methods on the averaged Pt–Pt bond length. ReaxFF behaves in the opposite way. Starting from considerably poor performances for Pt_{13} and Pt_{55} (both for geometries and for energies), its results get better for bigger NPs, becoming competitive with GFN0-xTB for Pt_{561}, even though the average Pt–Pt bond length is still not well represented. One last notable conclusion can be drawn about vibrational frequencies: independently from the parametrization and level of theory, all of the tested methods show a deviation in the description of vibrational features of Pt_{13}. Since the largest part of the error lies on the

vibrational entropy, this indicates a shared intrinsic difficulty in the description of potential wells related to collective vibrations. However, the error on G_{vib} is around 10 kJ/mol for DFTB, and even smaller for GFN0-xTB. Although this is far from being perfect, it still represents a good compromise due to the gain in CPU.

Considering what is here summarized, DFTB turns out to be the most cost-effective method for predicting geometries and energetics of Pt NPs of all of the investigated sizes and morphologies. However, since our task is to propose a low-level computational method for fast screening through candidate structures within the "multilevel modelling" of phenomena involving Pt NPs, a few final remarks have to be made. Although DFTB is the best performing method presented in this paper, the cheaper GFN0-xTB and ReaxFF should not be entirely discarded. The systematic error on structural parameters shown by ReaxFF suggests that a reoptimization of the parametrization could sensibly improve its performances. At the same time, the atom-specific parametrization on which GFN0-xTB relies indeed allows one to effortlessly include other atoms into the simulation (while DFTB would require a reparametrization), thus opening the path to the simulations of structures involving adsorbates or nanoalloys.

■ ASSOCIATED CONTENT

Ⓢ Supporting Information

The Supporting Information is available free of charge at https://pubs.acs.org/doi/10.1021/acs.jpcc.3c02799.

> Comparison between different GGA functionals on the details on the Pt_{13} small dataset (S1), CPU times (S2), additional data concerning histograms reporting errors on geometries (S3), regression analysis on relative stabilities (S4), thermochemical properties (S5) and relative stabilities (S6) for the Pt_{13} small dataset, theoretical background and additional data concerning KDE plots (S7), additional data concerning the regression analysis on relative stabilities for the Pt_{13} and Pt_{55} amorphous dataset (S8); amorphization energies (S9) (PDF)

> Coordinates optimized at PBE-dDsC level in XYZ format of (1) all the structures of the Pt_{13} small dataset, (2) the five lowest-energy structures of the Pt_{13} amorphous dataset, (3) the five lowest-energy structures of the Pt_{55} amorphous dataset, and (4) the amorphous Pt_{147}, Pt_{309}, Pt_{561} (TXT)

■ AUTHOR INFORMATION

Corresponding Authors

Alberto Ricchebuono — *Department of Chemistry, INSTM and NIS Centre, University of Torino, Torino I-10135, Italy;* ● orcid.org/0000-0003-0497-3785; Email: alberto.ricchebuono@unito.it

Céline Chizallet — *IFP Energies nouvelles, 63960 Solaize, France;* ● orcid.org/0000-0001-5140-8397; Email: celine.chizallet@ifpen.fr

Authors

Eleonora Vottero — *Department of Chemistry, INSTM and NIS Centre, University of Torino, Torino I-10135, Italy;* ● orcid.org/0000-0002-0183-0669

Andrea Piovano − *Institut Laue-Langevin (ILL), Grenoble 38000, France;* ⦿ orcid.org/0000-0002-5005-6307

Elena Groppo − *Department of Chemistry, INSTM and NIS Centre, University of Torino, Torino I-10135, Italy;* ⦿ orcid.org/0000-0003-4153-5709

Pascal Raybaud − *IFP Energies nouvelles, 63960 Solaize, France;* ⦿ orcid.org/0000-0003-4506-5062

Complete contact information is available at:
https://pubs.acs.org/10.1021/acs.jpcc.3c02799

Notes

The authors declare no competing financial interest.

REFERENCES

(1) Xu, Y.; Zhang, B. Recent Advances in Porous Pt-Based Nanostructures: Synthesis and Electrochemical Applications. *Chem. Soc. Rev.* **2014**, *43* (8), 2439−2450.

(2) Khan, M. A. R.; Mamun, M. S. Al; Ara, M. H. Review on Platinum Nanoparticles: Synthesis, Characterization, and Applications. *Microchem. J.* **2021**, *171* (September), No. 106840.

(3) Chen, A.; Holt-hindle, P. Platinum-Based Nanostructured Materials: Synthesis, Properties, and Applications. *Chem. Rev.* **2010**, *110*, 3767−3804.

(4) Campelo, J. M.; Luna, D.; Luque, R.; Marinas, J. M.; Romero, A. A. Sustainable Preparation of Supported Metal Nanoparticles and Their Applications in Catalysis. *ChemSusChem* **2009**, *2* (1), 18−45.

(5) Boudart, M. Catalysis by Supported Metals. *Adv. Catal.* **1969**, *20* (C), 153−166.

(6) Heck, R. M.; Farrauto, R. J. Automobile Exhaust Catalysts. *Appl. Catal. A Gen.* **2001**, *221* (1), 443−457.

(7) Gänzler, A. M.; Casapu, M.; Vernoux, P.; Loridant, S.; Cadete Santos Aires, F. J.; Epicier, T.; Betz, B.; Hoyer, R.; Grunwaldt, J. D. Tuning the Structure of Platinum Particles on Ceria In Situ for Enhancing the Catalytic Performance of Exhaust Gas Catalysts. *Angew. Chem., Int. Ed.* **2017**, *56*, 13078−13082.

(8) Keppeler, M.; Bräuning, G.; Radhakrishnan, S. G.; Liu, X.; Jensen, C.; Roduner, E. Reactivity of Diatomics and of Ethylene on Zeolite-Supported 13-Atom Platinum Nanoclusters. *Catal. Sci. Technol.* **2016**, *6* (18), 6814−6823.

(9) Chen, S.; Chang, X.; Sun, G.; Zhang, T.; Xu, Y.; Wang, Y.; Pei, C.; Gong, J. Propane Dehydrogenation: Catalyst Development, New Chemistry, and Emerging Technologies. *Chem. Soc. Rev.* **2021**, *50* (5), 3315−3354.

(10) Docherty, S. R.; Rochlitz, L.; Payard, P. A.; Copéret, C. Heterogeneous Alkane Dehydrogenation Catalysts Investigated via a Surface Organometallic Chemistry Approach. *Chem. Soc. Rev.* **2021**, *50* (9), 5806−5822.

(11) Sattler, J. J. H. B.; Ruiz-Martinez, J.; Santillan-Jimenez, E.; Weckhuysen, B. M. Catalytic Dehydrogenation of Light Alkanes on Metals and Metal Oxides. *Chem. Rev.* **2014**, *114*, 10613−10653.

(12) Goodier, J. Springer Handbook of Petroleum Technology. *Ref. Rev.* **2018**, *32* (7/8), 36−36.

(13) Le Goff, P. Y.; Kostka, W.; Ross, J. *Catalytic Reforming.* Springer Handbooks; Springer, 2017; Vol. *PartF1*, pp 589−616, DOI: 10.1007/978-3-319-49347-3_18.

(14) Piccolo, L. Restructuring Effects of the Chemical Environment in Metal Nanocatalysis and Single-Atom Catalysis. *Catal. Today* **2021**, *373* (April 2020), 80−97.

(15) Batista, A. T. F.; Baaziz, W.; Taleb, A. L.; Chaniot, J.; Moreaud, M.; Legens, C.; Aguilar-Tapia, A.; Proux, O.; Hazemann, J. L.; Diehl, F.; et al. Atomic Scale Insight into the Formation, Size, and Location of Platinum Nanoparticles Supported on γ-Alumina. *ACS Catal.* **2020**, *10*, 4193−4204.

(16) Vottero, E.; Carosso, M.; Ricchebuono, A.; Jiménez-Ruiz, M.; Pellegrini, R.; Chizallet, C.; Raybaud, P.; Groppo, E.; Piovano, A. Evidence for H_2-Induced Ductility in a Pt/Al_2O_3 Catalyst. *ACS Catal.* **2022**, *12* (10), 5979−5989.

(17) Avanesian, T.; Dai, S.; Kale, M. J.; Graham, G. W.; Pan, X.; Christopher, P. Quantitative and Atomic-Scale View of CO-Induced Pt Nanoparticle Surface Reconstruction at Saturation Coverage via DFT Calculations Coupled with in Situ TEM and IR. *J. Am. Chem. Soc.* **2017**, *139* (12), 4551−4558.

(18) Sangnier, A.; Genty, E.; Iachella, M.; Sautet, P.; Raybaud, P.; Matrat, M.; Dujardin, C.; Chizallet, C. Thermokinetic and Spectroscopic Mapping of Carbon Monoxide Adsorption on Highly Dispersed Pt/γ-Al_2O_3. *ACS Catal.* **2021**, *11* (21), 13280−13293.

(19) Zhai, H.; Alexandrova, A. N. Fluxionality of Catalytic Clusters: When It Matters and How to Address It. *ACS Catal.* **2017**, *7* (3), 1905−1911.

(20) Chizallet, C.; Raybaud, P. Density Functional Theory Simulations of Complex Catalytic Materials in Reactive Environments: Beyond the Ideal Surface at Low Coverage. *Catal. Sci. Technol.* **2014**, *4* (9), 2797−2813.

(21) Hu, C. H.; Chizallet, C.; Toulhoat, H.; Raybaud, P. Structural, Energetic, and Electronic Trends in Low-Dimensional Late-Transition-Metal Systems. *Phys. Rev. B - Condens. Matter Mater. Phys.* **2009**, *79* (19), 1−11.

(22) Ellaby, T.; Aarons, J.; Varambhia, A.; Jones, L.; Nellist, P.; Ozkaya, D.; Sarwar, M.; Thompsett, D.; Skylaris, C. K. Ideal versus Real: Simulated Annealing of Experimentally Derived and Geometric Platinum Nanoparticles. *J. Phys.: Condens. Matter* **2018**, *30* (15), 155301.

(23) Van Den Bossche, M. DFTB-Assisted Global Structure Optimization of 13- and 55-Atom Late Transition Metal Clusters. *J. Phys. Chem. A* **2019**, *123* (13), 3038−3045.

(24) Yang, Q.; Jiang, G. D.; He, S. G. Enhancing the Performance of Global Optimization of Platinum Cluster Structures by Transfer Learning in a Deep Neural Network. *J. Chem. Theory Comput.* **2023**, *19* (6), 1922−1930.

(25) Raybaud, P.; Chizallet, C.; Mager-Maury, C.; Digne, M.; Toulhoat, H.; Sautet, P. From γ-Alumina to Supported Platinum Nanoclusters in Reforming Conditions: 10 Years of DFT Modeling and Beyond. *J. Catal.* **2013**, *308*, 328−340.

(26) Mager-Maury, C.; Bonnard, G.; Chizallet, C.; Sautet, P.; Raybaud, P. H_2-Induced Reconstruction of Supported Pt Clusters: Metal-Support Interaction versus Surface Hydride. *ChemCatChem.* **2011**, *3* (1), 200−207.

(27) Hu, C. H.; Chizallet, C.; Mager-Maury, C.; Corral-Valero, M.; Sautet, P.; Toulhoat, H.; Raybaud, P. Modulation of Catalyst Particle Structure upon Support Hydroxylation: Ab Initio Insights into Pd_{13} and Pt_{13}/γ-Al_2O_3. *J. Catal.* **2010**, *274* (1), 99−110.

(28) Kaiser, S.; Maleki, F.; Zhang, K.; Harbich, W.; Heiz, U.; Tosoni, S.; Lechner, B. A. J.; Pacchioni, G.; Esch, F. Cluster Catalysis with Lattice Oxygen: Tracing Oxygen Transport from a Magnetite (001) Support onto Small Pt Clusters. *ACS Catal.* **2021**, *11* (15), 9519−9529.

(29) Xu, Y.; Shelton, W. A.; Schneider, W. F. Effect of Particle Size on the Oxidizability of Platinum Clusters. *J. Phys. Chem. A* **2006**, *110* (17), 5839−5846.

(30) Laletina, S. S.; Mamatkulov, M.; Shor, E. A.; Kaichev, V. V.; Genest, A.; Yudanov, I. V.; Rösch, N. Size-Dependence of the

Adsorption Energy of CO on Pt Nanoparticles: Tracing Two Intersecting Trends by DFT Calculations. *J. Phys. Chem. C* **2017**, *121* (32), 17371−17377.

(31) Calle-Vallejo, F.; Sautet, P.; Loffreda, D. Understanding Adsorption-Induced Effects on Platinum Nanoparticles: An Energy-Decomposition Analysis. *J. Phys. Chem. Lett.* **2014**, *5* (18), 3120−3124.

(32) Grimme, S.; Schreiner, P. R. Computational Chemistry: The Fate of Current Methods and Future Challenges. *Angew. Chemie - Int. Ed.* **2018**, *57* (16), 4170−4176.

(33) Aarons, J.; Sarwar, M.; Thompsett, D.; Skylaris, C.-K. Perspective: Methods for Large-Scale Density Functional Calculations on Metallic Systems. *J. Chem. Phys.* **2016**, *145* (22), 220901.

(34) Bannwarth, C.; Caldeweyher, E.; Ehlert, S.; Hansen, A.; Pracht, P.; Seibert, J.; Spicher, S.; Grimme, S. Extended Tight-Binding Quantum Chemistry Methods. *Wiley Interdiscip. Rev. Comput. Mol. Sci.* **2021**, *11* (2), 1−49.

(35) Caldeweyher, E.; Ehlert, S.; Hansen, A.; Neugebauer, H.; Spicher, S.; Bannwarth, C.; Grimme, S. A Generally Applicable Atomic-Charge Dependent London Dispersion Correction. *J. Chem. Phys.* **2019**, *150* (15), 154122.

(36) Sarwar, M.; Cooper, C.; Briquet, L.; Ukpong, A.; Perry, C.; Jones, G. Atomic-Scale Modelling and Its Application to Catalytic Materials Science. *Johnson Matthey Technol. Rev.* **2015**, *59* (3), 257−283.

(37) Fung, V.; Jiang, D. E. Exploring Structural Diversity and Fluxionality of Pt_n (n = 10−13) Clusters from First-Principles. *J. Phys. Chem. C* **2017**, *121*, 10796−10802.

(38) Zhai, H.; Ha, M. A.; Alexandrova, A. N. AFFCK: Adaptive Force-Field-Assisted Ab Initio Coalescence Kick Method for Global Minimum Search. *J. Chem. Theory Comput.* **2015**, *11* (5), 2385−2393.

(39) Heiles, S.; Johnston, R. L. Global Optimization of Clusters Using Electronic Structure Methods. *Int. J. Quantum Chem.* **2013**, *113* (18), 2091−2109.

(40) Chang, C. M.; Chou, M. Y. Alternative Low-Symmetry Structure for 13-Atom Metal Clusters. *Phys. Rev. Lett.* **2004**, *93* (13), 1−4.

(41) Li, S.; Li, H.; Liu, J.; Xue, X.; Tian, Y.; He, H.; Jia, Y. Structural and Electronic Properties of Ru_n Clusters (n = 2−14) Studied by First-Principles Calculations. *Phys. Rev. B - Condens. Matter Mater. Phys.* **2007**, *76* (4), 1−9.

(42) Vargas, A.; Santarossa, G.; Iannuzzi, M.; Baiker, A. Fluxionality of Gold Nanoparticles Investigated by Born-Oppenheimer Molecular Dynamics. *Phys. Rev. B - Condens. Matter Mater. Phys.* **2009**, *80* (19), 1−13.

(43) Pavan, L.; Di Paola, C.; Baletto, F. Sampling the Energy Landscape of Pt_{13} with Metadynamics. *Eur. Phys. J. D* **2013**, *67*, 24.

(44) Pracht, P.; Bohle, F.; Grimme, S. Automated Exploration of the Low-Energy Chemical Space with Fast Quantum Chemical Methods. *Phys. Chem. Chem. Phys.* **2020**, *22* (14), 7169−7192.

(45) Hourahine, B.; Aradi, B.; Blum, V.; Bonafé, F.; Buccheri, A.; Camacho, C.; Cevallos, C.; Deshaye, M. Y.; Dumitric, T.; Dominguez, A.; et al. DFTB+, a Software Package for Efficient Approximate Density Functional Theory Based Atomistic Simulations. *J. Chem. Phys.* **2020**, *152* (12), 124101.

(46) Pracht, P.; Caldeweyher, E.; Ehlert, S.; Grimme, S. A Robust Non-Self-Consistent Tight-Binding Quantum Chemistry Method for Large Molecules. *ChemRxiv* **2019**, DOI: 10.26434/chemrxiv.8326202.v1.

(47) Grimme, S.; Bannwarth, C.; Shushkov, P. A Robust and Accurate Tight-Binding Quantum Chemical Method for Structures, Vibrational Frequencies, and Noncovalent Interactions of Large Molecular Systems Parametrized for All spd-Block Elements (Z = 1−86). *J. Chem. Theory Comput.* **2017**, *13* (5), 1989−2009.

(48) Bannwarth, C.; Ehlert, S.; Grimme, S. GFN2-xTB - An Accurate and Broadly Parametrized Self-Consistent Tight-Binding Quantum Chemical Method with Multipole Electrostatics and Density-Dependent Dispersion Contributions. *J. Chem. Theory Comput.* **2019**, *15* (3), 1652−1671.

(49) Senftle, T. P.; Hong, S.; Islam, M. M.; Kylasa, S. B.; Zheng, Y.; Shin, Y. K.; Junkermeier, C.; Engel-Herbert, R.; Janik, M. J.; Aktulga, H. M. The ReaxFF Reactive Force-Field: Development, Applications and Future Directions. *npj Comput. Mater.* **2016**, *2*, 15011.

(50) Van Duin, A. C. T.; Dasgupta, S.; Lorant, F.; Goddard, W. A. ReaxFF: A Reactive Force Field for Hydrocarbons. *J. Phys. Chem. A* **2001**, *105* (41), 9396−9409.

(51) Chen, Y.; Cheng, T.; Goddard, W. A. Atomistic Explanation of the Dramatically Improved Oxygen Reduction Reaction of Jagged Platinum Nanowires, 50 Times Better than Pt. *J. Am. Chem. Soc.* **2020**, *142* (19), 8625−8632.

(52) Shin, Y. K.; Gai, L.; Raman, S.; Van Duin, A. C. T. Development of a ReaxFF Reactive Force Field for the Pt-Ni Alloy Catalyst. *J. Phys. Chem. A* **2016**, *120* (41), 8044−8055.

(53) Chenoweth, K.; Van Duin, A. C. T.; Persson, P.; Cheng, M. J.; Oxgaard, J.; Goddard, W. A. Development and Application of a ReaxFF Reactive Force Field for Oxidative Dehydrogenation on Vanadium Oxide Catalysts. *J. Phys. Chem. C* **2008**, *112* (37), 14645−14654.

(54) Zou, C.; Van Duin, A. Investigation of Complex Iron Surface Catalytic Chemistry Using the ReaxFF Reactive Force Field Method. *Jom* **2012**, *64* (12), 1426−1437.

(55) Priyadarsini, A.; Mallik, B. S. Comparative First Principles-Based Molecular Dynamics Study of Catalytic Mechanism and Reaction Energetics of Water Oxidation Reaction on 2D-Surface. *J. Comput. Chem.* **2021**, *42* (16), 1138−1149.

(56) Lourenço, M. P.; Herrera, L. B.; Hostaš, J.; Calaminici, P.; Köster, A. M.; Tchagang, A.; Salahub, D. R. Automatic Structural Elucidation of Vacancies in Materials by Active Learning. *Phys. Chem. Chem. Phys.* **2022**, *24* (41), 25227−25239.

(57) O'carroll, D.; English, N. J. A DFTB-Based Molecular Dynamics Investigation of an Explicitly Solvated Anatase Nanoparticle. *Appl. Sci.* **2022**, *12* (2), 780.

(58) Liu, X.; Salahub, D. R. Molybdenum Carbide Nanocatalysts at Work in the in Situ Environment: A Density Functional Tight-Binding and Quantum Mechanical/Molecular Mechanical Study. *J. Am. Chem. Soc.* **2015**, *137* (12), 4249−4259.

(59) Spicher, S.; Bursch, M.; Grimme, S. Efficient Calculation of Small Molecule Binding in Metal-Organic Frameworks and Porous Organic Cages. *J. Phys. Chem. C* **2020**, *124* (50), 27529−27541.

(60) Pracht, P.; Grant, D. F.; Grimme, S. Comprehensive Assessment of GFN Tight-Binding and Composite Density Functional Theory Methods for Calculating Gas-Phase Infrared Spectra. *J. Chem. Theory Comput.* **2020**, *16* (11), 7044−7060.

(61) Kruse, H.; Banáš, P.; Šponer, J. Investigations of Stacked DNA Base-Pair Steps: Highly Accurate Stacking Interaction Energies, Energy Decomposition, and Many-Body Stacking Effects. *J. Chem. Theory Comput.* **2019**, *15* (1), 95−115.

(62) Cutini, M.; Bechis, I.; Corno, M.; Ugliengo, P. Balancing Cost and Accuracy in Quantum Mechanical Simulations on Collagen Protein Models. *J. Chem. Theory Comput.* **2021**, *17* (4), 2566−2574.

(63) Perdew, J. P.; Burke, K.; Ernzerhof, M. Generalized Gradient Approximation Made Simple. *Phys. Rev. Lett.* **1996**, *77* (18), 3865−3868.

(64) Steinmann, S. N.; Corminboeuf, C. Comprehensive Benchmarking of a Density-Dependent Dispersion Correction. *J. Chem. Theory Comput.* **2011**, *7* (11), 3567−3577.

(65) Kresse, G.; Hafner, J. Ab Initio Molecular-Dynamics Simulation of the Liquid-Metalamorphous- Semiconductor Transition in Germanium. *Phys. Rev. B* **1994**, *49* (20), 14251−14269.

(66) Kresse, G.; Furthmüller, J. Efficiency of Ab-Initio Total Energy Calculations for Metals and Semiconductors Using a Plane-Wave Basis Set. *Comput. Mater. Sci.* **1996**, *6* (1), 15−50.

(67) Janthon, P.; Kozlov, S. M.; Viñes, F.; Limtrakul, J.; Illas, F. Establishing the Accuracy of Broadly Used Density Functionals in Describing Bulk Properties of Transition Metals. *J. Chem. Theory Comput.* **2013**, *9* (3), 1631−1640.

(68) Vega, L.; Ruvireta, J.; Viñes, F.; Illas, F. Jacob's Ladder as Sketched by Escher: Assessing the Performance of Broadly Used

Density Functionals on Transition Metal Surface Properties. *J. Chem. Theory Comput.* **2018**, *14* (1), 395−403.

(69) Steinmann, S. N.; Corminboeuf, C. A Generalized-Gradient Approximation Exchange Hole Model for Dispersion Coefficients. *J. Chem. Phys.* **2011**, *134* (4), 044117.

(70) Gautier, S.; Steinmann, S. N.; Michel, C.; Fleurat-Lessard, P.; Sautet, P. Molecular Adsorption at Pt(111). How Accurate Are DFT Functionals? *Phys. Chem. Chem. Phys.* **2015**, *17* (43), 28921−28930.

(71) Kresse, G.; Joubert, D. From Ultrasoft Pseudopotentials to the Projector Augmented-Wave Method. *Phys. Rev. B - Condens. Matter Mater. Phys.* **1999**, *59* (3), 1758−1775.

(72) Perdew, J. P.; Ruzsinszky, A.; Csonka, G. I.; Vydrov, O. A.; Scuseria, G. E.; Constantin, L. A.; Zhou, X.; Burke, K. Restoring the Density-Gradient Expansion for Exchange in Solids and Surfaces. *Phys. Rev. Lett.* **2008**, *100* (13), 1−4.

(73) Gale, J. D.; Rohl, A. L. The General Utility Lattice Program (GULP). *Mol. Simul.* **2003**, *29* (5), 291−341.

(74) Sanz-Navarro, C. F.; Astrand, P.-O.; Chen, D.; Rønning, M.; van Duin, A. C. T.; Jacob, T.; Goddard, W. A. Molecular Dynamics Simulations of the Interactions between Platinum Clusters and Carbon Platelets. *J. Phys. Chem. A* **2008**, *112* (7), 1392−1402.

(75) McDouall, J. J. W. *Computational Quantum Chemistry: Molecular Structure and Properties in Silico*; RSC theoretical and computational chemistry series; RSC Publishing, 2013.

(76) Nosé, S. An Extension of the Canonical Ensemble Molecular Dynamics Method. *Mol. Phys.* **1986**, *57*, 187−191.

(77) Berendsen, H. J. C.; Postma, J. P. M.; Van Gunsteren, W. F.; Dinola, A.; Haak, J. R. Molecular Dynamics with Coupling to an External Bath. *J. Chem. Phys.* **1984**, *81* (8), 3684−3690.

(78) Lambie, S. G.; Weal, G. R.; Blackmore, C. E.; Palmer, R. E.; Garden, A. L. Contrasting Motif Preferences of Platinum and Gold Nanoclusters between 55 and 309 Atoms. *Nanoscale Adv.* **2019**, *1* (6), 2416−2425.

(79) Momma, K.; Izumi, F. VESTA3 for Three-Dimensional Visualization of Crystal, Volumetric and Morphology Data. *J. Appl. Crystallogr.* **2011**, *44* (6), 1272−1276.

(80) Humphrey, W.; Dalke, A.; Schulten, K. VMD: Visual Molecular Dynamics. *J. Mol. Graph.* **1996**, *14* (1), 33−38.

(81) Waskom, M. Seaborn: Statistical Data Visualization. *J. Open Source Softw.* **2021**, *6* (60), 3021.

(82) Li, L.; Larsen, A. H.; Romero, N. A.; Morozov, V. A.; Glinsvad, C.; Abild-Pedersen, F.; Greeley, J.; Jacobsen, K. W.; Nørskov, J. K. Investigation of Catalytic Finite-Size-Effects of Platinum Metal Clusters. *J. Phys. Chem. Lett.* **2013**, *4* (1), 222−226.

(83) McQuarrie, D. A.; Simon, J. D. *Physical Chemistry: A Molecular Approach*; University Science Books: Sausalito, CA, 1997.